AD-A280 327

(11)

PROCESS SIMULATION AND MODELING FOR ADVANCED INTERMETALLIC ALLOYS

FINAL REPORT

DTIC
ELECTE
JUN 16 1994
S D
F

OFFICE OF NAVAL RESEARCH
Contract No. N00014-89-J-3166

September 1, 1989 to August 31, 1993

CLEMSON UNIVERSITY
Clemson, SC 29634

DTIC QUALITY INSPECTED 2

Principal Investigator: H. J. Rack

This document has been approved for public release and sale; its distribution is unlimited.

June 1, 1994

23RD 94-18508

94 6 14 172

REPORT DOCUMENTATION PAGE

Form Approved
OMB No. 0704-0188

Public reporting burden for this collection of information is estimated to average 1 hour per response, including the time for reviewing instructions, searching existing data sources, gathering and maintaining the data needed, and completing and reviewing the collection of information. Send comments regarding this burden estimate or any other aspect of this collection of information, including suggestions for reducing this burden, to Washington Headquarters Services, Directorate for Information Operations and Reports, 1215 Jefferson Davis Highway, Suite 1204, Arlington, VA 22202-4302, and to the Office of Management and Budget, Paperwork Reduction Project (0704-0188), Washington, DC 20503.

1. AGENCY USE ONLY (Leave blank)	2. REPORT DATE	3. REPORT TYPE AND DATES COVERED
	June 1, 1994	Final Report from 9/1/89 - 8/31/93

4. TITLE AND SUBTITLE
Process Simulation and Modeling for Advanced Intermetalic Alloys

5. FUNDING NUMBERS
Contract No.
N 00014-89-J-3166
(R&T Project No:
DU 89005)

6. AUTHOR(S)
H. J. Rack

7. PERFORMING ORGANIZATION NAME(S) AND ADDRESS(ES)
Department of Mechanical Engineering
Clemson University
Clemson, SC 29634-0921

8. PERFORMING ORGANIZATION REPORT NUMBER

9. SPONSORING/MONITORING AGENCY NAME(S) AND ADDRESS(ES)
Office of Naval Research
800 N. Quincy Street
Arlington, VA 22217-5000

10. SPONSORING/MONITORING AGENCY REPORT NUMBER

11. SUPPLEMENTARY NOTES

12a. DISTRIBUTION/AVAILABILITY STATEMENT

12b. DISTRIBUTION CODE

13. ABSTRACT (Maximum 200 words)

This Final Report summarizes the technical effort for contract "Process Simulation and Modeling for Advanced Intermetallic Alloys" undertaken under N00014-89-J-3166 (R&T Project Number: DU 89005) at Clemson University with H. J. Rack, Professor of Mechanical Engineering and Metallurgy acting as Principal Investigator. The report contains two major parts, Phase Stability (Part 1) and High Temperature Deformation Processing (Part 2).

Part 1 contains nine (9) papers describing the high temperature phase stability of Ti-Al-Nb and Ti-Al-V intermetallic alloys, primary attention being focused on the temperature regimes normally associated with deformation processing. Part 2 contains three (3) papers which demonstrate the utility of combining phase equilibria studies with Dynamic Material Modeling to simulate and model the high temperature deformation processing response of $\alpha + \beta$ and $\alpha_2 + \beta$ titanium alloys.

14. SUBJECT TERMS	15. NUMBER OF PAGES
Processing, Intermetallics	243
	16. PRICE CODE

17. SECURITY CLASSIFICATION OF REPORT	18. SECURITY CLASSIFICATION OF THIS PAGE	19. SECURITY CLASSIFICATION OF ABSTRACT	20. LIMITATION OF ABSTRACT
			unlimited

BLANK

TABLE OF CONTENTS

Page

SUMMARY 1

TECHNICAL PROGRESS REPORT

PART 1, Phase Stability

P. K. Chaudhury, M. Long and H. J. Rack, EFFECT OF V ON ELEVATED TEMPERATURE PHASE RELATIONS IN TITANIUM ALUMINIDES CONTAINING 43 at% Al, Mat'l Sci. Eng., Vol. A152, 37 (1992). 5

P. K. Chaudhury and H. J. Rack, Ti-Al-V TERNARY PHASE STABILITY AT ELEVATED TEMPERATURES, Scripta Met. Mat., Vol. 26, 691 (1992). 24

S. Guillard, D. Larsen and H. J. Rack, HIGH TEMPERATURE STABILITY OF XD™ TiB_2 REINFORCED NEAR-GAMMA Ti-48Al-2Nb-2Mn, Proc. 7th World Conf. on Titanium, I. L. Caplan and F. H. Froes, eds., TMS (Warrendale, PA), 1993, pp. 587-594. 29

M. Long, P. K. Chaudhury and H. J. Rack, ELEVATED TEMPERATURE PHASE STABILITY IN Ti-25Al-11Nb, Proc. 7th World Conf. on Titanium, I. Caplan and F. H. Froes, eds., TMS (Warrendale, PA), 1993, pp. 595-602. 41

S. Guillard and H. J. Rack, PHASE TRANSFORMATIONS IN XD™ TiB_2 REINFORCED NEAR-GAMMA Ti-48Al-2Nb-2Mn, Mat'l Sci. & Eng., in press. 53

T. Ahmed, H. J. Rack and H. M. Flowers, LIQUIDUS PROJECTION OF Ti-Al-V SYSTEM BASED ON ARC MELTED AND CAST MICROSTRUCTURES, Mat'l Sci & Tech., in press. 87

M. Long and H. J. Rack, PHASE STABILITY DURING CONTINUOUS HEATING/COOLING OF Ti_3Al-(Nb,V,Mo) TITANIUM ALUMINIDE ALLOYS, Mat'l Sci & Tech., in press. 114

M. Long and H. J. Rack, ENVIRONMENTAL EFFECTS ON HIGH TEMPERATURE PHASE STABILITY IN Ti-26Al-10Nb-3V-1Mo, submitted Scripta Met. Mat. 137

Accesion For

NTIS CRA&I ☒
DTIC TAB ☐
Unannounced ☐
Justification .....

By .....
Distribution /

Availability Codes

Dist | Avail and / or Special

A-1

T. Ahmed, F. Hayes and H. J. Rack, AGE HARDENING RESPONSE OF β_2 Ti-Al-V, submitted Mat'ls Sci Eng. 143

PART 2, High Temperature Deformation Processing

H. J. Rack and A. Wang, HIGH TEMPERATURE FLOW LOCALIZATION IN COARSE GRAINED β- PROCESSED Ti-6Al-4V, Proc. 7th World Conf. on Titanium, I. Caplan and F. H. Froes, eds., TMS(Warrendale, PA), 1993, pp. 1379-1386. 166

M. Long and H. J. Rack, THERMO-MECHANICAL STABILITY OF FORGED Ti-25Al-11Nb (at.%), Mat'l Sci. Eng., Vol. A170 215 (1993). 177

M. Long and H. J. Rack, THERMO-MECHANICAL STABILITY OF FORGED Ti-26Al-10Nb-3V-1Mo (at.%), submitted Mat'l Sci & Eng. 207

SUMMARY

This Final Report summarizes the technical effort for contract "Process Simulation and Modeling for Advanced Intermetallic Alloys" undertaken under N00014-89-J-3166(R&T Project Number: DU 89005) at Clemson University with H. J. Rack, Professor of Mechanical Engineering and Metallurgy acting as Principal Investigator. The report contains two major parts, Phase Stability(Part 1) and High Temperature Deformation Processing(Part 2).

Part 1 contains nine(9) papers describing the high temperature phase stability of Ti-Al-Nb and Ti-Al-V intermetallic alloys, primary attention being focused on the temperature regimes normally associated with deformation processing. This effort has demonstrated that interstitial or ß stabilizing additions drastically alter the elevated temperature phase equilibria observed in these systems. Further, the presence of equilibrium ß has been shown to be prevalent throughout the normal range of compositions being considered for commercial application. Finally, the potential for synthesizing a stable $ß_2$ + γ titanium intermetallic alloys has been examined.

Part 2 contains three(3) papers which demonstrate the utility of combining phase equilibria studies with Dynamic Material Modeling to simulate and model the high temperature deformation processing response of α + ß and α_2 + ß titanium alloys.

BLANK

PART 1

PHASE STABILITY

BLANK

Mat'l Sci. Eng.
Vol. A152, 37(1992)

EFFECT OF V ON ELEVATED TEMPERATURE PHASE RELATIONS IN TITANIUM ALUMINIDES CONTAINING 44 at. pct. Al

Prabir K. Chaudhury, M. Long and H. J. Rack
Department of Mechanical Engineering
Clemson University, Clemson, SC 29634

ABSTRACT

Differential scanning calorimetry(DSC), complemented by in-situ high temperature x-ray diffraction(HTXRD), has been utilized to examine phase stability in V containing TiAl($L1_0$) alloys over the temperature range 298 to 1773 K. Observations from alloys containing 4, 7 and 15 at. pct. V - 44 at. pct. Al - bal. Ti have shown that increasing V content results in the stabilization of the *bcc*, β, phase throughout the investigated temperature range. These additions of V do not however influence either the $\alpha \rightarrow \alpha_2 + \gamma$ eutectoid temperature or the stability of α_2 within the $\alpha + \alpha_2 + \beta$ phase region.

INTRODUCTION

Gamma titanium aluminide, TiAl($L1_0$), due to its low density, excellent oxidation resistance and good elevated temperature strength/modulus, shows great potential for elevated temperature application[1-3]. However, its ambient temperature properties, particularly its tensile ductility and fracture toughness remain low[4]. Nevertheless improvements in the mechanical properties of binary TiAl alloys have been achieved, a ductility of 2.7% having been attained by minimizing Al content in the γ phase[4,5], limiting oxygen content to 370 ppm[6] and introducing a small quantity of a second phase, α_2[5,7]. However continued interest

remains in achieving further enhancements in the ambient temperature properties of TiAl based alloys, particularly if this improvement could be accomplished without unduly sacrificing the alloys elevated temperature performance. Noteable have been attempts to introduce controlled quantities of the ductile ß phase, in a manner analagous to α_2 (Ti_3Al) alloys, and to more closely control the $\alpha_2 + \gamma$ TiAl alloy microstructure through appropriate thermomechanical treatment[4]. The ultimate success of either of these approaches will however require a more detailed knowledge of elevated temperature phase equilibria in complex Ti-Al-X alloy systems. The current study therefore has considered the effects of V, a known ß isomorphous stabilizing element, on phase stability in a 44 at. pct ($\alpha_2 + \gamma$) TiAl alloy, the latter representing a two-phase $\alpha_2 + \gamma$ alloy.

EXPERIMENTAL PROCEDURE

The chemical compositions of the triple vacuum melted alloys utilized in this investigation are tabulated in Table 1. Differential scanning calorimetry, using a Stanton Redfern/Omnitherm DSC 1500 thermal analysis system, was the primary experimental tool for this investigation. Modification of the instrument was necessary to ensure that the heating/cooling experiments were unaffected by the test environment. As depicted schematically in Fig. 1, this involved replacement of the original atmosphere control system with a seamless stainless delivery system, incorporation of a titanium gettering furnace and placement of an in-situ titanium getter in the hot zone of the furnace. The

purity of the reconfigured system was established by repeated heating/cooling of a high purity α-Ti sample, the lack of change in the ß transus temperature being taken as evidence of the system's ability to maintain atmosphere control.

DSC samples, weighing between 50 and 110 mg, were cut from the cast alloys with a rotating diamond blade, and washed with acetone/alcohol. Phase transformation temperatures utilizing the modified DSC apparatus were determined from 973 to 1748 K with duplicate samples during both heating and cooling in a high purity argon atmosphere at a rate of 20K/min. The DSC instrumental baseline was obtained using both empty pans and a high purity Al_2O_3 (sapphire) powder sample, with temperature calibration being performed with Al_2O_3 and high purity Mn standards[8].

High temperature x-ray diffraction experiments were undertaken to complement the DSC experiments. These utilized a Scintag diffractometer equipped with a high temperature furnace/vacuum chamber, which had again been modified in a manner similar to that outlined above for the DSC apparatus, to introduce and maintain an high purity inert argon gas atmosphere at a desired pressure. The high temperature x-ray diffraction samples, having dimensions of 10 mm x 25 mm x 0.25 mm, were prepared by wafering and grinding, with final preparation involving removal of 20 μm minimum surface layer by chemical thinning in a bath of 10 ml HNO_3 + 5 ml HF + 50 ml H_2O to eliminate deformation layer due to previous grinding. Samples were stored in a vacuum dessicator after washing in methanol, water and ethanol, and drying in air.

Initially, ambient temperature 2θ scans from 15 - 90° were obtained, the sample then being heated through a series of temperatures from 673 - 1773 K, diffraction spectra being collected at pre-selected temperatures. Typically, three to four samples of each alloy were examined, with rocking curves being obtained where deemed necessary to verify the presence, or absence, of phases at elevated temperatures. It should be noted however that this X-ray diffraction technique looses its sensitivity when volume fractions of the phases being identified are below approximately 5 percent. In addition, the large grain size of the alloys examined in this study precluded quantitative phase determination. Following data collection, the x-ray diffraction spectra were analyzed and the peaks indexed utilizing an iterative computer program that is capable of fitting the observed data to given cell structures using a least squares procedure.

RESULTS

The results of the DSC observations are shown in Figs. 2 thru 4. On heating, Ti-44Al-4V exhibited three distinct transformations, Fig. 2(a), however, only two transformations were noted on cooling, Fig. 2(b). Increasing V content also tended to blur the distinction between the two lower temperature trans-formations observed in Ti-44Al-4V, compare Figs. 3(a) and 4(a) with Fig. 2(a), while the presence of the two cooling transformations was replicated in Ti-44Al-7V and Ti-44Al-15V, Figures 3(b) and 4(b). Finally, the DSC results obtained upon heating Ti-44Al-15V suggested the presence of a transformation initiating below 1250 K,

this transformation not being observed in either Ti-44Al-4V or Ti-44Al-7V.

Typical x-ray diffraction data obtained for Ti-44Al-15V are presented in Fig. 5. These data show that Ti-44Al-15V was two phase($\beta + \gamma$) from 298 to 1198 K. At higher temperatures $\alpha_2(DO_{19})$ formation occurred and Ti-44Al-15V became three phase, $\alpha_2 + \beta + \gamma$. Ultimately above 1358 K the γ phase disappeared, above 1548 K the α_2 phase disordered to α phase, and finally, above 1673 K, Ti-44Al-15V was single phase β.

Similar elevated temperature phase transitions involving transformation from a three phase $\alpha_2 + \beta + \gamma$ to a three phase $\alpha + \alpha_2 + \gamma$ alloy, disappearance of the ordered α_2 phase, and finally transformation to a single phase β alloy were observed in Ti-44Al-4V and Ti-44Al-7V. However, neither of these alloys exhibited the $\beta + \gamma$ to $\alpha_2 + \beta + \gamma$ transition observed in Ti-44Al-15V, both were three phase $\alpha_2 + \beta + \gamma$ at 298 K, although the quantity of β in Ti-44Al-4V was low, approaching the resolution of the diffraction techniques.

DISCUSSION

The combined observations of the differential scanning calorimetry and in-situ high temperature x-ray diffraction experiments can be utilized to establish the range of phase stability for the Ti-44Al-xV alloys examined. Ambient temperature X-ray analysis indicates that increasing V content leads to a decrease in α_2 stability and increased stabilization of the bcc, β, and γ phases. For example, detection of the β phase was difficult

in Ti-44Al-4V, suggesting that this alloy contained a maximum of 5 volume percent ß, α_2 and γ being the predominant phases present at ambient temperatures, while α_2 was absent in Ti-44 Al-15 V, a two phase ß + γ alloy at ambient temperatures.

Table 2 lists the temperatures for the α + ß -> ß transus as determined from the DSC experiments, the ß transus temperature for binary Ti-44Al[9] also being included for comparison. These results indicate that an approximate 35K difference in ß transus temperature was observed when determined by DSC heating and cooling experiments. Prior studies[10] of ß transus determination in Ti-6Al-4V utilizing both DSC and metallographic methods suggest that this difference is due to the initial sluggishness of the ß -> α + ß reaction on cooling and that the ß transus as determined during heating gives a more accurate ß transus temperature. Notwithstanding this difference, the DSC results do indicate that increasing V content results in a decrease in the ß transus temperature.

In contrast, the α -> α_2 + γ eutectoid temperatures were, as determined through either DSC heating or cooling experiments, within experimental accuracy, identical, Table 3. Comparison with the eutectoid temperature reported for Ti-44Al[9], indicates that the addition of V, at least within the range investigated, has a negligible effect on the α -> α_2 + γ eutectoid temperature. This lack of sensitivity to V content is apparently associated with extensive partitioning of V to the ß phase, the latter phase not participating in the invariant eutectoid reaction.

The extent and importance of this partitioning was reinforced by in-situ x-ray observations which showed that α_2 stability, as characterized by the temperature for completion of $\alpha + \alpha_2 + \beta \rightarrow \alpha + \beta$ transformation, was relatively unaffected by the range of V additions considered in this investigation, Table 4.

Based on the combined DSC and x-ray results, it is possible to describe the phase transformations expected in Ti-44Al-xV alloys during heating/cooling:

Ti-44Al-4V:

$$\alpha_2+\beta+\gamma \xrightarrow{1373} \alpha_2+\alpha+\beta \xrightarrow{1540} \alpha+\beta \xrightarrow{1711} \beta$$

Ti-44Al-7V:

$$\alpha_2+\beta+\gamma \xrightarrow{1378} \alpha_2+\alpha+\beta \xrightarrow{1538} \alpha+\beta \xrightarrow{1676} \beta$$

Ti-44Al-15V:

$$\beta + \gamma \xrightarrow{1198} \alpha_2+\beta+\gamma \xrightarrow{1358} \alpha_2+\alpha+\beta \xrightarrow{1538} \alpha+\beta \xrightarrow{1643} \beta$$

where the V enriched β phase does not participate in the $\alpha_2 + \gamma \rightarrow \alpha$ eutectoid reaction.

Finally, a comparison of the present results with currently available Ti-Al-V ternary isotherms at 1073 and 1273 K[11] shows that while the phase equilibria observed in Ti-44Al-7V agrees with both isotherms, differences exist for the other two alloys. The prior isotherms indicate Ti-44Al-4V to be $\alpha_2+\gamma$ and Ti-44Al-15V to be $\beta+\gamma$ at both 1073 and 1273 K. However, the present results show that Ti-44Al-4V is a three phase $\alpha_2+\beta+\gamma$ alloy at 1048 K and remains

in the three-phase field well above 1273 K. In contrast, Ti-44Al-15V, was observed to be in the $\beta+\gamma$ phase field at 1073 K, transforming to a $\alpha_2+\beta+\gamma$ alloy above 1200 K.

CONCLUSIONS

1. The addition of V to α_2 + γ Ti-44Al results in
   (a) an increase in the ambient temperature stability of the β and γ phases, and
   (b) a decrease in the β transus temperature.
2. V additions, in contrast, have a negligible effect on
   (a) the α -> α_2 + γ eutectoid transformation temperature, or
   (b) the elevated temperature stability of α_2 within the α + α_2 + γ phase field.

ACKNOWLEDGEMENT

This research was sponsored by the Defense Advanced Research Projects Agency unde. the contract N00014-89-J-3166 supervised by Mr. W. Barker and monitored by Dr. G. Yoder of the Office of Naval Research. The alloys were prepared by TIMET, Inc., under the direction of Dr. P. Bania. Initial X-ray investigations were undertaken in cooperation with the High Temperature Materials Laboratory at Oak Ridge National Laboratory. Finally, the experimental assistance provided by R. Gallahorn is gratefully acknowledged.

REFERENCES

1. S. M. L. Sastry and H. A. Lipsitt, Met. Trans., 8A (1977) 1543.

2. M. J. Blackburn and M. P. Smith, Air Force Wright Aeronautical Laboratories Report (No. AFWAL-TR-82-4086), (1982).

3. H. A. Lipsitt, in C. C. Koch, C. T. Liu and N. S. Stoloff (eds.), High Temperature Ordered Intermetallic Alloys, MRS, Pittsburgh, Pa, 1984, p.351.

4. Y-W. Kim, in J.O. Stiegler, L. A. Johnson and D. P. Pope (eds.), High Temperature Ordered Intermetallic Alloys IV, Vol. 213, 1991, in press.

5. S-C. Huang and E. L. Hall, in C. T. Liu, A. I. Taub, N. S. Stoloff and C. C. Koch (eds.), High Temperature Ordered Intermetallic Alloys III, MRS, Pittsburgh, Pa, Vol. 133, 1989, p. 373.

6. T. Kawabata, M. Tadano and O. Izumi, Scripta Met., 22 (1988) 1725.

7. Y-W. Kim, Jn of Metals, July 1989, 24.

8. M. Long, P. Chaudhury and H. J. Rack, Clemson University, Unpublished Research, 1991.

9. C. McCullough, J. J. Valencia, C. G. Levi and R. Mehrabian, Acta Met., 37 (1989) 1321.

10. A. Wang and H. J. Rack, Clemson University, Unpublished Research, 1991.

11. K. Hashimoto, H. Doi and T. Tsujimoto, Trans. Jap. Inst. Met., 27 (1986) 741.

TABLE 1 : Chemical Composition of Ti-Al-V Alloys.

Alloy	Elements (wt.%)					
	Al	V	Fe	O	N	Ti
Ti-44Al-4V	30.5	5.03	0.091	0.076	0.004	Bal.
Ti-44Al-7V	30.55	8.92	0.095	0.067	0.006	Bal.
Ti-44Al-15V	30.45	19.8	0.120	0.056	0.012	Bal.

TABLE 2: β-Transus Temperatures of Ti-Al-V Alloys

Alloy	Temperature(K)	
	Heating	Cooling
Ti-44Al	1730	
Ti-44Al-4V	1711	1680
Ti-44Al-7V	1676	1641
Ti-44Al-15V	1643	1603

TABLE 3: Eutectoid Temperatures of Ti-Al-V Alloys

Alloy	Temperature(K)	
	Heating	Cooling
Ti-44Al	1390	
Ti-44Al-4V	1373	1383
Ti-44Al-7V	1378	1373
Ti-44Al-15V	1358	1376

TABLE 4: α_2 Stability Temperature

Alloy	Temperature(K)
Ti-44Al-4V	1540
Ti-44Al-7V	1538
Ti-44Al-15V	1538

LIST OF FIGURES

Figure 1. Schematic diagram of inert atmosphere differential scanning calorimeter(DSC).

Figure 2. DSC curve for Ti-44Al-4V at heating rate of 20K/min.

Figure 3. DSC curve for Ti-44Al-7V at heating rate of 20K/min.

Figure 4. DSC curve for Ti-44Al-15V at heating rate of 20K/min.

Figure 5. Typical X-ray diffraction data obtained from Ti-44Al-15V.

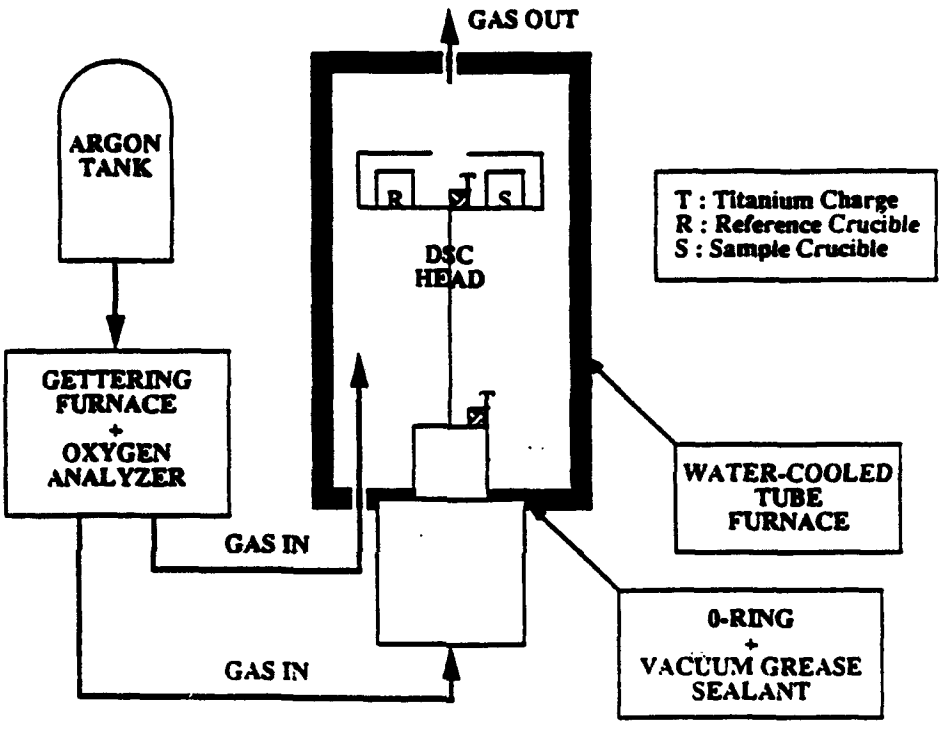

Figure 1. Schematic diagram of inert atmosphere differential scanning calorimeter(DSC).

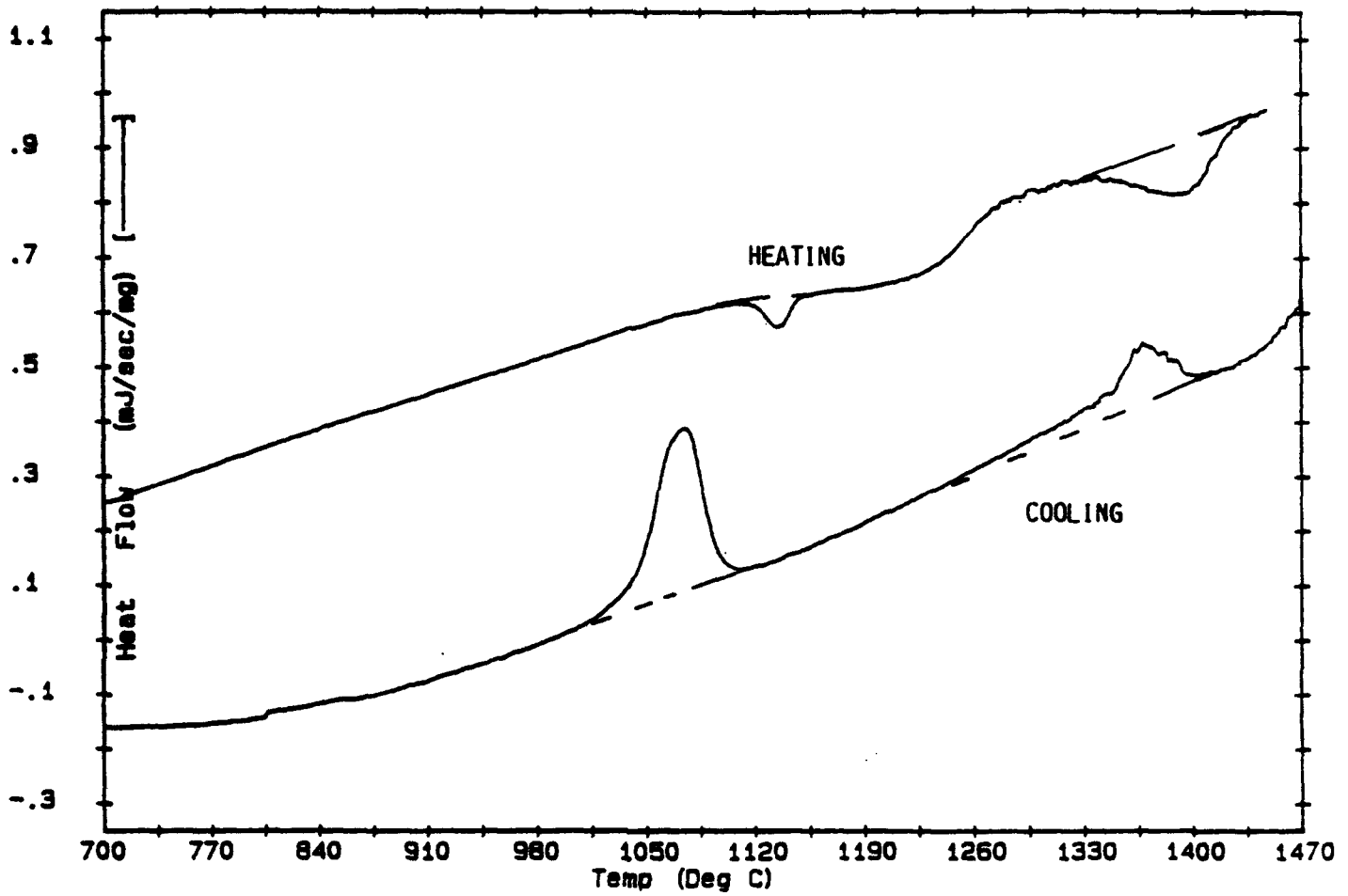

Figure 2. DSC curve for Ti-44Al-4V at heating rate of 20K/min.

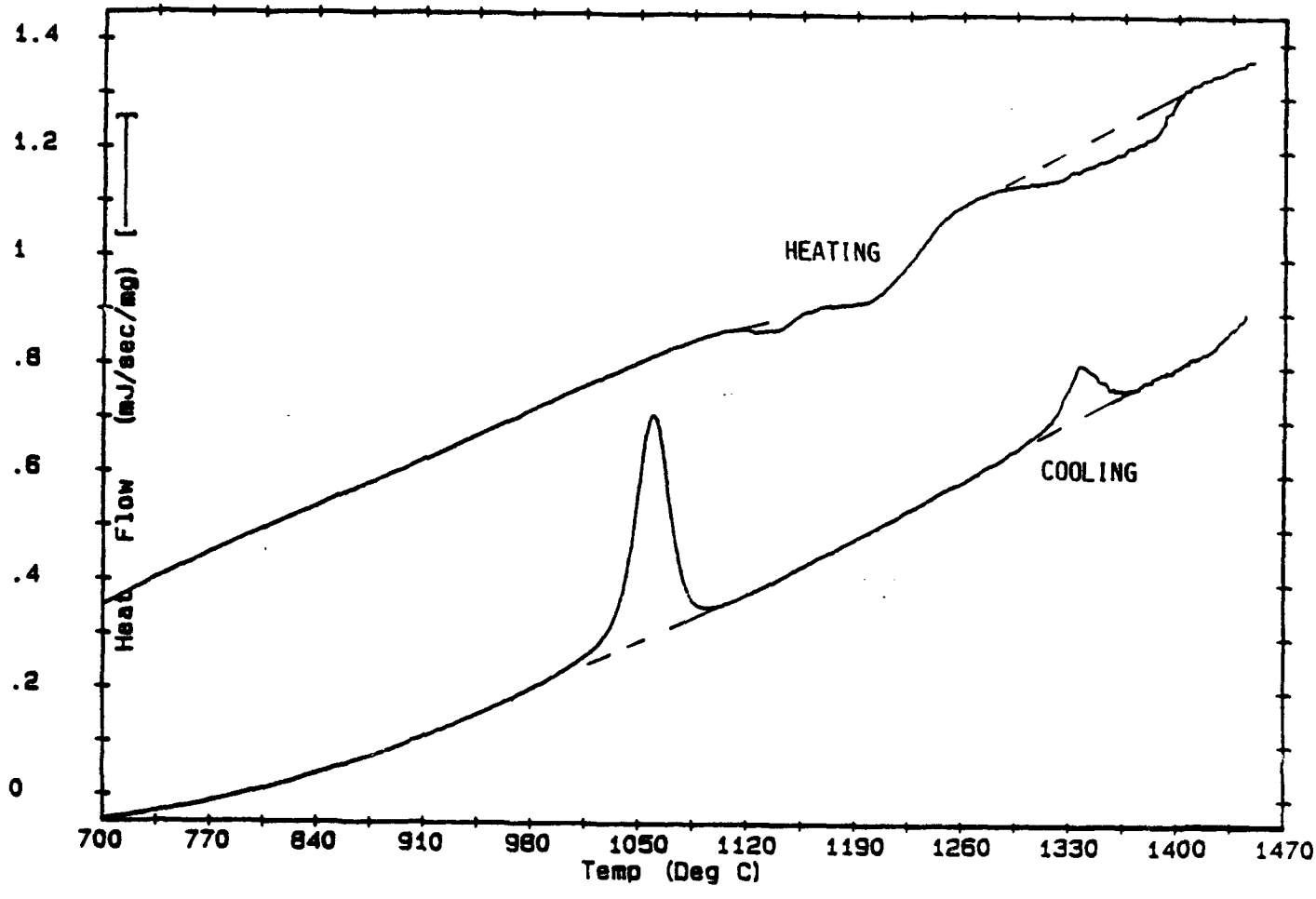

Figure 3. DSC curve for Ti-44Al-7V at heating rate of 20K/min.

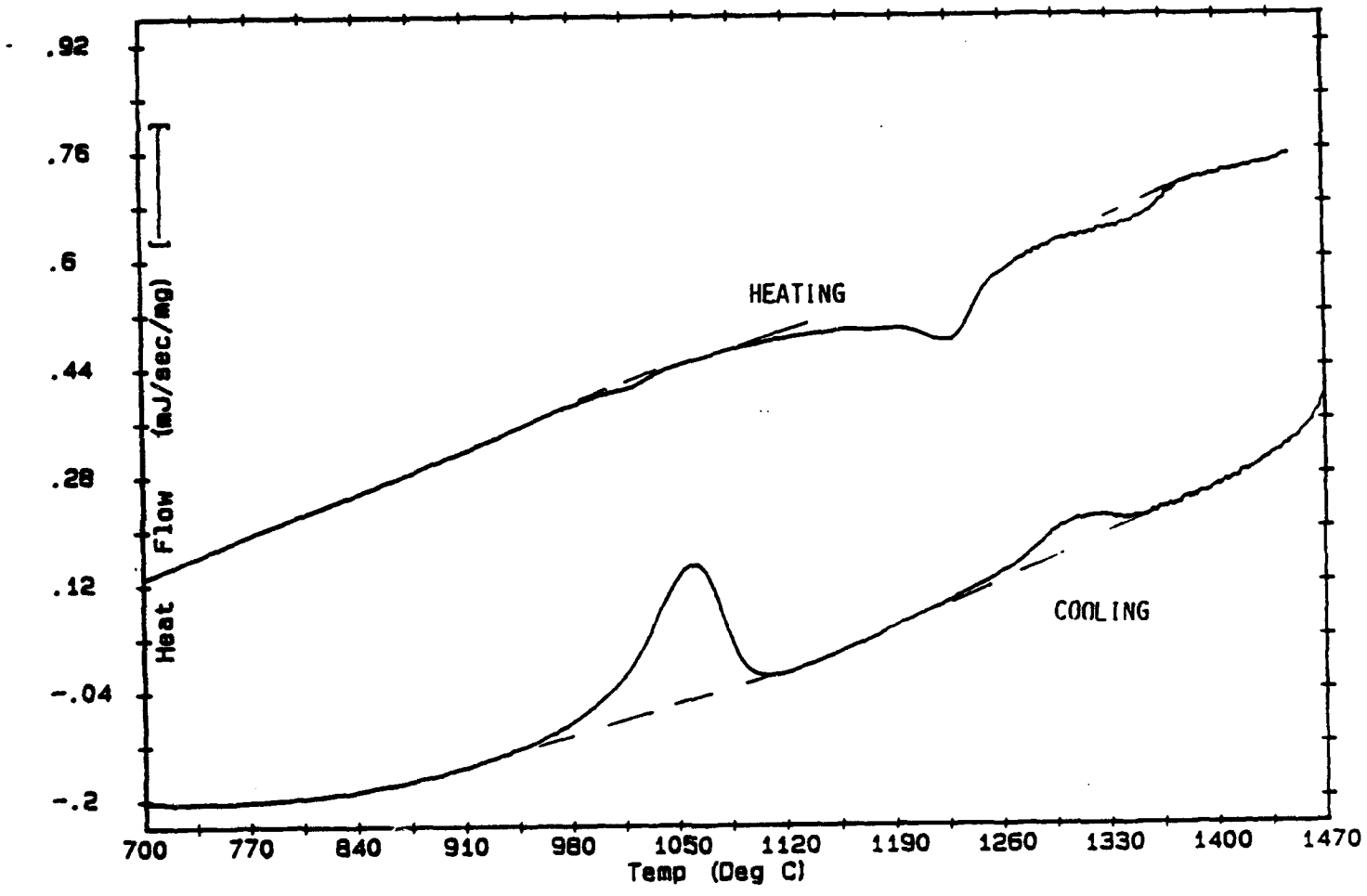

Figure 4. DSC curve for Ti-44Al-15V at heating rate of 20K/min.

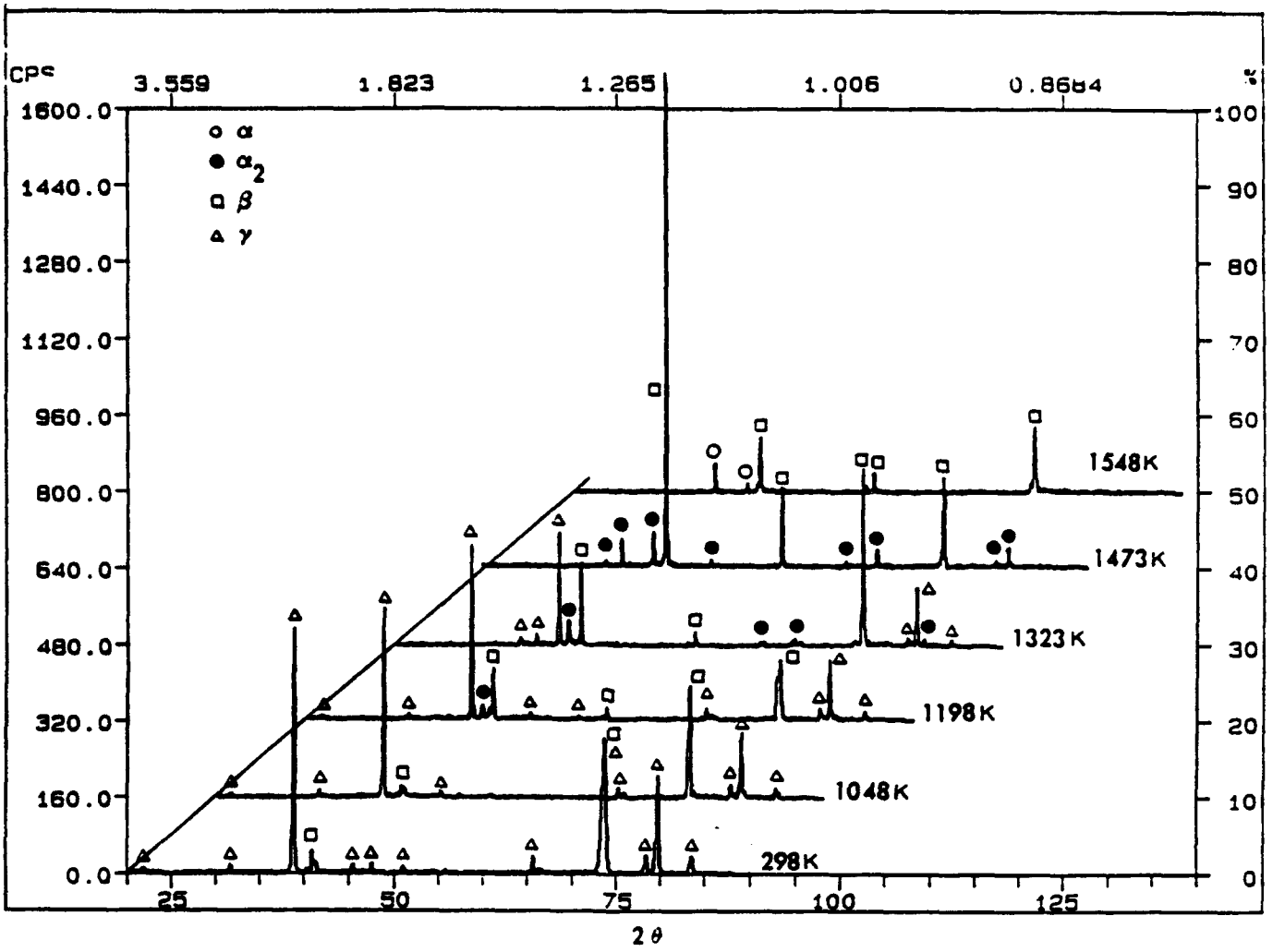

Figure 5. Typical X-ray diffraction data obtained from Ti-44Al-15V.

Scripta Met. Mat.
Vol. 26, 691(1992)

Ti-Al-V TERNARY PHASE STABILITY AT ELEVATED TEMPERATURES

Prabir K. Chaudhury and H. J. Rack
Department of Mechanical Engineering
Clemson University, Clemson, SC 29634

Introduction

Ternary additions of the beta isomorphous elements, Nb, V, Mo and Ta, have long been known to improve the ambient temperature ductility and fracture toughness of α_2 (Ti_3Al) and γ (TiAl) intermetallic alloys [1 - 4]. In the former the increase has been related to the stabilization of the ductile β phase, while the latter enhancement has been related to changes in tetragonality, unit cell volume, twin density and/or electronic structure. Control of the mechanical properties of ternary and more complex α_2(Ti_3 Al) and γ(Ti Al) intermetallic alloys will require optimization of their prior thermomechanical history. Such control can be achieved through a knowledge of relevant high temperature phase equilibria; indeed, establishment of appropriate phase equilibria in the Ti-Al-Nb ternary system continues to be the subject of an extensive investigation at the University of Wisconsin [5].

The earliest study of the Ti-Al-V system is that reported by Raman [6], who presented an isotherm at 1373 K. Hashimoto et al [7] extended this study to lower temperatures, i.e., 1073 and 1273 K. Neither investigation, however, considered alloys that would be expected to fall within the $\alpha_2 + \gamma$ phase field. In addition, neither reported the interstitial content (O + N + C) of their alloys, thereby neglecting the important influence that interstutials may have in Ti-Al-V elevated temeratnre phase stability. Finally these studies utilized samples that had been quenched from elevated temperature, subsequent phase determination involving room temperature x-ray analysis. This procedure may yield spurious results; for example, Blackburn [8] has shown that the $\alpha \rightarrow \alpha_2$ transformation cannot be suppressed at dilute Al compositions. In addition, quenching can result in complex phase transformations; for example, quenching Ti-Al-Nb alloys from the β phase field may lead to formation of α_2, β_0, an ordered bcc structure, ω or O, an orthorombic phase [9-16].

Accordingly, this communication presents the preliminary results of a re-examination of the Ti-Al-V system emphasizing alloys in the $\alpha_2 + \gamma$, $\alpha_2 + \beta$, $\beta + \gamma$ and $\alpha_2 + \beta + \gamma$ phase fields. The principal experimental procedure utilized was *in-situ high temperature* x-ray diffraction (HTXRD).

Experimental Procedures

The chemical compositions (in wt.%) of the five Ti-Al-V alloys prepared by TIMET, Inc., Henderson, Nevada are presented in Table 1. These alloys were received as 15 kg. triple vacuum melted ingots. Thin slices for high temperature x-ray diffraction were removed from these ingots by wafering, grinding and chemical thinning in a solution of 10 ml HNO_3 + 5 ml HF + 50 ml H_2O to a final dimension of 10 mm x 25 mm x 0.2 mm. The HTXRD specimens were then washed in methanol, water and ethanol, and dried.

Duplicate x-ray diffraction patterns were obtained utilizing Cu Kα radiation with a high temperature vacuum/inert atmosphere chamber having a dual resistance heating arrangement, i.e., Ta strip and shell heaters. To ensure an oxygen free inert atmosphere, the chamber was repeatedly evacuated and flushed with gettered argon gas, with, in addition, pure Ti gettering coils being placed between the shell and the strip heaters for in-situ oxygen removal. Specimens were heated at 40 K/min, to 1073, 1273 and 1373 K, either in 50 to 100 K increments, allowing 5 - 10 min. at every temperature, or directly to the desired temperature. Temperatures were monitored by a c-type thermocouple attached to the specimen and maintained within $\pm$ 0.5 K using a microcontroller.

The x-ray diffraction data collected were analyzed and peaks indexed utilizing a computer program that fit the observed 2θ angles, calculating, by a least square fit, appropriate lattice parameters through successive approximation.

Results And Discussion

Typical x-ray diffraction patterns of V5 at 1073 and 1273 K are shown in Figures 1 and 2. Due to the large grain size in the cast material it was not possible to observe all diffracting planes for each of the phases, and the peak intensities do not, therefore, represent those expected from a randomly oriented polycrystalline specimen. The diffraction patterns shown were obtained immediately after attaining thermal equilibrium, Figures 1a and 2a, following a one hour isothermal hold, Figures 1b and 2b, and finally, following two hours at temperature, Figures 1c and 2c. These results, which were replicated by all alloys examined, indicate that no change in phase identity, only peak intensities changes due to grain growth and/or re-orientation, was occasioned by prolonged exposure at these elevated temperatures. This confirms that, at least for the Ti-Al-V system, thermodynamic equilibria can be achieved utilizing the current experimental procedures.

Phase identification at 1073, 1273 and 1373 K for all alloys is summarized in Table 2. Ternary isotherms at 1073, 1273 and 1373 K have been drawn based on these results and incorporating those of Hashimoto et al [7], Figures 3a and 3b, and Raman [6], Figure 3c. While the majority of the results are consistent with these prior investigations, some differences in phase boundary location do exist. For example, Figures 3a and b indicate that the $\alpha_2 + \beta + \gamma$ phase-field at 1073 and 1273 K exist to lower V contents 4 at. pct versus 7 at. pct as originally reported by Hashimoto et al [7]. Furthermore, examination of the three isotherms suggests that both the β and γ phase fields expand with increasing temperature, and that the extent of the $\alpha_2 + \beta + \gamma$ three-phase field initially increases with increasing temperature from 1073 to 1273 K, then contracts at higher temperatures, 1373 K.

Summary and Conclusion

This study has shown that high temperature x-ray diffraction can be utilized to establish phase equilibria in Ti-Al-V alloys. The results indicate that the ternary $\alpha_2 + \beta + \gamma$ phase field may be wider than previously recognized, while both the β and γ phase fields expand with increasing temperature.

Acknowledgement

This research was sponsored by the Defense Advanced Research Projects Agency under contract N00014-89-J-3166 supervised by Mr. W. Barker and monitored by Dr. G. Yoder of the Office of Naval Research. The experimental assistance of M. Long is gratefully acknowledged.

References

(1) S. M. L. Sastry and H. A. Lipsitt, Met. Trans., 8A 1543 (1977).
(2) M. J. Blackburn and M. P. Smith; Air Force Wright Aeronautical Laboratories Report (No. AFWAL-TR-82-4086) (1982).
(3) H. A. Lipsitt, in High Temperature Ordered Intermetallic Alloys, C. C. Koch, C. T. Liu and N. S. Stoloff, eds., Mat Res. Soc., Pittsburgh, PA (1984), p. 351.
(4) Y-W. Kim, in High Temperature Ordered Intermetallic Alloys IV, J. O. Stiegler, L. A. Johnson and D. P. Pope, eds. to be published.
(5) J. H. Perepezko, Y. A. Chang, L. E. Seitzman, J. C. Lin, N. R. Bonda, T. J. Jewett and J. C. Mishurda, in High Temperature Aluminides and Intermetallics, S. H. Whang, C. T. Liu, D. P. Pope and J. O. Stiegler, eds., The Mineral Metals and Materials Society (1990), p. 19.
(6) V. A. Raman; Z. Metallkde., 53, 535(1966).
(7) K. Hashimoto, Haruo Doi and T. Tsujimoto, Trans. Jap. Inst. Met., 27, 741(1986).
(8) M. J. Blackburn, in The Science Technology and Application of Titanium, R. I. Jaffee and N. E. Promisel, eds. Pergamon Press, Oxford(1970), p. 633.
(9) K. Kaltenbach, S. Gama, D. G. Pinatti, K. Schulze and E-T. Henig, Z. Metallkde., 80, 535(1989).
(10) H. T. Kestner-Weykamp, C. H. Ward, T. F. Broderik and M. J. Kaufman, Scripta Met., 23, 1697(1989).
(11) D. Banerjee, A. K. Gogia, T. K. Nandi and V. A. Joshi, Acta Met., 36, 871(1988).
(12) R. Strychor, J. C. Williams and W. A. Soffa, Met. Trans., 19A, 225(1988).
(13) O. N. Andreyev, Russian Metallurgy, 1, 127(1970).

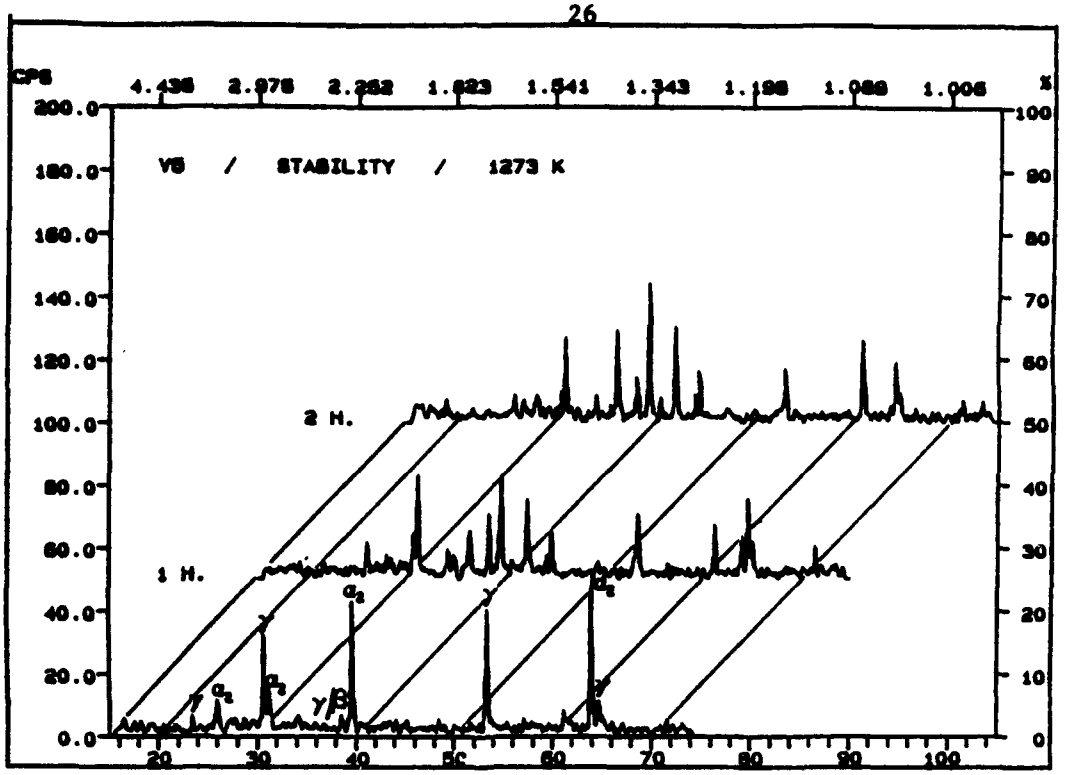

Figure 2. High temperature x-ray diffraction patterns for V5 alloy immediately after thermal equilibrium, after one hour and after two hours at 1273 K.

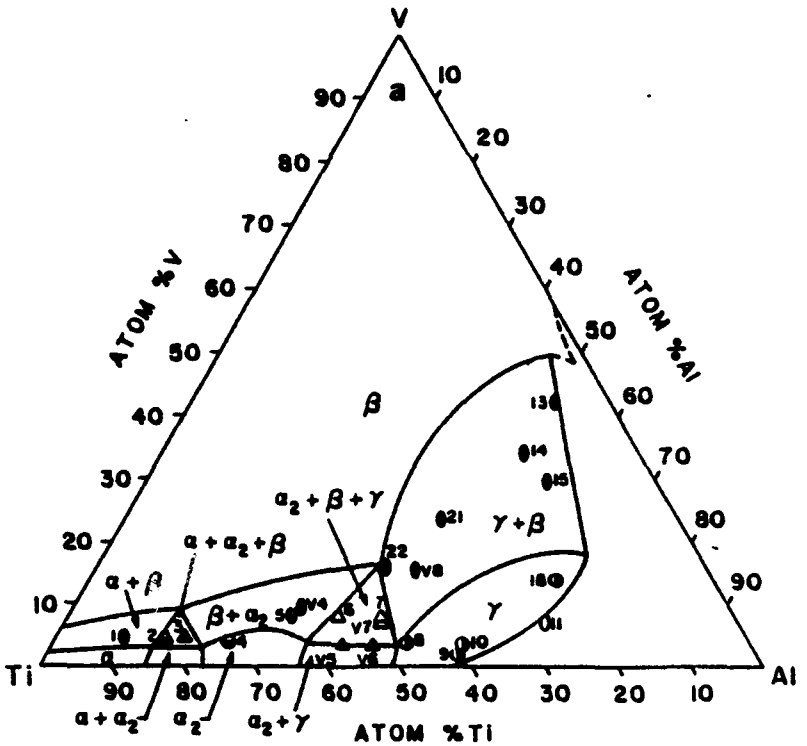

Figure 3. Ternary isothermal diagram at (a) 1073 K

(14) T. T. Nartova and G. G. Sopochkin, Russian Metallurgy, 2, 138(1970).
(15) M. J. Cieslak, T. J. Headley and W. A. Baselack III, Met. Trans., 21A, 1273(1990).
(16) K. Murleedharan and D. Banerjee, Met. Trans., 20A, 1139(1989).

TABLE 1. Chemical composition of the Ti-Al-V alloys.

Alloys	Elements (wt.%)					
	Al	V	Fe	O	N	Ti
V4	20.4	11.6	0.135	0.063	0.008	Bal.
V5	27.95	5.11	0.093	0.085	0.004	Bal.
V6	30.5	5.03	0.091	0.076	0.004	Bal.
V7	30.55	8.92	0.095	0.067	0.006	Bal.
V8	30.45	19.8	0.120	0.056	0.012	Bal.

TABLE 2: Equilibrium phase constituents at 1073, 1273 and 1373 K.

Alloy	Composition at.% Ti-Al-V	1073 K	1273 K	1373 K
V4	59-32-9	$\alpha_2 + \beta$	$\alpha_2 + \beta$	$\alpha_2 + \beta$
V5	57-39-4	$\alpha_2 + \beta + \gamma$	$\alpha_2 + \beta + \gamma$	$\alpha_2 + \beta + \gamma$
V6	52-44-4	$\alpha_2 + \beta + \gamma$	$\alpha_2 + \beta + \gamma$	$\alpha_2 + \beta + \gamma$
V7	49-44-7	$\alpha_2 + \beta + \gamma$	$\alpha_2 + \beta + \gamma$	$\alpha_2 + \beta + \gamma$
V8	41-44-15	$\beta + \gamma$	$\alpha_2 + \beta + \gamma$	$\alpha_2 + \beta + \gamma$

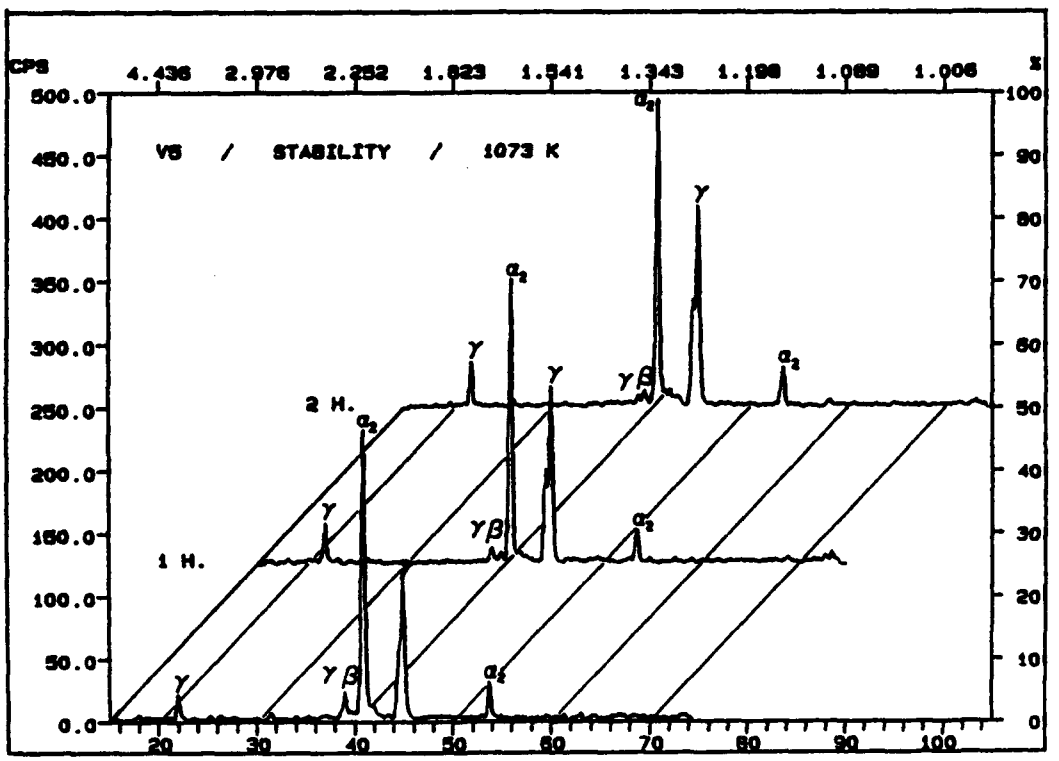

Figure 1. High temperature x-ray diffraction patterns for V5 alloy immediately after thermal equilibrium, after one hour and after two hours at 1073 K.

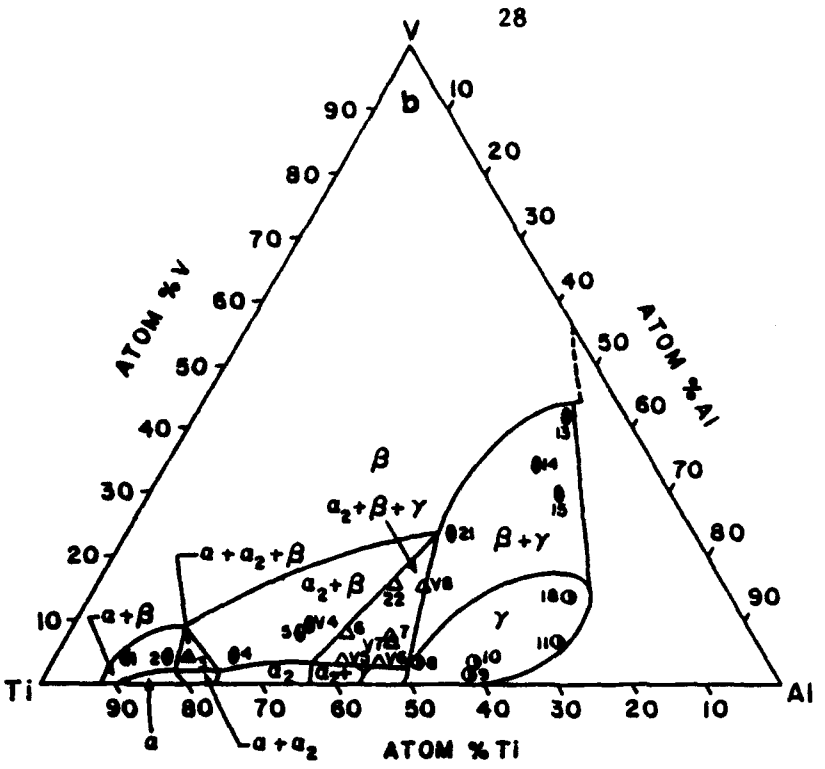

Figure 3 cont. (b) 1273 K

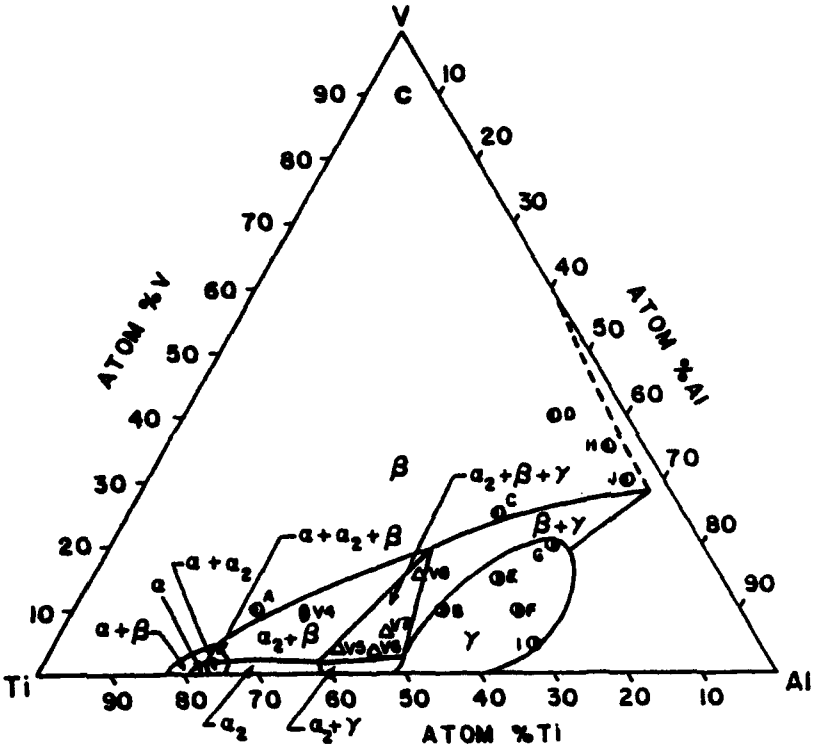

Figure 3 cont. (c) 1373 K.

HIGH TEMPERATURE PHASE STABILITY IN XD™ TiB_2 REINFORCED NEAR-GAMMA Ti-48Al-2Nb-2Mn

S. Guillard, H.J. Rack and D.E. Larsen*
Materials Science and Engineering Program
Clemson University
Clemson, South Carolina 29634-0921

* Applied Research Division
Howmet Corporation
Whitehall, MI 49461-1895

Published in Titanium '92
Science and Technology
Edited by F.H. Froes and I. Caplan
The Minerals, Metals & Materials Society
1993, pp. 587-594

Abstract

The elevated temperature phase stability of investment cast and HIP'ed near-gamma Ti-48Al-2Nb-2Mn containing 0, 0.5, 1, 2 and 7 vol.% TiB_2 has been investigated utilizing in-situ high temperature x-ray and thermal analysis. These studies have shown that the following reversible solid state phase transformations occur

$$\alpha_2 + \gamma \dashrightarrow \alpha + \gamma \dashrightarrow \alpha + \beta + \gamma \dashrightarrow \beta + \gamma$$

It is proposed that these reactions involve a low temperature eutectoid transformation, $\alpha_2 + \gamma \dashrightarrow \alpha$, followed by β precipitation and γ dissolution, and ultimately a high temperature peritectoid reaction, $\alpha \dashrightarrow \beta + \gamma$.

Changes in the transformation temperatures associated with each of the proposed reactions are not directly related to the TiB_2volume fraction, rather these appear to be controlled by the total interstitial content of each alloy.

Introduction

Because of their combination of low density and high temperature properties, near-γ titanium aluminides are attractive candidates for applications in advanced turbine engines and airframe designs. While they combine good oxidation resistance, relatively high modulus and good strength retention at high temperature [1], their low toughness and low room-temperature ductility, <3.5%, has restricted their applicability. Fortunately recent investigations have demonstrated that significant gains in fracture toughness can be achieved thru use of appropriate processing methods and heat treatments. For example, a fully lamellar ($\alpha_2+\gamma$) microstructure, which may be achieved thru heat treatment high in the ($\alpha_2+\gamma$) phase field, displays a higher fracture toughness than does an equiaxed microstructure [1-5].

While thermal treatments alone may be utilized to promote the ($\alpha_2+\gamma$) lamellar microstructure, these treatments are typically accompanied by an increase in grain size and therefore a further reduction in tensile ductility [3,4]. Other studies suggest that the formation of the ($\alpha_2+\gamma$) lamellar microstructure may be enhanced in binary TiAl thru the addition of TiB_2 particles [6]. In addition, these particles have the further beneficial effect of promoting a decrease in α_2/γ colony size [7] and grain size [8-11]. When combined, i.e., a decreased colony/grain size and a ($\alpha_2+\gamma$) lamellar microstructure, these results suggest that TiB_2 containing titanium aluminides may have both enhanced fracture toughness and tensile ductility when compared to unreinforced alloys.

Further advancements in utilizing this approach to improve the mechanical properties of near-γ titanium aluminides should be possible once the stability and performance of these materials are understood. The present investigation was therefore undertaken to determine the phase stability of a prototypical near-γ alloy, Ti-48Al-2Nb-2Mn, containing various volume fractions of titanium diboride.

Experimental Procedures

Ti-48Al-2Nb-2Mn ingots, Table I, with 0, 0.5, 1, 2 and 7 vol.% TiB_2 were produced by double vacuum arc remelting (VAR), TiB_2 being introduced via the XD™ process [11]. Cylindrical bars of 15.875mm X 203.2 mm were then investment cast and HIP'ed for 4 hours at 1533 K and 175 MPa, HIP'ing being terminated by cooling to room temperature at a rate less than 30 K/min.

Optical microscopy of these cast and HIP'ed materials showed that unreinforced Ti-48Al-2Nb-2Mn had a microstructure consisting of ($\alpha_2+\gamma$) lamellar colonies, L, and equiaxed gamma grains, G, Figure 1. In contrast, scanning electron microscopy reveals that the introduction of TiB_2 led to a reduction in grain size and a completely ($\alpha_2+\gamma$) lamellar microstructure, Figure 2 [7-10].

Three TiB_2 morphologies were observed in these materials, the diboride phase evolving from a predominantly lacey structure at 0.5 vol.%, figure 2(a), to needles and blocky particles at 1 and 2 vol.%, figures 2(b) and 2(c), and finally to predominantly blocky particles at 7 vol.%, figure 2(d). A similar evolution of the titanium boride morphology has been reported by others [8,12,13], who further confirmed by x-ray diffraction of the extracted particles [8] and by transmission electron microscopy [12,13] that all three morphologies are indeed TiB_2.

Table I
Alloy Composition

ALLOY #	O_2 (ppm)	Al (at%)	Nb (at%)	Mn (at%)	TiB_2* (vol%)
TARGET	<800	48.0	2.0	2.0	-
NM0	-	48.1	2.0	1.4	0
NM0.5	539	47.4	2.0	1.7	0.5
NM1	540	47.0	1.9	1.6	1
NM2	560	47.4	2.0	1.6	2
NM7	620	46.9	1.8	1.5	7

* Calculated from the analyzed boron contents.

The high temperature stability of these alloys was assessed using calorimetric differential thermal analysis (CDTA)[14] and high temperature x-ray diffraction (HTXRD)[15]. Phase transformation temperatures were determined from calorimetric observations between 873 K and 1703 K during both heating and cooling at rates of 5, 10, 20 and 40 K/min. The samples, having been placed in alumina crucibles, were introduced into a Stanton Redcroft / Omnitherm DSC 1500 thermal analysis system modified to be run in a flowing high purity (1 ppb) argon atmosphere [16].

In order to determine the reaction temperatures associated with each transformation, both the heat flow J, normalized per unit mass ($mJ.sec^{-1}.mg^{-1}$), and its first derivative with respect to temperature, J'=dJ/dT ($mJ.sec^{-1}.mg^{-1}.deg^{-1}$), were recorded. Transformation temperatures were determined from the CDTA thermograms by establishing those temperatures where the J and J' curves deviated from the baseline, and in the case of overlapping peaks, where the J' curve exhibited a curvature anomaly.

Additionally, high temperature x-ray diffraction studies were undertaken to identify the various phases present at elevated temperature. The procedure utilized a Scintag 1500 diffractometer equipped with a high temperature/vacuum chamber modified to introduce and maintain a high purity inert argon gas atmosphere at a desired pressure of 0.60 Pa. HTXRD samples, having dimensions of 8 mm X 20 mm X 0.25 mm, were prepared by wafering and grinding, with final preparation involving chemical removal of a 20 μm minimum surface layer in a bath of 10 ml HNO_3 + 5 ml HF + 50 ml H_2O, followed by washing in ethanol and water, drying in air and finally, storage in a vacuum dessicator.

Initially, ambient temperature 2Θ-scans from 15° to 85° were obtained. The sample was then heated at a rate of 20K/min, up to 1703K with diffraction spectra being acquired at selected temperatures. Typically, data were recorded after a 5-minute stabilization period at temperature with data acquisition lasting 7 minutes. Four to five samples of each alloy were examined, with

rocking curves being obtained where deemed necessary to verify the presence, or absence, of phases at elevated temperatures. Finally, following data collection, the x-ray diffraction spectra were analyzed and the peaks indexed utilizing an iterative computer program capable of fitting the observed data to given cell structures using a least squares method.

Results

Ti-48Al-2Nb-2Mn

Calorimetric differential thermal analysis, Figures 3(a) and 3(b), showed that, independent of heating/cooling rate, three reversible reactions, T1 thru T3, were observed during heating and cooling of unreinforced Ti-48Al-2Nb-2Mn. In addition, a fourth reaction, T4, was observed on heating and was associated with melting of the CDTA sample. Temperatures for the onset and completion of these reactions are summarized in Table II. X-ray diffraction analysis of Ti-48Al-2Nb-2Mn suggested that this alloy was two phase ($\alpha_2+\gamma$) at room temperature, Figure 4(a)[1].

Upon heating no discernable differences in x-ray results were observed until 1523K, at which temperature the $(110)_\beta$ appeared, the structure now consisting of $\alpha + \gamma + \beta$, the α_2 having disordered. A further temperature increase to 1623K resulted in an increase in the β peak intensities relative to the γ peaks. Finally, above 1623K, the alloy was two-phase $\beta + \gamma$, all evidence of α having disappeared.

Ti-48Al-2Nb-2Mn/TiB_2

Typical calorimetric differential thermal analysis results for both heating and cooling of the TiB_2 reinforced Ti-48Al-2Nb-2Mn alloys are illustrated for Ti-48Al-2Nb-2Mn/7 vol. % TiB_2 in Figure 3(c) and 3(d). The three solid state reactions observed, T1,T2 and T3, as well as that associated with melting, T4, were similar to those found in unreinforced Ti-48Al-2Nb-2Mn, see Table II.

Correspondingly, ambient and elevated temperature x-ray diffraction results for the TiB_2 reinforced Ti-48Al-2Nb-2Mn were similar to those of the unreinforced alloy, Figure 4(b). For example, at low temperatures Ti-48Al-2Nb-2Mn/7 vol. % TiB_2 was $\alpha_2 + \gamma$, transforming to $\alpha + \gamma + \beta$ above 1548K and finally to $\beta + \gamma$ above 1648K.

---

[1] It was confirmed by transmission electron microscopy that no β phase is present at room temperature.

Table II
Transformation Temperatures

	HEATING	HEATING	HEATING		COOLING	COOLING	COOLING
	T1 onset complete	T2 onset complete	T3 onset complete	T4	T3 onset complete	T2 onset complete	T1 onset complete
NMO	1458 1485	1536 1623	1623 1646	1690	1628 1597	1603 1563	1465 1438
NM0.5	1470 1498	1515 1626	1626 1659	1677	1625 1600	1621 1584	1476 1445
NM1	1468 1486	1513 1620	1620 1661	1670	1628 1605	1615 1590	1485 1468
NM2	1475 1490	1519 1625	1625 1656	1666	1633 1604	1611 1590	1483 1463
NM7	1529 1539	1555 1630	1630 1652	1664	1648 1633	1633 1603	1568 1521

Discussion

The combined thermal analysis and x-ray diffraction observations can be utilized to examine the influence of TiB_2 addition on phase stability in Ti-48Al-2Nb-2Mn. In general, independent of TiB_2 content, heating/cooling results in the following solid state transformations:

$$\alpha_2+\gamma \dashrightarrow \alpha+\gamma \dashrightarrow \alpha+\beta+\gamma \dashrightarrow \beta+\gamma$$

with melting occurring at the highest temperatures examined. Comparison of the calorimetric differential thermal analysis results, Table II, with the HTXRD results supports the suggestion that reaction T1, occurring at approximately 1470 K for NM0 and 1530 K for NM7, is the eutectoid transformation $\alpha_2+\gamma \dashrightarrow \alpha$, i.e., α_2 is not observed above T1. In addition, the T1 reaction occurrs at temperatures close to the reported eutectoid temperature in binary Ti-48.65Al, 1450 K [17]. Precipitation of β commences at temperatures between T1 and T2, with T2 corresponding to increasing β precipitation and dissolution of γ. T3 then coincides with the proposed $\alpha \dashrightarrow \beta+\gamma$ peritectoid transformation. The results also indicate that, in contrast with binary TiAl/TiB_2 alloys, α is <u>not</u> the high temperature equilibrium phase for Ti-48Al-2Nb-2Mn, a two-phase $\beta + \gamma$ region existing in the latter alloy immediately below the solidus. This difference between the Ti-48Al-2Nb-2Mn and binary alloys [6] is presumably due to the β-stabilizing effect of the two additions, i.e. Nb and Mn. Failure of previous investigators [18] to recognize the presence of the $\beta + \gamma$ phase field at high temperature during their study of Ti-48Al-2Nb-2Mn is not surprising, CDTA by itself not being able to define the reactant or the product phases participating in a phase transformation.

Finally, the results suggest that the influence of the TiB_2 reinforcements on the transformation temperatures is not directly correlatable to the TiB_2 volume fraction. Rather it appears that the transformation temperatures are more directly related to the total interstitial content (O+N+B+C+H). For example, the eutectoid transformation temperature increases with increasing interstitial content. Further study continues towards quantifying this interstitial effect.

Conclusions

The elevated temperature phase stability of investment cast and HIP'ed near-gamma Ti-48Al-2Nb-2Mn containing 0, 0.5, 1, 2 and 7 vol.% TiB_2 involves the following reversible solid state phase transformations:

$$\alpha_2+\gamma \dashrightarrow \alpha+\gamma \dashrightarrow \alpha+\beta+\gamma \dashrightarrow \beta+\gamma$$

These reactions involve a low temperature eutectoid transformation, $\alpha_2 + \gamma \dashrightarrow \alpha$, a precipitate reaction leading to the presence of the β phase and a high temperature peritectoid, $\alpha \dashrightarrow \beta + \gamma$.

The total interstitial content seems to have much more influence on the phase stability of these materials than the TiB_2 content.

Acknowledgements

This research was sponsored by the Defense Advanced Research Projects Agency under the contract N00014-89-J-3166 supervised by Mr. W. Baker and monitored by Dr. G. Yoder of the Office of Naval Research. The assistance of Dr. P. Chaudhury and M. Long is gratefully acknowledged.

References

1. Y.W. Kim and D.M. Dimiduk, "Progress in the Understanding of Gamma Titanium Aluminides", Jn of Metals, Aug.1991, 40-47.
2. K-W. Kim, "Recent Advances in Gamma Titanium Aluminide Alloys", in High-Temperature Ordered Intermetallic Alloys IV, eds. L. A. Johnson, D. P. Pope and J. O. Steigler, Vol. 213, MRS, Pittsburgh, PA, (1991), 777-794.
3. Y.W. Kim, "Microstructural Evolution and Mechanical Properties in Gamma Titanium Aluminides", in Microstructure/Property Relationships in Titanium Aluminides and Alloys, eds. Y-W. Kim and R.R. Boyer, The Minerals, Metals and Materials Society, Warrendale, PA, (1991), 91-103.
4. S-C. Huang and D. S. Shih, "Microstructure-Property Correlation in TiAl-Base Alloys", in Microstructure/Property Relationships in Titanium Aluminides and Alloys, eds. Y-W. Kim and R.R. Boyer, The Minerals, Metals and Materials Society, Warrendale, PA, (1991), 105-122.
5. K. S. Chan and Y-W. Kim, "Fracture Processes in a Two-Phase Gamma Titanium Aluminide Alloy", in Microstructure/Property Relationships in Titanium Aluminides and Alloys, eds. Y-W. Kim and R.R. Boyer, The Minerals, Metals and Materials Society, Warrendale, PA, (1991), 179-196.
6. C.R. Feng, D.J. Michel and C.R. Crowe, "Microstructures of XD™ Titanium Aluminide at Elevated Temperatures", Scripta Met., 24 (1990) 1297-1301.
7. J. D. Bryant, L. Christodoulou and J. R. Maisano, "Effect of TiB_2 Additions on the Colony Size of Near Gamma Titanium Aluminides", Scripta Met., 24 (1990) 33-38.
8. D.E. Larsen, S. Kampe and L. Christodoulou, "Effect of XD™ TiB_2 Volume Fraction on the Microstructure of a Cast Near-Gamma Titanium Aluminide Alloy, in Intermetallic Matrix Composites, eds. D.L. Anton, P.L. Martin, D.B. Miracle and R. McMeeking, Vol. 194, MRS, Pittsburgh, PA, (1990), 285-292.
9. D.E. Larsen, M. L. Adams, S. L. Kampe, L. Christodoulou and J. D. Bryant, "Influence of Matrix Phase Morphology on Fracture Toughness in a Discontinously Reinforced XD™ Titanium Aluminide Composite", Scripta Met., 24 (1990) 851-856.
10. D. E. Larsen, "Effects of XD™ TiB_2 Volume Fraction on the Microstructure and Mechanical Properties of a Cast XD™ Near-Gamma Alloy", in Microstructure/Property Relationships in Titanium Aluminides and Alloys, eds. Y-W. Kim and R.R. Boyer, The Minerals, Metals and Materials Society, Warrendale, PA, (1991), 345-360.
11. L. Christodoulou, P.A. Parrish and C.R. Crowe, in High Temperature/High Performance Composites, eds. F.D. Lemkey, S.G. Fishman, A.G. Evans and J.R. Strife, Vol. 120, MRS, Pittsburgh, PA, (1988), 29-34.
12. M. E. Hyman, C. McCullough, J. J. Valencia, C. G. Levi and R. Mehrabian, "Microstructure Evolution in TiAl Alloys with B Additions: Conventional Solidification", Metall. Trans., 20A (1989) 1847-1859.
13. M.E. Hyman, C. McCullough, C. G. Levi and R. Mehrabian, "Evolution of Boride Morphologies in TiAl-B Alloys", Metall. Trans., 22A (1991) 1647-1662.
14. Differential Thermal Analysis, ed. R.C. Mackenzie, Academic Press, (1972).
15. P. K. Chaudhury, M. Long and H. J. Rack, "Effect of Vanadium on Elevated Temperature Phase Relations in Titanium Aluminides containing 44 at. % Al", Mat'ls Sci. Eng., in press.
16. P. K. Chaudhury and H. J. Rack, "Ti-Al-V Ternary Phase Stability at Elevated Temperatures", Scripta Met., 26, (1992), 691-695.

17. J.C. Mishurda and J.H. Perepezko, "Phase Equilibria in Ti-Al Alloys", in Microstructure/Property Relationships in Titanium Aluminides and Alloys, eds. Y.W. Kim and R.R. Boyer, The Minerals, Metals and Materials Society, Warrendale, PA, (1991), 3-30.
18. P.A. McQuay, D.M. Dimiduk and S.L. Semiatin, "The Decomposition of Alpha Phase During Continuous Cooling and Isothermal Transformation in Gamma Titanium Aluminide", Scripta Metall., 25, (1991), 1689-1694.

Figure 1. Optical micrograph of Ti-48Al-2Nb-2Mn illustrating mixed microstructure consisting of equiaxed γ grains [G] and (α_2 + γ)lamellar colonies, [L].

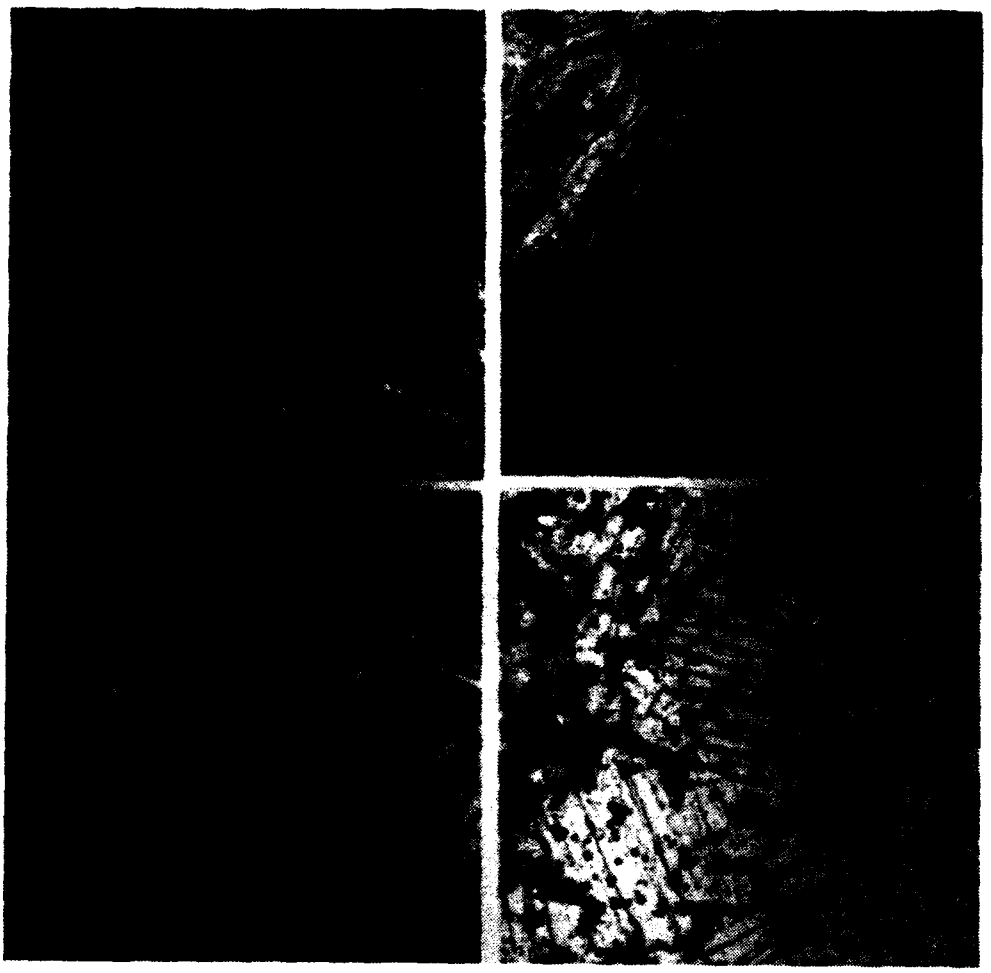

Figure 2. Scanning electron micrographs illustrating TiB_2 morphology in Ti-48Al-2Nb-2Mn containing (a) 0.5 vol. % TiB_2, (b) 1 vol. % TiB_2, (c) 2 vol. % TiB_2, and (d) 7 vol. % TiB_2.

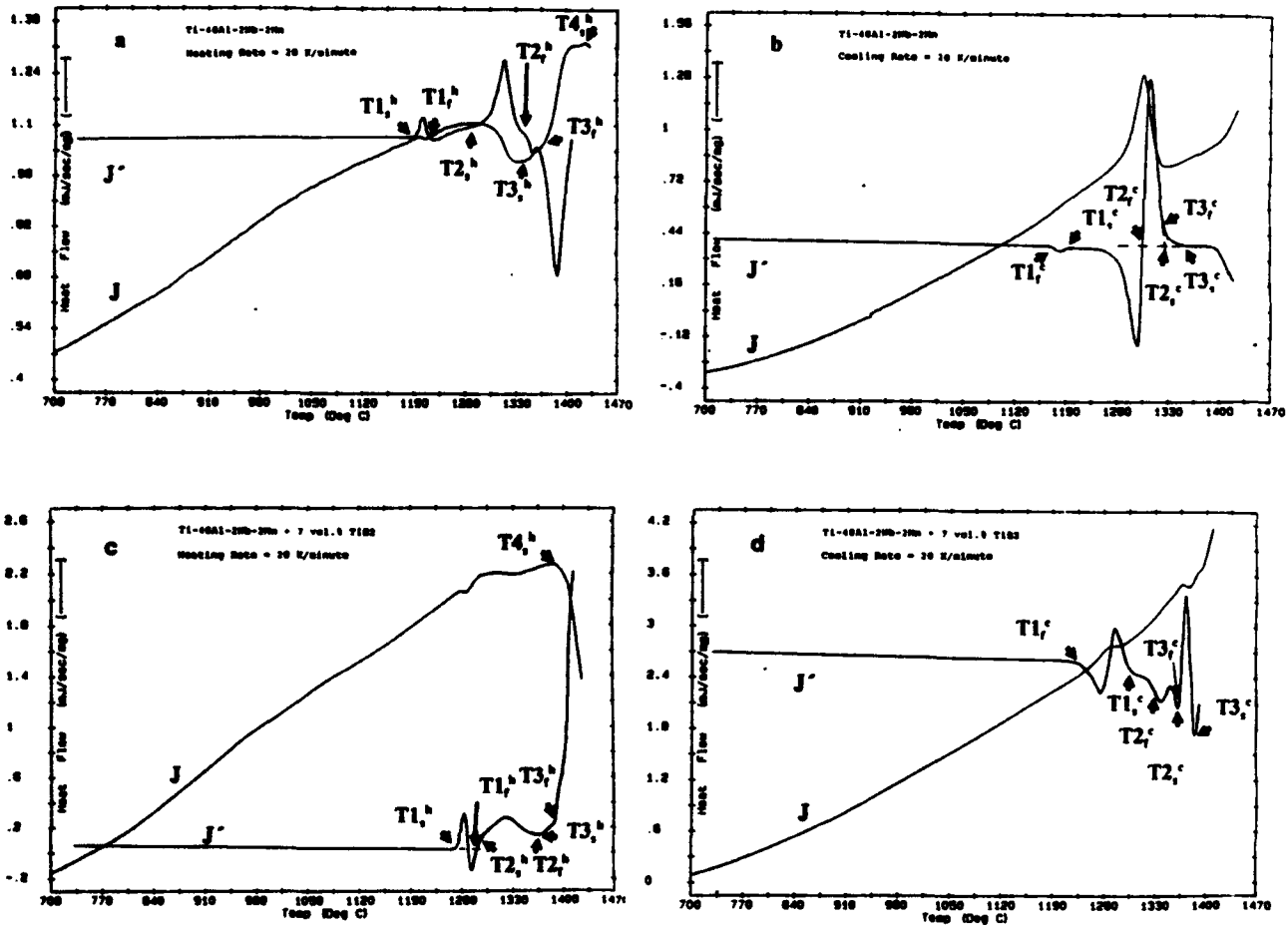

Figure 3. Thermograms of (a) Ti-48Al-2Nb-2Mn on heating, (b) Ti-48Al-2Nb-2Mn on cooling, (c) Ti-48Al-2Nb-2Mn/7 vol.% TiB_2 on heating and (d) Ti-48Al-2Nb-2Mn/7 vol.% TiB_2 on cooling at 20 K/min.

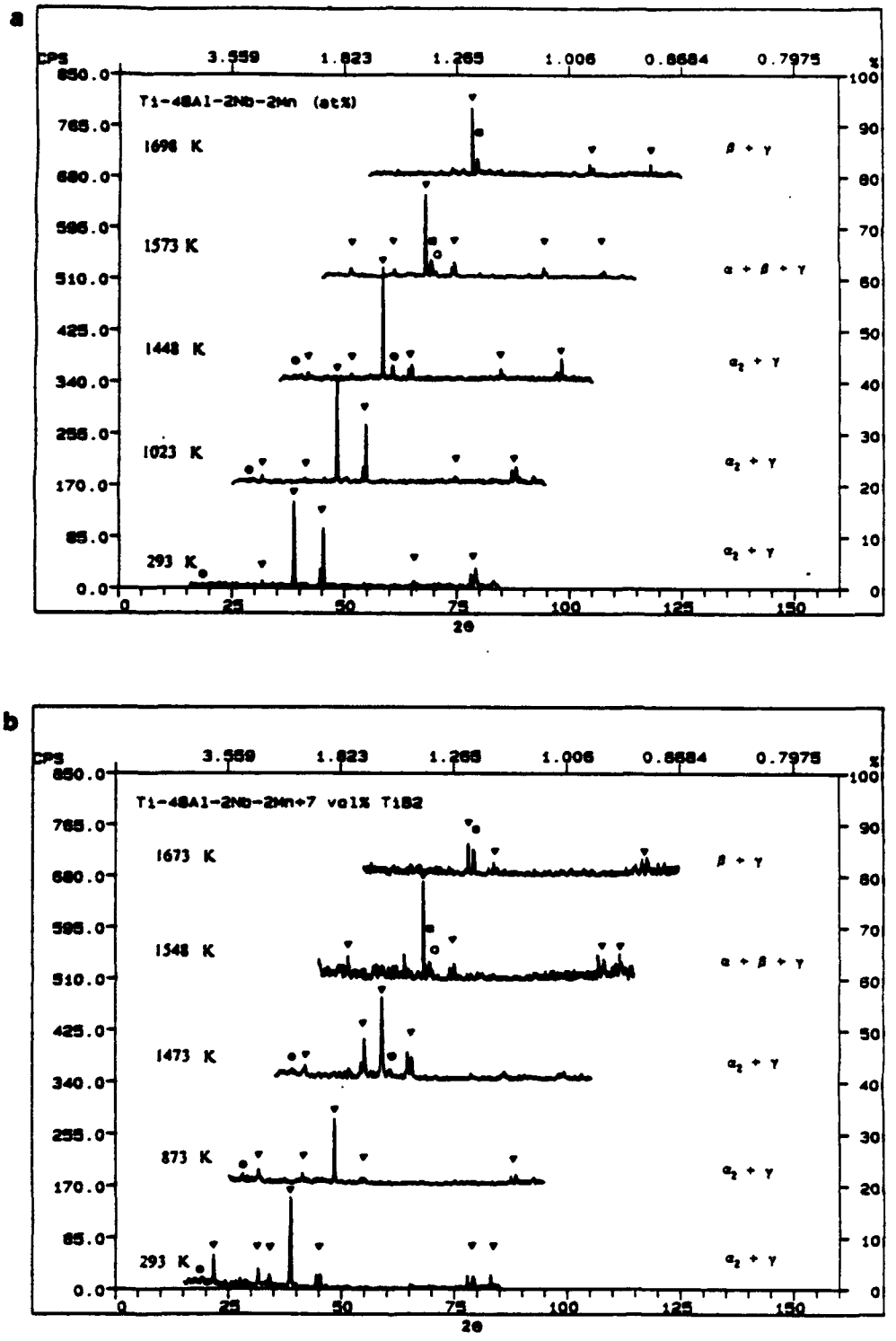

Figure 4. X-ray spectra showing the phases present at selected temperatures for (a) Ti-48Al-2Nb-2Mn and (b) Ti-48Al-2Nb-2Mn/7 vol. % TiB_2. (• α_2, o α, ■ β, ▽ γ).

ELEVATED TEMPERATURE PHASE STABILITY OF Ti-25Al-11Nb

Marc Long, Prabir K. Chaudhury, and H. J. Rack
Materials Science and Engineering Program
Department of Mechanical Engineering
Clemson University
Clemson, South Carolina 29634-0921

Published in
Titanium '92, Science and Technology
Edited by F.H. Froes and I. Caplan
The Minerals, Metals & Materials Society - 1993
pp. 595-602

Abstract

The elevated temperature phase stability of triple vacuum melted and forged Ti-25Al-11Nb has been investigated utilizing optical microscopy, calorimetric differential thermal analysis and *in-situ* high temperature x-ray diffraction. These studies have shown that slow cooling after forging resulted in a microstructure consisting of primary, blocky α_2 colonies (α_2^P) in a matrix of secondary, 'basketweave' α_2 (α_2^S) + transformed disordered β (β_t) + orthorhombic phase O. Upon continuous heating sequential dissolution of orthorhombic O and the morphologically distinct ordered α_2 phases was observed, with α_2 disordering to α below the β transus. Similar reversible transformations were observed on cooling from the β phase field; the quantities of α_2^P and α_2^S in the alloy microstructure after cooling being rate dependent, decreasing cooling rate increasing the volume fraction of α_2^P.

Introduction

Ti_3Al based intermetallic alloys (based on the α_2 phase, ordered hcp, DO_{19} structure) exhibit superior elevated temperature strength and creep resistance when compared to conventional titanium alloys. Their low ambient temperature ductility and fracture toughness has, however, required alloy modification. Among several modifications investigated, the most promising involves incorporation of β stabilizers, such as Nb, V and Mo, to levels which result in the introduction of controlled quantities of a ductile β phase (1). One of the most interesting alloys in this regard is the commercial Ti-24Al-11Nb alloy. While the addition of niobium in this alloy promotes the formation of a two phase $\alpha_2+\beta$ (or ordered β, β_0, with the CsCl structure B2) mixture (2,3), recent investigations of the Ti_3Al-Nb pseudo-binary system (3-7) have demonstrated that complex phase relationships exist in this system. For example, depending upon exact alloy chemistry and prior thermo-mechanical history phases reported in the Ti_3Al-Nb system include β (disordered bcc) (6,7), β_0 (ordered bcc, B2 structure) (8), α (disordered hcp) (9), α_2 (ordered hcp, DO_{19} structure), O/O′(orthorhombic phase derived from the DO_{19} phase) (10), and recently a new tetragonal phase (DO_3-like structure) (11).

A definition of the high temperature in-situ phase stability is therefore essential for the development of appropriate elevated temperature thermo-mechanical processing of Ti_3Al-Nb alloys. To achieve this goal, the present study establishes the phase relationships at elevated temperatures, upon continuous heating/cooling, of the commercial Ti-24Al-11Nb (true composition Ti-25Al-11Nb) alloy.

Experimental Procedures

The chemical composition of the investigated Ti-25Al-11Nb (at.%) alloy is given in Table I. This alloy was received as a 152.4 mm. thick slab having been forged from a 3400 kg. triple vacuum melted production ingot. During prior processing, the material had been heated to 1533 K, held at this temperature for 8 hours, forged, and then air cooled. Metallographic examination of sections prepared using conventional techniques (grinding, polishing and etching with Kroll's reagent), Figure 1, showed that the microstructure consisted of uniform primary, blocky α_2 (α_2^p) in a transformed β (Widmanstätten secondary α_2^s + β_t) matrix. Ambient temperature x-ray diffraction revealed an $\alpha_2+\beta$(disordered) structure, with a small quantity of an orthorhombic-like phase O characterized by the presence of 'shoulders' at the identified α_2 peaks.

Characterization of the high temperature stability utilized calorimetric differential thermal analysis (CDTA) and high temperature in-situ x-ray diffraction (HTXRD). The former used a Stanton Redcroft/Omnitherm DSC 1500 thermal analysis system, modified to ensure that the heating/cooling experiments were unaffected by the test environment (12). Phase transformation temperatures from 873 K to 1573 K were determined during both heating and cooling in a high purity argon atmosphere at 5, 10, 20, and 40 K/min rates. In order to precisely determine each transformation, both the heat flow, normalized per unit mass ($mJ.sec^{-1}.mg^{-1}$.), and its first derivative with respect to temperature, $J'=dJ/dT$ ($mJ.sec^{-1}.mg^{-1}.deg^{-1}$), were recorded and analyzed. Transformation temperatures were determined from the CDTA thermograms by establishing those temperatures where the J and J′ curves deviated from the baseline (T_O^s, T_O^f, T_S^h, and T_B^h on heating and T_B^c, T_D^c, and T_S^c on cooling), and in the case of overlapping peaks, where the J′ curve showed a curvature anomaly (T_L^h and T_D^h on heating and T_L^c on cooling). The

average standard deviation observed for the measured reaction temperatures was ± 5 K.

In-situ high temperature x-ray diffraction (HTXRD) experiments were undertaken to complement the CDTA experiments. These utilized a Scintag diffractometer equipped with a high temperature furnace/vacuum chamber, the latter having again been modified to introduce and maintain a high purity inert argon gas atmosphere at a pressure of 0.6 bar (12).

Results

The results of the thermal analysis observations during continuous heating and cooling are shown in Figure 2 and 3, respectively. Independent of heating rate, Ti-25Al-11Nb exhibited a low temperature transformation below 1123 K (850°C). This transformation, starting at T_O^s and ending at T_O^f, was followed by a complex sequence of transformations, T_S^h thru T_B^h. Above T_S^h, where both J and J′ curves deviated from the baseline, ensuing reactions, as defined by anomalies in J′, were observed at T_L^h and T_D^h. Finally this sequence of transformations was completed at T_B^h.

Cooling thermograms exhibited three distinct transformations in the 1348-1173 K (1075°-900°C) range, except at the lowest rate examined, 5 K/min, where only two reactions were recorded. The first reaction which had an onset at T_B^c and finished at T_D^c, was immediately followed by a second reaction which terminated at T_S^c. At cooling rates above 5 K/min, a third reaction appeared, interrupting the T_D^c-T_S^c reaction at a temperature T_L^c, with the extent of this additional transformation increasing with increasing cooling rate.

In order to estimate the equilibrium reaction temperatures, that is to eliminate the influence of heating or cooling rate on the observed transformation temperatures, the temperature *vs.* rate curves were assumed to be a linear function of rate and were extrapolated to an ideal 0 K/min rate corresponding to the equilibrium state, Table II.

High temperature x-ray diffraction data at 20 K/min for Ti-25Al-11Nb are summarized in Table III. These data show that Ti-25Al-11Nb was three phase (α_2+β+O) up to 1123 K (850°C), the major β peak. β(110) at 2θ=38.8°, overlapping with the α_2(002) peak at 2θ=38.2°. The orthorhombic peaks, characterized by small 'shoulders' at α_2 peaks, started disappearing at approximately 923 K (650°C) with the completion of this transformation at 1123 K (850°C).

Between 1173 K (900°C) and 1323 K (1050°C), the alloy was two phase (α_2+β). Above 1348 K (1075°C) a new peak, which could be indexed as a satellite α/α_2 reflection, started to appear, *i.e.*, the major peak of the x-ray diffraction scan (α_2(002)/2θ=38°) separated into two peaks. At 1448 K (1175°C) this satellite reflection disappeared and the alloy was in the α+β phase field. Due to the overlapping of the α_2 and α peaks, the $\alpha_2 \rightarrow \alpha$ disordering transformation was verified with rocking curves at low angles 2θ=17.5°, α_2(100), and 2θ=26°, α_2(110). The expected peaks characteristic only of the ordered α_2 phase were absent at 1448 K. Finally, at 1473 K (1200°C) and above, the x-ray scans showed no distinct peaks, however rocking curves indicated that the alloy was single phase, disordered bcc β phase, above this temperature.

Upon cooling, x-ray scans were also taken and were found to be qualitatively identical to those on heating, the intensity of the peaks being randomly modified. Between 1348 K (1075°C) and 1298 K (1025°C), the presence of an α+β structure was identified, transforming to α_2+β below 1273 K (1000°C). Ultimately a three phase structure, α_2+β+O, appeared below 1123 K (850°C), this structure remaining till room temperature.

Discussion

Using the combination of the CDTA and in-situ HTXRD experiments, the phase stability of Ti-25Al-11Nb at elevated temperatures was established during continuous heating/cooling. By analogy with conventional titanium alloys (13), transformations on heating Ti-25Al-11Nb involved dissolution processes while, on cooling, the reverse transformations involved precipitation of α/α_2.

Initially the microstructure of the alloy examined consists of $\alpha_2^P+\{\alpha_2^S+\beta_t\}+O$, with two distinct α_2 morphologies, primary blocky α_2^P, and secondary α_2^S. Upon heating, Table IV, the first transformation consists of orthorhombic phase dissolution as defined by temperatures between T_O^s and T_O^f, Figure 2.

Further transformations then involve the dissolution of the morphologically different α_2 phases. This initially entails the resolution of α_2^S within transformed β, followed by the dissolution of α_2^P. Such a dual process, eventually followed by the disordering of both α_2 morphologies, was demonstrated by the CDTA thermograms, where complex phase transformations are observed above T_S^h, Figure 2. The first of these is characterized as the dissolution of the α_2^S, and is associated with the major peak for each heating rate, the shape of this peak being representative of a diffusion controlled transformation (17). While the onset of primary α_2^P dissolution cannot be precisely defined from the CDTA thermograms, the appearance of the α_2/α satellite reflection at approximately 1338 K (1075°C) in the x-ray pattern suggests that a difference in chemical composition between the primary and secondary α_2 phases may develop during dissolution at high temperature, as expected in a diffusion-controlled transformation. Similar alloy partitioning between the α_2 and β phases, which become respectively Al-enriched and Nb-enriched, has also been observed in Ti-24Al-11Nb (14,16). It is proposed therefore that T_L^h represents the transition temperature where α_2^P becomes predominant in the alloy structure, the α_2^S morphology being virtually extinct. The x-ray results further indicate that the α_2^P phase is present till 1423 K, completion of the $\alpha_2 \rightarrow \alpha$ disordering transformation occuring slightly below the β transus, T_B^h, 1432 K (1159°C).

The CDTA thermograms suggest that an additional transformation, identified by T_D^h, takes place in the high temperature range immediately below the β transus. This reaction may be associated with the dissolution of either grain boundary α_2^{GB} or martensitic α' (hcp), the former reverse transformation, $\beta \rightarrow \alpha_2^{GB}$, being a cellular-type associated with the growth of blocky α/α_2 (3), the latter, $\beta \rightarrow \alpha'$, involving a shear transformation of β to α' with subsequent ordering to α_2 (15,16). Similarly, the first transformation involved upon cooling from the β phase is the formation of primary α^P which begins at the temperature T_D^c. This is followed by α_2^P ordering, as depicted in Figure 3 by the broad peak between T_D^c and T_L^c. Moreover, prior to completion of α_2^P formation, precipitation of secondary α_2^S from the β phase occurs, temperature T_L^c. The extent of α_2^S precipitation is expected to be a function of cooling rate. Figure 3 supports this conclusion, the difference in intensity of the α_2^S peak, relative to α_2^P, increasing with increasing cooling rate. In contrast, an $\alpha_2^P+\beta$ microstructure is characteristic of slower cooling rates, *i.e.* those permitting long-range diffusion processes to occur. Therefore, by analogy with the transformations observed on heating, the T_L^c temperature represents the transition from a predominant α_2^P to an increasing quantity of α_2^S with increasing cooling rates. Table V summarizes the phase transformations path on cooling where the temperatures are given at equilibrium.

Demonstration of this effect of rate on the phase morphology of Ti-25Al-11Nb was observed in the microstructure of the CDTA samples after cooling, Figure 4. As the cooling rate

decreased, coarsening of α_2^P was observed, the as-cooled microstructure changing from a fine $\alpha_2^S+\beta_t$ to a coarse $\alpha_2^P+\beta_t$ morphology. This morphological transition was confirmed at the lowest cooling rate, *i.e.* 5 K/min, when the α_2^S was absent in the microstructure of the CDTA specimen after cooling, Figure 4d, an observation consistent with the disappearance of the peak associated with α_2^S formation in the CDTA thermogram Figure 3d.

Conclusions

High temperature phase stability has been established for the Ti-25Al-11Nb (at.%). Transformations on heating involve the sequential dissolution of orthorhombic O and the morphologically distinct α_2 phases, such as α_2^P and α_2^S, present in the as-received alloy. Similar reversible reactions occur on cooling from the high temperature single phase β, the relative amount of the morphologically different α_2 phases exhibiting a clear cooling rate dependency.

Acknowledgements

This research was sponsored by the Defense Advanced Research Projects Agency under contract N00014-89-J-3166 supervised by Mr. W. Barker and monitored by Dr. G. Yoder of the Office of Naval Research. The Ti-25Al-11Nb alloy utilized was provided by Mr. Ed Mild of TIMET, Inc. Finally, the authors thank Mr. R. Gallahorn for his experimental assistance.

References

1. J. M. Larsen, K. A. Williams, S. J. Balsone, and M. A. Stucke, "Titanium Aluminides for Aerospace Applications", High Temperature Aluminides and Intermetallics, ed. S. H. Whang, C. T. Liu, D. P. Pope and J. O. Stiegler (The Minerals, Metals & Materials Society, Warrendale, PA, 1990), 521-556.
2. R. G. Rowe, "Recent Developments in Ti-Al-Nb Titanium Aluminides", High Temperature Aluminides and Intermetallics, ed. S. H. Whang, C. T. Liu, D. P. Pope and J. O. Stiegler (The Minerals, Metals & Materials Society, Warrendale, PA, 1990), 375-401.
3. C. H. Ward, "Microstructure Evolution and its Effects on the Fracture Behavior of Ti_3Al Intermetallics", International Materials Review, in press.
4. M. J. Kaufman, T. F. Broderick, C. H. Ward, J. K. Kim, R. G. Rowe and F. H. Froes, "Phase Relationships in the Ti_3Al+Nb System", Sixth World Conference on Titanium, ed. P. Lacombe, R. Tricot, G. Béranger (Les éditions de physique, Les Ulis Cedex, France, 1988), 985-990.
5. D. Banerjee, T. K. Nandy, A. K. Gogia and K. Muraleedharan, "Microstructure and Phase Relations in the Ti_3Al-Nb Section", Sixth World Conference on Titanium, ed. P. Lacombe, R. Tricot, G. Béranger (Les éditions de physique, Les Ulis Cedex, France, 1988), 1091-1096.
6. J. H. Perepezko, Y. A. Chang, L. E. Seitzman, J. C. Lin, N. R. Bonda, T. J. Jewett and J. C. Mishurda, "High Temperature Phase Stability in the Ti-Al-Nb System", High Temperature Aluminides and Intermetallics, ed. by S. H. Wang, C. T. Liu, D. P. Pope and J. O. Stiegler (The Minerals, Metals & Materials Society, Warrendale, PA, 1990), 19-47.

7. H. T. Kestner-Weykamp, C. H. Ward, T. F. Broderick and M. J. Kaufman, "Microstructures and Phase Relationships in the Ti_3Al+Nb System", Scripta Metallurgica, 23 (1989), 1697-1702.
8. L. A. Bendersky and W. J. Boettinger, "Investigation of B2 and Related Phases in the Ti-Al-Nb Ternary System", High-Temperature Ordered Intermetallic Alloys III (MRS, Pittsburgh, PA, 1989), 45-50.
9. S. M. L. Sastry and H. A. Lipsitt, "Ordering Transformations and Mechanical Properties of Ti_3Al and Ti_3Al-Nb Alloys", Metallurgical Transactions A, 8 (A) (1977), 1543-1552.
10. D. Banerjee, A. K. Gogia, T. K. Nandi and V. A. Joshi, "A New Ordered Orthorhombic Phase in a Ti_3Al-Nb Alloy", Acta Metallurgica, 36 (4) (1988), 871-882.
11. L. M. Hsiung and H. N. G. Wadley, "A New Ordered Tetragonal Phase in the Ti_3Al+Nb System", Scripta Metallurgica et Materiala, 26 (1992), 35-40.
12. P. K. Chaudhury, M. Long, and H. J. Rack, "Effects of Vanadium on Elevated Temperature Phase Relations in Titanium Aluminides Containing 44 at.% Al", Materials Science and Engineering, Vol. A152, 1992, pp. 37-40.
13. "The Physical Metallurgy of Titanium Alloys", edited by E. W. Collings, ASM Series in Metal Processing, H. L. Gegel Series editor, American Society for Metals, Metal Park, OH, 1984.
14. K. Muraleedharan and D. Banerjee, "Alloy Partitioning in Ti-24Al-11Nb by Analytical Electron Microscopy", Metallurgical Transactions A, 20 (A) (1989), 1139-1142.
15. H. T. Weykamp, D. R. Baker, D. M. Paxton, and M. J. Kaufman, "Continuous Cooling Transformations in Ti_3Al+Nb Alloys", Scripta Metallurgica et Materiala, 24 (1990), 445-450.
16. M. J. Cieslak, T. J. Headley, and W. A. Baeslack III, "Effect of Thermal Processing on the Microstructure of Ti-26Al-11Nb: Applications to Fusion Welding", Metallurgical Transactions A, 21 (A) (1990), 1273-1286.
17. Differential Thermal Analysis, edited by R. C. MacKenzie, Academic Press, London and New York, Vol. 2, 1972.

Table I. Chemical composition of Ti-25Al-11Nb

	Ti	Al	Nb	O	C	N	Fe
at.%	bal.	24.95	10.83	0.26	0.26	0.04	0.04
wt.%	bal.	14.25	21.30	0.09	0.09	0.01	0.05

Table II. Transformation temperatures as a function of heating/cooling rates

Heating/Cooling Rate (K/min)	Transformation Temperatures (K) [Heating(T_x[b])/Cooling(T_x[c])]					
	T_o	T_o	T_s	T_L	T_D	T_B
40	943/ND[a]	1109/ND	1210/1107	1401/1231	ND/1304	1485/1349
20	928/ND	1091/ND	1211/1172	1389/1238	1425/1320	1456/1353
10	913/ND	1083/ND	1208/1198	1378/1242	1407/1334	1443/1351
5	909/ND	1086/ND	1206/1225	1371/ND	1401/1338	1441/1355
0[b]	905/ND	1079/ND	1207/1236	1369/1246	1394/1343	1432/1354

[a] non-detected [b] extrapolated

Table III. Phase structures determined by HTXRD at 20 K/min heating rate

Temperature (K)	298 - 1123	1173 - 1323	1348 - 1423	1448	1473
Phases	$\alpha_2 + \beta + O$	$\alpha_2 + \beta$	*split* $\alpha/\alpha_2 + \beta$	$\alpha + \beta$	β

Table IV. Phase transformations upon heating for the Ti-25Al-11Nb alloy

T (K)	< 1079	1079 - 1207	1207 - 1369	1369 - 1394	1394 - 1432	> 1432
Phases	$\{\beta_t+\alpha_2^S\}+\alpha_2^P+O$	$\{\beta_t+\alpha_2^S\}+\alpha_2^P$	$\{\beta_t+(\alpha_2\rightarrow\alpha)^S\}$ + $(\alpha_2\rightarrow\alpha)^P$	$\beta+(\alpha_2/\alpha)^P$	$\beta+\alpha^P$	β

Table V. Phase transformations upon cooling for Ti-25Al-11Nb

T (K)	1354	1354 - 1343	1343 - 1246	1246 - 1236	< 1236
Phases	β	$\beta+\alpha^P$	$\beta+(\alpha\rightarrow\alpha_2)^P$	$\{\beta_t+\alpha_2^S\}+\alpha_2^P$	$\{\beta_t+\alpha_2^S\}+\alpha_2^P+O$

Figure 1 - Ti-25Al-11Nb as-forged microstructure exhibiting primary, blocky α_2^P [P] and a mixture of secondary, 'basketweave' α_2^S [S] and retained β_r.

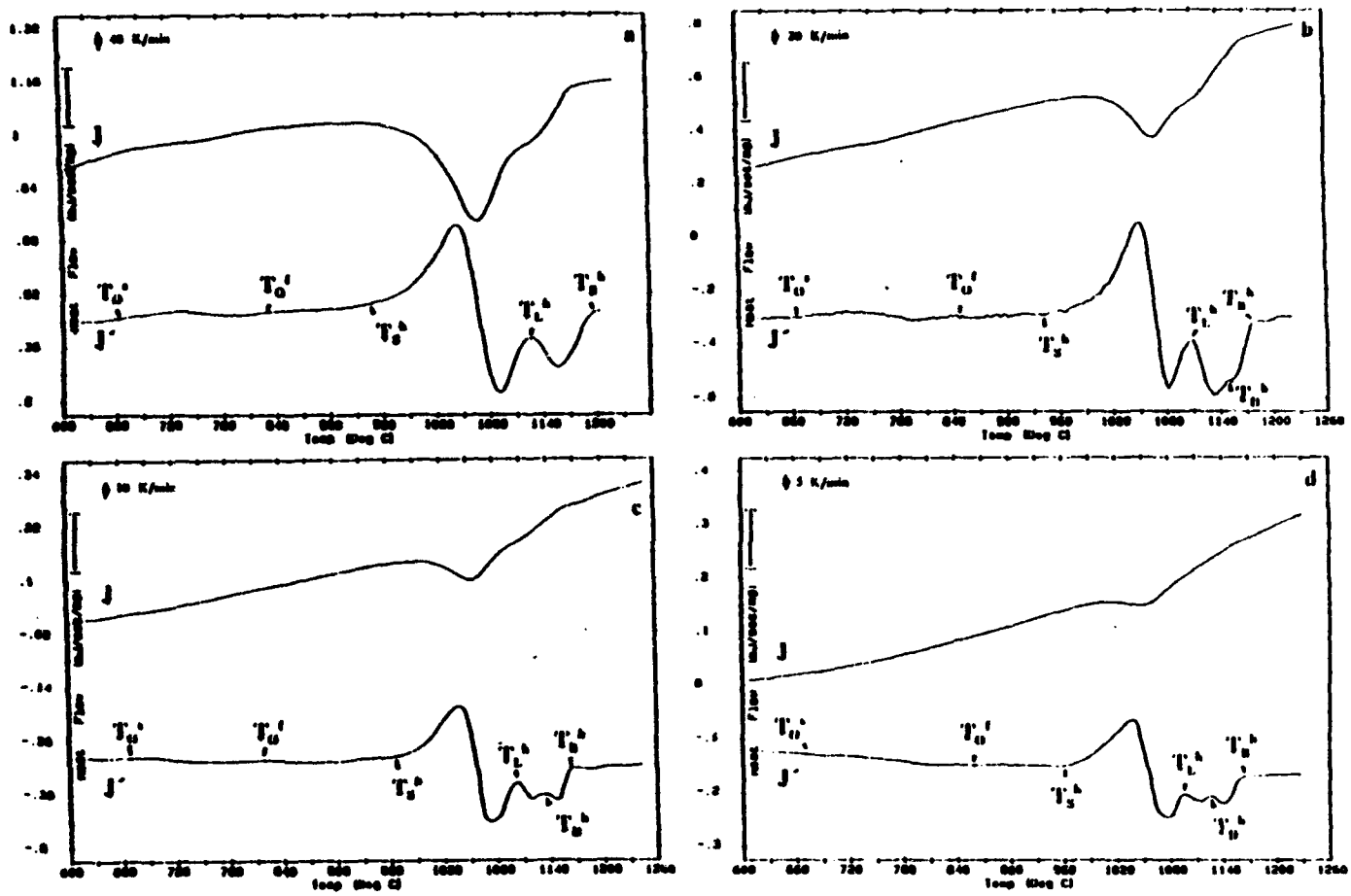

Figure 2 - CDTA thermograms for Ti-25Al-11Nb on heating at (a) 40, (b) 20, (c) 10, and (d) 5 K/min. Heat flow J ($mJ.sec^{-1}.mg^{-1}$) and its first derivative J′ ($mJ.sec^{-1}.mg^{-1}.deg^{-1}$).

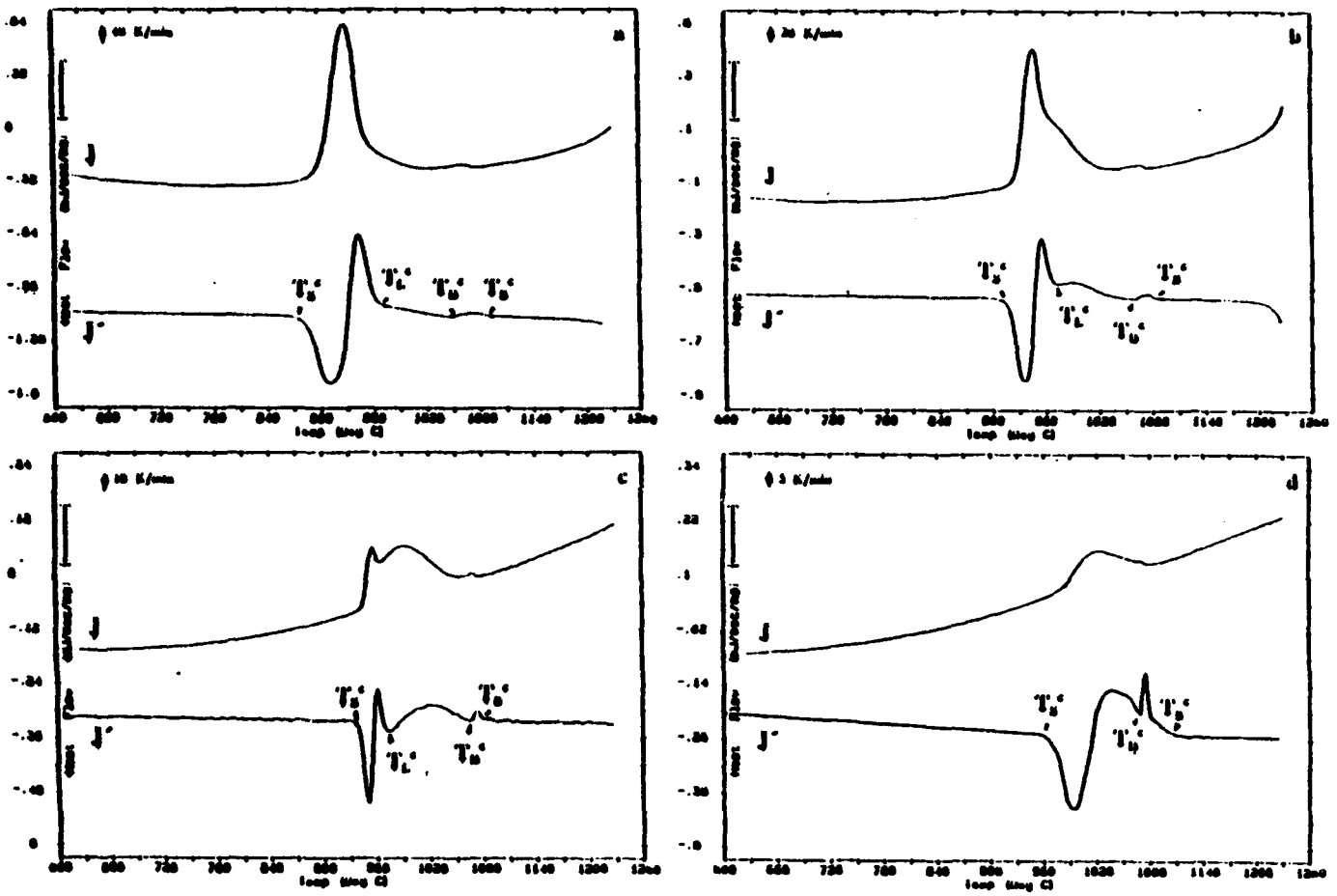

Figure 3 - CDTA thermograms for Ti-25Al-11Nb on cooling at (a) 40, (b) 20, (c) 10, and (d) 5 K/min. Heat flow J ($mJ.sec^{-1}.mg^{-1}$) and its first derivative J' ($mJ.sec^{-1}.mg^{-1}.deg^{-1}$).

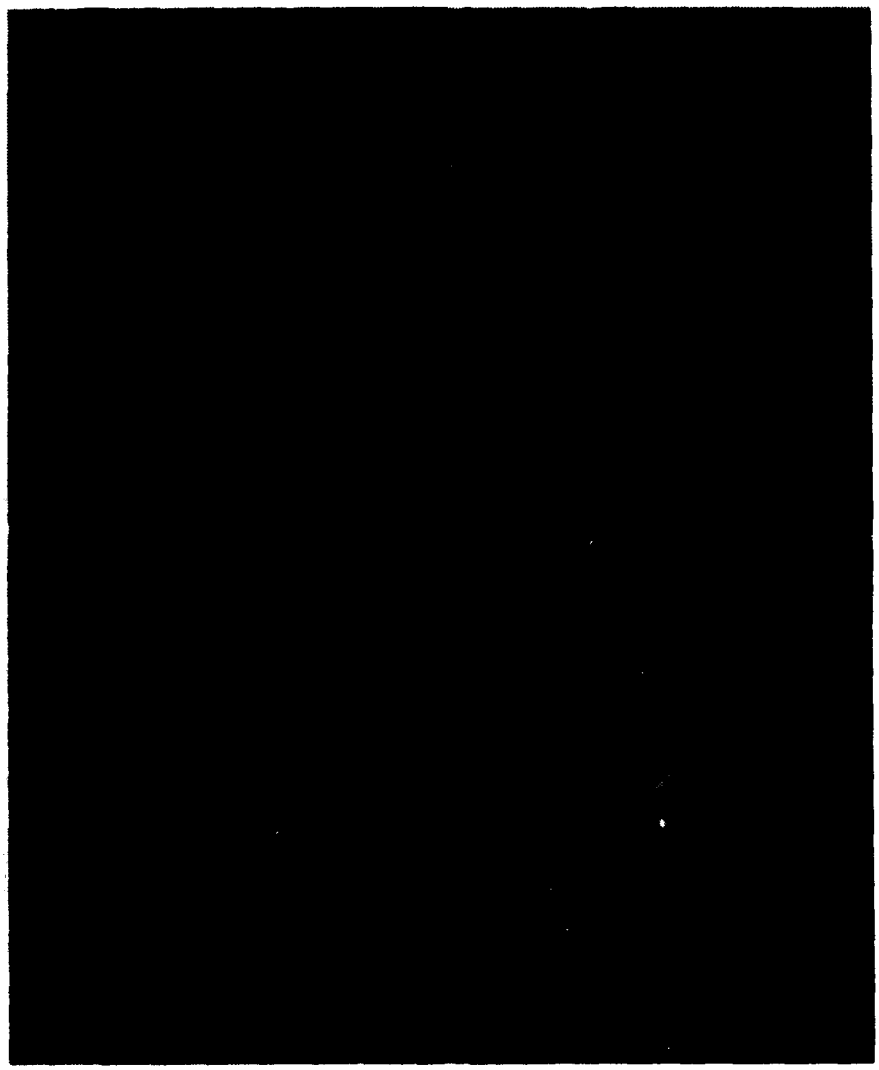

Figure 4 - Microstructures of the CDTA samples from Ti-25Al-11Nb after cooling at various cooling rates (a) 40 K/min (b) 20 K/min (c) 10 K/min (d) 5 K/min.

PHASE TRANSFORMATIONS IN XD™ TiB_2 REINFORCED NEAR-GAMMA Ti-48Al-2Nb-2Mn

S. Guillard and H.J. Rack
Materials Science and Engineering Program,
Department of Mechanical Engineering,
Clemson University, Clemson, SC 29634-0921

To be published in
Materials Science and Engineering

Abstract

The elevated temperature phase transformations occurring in investment cast and HIP'ed near-gamma Ti-48Al-2Nb-2Mn containing 0, 0.5, 1, 2 and 7 volume pct TiB_2 have been investigated utilizing in-situ thermal analysis, high temperature x-ray, optical and transmission electron microscopy. A series of reversible transformations were observed during heating/cooling:

$$\alpha_2+\gamma \dashrightarrow \alpha+\gamma \dashrightarrow \alpha+\beta+\gamma \dashrightarrow \beta+\gamma \dashrightarrow \beta + L$$

where on heating the low temperature eutectoid transformation, $\alpha_2 + \gamma \dashrightarrow \alpha$, is followed by β precipitation and γ dissolution, a high temperature reverse peritectoid reaction, $\alpha \dashrightarrow \beta + \gamma$ and finally an inverse peritectic reaction $\gamma \dashrightarrow \beta + L$.

Further, the variable TiB_2 morphologies observed suggest that TiB_2 redissolves during XD™ processing, re-precipitating during subsequent solidification, its morphology evolving from lacey to plate/needle-like to blocky as boron content or distance from the ingot periphery increases.

Finally, it was shown that, rather than the TiB_2 content per se, elemental boron content, and by extension total interstitial content, was the primary factor influencing the differences in phase transitions temperatures observed in these materials. As the interstitial content increased, the eutectoid transformation temperature increased, the peritectoid transformation temperature was not affected and the peritectic transformation temperature decreased.

Introduction

Because of their low density, good oxidation resistance, relatively high modulus and good strength retention at elevated temperature[1] (α_2 + γ) Ti-Al alloys are attractive candidates for advanced turbine and airframe applications. Originally their applicability was restricted because of their low ambient temperature fracture toughness and ductility. Recent investigations have however demonstrated that significant gains in fracture toughness and ductility can be achieved through chemistry modification, principally through the addition of β stabilizing elements[2], selection of appropriate processing methods[3] and varying heat treatment[4]. For example, Kim and co-workers have shown that development of a fully lamellar (α_2+γ) microstructure results in a two fold increase in fracture toughness when compared to an equiaxed (α_2 + γ) microstructure[5].

While relatively simple thermal treatments may be utilized to promote the (α_2+γ) lamellar microstructure, and thereby increase the fracture toughness, these treatments are normally accompanied by an increase in grain size and, therefore, a further reduction in tensile ductility[3,4]. Larsen and co-workers indicate however that the formation of the (α_2+γ) lamellar microstructure can be enhanced and the fracture toughness increased in binary TiAl, without a reduction of tensile ductility, through the addition of 7 vol. pct. TiB_2 particles[6]. Further observations indicate that TiB_2 has the additional beneficial effect of promoting a decrease in α_2/γ colony size[7] and grain size[8,9].

Prompted by these results, several detailed investigations have been undertaken to examine the evolution of binary (α_2+γ) Ti-Al alloys following the addition of elemental B and TiB_2. For example, Hyman et al[10-12] have shown that B concentration, at a fixed Ti:Al ratio, solidification cooling rate and solidification undercooling, all have a significant effect on the Ti boride morphology and crystal structure formed during solidification of binary Ti-Al alloys. Namely, as boron concentration increases, TiB_2 evolves from a lacey to a needle/plate-like morphology and finally to a blocky morphology, whereas increasing the cooling rate or the amount of supercooling results in fine equiaxed TiB_2 particles.

Significantly less is known about the effect of B/TiB_2 on the solid-state transformations observed in Ti-Al alloys. The limited information presented by Feng et al[13] suggests that the addition of TiB_2 in binary (α_2+γ) Ti-Al acts in a manner qualitatively similar to O[8,14-16], i.e., enlarging the (α + γ) and raising the (α_2 + γ) eutectoid transformation temperature.

More recently, attention has focused on the addition of TiB_2/B in ternary and quaternary (α_2+γ) Ti-Al alloys. Huang and Hall[14] have shown that a reduction of grain size and the retention of a fully lamellar microstructure may be accrued through the addition of > 1 atom pct B or 0.5 atom pct N to Ti-45.5Al-2Cr. Other studies by Larsen et al.[6] have confirmed that TiB_2 additions to Ti-48Al-2Nb-2Mn act in an analogous manner, and that these additions result in enhanced fracture toughness and strength, the latter without substantial ductility penalty. To complement these studies, the results reported herein are aimed at achieving an understanding of the effect of TiB_2 additions on the phase transformations in a quaternary Ti-Al-Nb-Mn (α_2+γ) alloy.

Experimental Procedures

Ti-48Al-2Nb-2Mn ingots with 0, 0.5, 1, 2 and 7 volume percent boride were produced by Howmet Corporation as double vacuum arc remelted investment castings, boron being introduced via the XD™ process[17]. Cylindrical bars of 15.9 mm X 203.2 mm were investment cast and HIP'ed for 4 hours at 1533 K and 175 MPa, HIP'ing being terminated by cooling to room temperature at a rate less than 30 K/min. Table 1 lists the chemical compositions of the castings produced in this manner, the interstitial contents having been determined by direct current plasma. The boride volume fraction was calculated from the analyzed boron content, i.e., assuming that all the boron is in the boride phase, the accuracy of the direct current plasma technique being 3 to 5% [18].

The high temperature stability of these alloys was assessed using calorimetric differential thermal analysis (CDTA) and high temperature x-ray diffraction (HTXRD). The former utilized samples, weighing between 35 and 55 mg, which were placed in alumina crucibles and introduced into a thermal analysis system modified to be operated in a flowing high purity (1 ppb) argon atmosphere. Phase transformation temperatures were determined from observations between 873 K and 1703 K during both heating and cooling at rates of 5, 10, 20 and 40 K/min. Both the heat flow J, normalized per unit mass ($mJ.sec^{-1}.mg^{-1}$), and its first derivative with respect to temperature, $J'=dJ/dT$ ($mJ.sec^{-1}.mg^{-1}.deg^{-1}$), were recorded, with the transformation temperatures being defined where J and J' deviated from the baseline and, in the case of overlapping peaks, where the J' curve exhibited a curvature anomaly. The equilibrium temperature was determined through linear extrapolation, Zhu and Devletian [19] having shown that this linear variation can be utilized to estimate the transformation temperature within an accuracy of ±3°C.

High temperature x-ray diffraction(HTXRD) studies were undertaken to complement the calorimetry by identifying the phases present at elevated temperature. The procedure utilized a diffractometer equipped with a high temperature/vacuum chamber modified to introduce and maintain a high purity inert argon gas atmosphere at a desired pressure of 0.60 Pa. HTXRD samples, having dimensions of 8 mm X 20 mm X 0.25 mm, were prepared by wafering and grinding, with final preparation, to remove the presence of a prior strain hardened surface, involving chemical removal of a 20 μm minimum surface layer in a bath of 10 ml HNO_3 + 5 ml HF + 50 ml H_2O, followed by washing in ethanol and water, drying in air and storage in a vacuum dessicator.

Initially, ambient temperature 2θ-scans from 15° to 85° were obtained utilizing Cu-K_α radiation at 40 kV and 30 mA. The sample was then heated at a rate of 20K/min to 1703K, with diffraction spectra being acquired at selected temperatures, the latter being monitored by a type-C thermocouple directly spot welded to the specimen. Typically, data were recorded after a five-minute stabilization period at temperature, with data acquisition performed at a 2θ-speed of 10 degrees per minute. Three to four samples of each alloy were examined, with rocking curves being obtained where deemed necessary to verify the presence, or absence, of phases at elevated temperatures. Following data collection, the x-ray diffraction spectra were analyzed and the peaks indexed utilizing a least squares method iterative computer program.

Finally, samples for optical and transmission electron microscopy were prepared. Optical microscopy samples were cut and polished utilizing standard techniques with final etching for 5 to 10 seconds in Kroll's reagent. Transmission electron microscopy samples were prepared by

grinding on SiC grit paper to 150 microns, spark cutting 3mm-discs from the foils thus produced, and electro-polishing in a solution of 30 ml perchloric acid + 175 ml n-butanol + 300 ml methanol under 15 to 20 volts below -30°C. Subsequent observation was carried out in a Hitachi 600AB operated at 100 kV.

Results

Ti-48Al-2Nb-2Mn

Optical examination of as-casted and HIP'ed Ti-48Al-2Nb-2Mn indicates that this alloy had a columnar grain structure, Figure 1-a, with the grains nucleating at the mold and growing radially inward. Figure 1-b reveals a microstructure consisting of large lamellar colonies, L, 1500 to 8000 μm, and small equiaxed gamma grains, G, 150 to 250 μm, all displaying serrated grain boundaries. X-ray diffraction analysis, Figure 2, indicates that this alloy, at room temperature, consists of two phases, α_2 and γ. The gamma lattice parameters, c and a, 4.06636 Å and 4.0004 Å respectively, correspond to a c/a ratio of 1.016.

This two phase ($\alpha_2+\gamma$) microstructure was confirmed by transmission electron microscopy, no evidence for β, either along the α_2/γ interfaces of the ($\alpha_2+\gamma$) lamellar microstructure, Figure 3-a, or at triple point boundaries, being noted. Selected area diffraction analysis, Figure 3-b, also showed that the orientation relationship between TiAl/Ti_3Al was $\{022\}_{TiAl}$ // $(0001)_{Ti3Al}$ and $\langle 011\rangle_{TiAl}$ // $\langle 2110\rangle_{Ti3Al}$, as reported by various previous investigators[3,20].

Calorimetric differential thermal analysis, Figure 4, shows that, independent of heating/cooling rate, three reversible reactions, T1 thru T3, are observed during heating and cooling of unreinforced Ti-48Al-2Nb-2Mn. In addition, a fourth reaction, T4, is observed on heating. Temperatures for the onset and completion of these reactions are summarized in Table 2[1].

Comparison of the elevated temperature x-ray results, Figure 5, with those obtained under ambient conditions indicate that upon heating no discernable changes are observed until 1523K, at which temperature the $(110)_\beta$ peak appears. Figure 6, an enlarged portion of the x-ray scan at this temperature, shows the emergence of this peak, the microstructure now consisting of (α + γ + β), the α_2 having disordered. Evidence of the characteristic $(101)_{\alpha 2}$ ordered peak was detected by rocking curve analysis about 2θ=26°, at and below 1448 K. However, this peak disappears at 1473 K, the remaining (201) peak at 2θ=40.3° being ascribed to disordered alpha.

A further temperature increase to 1623K results in an increase in the (110) β peak intensities relative to the (111) γ peak, while the intensity of the (201) α peak relative to the (111) γ peak remains approximately constant, Figure 7, the vertical lines shown depicting the onset and completion of reaction T3 as defined by the CDTA results. Finally, above 1623K, the

---

[1] These values were obtained by extrapolating results from experiments at 3 different heating/cooling rates to a heating/cooling rate of 0 K/min. The precision due to this approximation along with the thermocouple precision at these temperatures leads to an estimated error of ± 4 K in the reported equilibrium transformation temperatures.

alloy is two phase ($\beta + \gamma$), all evidence of α having disappeared, with the ratio of $(110)_\beta/(111)_\gamma$ still increasing.

Ti-48Al-2Nb-2Mn/TiB_2

Ambient temperature x-ray diffraction results for the TiB_2 reinforced Ti-48Al-2Nb-2Mn were similar to those of the unreinforced alloy, Figure 8, i.e., the alloys were two-phase ($\alpha_2 + \gamma$) at room temperature. However, additional peaks were present in the x-ray spectrum for alloys containing boride volume percents equal to and greater than 1 percent. This is illustrated in Figure 8 for Ti-48Al-2Nb-2Mn containing 7 volume percent boride[2]. Table 3 shows that all the observed peaks can be attributed to either α_2, γ or TiB_2[3]. Examination of this data shows that TiB_2, which has the hexagonal C32 crystal structure, is the boride phase present in these materials and TiB, which has been detected in a previous investigation[21] by adding boron to Ti-Al-Nb or Ti-Al-Ta, is not observed. This observation has also been reported by Larsen[8] and Hyman et al.[10,11] who identified by x-ray diffraction and transmission electron microscopy of the extracted particles, that all three morphologies, lacey, needle and blocky, were TiB_2 (C32).

Optical microscopy showed that the introduction of TiB_2 has three major effects on microstructure. First, while Ti-48Al-2Nb-2Mn containing 0.5 volume percent TiB_2 exhibited large columnar grains similar in size to those in the unreinforced material, the alloys containing 1, 2 and 7 volume percent TiB_2 displayed small, equiaxed grains, approximately 50 to 150 μm in size, independent of diboride volume fraction, Figure 9.

Second, the introduction of TiB_2 at all levels investigated resulted in a fully lamellar ($\alpha_2+\gamma$) microstructures.

Third, three morphologically distinct TiB_2 phases are observed in the central region of the ingots, depending on the TiB_2 volume fraction. At 0.5 volume percent TiB_2, the diboride appears as lacey particles, 20 to 100 μm long. As the TiB_2 content increases to 1 and 2 volume percent the diboride phase evolves to a mixture of needles and blocky particles, and finally to predominantly blocky particles at 7 volume percent. Moreover, independent of TiB_2 content, the borides at the periphery of all the ingots display the lacey morphology. Figure 10 summarizes these two effects showing that the boride morphology is a function of both the TiB_2 content and the location within the ingot.

Transmission electron microscopy confirmed the x-ray diffraction results, the room-temperature microstructure consisting of ($\alpha_2+\gamma$) lamellae, no evidence of β phase being detected, Figure 11. Again, the orientation relationship between α_2 and γ was identical to the unreinforced material, i.e. $\{022\}_{TiAl}$ // $(0001)_{Ti3Al}$ and $<011>_{TiAl}$ // $<2110>_{Ti3Al}$. However, in contrast to the unreinforced alloy, a high dislocation density exists within both the α_2 and γ lamellae. The occurrence of this dislocation substructure presumably arises from the relaxation of stresses due to the difference in the coefficients of thermal expansion between matrix and diboride particles. Dislocations around a blocky TiB_2 particle in a γ phase lamella are shown in Figure 12.

---

[2] The absence of such peaks in Ti-48Al-2Nb-2Mn + 0.5 vol.% boride is due to the low boride volume fraction in this material.

[3] The most intense TiB_2 peak corresponds to a 2θ value of 44.44 and is probably masked by the (002) γ peak.

Typical calorimetric differential thermal analysis results for both heating/cooling of the TiB_2 reinforced Ti-48Al-2Nb-2Mn alloys are illustrated in Figures 13 by the scans coresponding to Ti-48Al-2Nb-2Mn/1 vol.% TiB_2. Four reactions were observed, T1, T2, T3 and T4, similar to those found in unreinforced Ti-48Al-2Nb-2Mn, Table 2.

Elevated temperature x-ray diffraction results were also similar to those of the unreinforced alloy, Figure 14. For example, at low temperatures Ti-48Al-2Nb-2Mn/7 volume percent TiB_2 was ($\alpha_2 + \gamma$); above 1548K it was ($\alpha + \gamma + \beta$) before finally transforming to ($\beta + \gamma$) above 1648K.

Discussion

The calorimetric experiments conducted during this study have shown that, independent of TiB_2 content, four reactions occur on heating, their identification being made using the x-ray diffraction results.

T1 separates a ($\alpha_2 + \gamma$) region from a ($\alpha + \gamma$) region according to x-ray analysis. This suggests that, as in the binary Ti-Al system, T1 is the eutectoid transformation $\alpha_2 + \gamma \longrightarrow \alpha$ originally proposed by Murray[22] and recently unambiguously confirmed[23] in the Ti-Al system. In addition, in the unreinforced material, the T1 reaction occurs at temperatures close to the reported eutectoid temperature in binary Ti-48.65Al, 1450 K[24] whereas, in Ti-48Al-2Nb-2Mn + 7 vol.% TiB_2, it occurs at the temperature reported for Ti-44Al + 7 vol.% TiB_2 and Ti-47Al + 7 vol.% TiB_2, 1523 K[13].

Reaction T2 occurs as temperature increases and corresponds to partial dissolution of gamma along with beta precipitation, the amount of alpha being relatively unchanged as temperature increases. Figure 15, showing a plot of the integrated intensities of the (111) γ, (201) α and (110) β peaks as a function of temperature for Ti-48Al-2Nb-2Mn containing 7 volume percent TiB_2, confirms this. Also shown as vertical lines in this figure are the onset and completion of reaction T3 as determined from the calorimetric experiment. They reveal that alpha starts disappearing when T3 begins, whereas both beta and gamma increase. Upon completion of T3, alpha has completely disappeared and only beta and gamma remain. This suggests that T3 is a $\alpha \longrightarrow \beta + \gamma$ peritectoid transformation.

Identification of reaction T4 is more challenging. Indeed, the x-ray scan at the highest temperature examined, 1698 K (Figure 5), indicates that a two-phase ($\beta + \gamma$) region exists at high temperature. This shows that, in contrast with binary TiAl alloys [25-27], α is <u>not</u> the high temperature equilibrium phase for Ti-48Al-2Nb-2Mn. This difference between the Ti-48Al-2Nb-2Mn and binary alloys[13] is presumably due to the β-stabilizing effect of the two alloying additions, i.e., Nb and Mn.

Additional evidence for the existence of beta at high temperature has been provided following isothermal forging of Ti-47Al-3Cr (at%) at 1596 K where precipitation of a chromium-enriched beta phase has been reported[28]. Huang et al.[29] also mention the presence of a B2-phase at room temperature after slow cooling, following a heat treatment of Ti-48Al-4Cr between 1523 and 1698 K for two hours. Moreover, in a study of homogenization treatments of Ti-46.1Al-3.1Cr, the authors[30] report that the grain size remained small even after prolonged exposure at 1596 K. This is in sharp contrast with the behavior of binary Ti-Al alloys which, being single-phase at these temperatures, undergo rapid grain growth[31]. Hence, Ti-46.1Al-3.1Cr

must be two-phase at high temperature, the β-phase presumably acting as a grain growth inhibitor.

The presence of β at high temperature was further demonstrated by heat treating Ti-48Al-2Nb-2Mn for 5 hours at 1675 K, and quenching in cold water. Room temperature x-ray diffraction of this sample reveals a three-phase ($\beta+\gamma+\alpha_2$) microstructure, Figure 16. This confirms that the β and γ phases are indeed present at 1675 K, the presence of α_2 suggesting that the eutectoid transformation cannot be suppressed on rapid cooling. Notably, earlier investigations of Ti-48Al-2Nb-2Mn[32,33], utilizing CDTA, failed to recognize the presence of the ($\beta + \gamma$) phase field at high temperatures, presumably because this technique by itself is not able to define the reactant or the product phases participating in a phase transformation. Moreover, our results, coupled with Mizuhara's study[30] indicate that retention of the β phase to room temperature is highly cooling rate dependent, with slow cooling leading to the cascade of reactions thereafter proposed and no β phase being detected at ambient temperature.

Finally, Figure 17 shows Ti-48Al-2Nb-2Mn + 2 volume percent TiB_2 both prior and after exposure to 1710K, that is above T4. The presence of a continuous phase in Figure 17-b, characteristic of partial melting, clearly demonstrates that T4 is the solidus. Further evidence is provided by Figure 15 which shows that the amount of beta phase increases and the amount of gamma phase decreases with increasing temperature above T3, suggesting that T4 corresponds to a $\gamma \dashrightarrow \beta + L$ peritectic reaction.

Summarizing, independent of TiB_2 content, it is proposed that heating/cooling of Ti-48Al-2Nb-2Mn results in the following transformations:

$$\underset{T1}{\alpha_2+\gamma} \dashrightarrow \underset{T2}{\alpha+\gamma} \dashrightarrow \underset{T3}{\alpha+\beta+\gamma} \dashrightarrow \underset{T4}{\beta+\gamma} \dashrightarrow \beta+L.$$

Although the introduction of TiB_2 does not alter the sequence of phase transformations observed in Ti-48Al-2Nb-2Mn, it does alter the transformation temperatures. In addition, the TiB_2 morphology is a function of both solidification rate and the volume percent introduced. In the XD™ process, TiB_2 is introduced as blocky particles utilizing a TiB_2-Al master alloy. However, the TiB_2 observed in the as-cast and HIP'ed Ti-48Al-2Nb-2Mn ingots appears with a lacey, needle-like, or blocky morphology. Moreover, when TiB_2 has a blocky morphology, its size differs from that in the master alloy[8]. This suggests that the diboride phase has redissolved during XD™ processing, with subsequent re-precipitation during solidification. On this basis, in a manner similar to that associated with solidification of binary Ti-Al containing varying elemental boron concentrations, the blocky and needle-like morphologies correspond to primary TiB_2 formed prior to the nucleation of any metallic phase [10] whereas the lacey particles are secondary borides which grow concurrently with the metallic phases and are therefore constrained during solidification. Whether lacey, needles or blocky borides develop depends upon how far the alloy composition is from the $L \dashrightarrow M + TiB_2$ monovariant line[10]. Hyman's analysis for ternary Ti-Al-X correlates well with the current microscopy results which illustrate the lacey to needle to blocky morphology evolution with increasing boron matrix supersaturation. It also explains the effect of TiB_2 content on the grain size. When the boron content in the matrix is such that only secondary borides precipitate, the metallic phase solidifies first and the grains, growing unhindered by particles, are similar to those found in an unreinforced matrix. For example, Ti-48Al-2Nb-2Mn + 0.5 % TiB_2 displays a lacey diboride phase, i.e., secondary diborides, and a columnar grain structure similar to the unreinforced material. With an increase in the boron content, primary diborides precipitate and become nucleation sites for metallic phase

solidification, yielding a small grain size. Therefore Ti-48Al-2Nb-2Mn + 1, 2 and 7 % TiB_2 display needle-like or blocky diboride particles, i.e., primary diborides, and have a refined grain size when compared to Ti-48Al-2Nb-2Mn and Ti-48Al-2Nb-2Mn + 0.5 % TiB_2.

The redissolution of the TiB_2 particles suggests that, rather than the TiB_2 content itself, the elemental boron content, and by extension the total interstitial content, is the primary factor that must be considered when examining the variations of solid-state transformation temperatures between the various materials in this study. Figures 18 thru 20 illustrate this dependence of the observed eutectoid, peritectoid and peritectic transformation temperatures on total (O+C+N+B+H) interstitial content. It was assumed in this analysis that the room-temperature solubility of boron in Ti-48Al-2Nb-2Mn was approximately 100 wppm (≈350 appm), recognizing that the addition of 500 wppm (≈1750 appm) boron to Ti-48Al-2Nb-2Mn leads to the formation of TiB_2 particles, indicating that the boron solubility limit had been exceeded[34]. It should be noted however that although this may be an overestimate of the boron solubility, the trends shown in Figures 18 thru 20 should remain unchanged.

Figure 18 shows that as total interstitial content increases, the eutectoid transformation (reaction T1) temperature increases, in agreement with Feng at al.[13]. This effect is well-known in the case of oxygen[8,14-16], a very potent α_2-stabilizer. Boron atoms have been shown to occupy octahedral sites in TiAl[31], precisely the same sites occupied by oxygen atoms and the other interstitials. It is proposed that they have the same α_2-stabilizing effect, corresponding to an increase of the eutectoid temperature of 6.7×10^{-4} K/appm interstitial content.

By contrast, the proposed peritectoid reaction, Figure 19, is not influenced by either the interstitial content or the TiB_2 volume fraction, possibly because of the sluggishness of this reaction.

Finally, Figure 20 shows that increasing total interstitial content initially results in a sharp decrease in the peritectic transformation temperature, the rate of change in this transformation temperature however decreasing with further increase in total interstitial content.

Conclusions

The elevated temperature phase stability of investment cast and HIP'ed near-gamma Ti-48Al-2Nb-2Mn containing 0, 0.5, 1, 2 and 7 vol.% TiB_2 involves the following reversible phase transformations:

$\alpha_2+\gamma \longrightarrow \alpha+\gamma \longrightarrow \alpha+\beta+\gamma \longrightarrow \beta+\gamma \longrightarrow \beta+L$

These reactions involve a low temperature eutectoid transformation, $\alpha_2 + \gamma \longrightarrow \alpha$, a precipitation reaction leading to the presence of the β phase, a high temperature peritectoid transformation, $\alpha \longrightarrow \beta + \gamma$ and finally a peritectic $\gamma \longrightarrow \beta + L$ reaction.

The varying TiB_2 morphologies observed as a function of both solidification rate and volume percent TiB_2 show that TiB_2, as introduced by the XD™ process, redissolves before precipitating during subsequent solidification. Therefore, rather than the TiB_2 content per se, elemental boron content, and by extension total interstitial content, is the primary factor influencing the differences in phase transitions temperatures observed in these materials. As the interstitial content increases, the eutectoid transformation temperature increases, the peritectoid transformation temperature is not affected and the peritectic transformation temperature decreases.

Acknowledgements

This research was sponsored by the Defense Advanced Research Projects Agency under the contract N00014-89-J-3166 supervised by Mr. W. Baker and monitored by Dr. G. Yoder of the Office of Naval Research. The authors would like to acknowledge Mr. Don Larsen of the Howmet Corporation for supplying the materials and the assistance of Dr. P. Chaudhury and M. Long.

References

1. Y.W. Kim and D.M. Dimiduk, *J. Metals*, Aug.1991, 40.
2. Y.W. Kim, in "High-Temperature Ordered Intermetallic Alloys IV", (eds. L. A. Johnson, D. P. Pope and J. O. Steigler), Vol. 213, 777-794; 1991, Pittsburgh, PA, Materials Research Society.
3. Y.W. Kim, in "Microstructure/Property Relationships in Titanium Aluminides and Alloys", (eds. Y-W. Kim and R.R. Boyer), 91-103; 1991, Warrendale, PA, The Minerals, Metals and Materials Society.
4. S-C. Huang and D. S. Shih, in "Microstructure/Property Relationships in Titanium Aluminides and Alloys", (eds. Y-W. Kim and R.R. Boyer), 105-122; 1991, Warrendale, PA, The Minerals, Metals and Materials Society.
5. K. S. Chan and Y-W. Kim, in "Microstructure/Property Relationships in Titanium Aluminides and Alloys", (eds. Y-W. Kim and R.R. Boyer), 179-196; 1991, Warrendale, PA, The Minerals, Metals and Materials Society.
6. D.E. Larsen, M. L. Adams, S. L. Kampe, L. Christodoulou and J. D. Bryant, *Scripta Met.*, 1990, **24**, 851.
7. J. D. Bryant, L. Christodoulou and J. R. Maisano, *Scripta Met.*, 1990, **24**, 33.
8. D.E. Larsen, S. Kampe and L. Christodoulou, in "Intermetallic Matrix Composites", (eds. D.L. Anton et al.), Vol. 194, 285-292; 1990, Pittsburgh, PA, Materials Research Society.
9. D. E. Larsen, L. Christodoulou, S. L. Kampe and P. Sadler, *Mater. Sci. Eng.*, 1991, **A144**, 45.
10. M. E. Hyman, C. McCullough, J. J. Valencia, C. G. Levi and R. Mehrabian, *Met. Trans.*, 1989, **20A**, 1847.
11. M.E. Hyman, C. McCullough, C. G. Levi and R. Mehrabian, *Met. Trans.*, 1991, **22A**, 1647.
12. M. DeGraef, J.P.A. Löfvander, C. McCullough and C. G. Levi, *Acta Met et Mat.*, 1992, **40**, 3395.
13. C.R. Feng, D.J. Michel and C.R. Crowe, *Scripta Met.*, 1990, **24**, 1297.
14. S. C. Huang and E. L. Hall, in "High-Temperature Ordered Intermetallic Alloys IV", (eds. L. A. Johnson et al.), Vol. 213, 827-832; 1991, Pittsburgh, PA, Materials Research Society.
15. M. J. Blackburn, in "The Science, Technology and Application of Titanium", (eds. R. I. Jaffee and N. E. Promisel), 633-643; 1970, Oxford, U.K., Pergamon Press.
16. A. Szaruga, M. Saqib, R. Omlor and H.A. Lipsitt, *Scripta Met.*, 1992, **26**, 787.
17. L. Christodoulou, P.A. Parrish and C.R. Crowe, in "High Temperature/High Performance Composites", (eds. F.D. Lemkey et al.), Vol. 120, 29-34, Pittsburgh, PA, Materials Research Society.
18. J. Merrell, Beckman Spectroscan 6, personal communication, 1993.
19. Y.T. Zhu and J.H. Devletian, *Met. Trans.*, 1991, **22A**, 1993.
20. C.R. Feng, D.J. Michel and C.R. Crowe, *Scripta Met.*, 1989, **23**, 1707.
21. J. J. Valencia, C. McCullough, J. Rösler, C. G. Levi and R. Mehrabian, in "Solidification of Metal Matrix Composites", (ed. P. Rohatgi), 133-150; 1990, Warrendale, PA, The Minerals, Metals and Materials Society.
22. J.L. Murray, *Met. Trans.*, 1988, **19A**, 243.
23. A. Hellwig, G. Inden and M. Palm, *Scripta Met*, 1992, **27**, 143.
24. J.C. Mishurda and J.H. Perepezko, in "Microstructure/Property Relationships in Titanium Aluminides and Alloys", (eds. Y.W. Kim and R.R. Boyer), 3-30; 1991, Warrendale, PA, The Minerals, Metals and Materials Society.

25. E.L. Hall and S.C. Huang, *Acta Met.*, 1990, **38**, 539.
26. C.D. Anderson, W.H. Hofmeister and R.J. Bayuzick, *Met. Trans.*, 1993, **24A**, 61.
27. C. McCullough, J. J. Valencia, H. Mateos, C. G. Levi, R. Mehrabian and K.A. Rhyne, *Scripta Met.*, 1988, **22**, 1131.
28. M. Yamaguchi, *Mater. Sci. Tech.*, 1992, **8**, 299.
29. S.C. Huang and E.L. Hall, *Met. Trans.*, 1991, **22A**, 2619.
30. Y. Mizuhara and N. Masahashi, *Scipta Met*, 1992, **27**, 1079.
31. S. C. Huang and P. A. Siemers, *Met. Trans.*, 1989, **20A**, 1899.
32. C.M. Lombard, R.M. Nekkanti and V. Seetharaman, *Scripta Met.*, 1992, **26**, 1559.
33. P.A. McQuay, D.M. Dimiduk and S.L. Semiatin, *Scripta Met.*, 1991, **25**, 1689.
34. D. Larsen, personal communication, 1993.

Table 1

ALLOYS COMPOSITIONS (AT%)

ALLOY	O_2 ppm	N_2 ppm	H_2 ppm	C ppm	Al	Nb	Mn	TiB_2 vol% (at% B)
NM0	1290	120	115	310	48.1	2.0	1.4	0
NM0.5	1280	80	115	390	47.4	2.0	1.7	0.5 (0.69)
NM1	1275	115	115	270	47.0	1.9	1.6	1 (1.44)
NM2	1325	115	115	265	47.4	2.0	1.6	2 (2.98)
NM7	1420	580	580	545	46.9	1.8	1.5	7 (10.07)

Note: all values, unless otherwise indicated, are in atomic percent.

Table 2

EQUILIBRIUM TRANSFORMATION TEMPERATURES (K)

	HEATING	HEATING	HEATING		COOLING	COOLING	COOLING
	T1 onset complete	T2 onset complete	T3 onset complete	T4	T3 onset complete	T2 onset complete	T1 onset complete
NM0	1458 1485	1536 1623	1623 1646	1690	1638 1597	1603 1563	1465 1438
NM0.5	1470 1498	1515 1626	1626 1659	1677	1631 1593	1621 1584	1476 1445
NM1	1468 1486	1513 1620	1620 1661	1670	1628 1605	1615 1590	1485 1468
NM2	1475 1490	1519 1625	1625 1656	1666	1633 1604	1611 1590	1483 1463
NM7	1529 1539	1545 1630	1630 1652	1664	1644 1619	1633 1603	1568 1521

Note: these values were obtained by extrapolating results from experiments at 3 different heating/cooling rates to a heating/cooling rate of 0 K/min. The imprecision due to this approximation along with the thermocouple imprecision at these temperatures lead to an error of ± 6 K.

Table 3

SUMMARY OF OBSERVED DIFFRACTION PEAKS
IN Ti-48Al-2Nb-2Mn + 7 vol.% TiB_2 AT ROOM TEMPERATURE

OBSERVED	α_2		γ		TiB_2*
2θ	(hkl)	2θ	(hkl)	2θ	2θ
21.82			(001)	21.77	
26.31	(101)	26.10			
27.70					27.60
31.65			(101)	31.58	
34.10					34.14
38.58			(111)	38.69	
44.25			(002)	44.38	
45.12			(200)	45.27	
65.34			(202)	65.26	
77.91	(222)	77.86			
79.23			(311)	79.16	

* As obtained from JCPDS card 35-741.

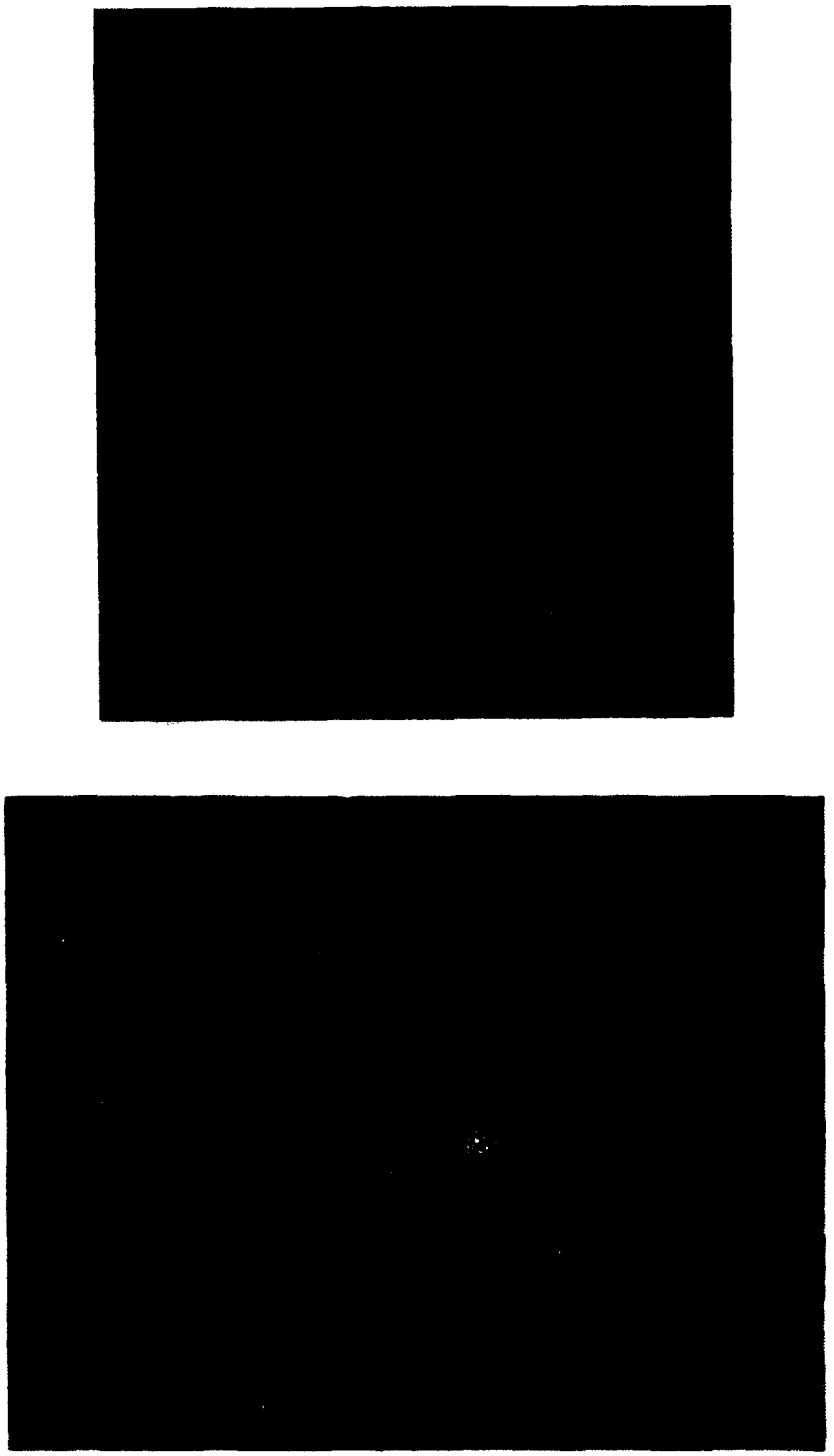

Figure 1. Optical Micrographs of Ti-48Al-2Nb-2Mn Illustrating (a) Columnar Grain Structure and (b) Microstructure Consisting of Equiaxed γ Grains, [G], and (α_2 + γ) Lamellar Colonies, [L].

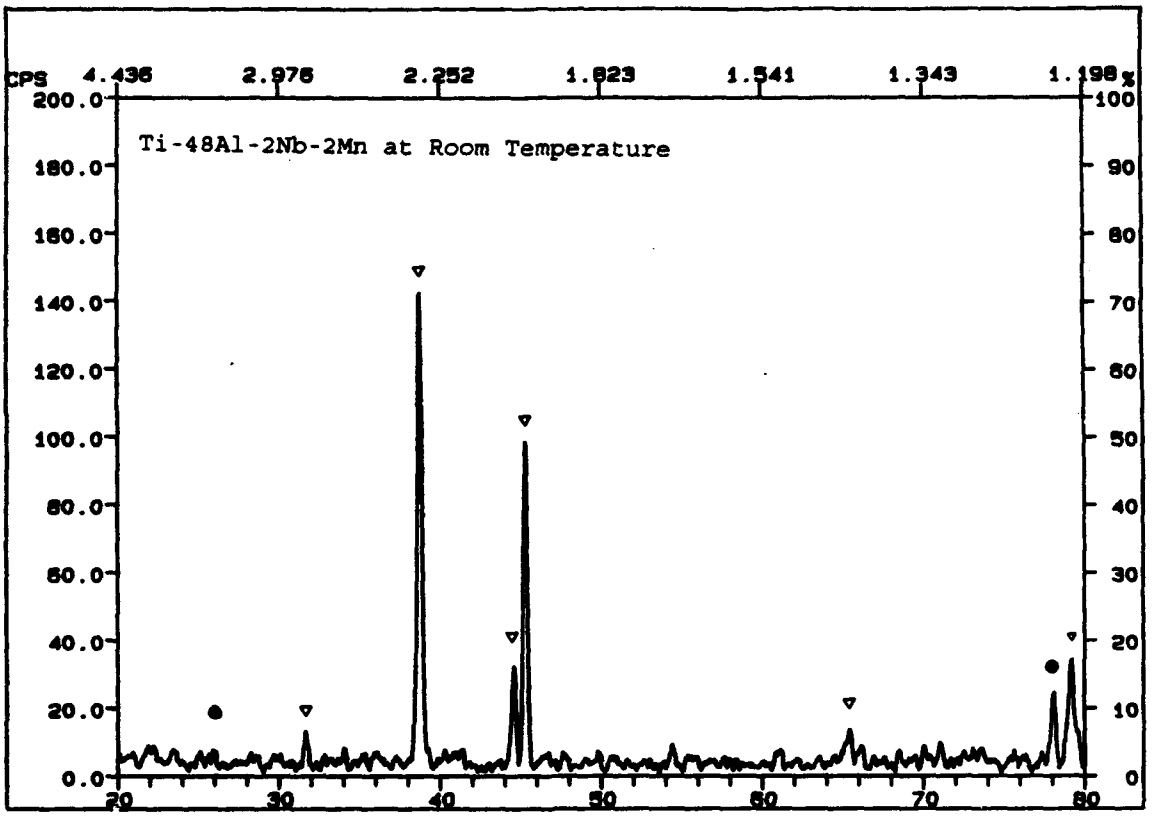

Figure 2. Room-Temperature X-Ray Scan for Ti-48Al-2Nb-2Mn (● α_2, ▽ γ).

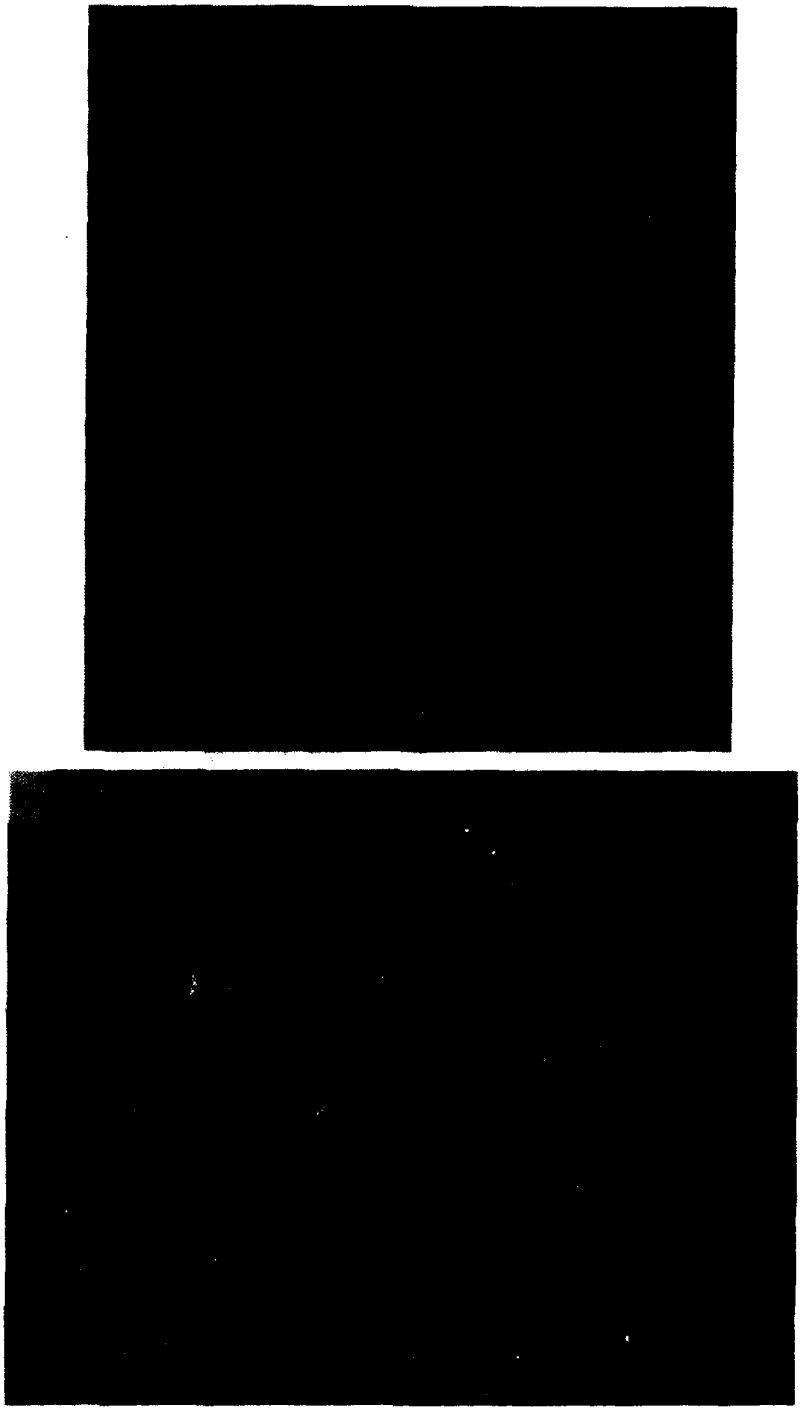

Figure 3. Transmission Electron Micrograph Showing (a) (α_2+γ) Lamellae at Room Temperature in Ti-48Al-2Nb-2Mn and (b) Corresponding Selected Area Diffraction Pattern Showing {022}//(0001) and <011>//<2110>.

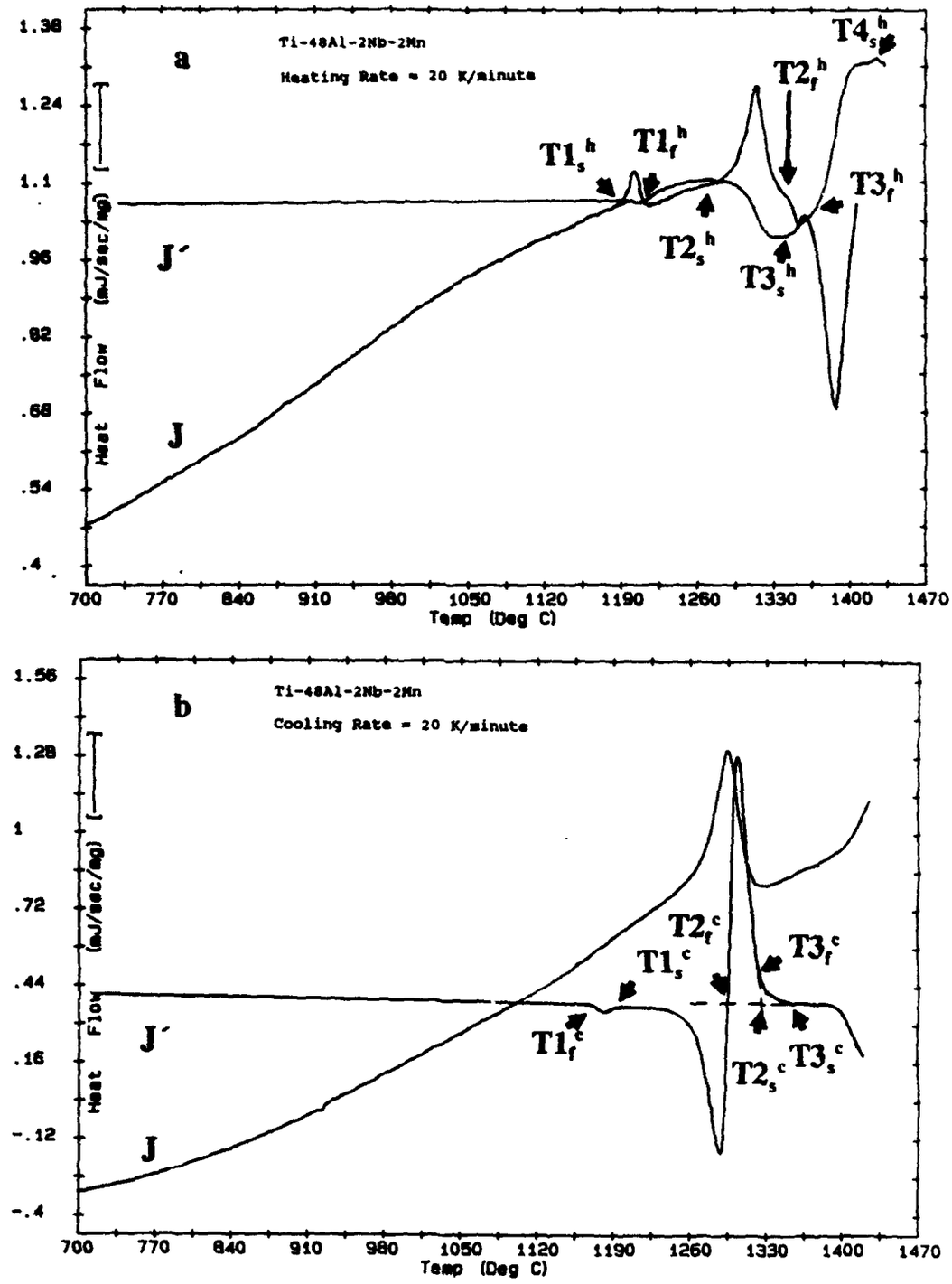

Figure 4. Thermograms of Ti-48Al-2Nb-2Mn on (a) heating, (b) on cooling at 20 K/min.

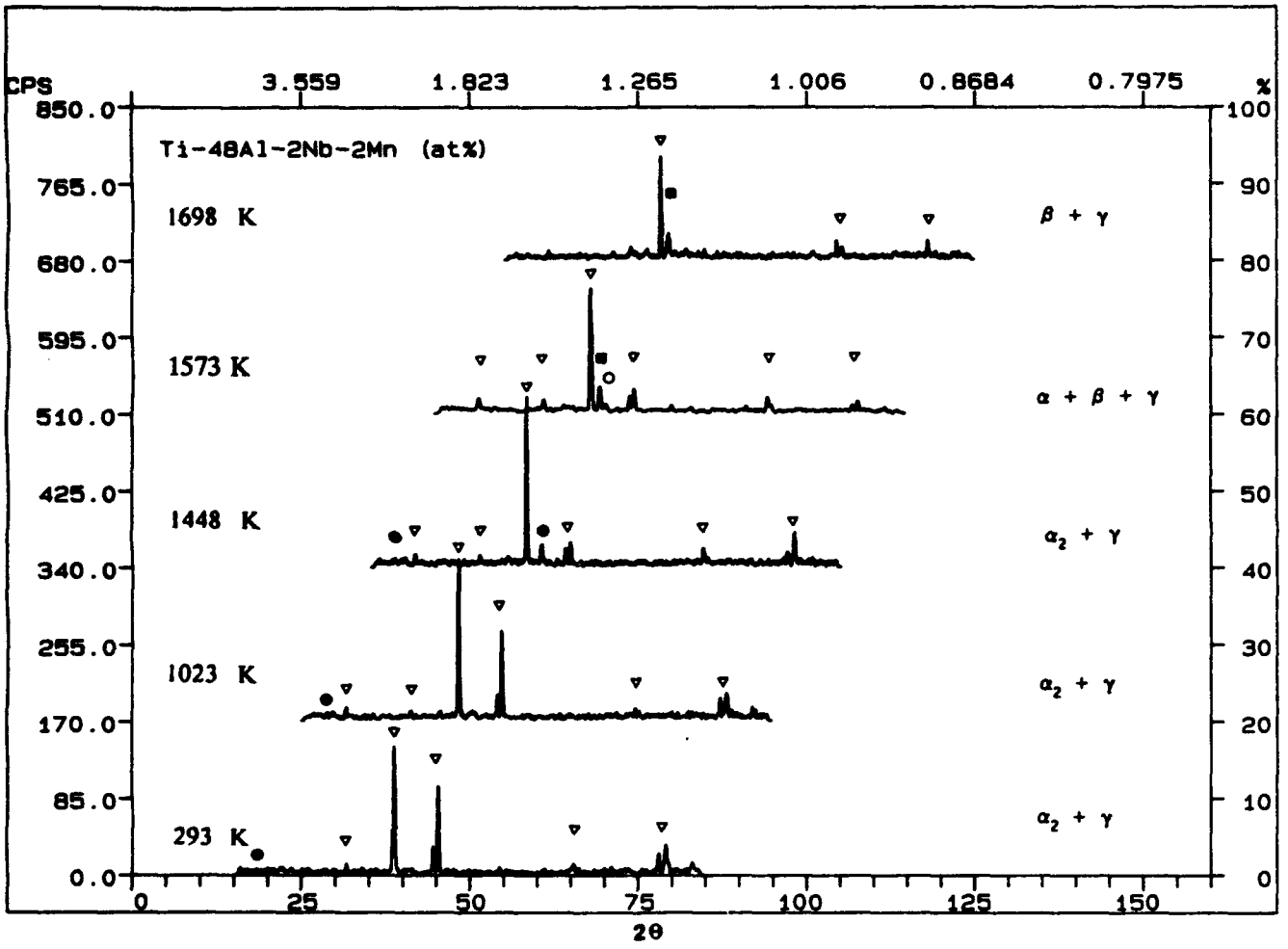

Figure 5. X-ray Spectra at Selected Temperatures for Ti-48Al-2Nb-2Mn (• α_2, o α, ■ β, ▽ γ).

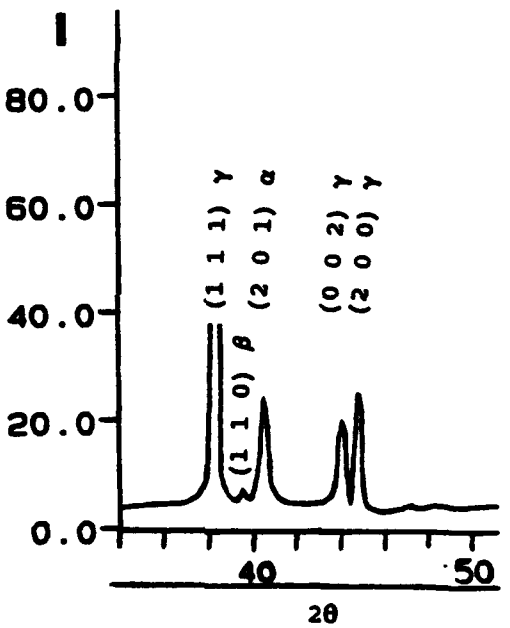

Figure 6. Enlarged Portion of Ti-48Al-2Nb-2Mn X-Ray Scan at 1523 K Illustrating Emergence of $(1\ 1\ 0)_\beta$ Peak.

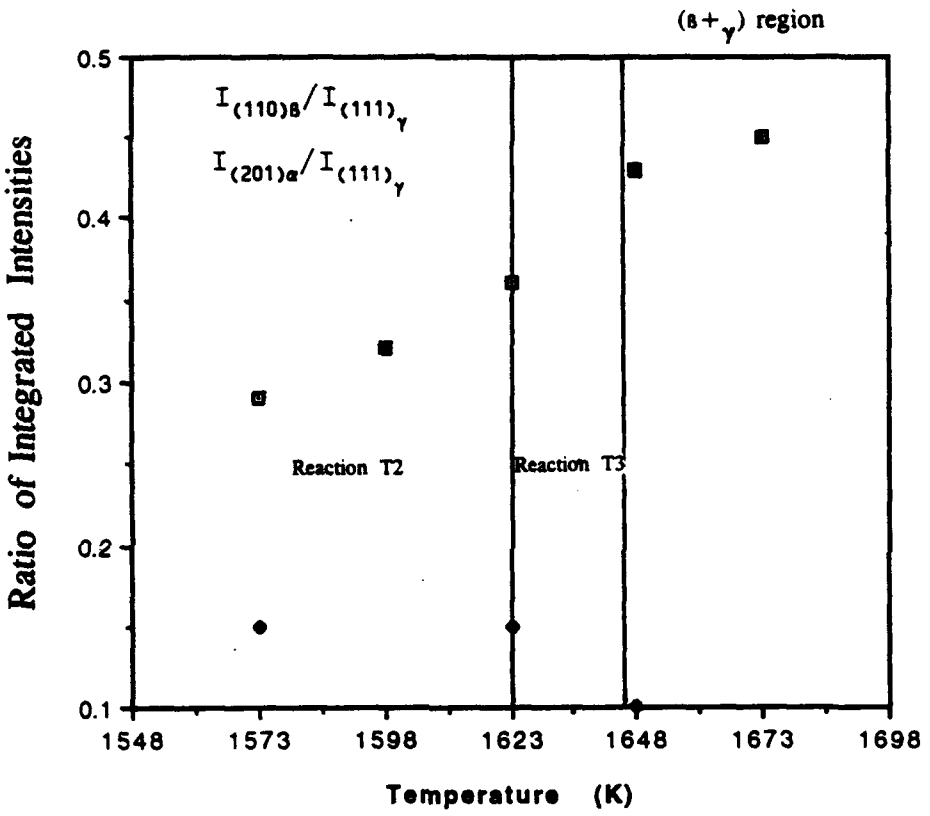

Figure 7. Ratio of the Integrated Intensities of the (110) β Peak and (201) α Peak to the (111) γ Peak as a Function of Temperature for Ti-48Al-2Nb-2Mn.

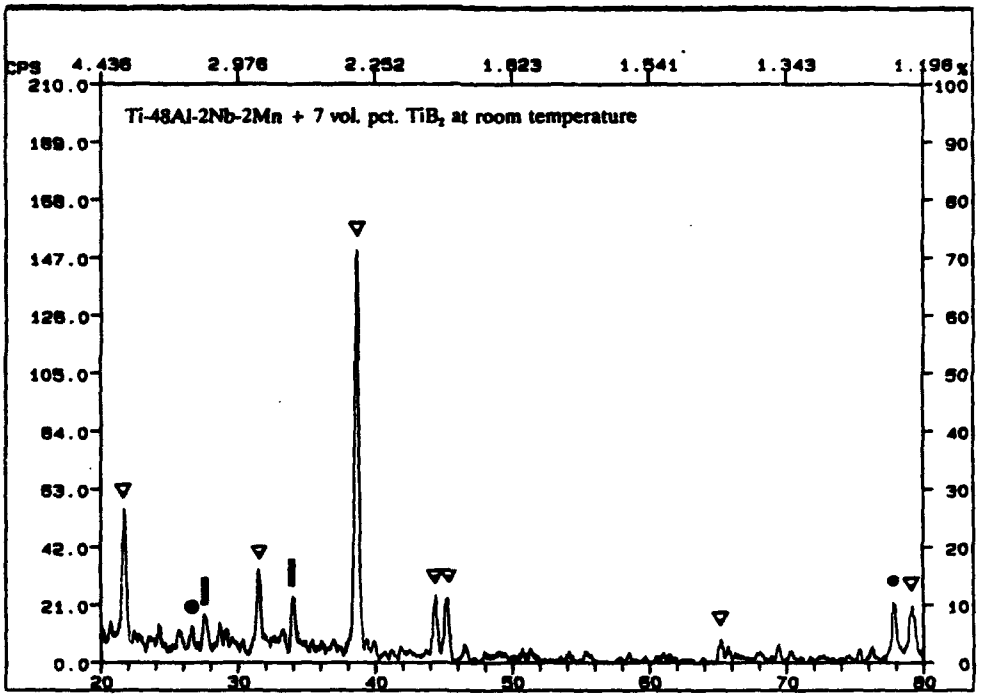

Figure 8. Room-Temperature X-Ray Scans for Ti-48Al-2Nb-2Mn Containing (a) 0.5 vol.% TiB_2, (b) 1 vol.% TiB_2, (c) 2 vol.% TiB_2, and (d) 7 vol.% TiB_2 (● α_2, ▽ γ, | TiB_2).

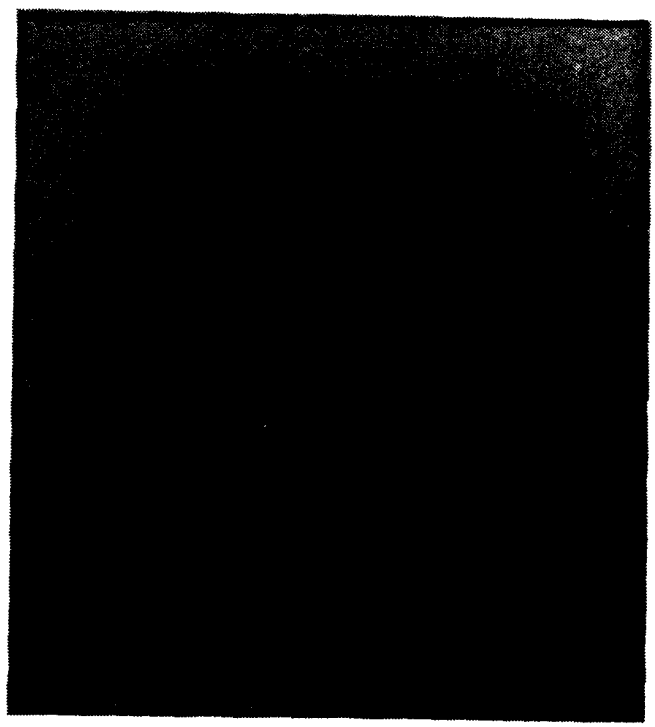

Figure 9. Optical Micrographs Illustrating Grain Structure in Ti-48Al-2Nb-2Mn Containing (a) 0.5 vol.% TiB_2, (b) 1 vol.% TiB_2, (c) 2 vol.% TiB_2, and (d) 7 vol.% TiB_2 (1/4 cross-sectional area shown).

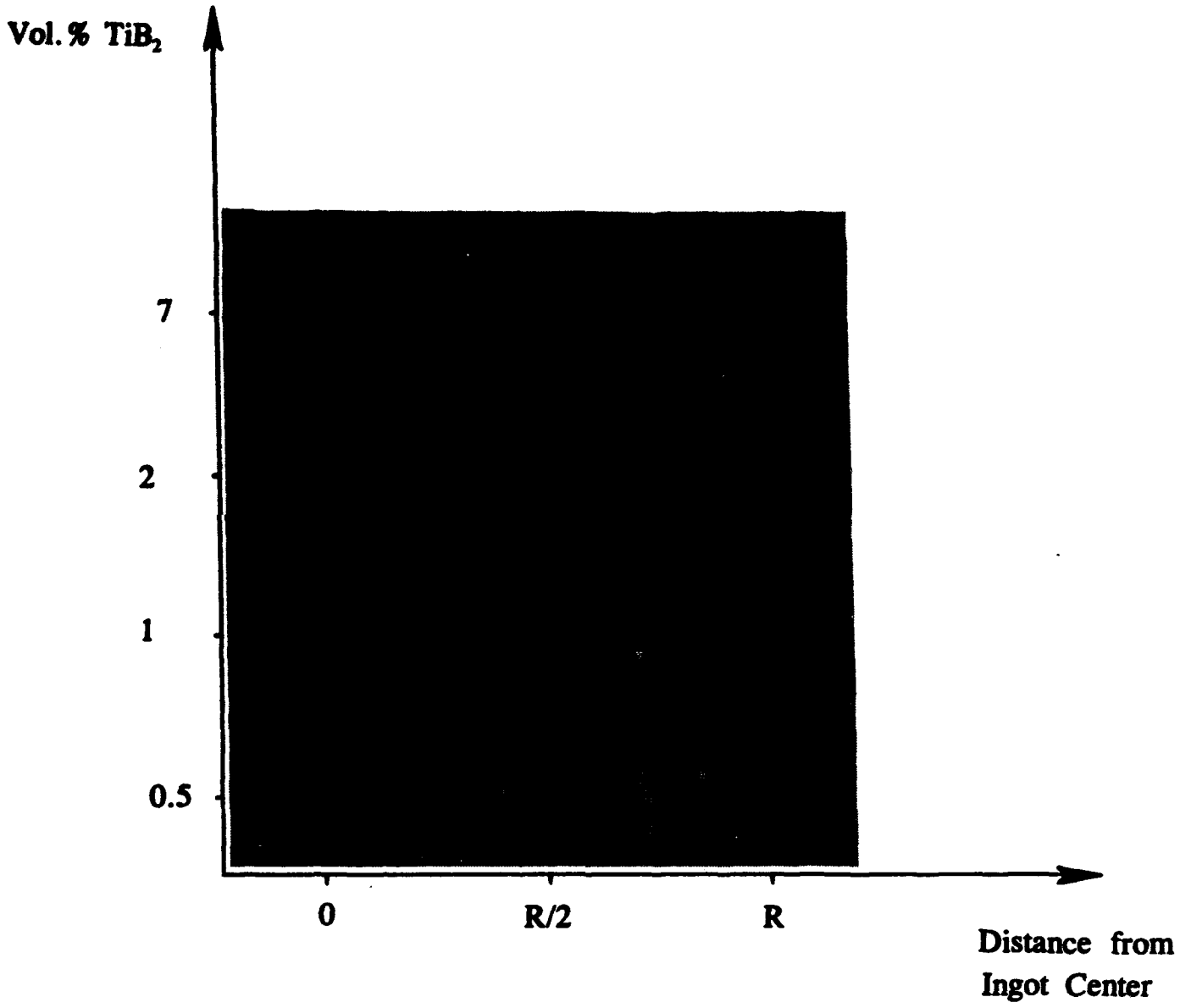

Figure 10. Effect of TiB_2 Content and Location in the Ingot on the Diboride Morphology.

Figure 11. Transmission Electron Micrograph Showing (a) (α_2+γ) Lamellae at Room-Temperature in Ti-48Al-2Nb-2Mn + 7 vol. % TiB_2.

Figure 12. Transmission Electron Micrograph of Ti-48Al-2Nb-2Mn + 7 vol. % TiB_2 Showing Dislocation Substructure Around TiB_2 Particle.

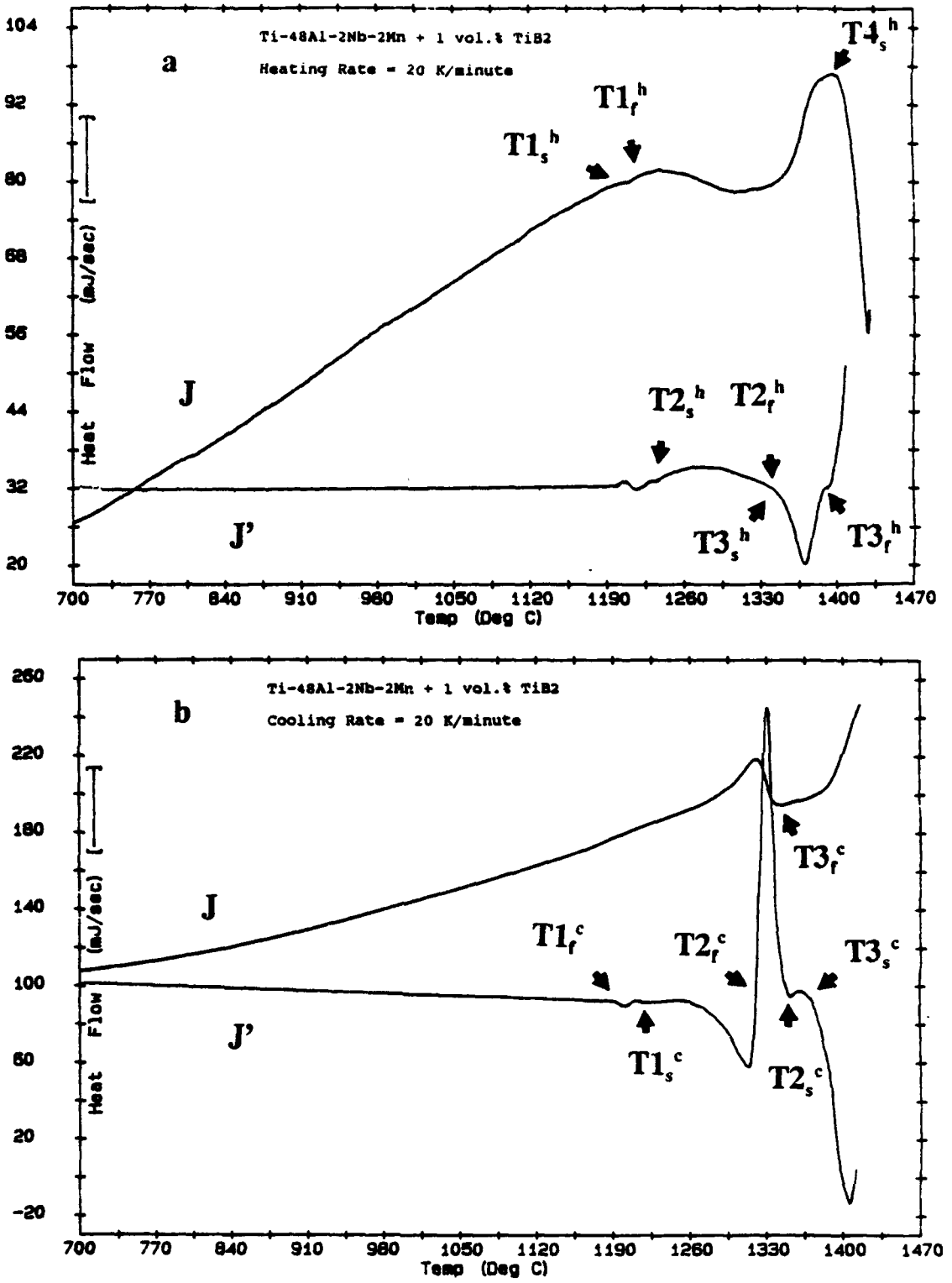

Figure 13. Thermograms of Ti-48Al-2Nb-2Mn/1 vol. % TiB_2 on (a) heating, (b) on cooling at 20 K/min.

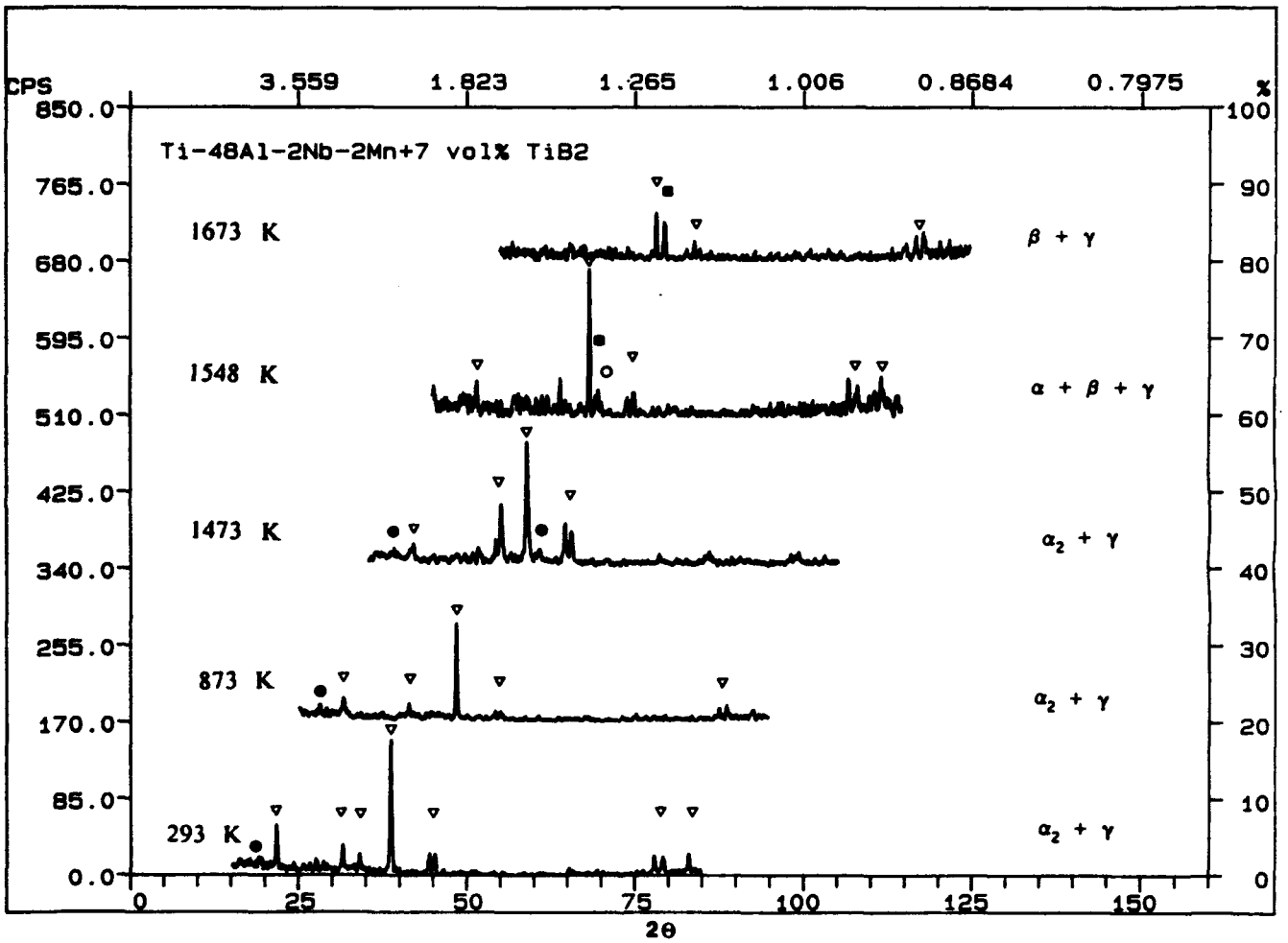

Figure 14. X-ray Spectra at Selected Temperatures for Ti-48Al-2Nb-2Mn + 7 vol.% TiB_2 (• α_2, o α, ■ β, ▽ γ).

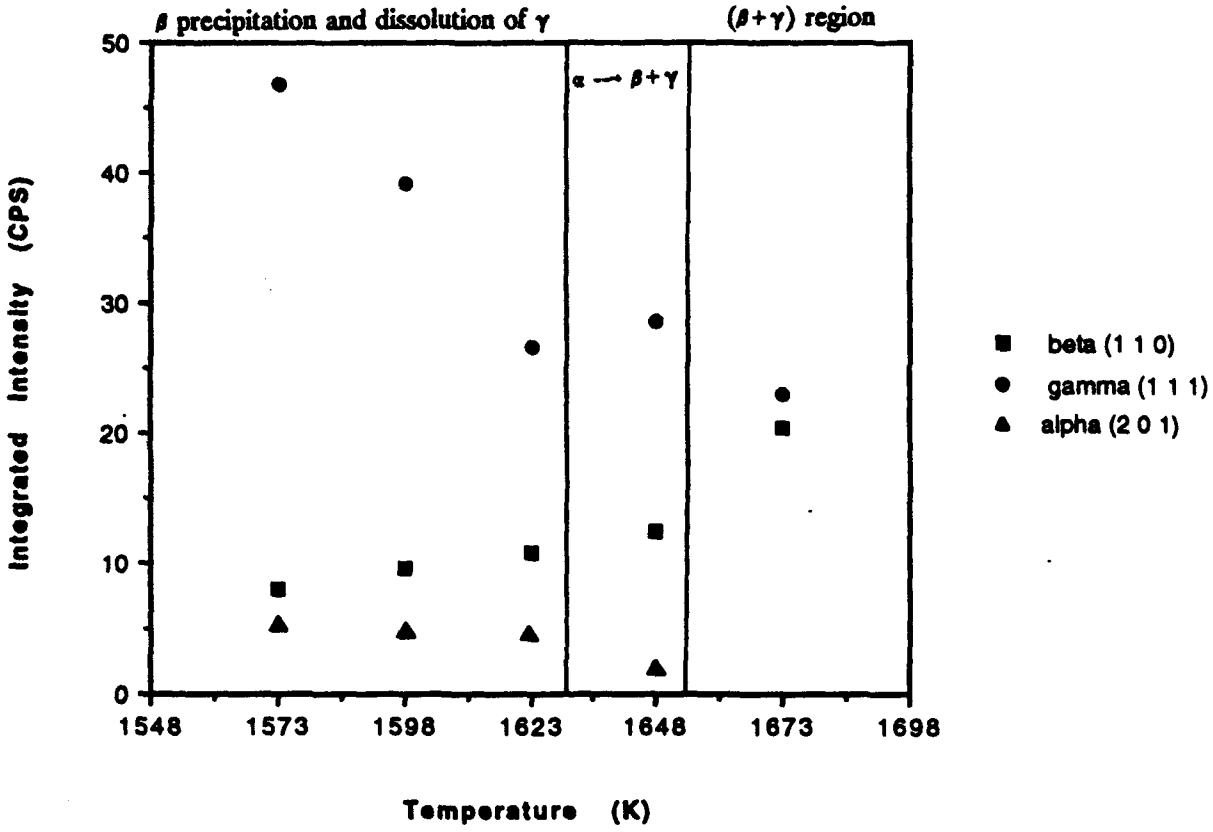

Figure 15. Integrated Intensities of (201) α-Peak, (110) β-Peak and (111) γ- Peak as a Function of Temperature for Ti-48Al-2Nb-2Mn + 7 vol.% TiB_2.

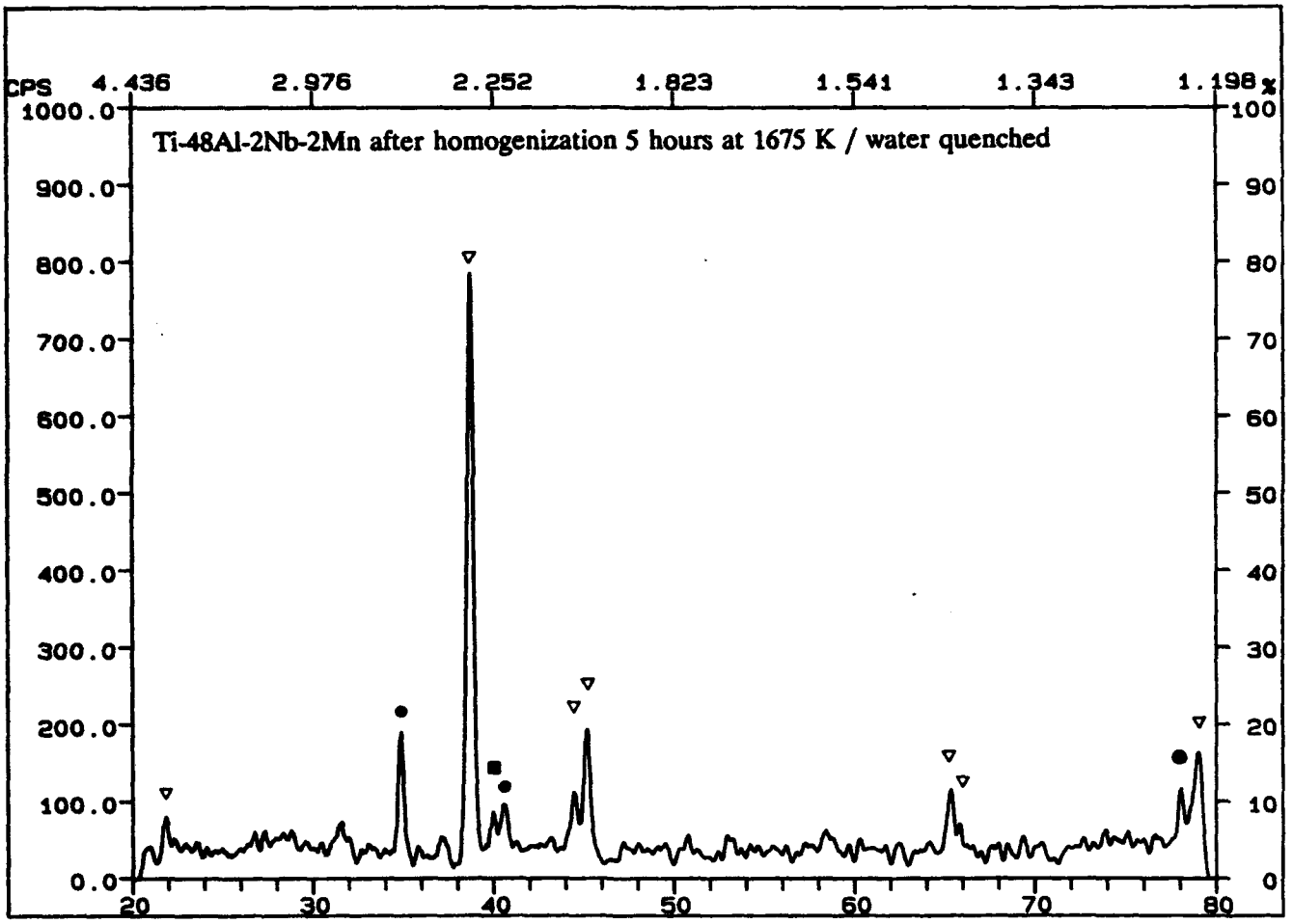

Figure 16. Room-Temperature X-Ray Scan for Ti-48Al-2Nb-2Mn after Homogenization for 5 Hours at 1675 K and Water Quench (● α_2, ■ β, ▽ γ).

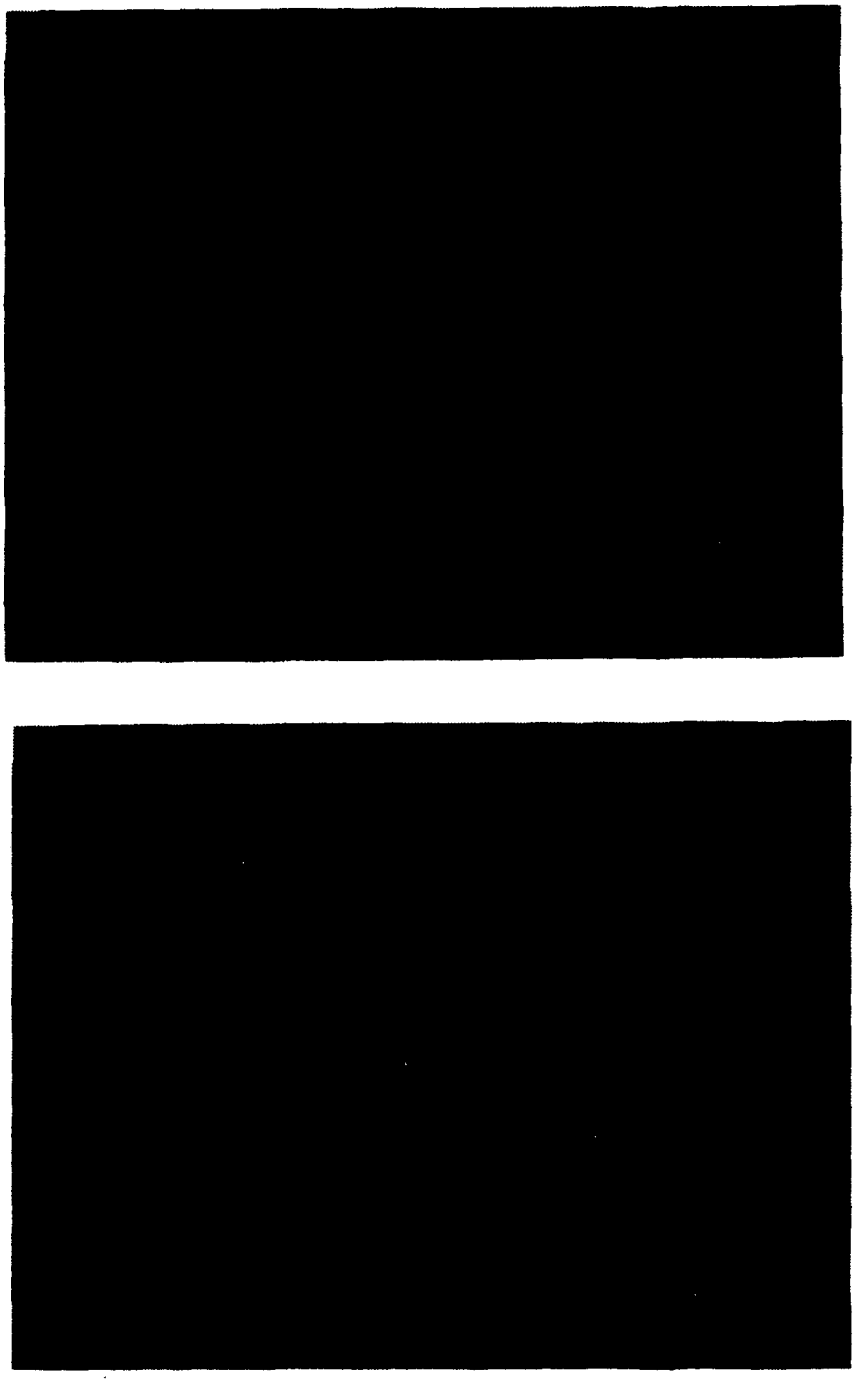

Figure 17. Comparison of (a) As Cast and HIP'ed and (b) Partially Melted CDTA Samples of Ti-48Al-2Nb-2Mn + 2 vol.% TiB_2.

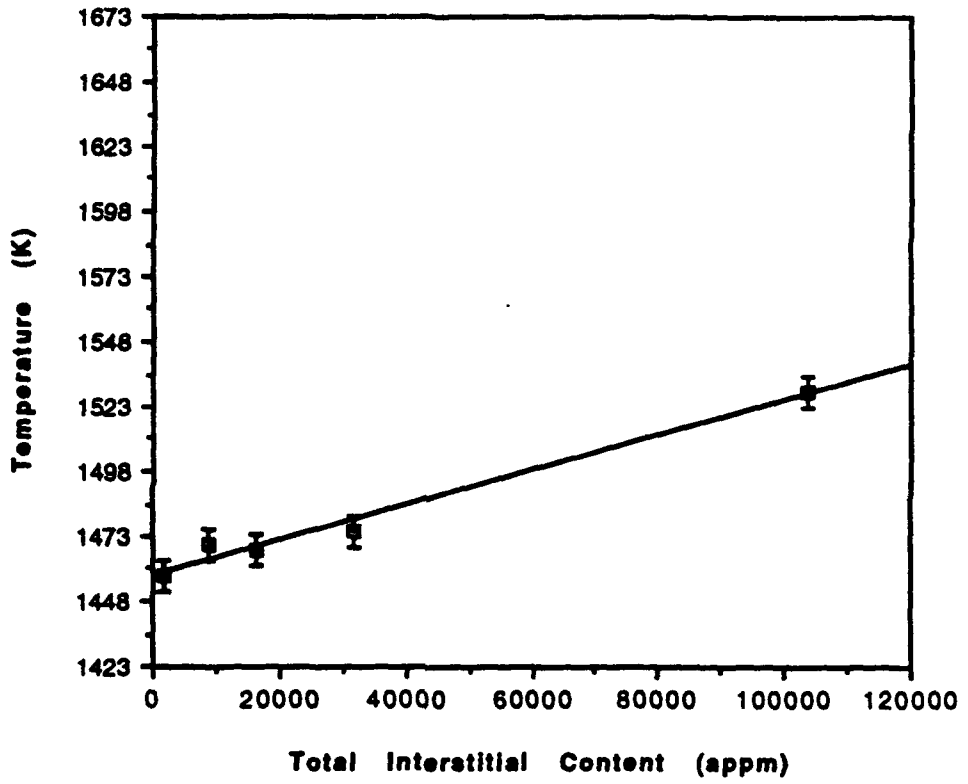

Figure 18. Eutectoid Transformation Temperature as a Function of Total Interstitial Content for Ti-48Al-2Nb-2Mn/TiB_2 Alloys.

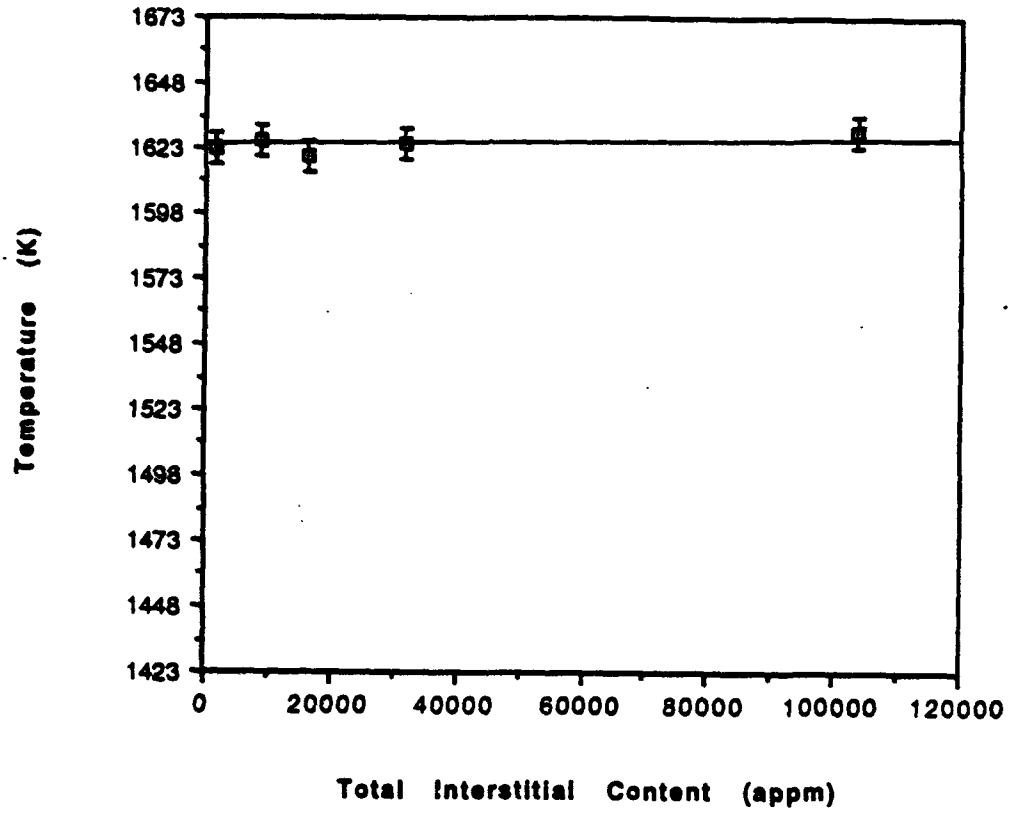

Figure 19. Peritectoid Transformation Temperature as a Function of Total Interstitial Content for Ti-48Al-2Nb-2Mn/TiB_2 Alloys.

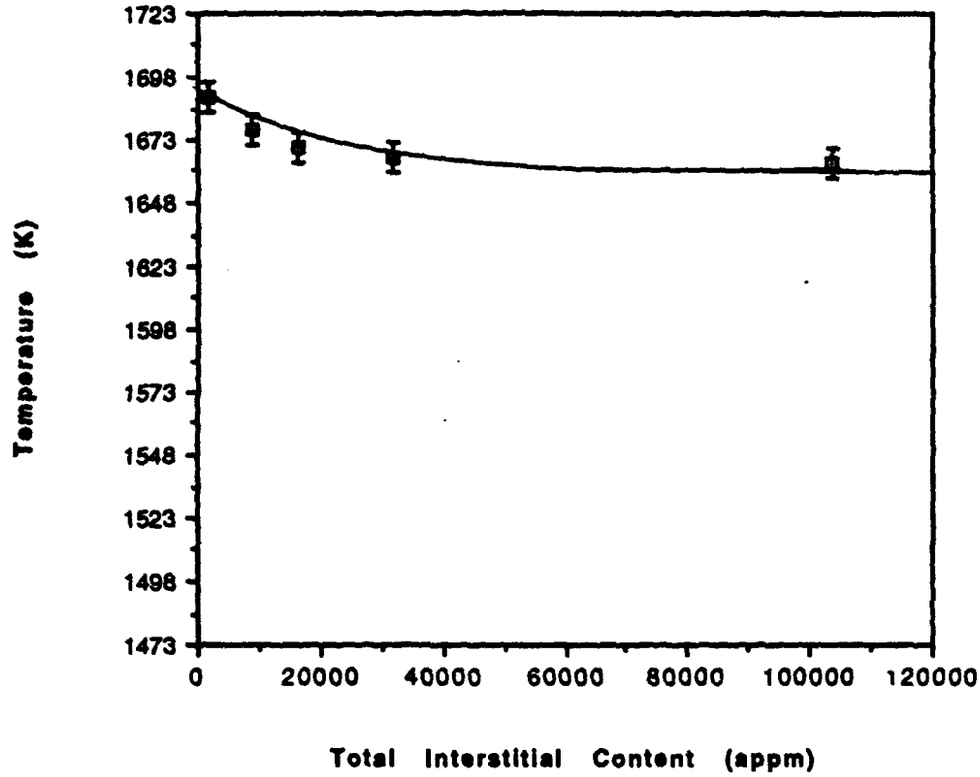

Figure 20. Peritectic Transformation Temperature as a Function of Total Interstitial Content for Ti-48Al-2Nb-2Mn/TiB_2 Alloys.

LIQUIDUS PROJECTION OF Ti-Al-V SYSTEM BASED ON ARC MELTED AND CAST MICROSTRUCTURES+

T. Ahmed, H. J. Rack and H. M. Flower*
Materials Science and Engineering Program,
Department of Mechanical Engineering,
Clemson University, Clemson, SC 29634, USA.
*Department of Materials, Imperial College, London SW7 2BP, UK.

Abstract

Arc melted and cast microstructures of Ti-Al-V alloys containing 10 to 57 wt% Al and 4 to 46 wt % V have been characterized by optical, scanning (SEM), transmission electron microscopy (TEM) and room temperature X-ray diffraction (RTXD). Chemical compositions of the phases present have been determined by energy dispersive X-ray (SEM-EDX), these results being utilized to plot a tentative non-equilibrium liquidus projection of the Ti-Al-V system. Five ternary peritectic reactions have been shown to be represented within the liquidus projection. Finally, these observations have been utilized to establish the solidification sequences of the Ti-Al-V alloys considered.

Introduction

Ti-Al-V alloys have made a major contribution to aerospace engineering, most notably the long established α+β alloy Ti-6Al-4V. Subsequent alloy development has resulted in the formulation of two new alloys based on this system, Ti-10V-2Fe-3Al and Ti-15Al-3Al-3Cr-3Sn (all compositions in this paper are in wt% unless otherwise stated). More recently there has also been a renewed interest in titanium aluminides, Ti_3Al (α_2) and TiAl (γ), where additions of β isomorphous elements, e.g., V and Mo have been made to modify the properties of both α_2 and γ titanium aluminides. In each instance knowledge of the phase equilibria is essential. The phase stability of α, α_2 and γ phases with V has been studied[1-9] at temperatures between 873 K to 1473 K. The works of Tsujimoto[2] and Maeda[4] were concentrated on Ti rich alloys whereas Hashimoto[3] and Paruchuri and Massalski[5] incorporated Al and V rich alloys. In the former study,[3] the isothermal sections were established at temperatures of 1073 K and 1273 K whereas results at 1173 K were presented by Paruchuri and Massalski.[5] In a recent study by the authors,[6,7] the phase stability of Ti-Al-V alloys containing α, α_2, β, γ, $TiAl_3(\xi)$ and $Al_8V_5(\delta)$ phases has been determined at temperatures of 1473, 1173, 1073, 973 and 873 K while Chaudhry and Rack[8,9] determined the phase equilibria of alloys containing α_2, γ and β phases between

+paper to be published in Materials Science and Technology.

temperatures of 873 K to 1773 K utilizing high temperature X-ray diffraction (HTXD) and differential scanning calorimetry (DSC).

In earlier studies,[1,3,5,8,9] the as-cast microstructures of the alloys utilized were not characterized. However, the as-cast microstructures (especially of Al and V rich alloys) affect the microstructures observed after subsequent equilibration treatments.[7] Therefore, it is important to characterize the as-cast microstructures and determine the primary phases of solidification.

The liquidus surface in the Ti-Al-V system is related to the associated binary invariant reactions. It has been shown by McCullough et al.[10] that the α phase is involved in two peritectic reactions $L+\beta\rightarrow\alpha$ and $L+\alpha\rightarrow\gamma$ in the Ti rich end of the Ti-Al binary system. Kaltenbach et al.[11] have determined two other peritectic reactions in alloys containing 55 to 70 wt% Al. These peritectic reactions are $L+\gamma\rightarrow\zeta$ and $L+\zeta\rightarrow\xi_1$, the ζ phase having a tetragonal structure based on Ti_5Al_{11} with lattice parameters a=0.3917 nm and b=3.4440 nm,[12] the ξ_1 phase having a tetragonal structure based on $TiAl_3$, an ordered ξ_1 superstructure (based on Ti_8Al_{24}) having been reported at lower temperatures with lattice parameters a=0.3849 nm and c=3.4440 nm.[13] Two binary peritectic reactions in the Al-V system of type $L+\beta\rightarrow\delta$ and $L+\delta\rightarrow\xi_{2}$ have been reported,[14] the δ phase having a superlattice relationship of $3a_{\beta}=a_{\delta}$ (with bcc crystal structure based on Al_8V_5 and a=0.9207 nm). ξ_2 has a face centered tetragonal structure based on VAl_3 with lattice parameters a=0.5343 nm and c=0.8324 nm.[14] Finally, no liquid phase invariant reactions have been reported in the Ti-V binary system.

The purpose of this paper is to establish the liquidus projection of the Ti-Al-V system and to utilize these results to examine the solidification behavior of arc melted and cast Ti-Al-V alloys containing 10 to 57 wt% Al and 4 to 46 wt% V. The as-cast microstructures were characterized by optical, scanning (SEM), transmission electron microscopy (TEM) and room temperature X-ray diffraction (RTXD), the chemical compositions of these phases being determined by energy dispersive X-ray (SEM-EDX).

Experimental

High purity sponge titanium (99.6%), vanadium turnings (99.7%) and cast aluminium (99.999%) were used for alloy preparation. Thirty (30) grams button were prepared from these with an accuracy of ±0.0005 g. The materials were melted in an argon arc furnace using a non consumable tungsten electrode on a water cooled copper hearth, the alloys being remelted six times, the button being inverted after each melt in order to ensure homogeneity. Average weight loss through melting was 0.38%, the maximum weight loss in a few high aluminium alloys being 0.96%, the nominal

compositions of ternary alloys prepared being given in Table 1. The cooling rates of alloys solidified in a water cooled copper hearth usually lie between 10-100°C/s. The oxygen contents of selected homogenized alloys 1 to 24 lay between 800 to 1500 ppm, whereas the oxygen contents of alloys 25 to 35 were between 300-600 ppm.

The as-cast samples were mechanically polished with SiC paper, polished with 7μm alumina and then electropolished or fine polished with 2 and 0.1 μm alumina. For optical microscopy the polished samples were etched in a solution of 3% HF, 10% HNO_3 in H_2O by volume. These samples were also used to distinguish different phases by back scattered electron imaging (BEI) in a JEOL JSM-T200 (25 kV) scanning electron microscope. The chemical compositions of the phases present in the as-cast alloys were determined by SEM-EDX, electropolished samples being examined in BEI or SEI (secondary electron imaging) mode in a JEOL JSM-35CF (20 kV) instrument with Link System ZAF4 software.

SEM-EDX chemical analyses were carried out for alloys with the dendritic microstructures only, these microstructures being observed in alloys containing >32 wt% Al. The remainder of the alloys had either solidified with a dominantly single phase microstructure or contained small amounts and sizes of other phases, as described below, the latter being below the spatial resolution of the chemical analysis system. The error in the results of the chemical analysis was observed to be in the range of ±0.5 wt%.

Further more detailed analysis of the as-cast microstructures utilized TEM and RTXD. Transmission electron microscopy was carried out on a JEOL 2000 FX (200kV), electropolishing of both TEM and optical specimen using a solution of 10% sulfuric acid and 90% methanol by volume.

Finally, room temperature X-ray diffraction studies of the electropolished samples were carried out with a Phillips diffractometer (Cu Kα radiation at 40 kV and 40 mA), the specimens being scanned at a speed of 2° 2θ/min and 1° 2θ/min from 20° to 130° 2θ. The crystal structures of the phases present was confirmed by using an iterative computer program which fits the observed d spacing values to a prescribed crystal structure.

Results

Microstructures

Representative microstructures are shown in Figs. 1 to 8 with the phases present in the as-cast alloys summarized in Table 1. In this table, the phases are listed in order of decreasing volume fraction, the phase at the extreme left of the column having the highest volume fraction.

Non-Dendritic Microstructures

Alloy 1 is typical of those alloy compositions (alloy 1 to 8) exhibiting a β as-cast microstructure, Fig. 1(a). All as-cast β microstructures had a large 2-3 mm equiaxed grain size, these alloys having solidified as β and undergoing a β to β_2 ordering transformation during cooling (as confirmed by the superlattice peaks in the X-ray diffraction patterns (XRDPs)).

Figs. 1(b) and (c) of alloys 9 and 10 typify the as-cast $\alpha_2+\beta_2$ microstructures where α_2 was predominant at ambient temperatures. The α_2 plates are observed at the prior β grain boundaries, these plates having nucleated heterogeneously at β grain boundaries after solidification. Further cooling then results in homogenous nucleation of α_2 within the β matrix, the primary difference in the microstructures of these alloys being the finer α_2 plates observed in the latter [Fig. 1(c)].

At low V contents, e.g. alloy 11, the as-cast microstructure consists of α_2 lath colonies with no apparent dendritic pattern [Fig. 1(d)]. XRDP of this alloy shows only one $\{110\}_\beta$ peak implying that the β (transformed to β_2 upon subsequent cooling) is present between the α_2 laths. Fig. 1(e) exhibits the as-cast microstructure of the alloy 12 which consists of coarse plates of α_2 present in a Widmanstatten morphology, the coarse microstructure being the result of a solid state β to α transformation at very high temperature. Comparison of these alloys indicates that increasing V content, at constant Al or increasing Al content at constant V, results in a refinement of the α_2 platelets, with α_2 precipitation occurring by initial heterogeneous β grain boundary nucleation.

Fig. 2(a) typifies the as-cast microstructure of $\beta_2+\alpha_2$ alloys where β_2 is the predominant phase at ambient temperatures. Alloys 13, 14 and 15 show similar microstructures. Here α_2 plates are present at the prior β grain boundaries with a much low concentration of α_2 within the grains. Again these alloys solidified as β with α_2 precipitation taking place at lower temperatures.

The microstructure of alloys 16 and 17 is shown in Fig. 2(b). The micrograph exhibits a high concentration of fine α_2 plates at prior β grain boundaries with a lower concentration within the grains. XRDPs of these alloys show intense β peaks along with relatively weaker α_2 and γ peaks. These alloys also solidified as β, with progressive precipitation of α_2 and γ with decreasing temperature.

Alloys 18 and 19 share a similar as-cast microstructure, an example being shown in Fig. 2(c). The microstructure is predominantly α_2 with β_2 interspersed. XRDPs of these alloys indicate the presence of α_2 and β_2 phases, XRDP of alloy 18 also indicating the presence of γ. This suggests that γ may also be present in alloy 19, however its volume fraction is very low, below the resolution of the X-ray diffraction system.

The as-cast microstructure of alloy 20 contains lenticular γ plates in a primary β matrix, Fig. 3(a). Alloy 21 shows a lamellar α_2/γ lamellar microstructure, according to X-ray diffraction studies, with γ, being a majority phase. This alloy solidified as β and then transformed to a $\alpha_2+\gamma$ lamellar product [Fig. 3(b)]. The as-cast microstructure of alloys 22 and 23 are typified in Fig. 3(c). This partially dendritic structure consists of α_2 laths separated by a few γ laths. Again these alloys solidified as β and transformed to $\alpha_2+\gamma$ on cooling.

Dendritic Microstructures

The dendritic microstructures observed in Ti-Al-V alloys are typified by the SEM-BEI micrograph of alloy 24, Fig. 4(a). In this alloy lamellar γ and α_2 phases are observed within dendrites and β phase within the inter dendritic region, the lamellar γ and α_2 phases morphology in the former having been verified by XRD and TEM studies, Fig. 4(b). A SADP from the $\gamma+\alpha_2$ lamellar area in the dendrites is shown in Fig. 4(c), the standard orientation relationship between the α_2 and γ lamellae being observed, i.e., $(0001)\alpha_2 \| \{111\}\gamma$ and $[2\bar{1}\bar{1}0]\alpha_2 \| \langle 110\rangle\gamma$. TEM also confirms the presence of the β phase in the interdendritic region, Fig. 4(d). It is believed that this alloy initially solidified as α, the liquid between dendrites finally having solidified as β. During solid state cooling, the α phase in the dendrites was transformed to alternate α_2 and γ lamellae via the eutectoid reaction $\alpha \rightarrow \alpha_2+\gamma$. The chemical compositions of α_2, β and γ phases determined by thin foil analysis (TEM-EDX) were Ti-35.2Al-25.5V, Ti-24.5Al-51.6V and Ti-36.7Al-19.6V, respectively.

Alloys 25 thru 28 exhibit dendritic as-cast microstructures, Figs. 5(a) to (d). XRDPs of alloys show the presence of strong γ peaks and weak α_2 peaks. While the dendritic regions again consist of lamellar γ and α_2 phases, the final liquid phase in these alloys solidified was γ. In addition, the secondary dendrite arms within the dendritic region appear to have grown at an angle between 50° to 70° to the primary arms. Similar types of hexagonal dendrites were observed by McCullough et al.[10,15,16] and Huang and Siemers[17] in Ti-36Al (Ti-50Al at%), Ti-39.8Al (Ti-54Al at%) and Ti-40.8Al (Ti-55Al) binary alloys, by Wardle[18] in Ti-37.9Al (Ti-52Al at%) and Ti-37.8Al-4.1V (Ti-52Al-3V at%) alloys and by Hashimoto et al.[19] in Ti-37.9 (Ti-52Al at%) Al alloy. In conformity with these authors, it is believed that alloys 25 thru 28 solidified as α through a peritectic reaction $L+\alpha \rightarrow \gamma$ with nucleation of γ in the liquid present between the dendrites, the primary α present within the dendrites then transforming to γ and α_2 lamellae.

Fig. 6(a) shows the as-cast microstructure of alloy 29. Orthogonal dendrites composed of lamellar γ and α_2 phases with a small amount of β present in the center of dendrites are observed. This separation suggests that the alloy initially solidified as β, the

α phase then nucleating in the liquid surrounding the β dendrites through a peritectic reaction, effectively masking the primary β dendrites. Similar orthogonal β dendrites were observed by Huang and Siemers[17] in as-cast structures of binary Ti-32.4Al (Ti-46Al at%) and by McCullough et al.[10,15,16] in binary Ti-27.3Al (Ti-40Al at%) and Ti-31.6Al (Ti-45Al at%) alloys. In the last stage of solidification the remaining liquid present between the α dendrites solidified as γ, α present in the dendrites then transforming to a lamellar mixture of $\gamma+\alpha_2$.

The as-cast microstructure of alloy 30 is similar to alloy 29, Fig. 6(b), the only difference being the presence of δ phase instead of α_2. Indeed, XRDP confirms the presence of δ, γ, and β phases. This micrograph also shows that the dendrites are composed of a lamellar mixture of $\delta+\gamma$, the primary β phase once again being coated by δ phase during solidification. γ is the last phase to solidified with the δ dendrites transforming to a lamellar mixture of $\delta+\gamma$.

Alloys 31, 32 and 33 share similar as-cast microstructures, Figs. 7(a) to (c). X-ray studies of all alloys show the presence of δ, γ, ξ_1 and β phases, with ξ_1, transforming into ordered superstructure during cooling.[13] In contrast, the δ and γ phases are present as lamellae. The liquid present between the dendrites is observed to solidify via an eutectic reaction $L \rightarrow \xi_1+\delta$, ξ_1 as the matrix with small second phase particles of δ. Further evidence that the eutectic reaction involves formation of $\xi_1+\delta$ is provided by combined area analysis carried out by SEM-EDX. The combined composition, e.g. in alloy 32, is determined to be Ti-54.2Al-29V, whereas the matrix has composition Ti-56.5Al-25V. It is found that the second eutectic phase has more V as compared to ξ_1 matrix phase, which is consistent with the composition of the δ phase. This agrees with the BEI contrast of this phase, compare Fig. 7(a) with (c).

Alloys 31 thru 33 solidified as β followed by nucleation of δ through a peritectic reaction. Ultimately γ nucleates, probably through a second peritectic reaction, the remaining liquid solidifying as a eutectic mixture of $\xi_1+\delta$, the δ phase in the dendrites then transforming to a lamellar $\delta+\gamma$ mixture. The amount of primary β phase in alloy 33 is low (XRDP of this alloy shows a very weak $\{110\}_\beta$ peak) and below the detection limit of the SEM during the EDX analysis [Fig. 7(c)]. The volume fraction of γ phase nucleating in the remaining liquid is larger in alloy 33 than in alloys 31 and 32, while the volume fraction of the primary β phase is higher in alloy 31, Fig. 7(a). Comparing the as-cast microstructures of alloys 31 thru 33, shows that the lamellar structure of $\delta+\gamma$ and "finger print" structure of the eutectic coarsens with increasing Al content from 42 to 48 wt% Al and decreasing V content from 46 to 32 wt%.

Fig. 8(a) shows a SEM-BEI micrograph of the as-cast microstructure of alloy 33. This as-cast microstructure is composed of primary solidified β with peritectically solidified δ phase, the last solidified liquid being composed of ξ_2 phase. The micrograph also reveals very fine particles of a transformation product present in the β phase.

Finally, Fig. 8(b) represents an optical micrograph of alloy 35. This two phase dendritic structure is a mixture of ξ_1 and δ.

Discussion

Liquidus Projection

The results of this study permit construction of the liquidus projection of the Ti-Al-V system, Fig. 9. Chemical compositions of the different phases present are indicated on the diagram and joined by tie lines. In this proposed diagram, the primary solidification phases are β, α, γ, δ, ξ_1, ξ_2 and ζ. The β liquidus surface is shown to cover the largest area in the liquidus projection while the α liquidus surface extends to 30 wt% V. The extension of the α liquidus surface to a high V contents of 30 wt% is due to the relatively fast cooling during arc melting. A similar large α surface was also observed in Ti-Al-Ta system where arc melted alloys of compositions up to Ti-26Al-50.8Ta showed hexagonal dendrites.[20] However, it has been observed in HTXD study of Ti-34Al-2.3V (Ti-48Al-2V at%)[21] and Ti-33.3Al-2.8Mn-4.8Nb (Ti-48Al-2Mn-2Nb at%)[22] alloys that slow heating of these compositions results in a γ+β phase field immediately below the solidus. This implies that under equilibrium conditions the penetration of the α liquidus surface does not extend beyond 5 wt% V. HTXD studies of other Ti-Al-V alloys in this phase field is currently underway to determine the extent of this surface. Finally, the γ liquidus surface is also extended to 30 wt% V content but it is wider than the α liquidus surface.

Binary peritectic reactions present in related binary systems as denoted by P_i are:

P_1	$L+\beta\rightarrow\delta$	1946 K (Ref. 14)
P_2	$L+\beta\rightarrow\alpha$	1748 K (Ref. 10)
P_3	$L+\alpha\rightarrow\gamma$	1723 K (Ref. 10)
P_4	$L+\gamma\rightarrow\zeta$	1688 K (Ref. 11)
P_5	$L+\zeta\rightarrow\xi_1$	1668 K (Ref. 11)
P_6	$L+\delta\rightarrow\xi_2$	1635 K (Ref. 14)

Five ternary peritectic reactions are indicated within the diagram. These peritectic reactions, U_i, and their approximate temperatures (estimated with the aid of the binary peritectic temperatures) are:

U_1	$L+\alpha\rightarrow\beta+\gamma$	1723>T>1673 K
U_2	$L+\zeta\rightarrow\gamma+\xi_1$	1668>T>1633K

U_3	$L+\beta \rightarrow \gamma+\delta$	1663 K (Ref. 23)
U_4	$L+\gamma \rightarrow \delta+\xi_1$	1633>T>1573 K
U_5	$L+\delta \rightarrow \xi_1+\xi_2$	1633>T>1573 K

Paruchuri and Massalski[5] recently determined a liquidus projection of Ti-Al-V system utilizing alloy compositions centered around reactions U_2, U_3 and U_4. While there is a general agreement between the primary phases observed by these authors with the present study, however, compositions Ti-50Al-30V, Ti-50Al-40V and Ti-55.5Al-37.4V were shown by Paruchuri and Massalski to have β as their primary phase. In the present liquidus projection these compositions are located on the δ liquidus surface with the first two compositions however being very close to the line P_1U_3. This discrepancy can be explained by the fact that the positions of lines P_1U_3 and P_6U_5 in the present study were determined utilizing the P_1 and P_6 compositions from the binary Al-V diagram determined by Carlson et al..[14] These compositions in the recent estimated Al-V diagram by Murray[24] are Ti-42.5V and Ti-23.5V respectively. In both diagrams the compositions of points P_1 and P_6 are estimated, not experimentally determined. Therefore, the positions of lines P_1U_3 and P_6U_5 are uncertain and are suggested as the reason for this discrepancy.

The peritectic reaction U_1 results in a $\alpha+\beta+\gamma$ three phase field and was observed experimentally in the isothermal section at 1473 K.[6,7] This reaction has been shown to present at approximately Ti-41Al-29V, the position of U_1 having been determined on the basis of the as-cast microstructures for alloys present in this region.

The format of reaction U_2 is proposed utilizing binary peritectic reactions P_4 and P_5. As no alloy was studied in this composition range, the position of this reaction is tentative.

Reactions U_3 and U_4 result in $\gamma+\beta+\delta$ and $\gamma+\delta+\xi_1$ three phase fields. These phase fields were also observed experimentally in the isothermal section at 1473 K.[6,7] The formats of these reactions have been suggested utilizing optical and SEM-BEI micrographs of alloys present in this region. The reaction U_3 was also shown by Volkova and Kornilov[23] at approximately 1673 K in their vertical section of Ti-Al-V system. Hayes[25] also suggested a similar reaction in his unpublished partial reaction scheme of the Ti-Al-V system based on previous experimental results of this system, although he suggested a different U_4 reaction, $L+\delta \rightarrow \gamma+\xi_2$. Hayes' U_4 reaction necessitates the presence of $\gamma+\delta+\xi_2$ three phase field at lower temperature, however the presence of a $\gamma+\delta+\xi_1$ three phase field at 1473 K has been confirmed by X-ray results.[7]

Paruchuri and Massalski[5] presented a different format of reactions U_3 and U_4, $L+\gamma \rightarrow \beta+\xi$ and $L+\beta \rightarrow \xi+\delta$ respectively. These reactions would result in $\gamma+\beta+\xi$ and $\beta+\xi+\delta$ three phase fields, again these phase fields have not been observed at temperatures >1273 K, three phase fields present at higher temperatures being $\gamma+\beta+\delta$ and $\gamma+\xi_1+\delta$.[7] Three

phase fields $\gamma+\beta+\xi$ and $\beta+\xi+\delta$ may nevertheless be observed at temperatures of <1273 K, their presence being a product of a ternary peritectoid reaction $\gamma+\delta\rightarrow\beta+\xi$.

Finally, no indication of an eutectic type reaction was observed by Paruchuri and Massalski[5] in alloys within the vicinity of these ternary reactions. Unfortunately these authors did not mention whether the microstructures reported were from as-cast or DTA melted samples. Thus there remains a possibility that the slow cooling in the DTA samples might have prevented this eutectic reaction. In that case, the eutectic type reaction observed in the present study could be due to the relatively fast cooling during arc melt solidification, effectively suppressing the eutectic temperature to a sufficiently low temperature.

A fifth ternary peritectic reaction U_5 has been suggested in the present study. In the work of Paruchuri and Massalski,[5] this reaction is absent because they considered ξ_1 and ξ_2 as a single phase. However, the crystal structure of ξ_2 phase present in alloy 34 is distinct from ξ_1. Indeed, the presence of ξ_2 requires the addition of reaction U_5 within the liquidus projection. In the liquidus projection determined by Paruchuri and Massalski,[5] the liquidus line from point U_4 was shown to move towards point P_6, whereas in the present liquidus projection, this line moves towards point U_5, in the Al rich direction, Fig. 9. But the position and direction of the liquidus line from point U_5 is not known due to lack of data available in this region. Apparently it should move downwards to the Al rich corner (as suggested by a broken line in Fig. 9) and take part in another ternary peritectic reaction in the Al rich corner due to the presence of a binary eutectic in the Al-V side and a binary peritectic in the Al-Ti side. Hayes' unpublished work[25] also indicates the presence of reaction U_5 but with a different format.

Solidification Paths of Alloys

Before examining the solidification paths of the prepared alloys it is emphasized that the alloys have undergone non-equilibrium cooling during preparation; therefore, these solidification paths should not be considered as equilibrium paths. These solidification paths are given in Table 2. The alloys are considered according to their primary phase of solidification.

Alloys with β Primary Phase ($L\rightarrow\beta$)

Reactions 1 thru 7 in Table 2 represent the solidification paths of alloys with β as the primary phase.

Alloys 1 thru 8 only undergo an ordering transformation of $\beta\rightarrow\beta_2$ following solidification, reaction 1.

In alloys 9 to 12, the addition of V decreases the α precipitation temperature ultimately allowing the retention of β at room temperature during cooling. The α precipitation takes place in disordered β at higher temperatures and is followed by the ordering of both α and β to α_2 and β_2 on subsequent cooling, reaction 2. According to the Ti-Al binary phase diagram[10,26] compositions of 25 to 27 wt% Al should contain an $\alpha_2+\gamma$ microstructure. The absence of the γ phase in alloys 9 to 12 could be due to non-equilibrium solidification and shift of the $\alpha/\alpha+\gamma$ phase boundary in the Al rich direction with V additions as observed in the isothermal section of Ti-Al-V diagram at 1473 K.[7]

In alloys 13 to 15, precipitation takes place at much lower temperatures than in alloys 9 thru 12 and involves direct precipitation of α_2 from ordered β_2, reaction 3.

The precipitation of α takes place in ordered β_2 (around 1373-1473 K) on cooling in alloys 16 and 17 and is followed by the nucleation of γ within the α phase, reaction 4.

In alloys 18 and 19, the precipitation of α in primary disordered β takes place at temperatures between approximately 1373-1500 K with γ precipitation in these alloys probably taking place at lower temperatures. In addition, both α and β undergo further ordering reactions, reaction 5.

The result of X-ray analysis of alloy 20 does not give any indication of α_2 phase (Table 1) which implies that the γ has precipitated from the β phase and this composition does not encounter the ternary peritectic reaction U_1 $L+\alpha\rightarrow\beta+\gamma$ proposed in Figure 9. The β phase also remains disordered at room temperature, reaction 6.

Finally, alloys 21 to 23 have α_2 and γ phases in their as-cast microstructures (Table 1) with α precipitation in β taking place at high temperatures (1700-1740 K) consuming the β phase. The α transforms to a lamellar mixture of $\alpha_2+\gamma$ by an eutectoid reaction $\alpha\rightarrow\alpha_2+\gamma$, the temperature of α_2 and γ precipitation depending upon the V content of the alloys, decreasing with increasing V content, reaction 7.

Alloys with β Primary Phase involved in a Peritectic Reaction ($L\rightarrow\beta+L$)

The reaction 8 thru 12 in Table 2 represent the solidification paths of alloys which involve a peritectic reaction.

In alloy 29, following β precipitation, the liquid composition moves along the β liquidus surface towards line P_2U_1. According to the liquidus projection the alloy should move towards U_1. But the liquid composition moves towards the α liquidus surface with the precipitation of α phase through a peritectic reaction $L+\beta\rightarrow\alpha$. The composition of the remaining liquid between the α dendrites (these dendrites have already partially consumed the primary β) moves towards the line P_3U_1 and solidifies as γ by another peritectic reaction $L+\alpha\rightarrow\gamma$. This could be due to the fact that the β liquidus surface is steeper than the α surface and the liquid composition on the α surface also moves down.

The difference in temperatures of the invariant reactions P_3 and U_1 is moreover not great; therefore, it is possible for the liquid to overshoot the U_1 reaction under the non-equilibrium cooling conditions, reaction 8.

The liquid composition in alloy 30 changes along the β liquidus surface after β precipitation towards line P_1U_3 and due to greater difference in temperatures of invariant reactions P_1 and U_3, it moves sharply downwards to point U_3 and solidifies thru the peritectic reaction $L+\beta\rightarrow\gamma+\delta$, reaction 9.

The volume fraction of β phase in alloy 31 is large as compared to other alloys in this range. The liquid composition moves along the β liquidus surface towards line P_1U_3 and then precipitation of δ occurs around β. The composition of the remaining liquid moves to the line $U_3U_4U_5$ and enters the pseudo binary eutectic reaction $L\rightarrow\xi_1+\delta$, which results in eutectic like microstructural features, reaction 10.

Alloys 32 and 33 go through two peritectic reactions. The liquid compositions move along the β liquidus surface to line P_1U_3. These compositions follow this line and go through first peritectic reaction at U_3 $L+\beta\rightarrow\gamma+\delta$. The remaining liquid compositions in both alloys follow the line U_3U_4. The solidification should be completed by the peritectic reaction U_4, $L+\gamma\rightarrow\delta+\xi_1$. However, the microstructural features suggest the presence of a eutectic reaction $L\rightarrow\delta+\xi_1$ which is not possible according to the tentative liquidus projection shown in Fig. 9. The only possibility is that alloys do not go through reaction U_4 and remaining liquid solidifies as a mixture of $\delta+\xi_1$. This could be possible in view of small differences in temperatures of reactions U_4 and U_5, therefore, the line U_4U_5 may act as a valley between δ and ξ_1 liquidus surfaces and due to non-equilibrium cooling the liquid can solidify as a eutectic like mixture of $\delta+\xi_1$. In alloy 33, the volume fraction of the primary phase β is very small and it appears to be consumed by the subsequent peritectic reaction U_3, reaction 11.

In alloy 34, the liquid composition moves along the β liquidus surface towards line P_1U_3. The liquid composition then changes along the δ liquidus surface with the precipitation of the δ phase, the volume fraction of the δ phase being the highest among all alloys present in this composition range. The composition of the liquid present between the big δ dendrites moves towards line P_6U_5 and the liquid solidifies as ξ_2, reaction 12.

Alloy with ξ_1 Primary Phase

Reaction 13 in Table 2 represents the solidification path of alloy 35. The solidification in this alloy takes place with the nucleation of the ξ_1 phase. The composition of the liquid changes along the ξ_1 liquidus surface towards line U_4U_5. The solidification was completed by the precipitation of the δ phase in the liquid.

Alloys with α Primary Phase

The solidification path of alloys 25 to 28 is given by reaction 14 in Table 2. The α primary phase is indicated by the presence of hexagonal dendrites in the as-cast microstructures of these alloys [Figs. 5(a) to (d)]. McCullough et al.[10,15,16] distinguished the morphologies of the α dendrites in the shrinkage cavities of the as cast binary Ti-36Al (Ti-50Al at%) and Ti-40.8Al (Ti-55Al at%) from that of the β dendrites in as-cast alloys of compositions Ti-27.3Al (Ti-40Al at%) and Ti-31.6Al (Ti-45Al at%). The alloys in the present study go through the binary peritectic reaction P_3, $L+\alpha \rightarrow \gamma$. The liquid composition in all alloys changes along the α liquidus surface towards the line P_3U_1 and the remaining liquid solidifies as γ.

The primary phase in alloy 24 is also α. The composition of the small amount of the liquid phase apparently moves down along the line P_2U_1 and solidifies as V rich β. The precipitation of γ in the α dendrites takes place in the solid state, reaction 15.

Conclusions

1- The arc melted and cast microstructures of Ti-Al-V alloys solidified at cooling rates lying between 10-100°C/s were characterized and it was determined that the alloys containing 10.5 to 32 wt% Al and 4 to 31 wt% V and alloys containing 40 to 48 wt% Al and 30 to 51 wt% V were solidified as β. The morphology of the dendrites was related to the type of the primary phase i.e. orthogonal for β and γ and hexagonal for α. The precipitation of α in the β phase was observed to occur at different temperatures in the solid state and the temperature appeared to determine the size and morphology of the α phase.

2- A tentative liquidus projection of the Ti-Al-V system has been presented. Five ternary peritectic reactions are suggested in the liquidus projection. Three ternary peritectic reactions have been confirmed in another study[6,7] due to the presence of their product three phase fields observed at lower temperatures. The α liquidus surface has been shown to extend to 30 wt% V. This extent was determined on the basis of the hexagonal dendrites in alloys present in this composition range. Therefore, it is concluded that non-equilibrium cooling promotes α phase instead of β or γ phases.

Acknowledgments

The work reported in this paper was carried out by Dr. T. Ahmed as a post graduate student in the Department of Materials, Imperial College. Dr. T. Ahmed thanks MOST (Pakistan) and the Department of Materials, Imperial College for their partial financial support during his stay at Imperial. Dr T. Ahmed and Prof. H. J. Rack also thank the Defence Advanced Research Project Agency (DARPA) under contract N00014-89-J-3166

supervised by Mr. W. Barker and monitored by Dr. G. Yoder of the Office of Naval Research for their sponsorship at Clemson University.

References

1. I. I. Kornilov and M. A. Volkova: 'Titanium Alloys for New Techniques', 78-89, 1966, Publ. 1968, Moscow, Nauka.
2. T. Tsujimoto: J. Jap. Inst. Metals, 1968, **32**, 970. Trans. Jap. Inst. Metals, 1969, **10**, 281.
3. K. Hashimoto, H. Doi and T. Tsujimoto: J. Jap. Inst. Metals, 1985, **31**, 410. Trans. Jap. Inst Metals, 1986, **27**, 741.
4. T. Maeda: PhD. Thesis, University of London (Imperial College), 1988.
5. M. Paruchuri and T. B. Massalski: Mater. Res. Soc. Symp. Proc., 1991, **213**, 143.
6. T. Ahmed and H. M. Flower: Mater. Sci. and Eng., 1992, **A152**, 31-36.
7. T. Ahmed and H. M. Flower: to be published in Mater. Sci. and Technol.
8. P. K. Chaudhury, M. Long and H. J. Rack: Mater. Sci. and Eng., 1992, **A152**, 37-40.
9. P. K. Chaudhury and H. J. Rack: Scripta Metall. Mater., 1992, **26**, 691-695.
10. C. McCullough, J. J. Valencia, C. G. Levi and R. Mehrabian: Acta Met, 1989, **37**, 1321.
11. K. Kaltenbach, S. Gama, D. G. Pinatti and K. Schulze: Z. Metallkde., 1989, **80**, 511.
12. A. Raman and K. Schubert: Z. Metallkde, 1965, **56**, 44.
13. F. J. J. van Loo and G. D. Rieck: Acta Met., 1973, **21**, 61.
14 O. N. Carlson, D. J. Kenney and H. A. Wilhelm: Trans. ASM., 1955, **47**, 520.
15. J. J. Valencia, C. McCullough, C. G. Levi and R. Mehrabian: Scripta Met, 1987, **21**, 1341.
16. C. McCullough, J. J. Valencia, H. Mateos, C. G. Levi and R. Mehrabian: Scripta Met, 1988, **22**, 1131.
17. S. C. Huang and P. A. Siemers: Met. Trans., 1989, **20A**, 1899.
18. S. M. Wardle: PhD. Thesis, University of Birmingham, 1991.
19. K. Hashimoto, H. Doi, K. Kashahara, T. Tsujimoto and T. Suzuki: J. Jap. Inst. Metal, 1988, **52**, 816.
20. C. McCullough, J. J. Valencia, C. G. Levi, R. Mehrabian, M. Maloney and R. Hecht: Acta Metall. Mater., 1991, **39**, 2745.
21. T. Ahmed, P. K. Chaudhury and H. J. Rack: unpublished research.

22. S. Guilliard and H. J. Rack: submitted to Mater. Sci. and Eng.
23. I. I. Kornilov and M. A. Volkova: Izvest. Akad. Nauk SSSR, Metally, 1970, (5), 202.
24. J. L. Murray: 'Binary Alloy Phase Diagrams', 232, 1990, Materials Park, Ohio, ASM.
25. F. H. Hayes: Private Communications.
26. J. L. Murray: 'Phase Diagrams of Binary Titanium Alloys', 319, 1987, Materials Park, Ohio, ASM.

Table 1: The phases present in the as cast alloys determined by optical microscopy, SEM, TEM and X-ray diffractometry.

Alloy No.	Nominal Compositions (wt%)	Phases	Alloy No.	Nominal Compositions (wt%)	Phases
1	Ti-10.5Al-20.5V	β_2	19	Ti-32Al-20V	$\alpha_2, \beta_2, \gamma$
2	Ti-15Al-20V	β_2	20	Ti-32Al-31V	γ, β
3	Ti-15Al-30V	β_2	21	Ti-32Al-4V	γ, α_2
4	Ti-20Al-15V	β_2	22	Ti-32.5Al-12V	α_2, γ
5	Ti-20Al-20V	β_2	23	Ti-32.5Al-15V	α_2, γ
6	Ti-20Al-25V	β_2	24	Ti-35Al-25V	γ, α_2, β
7	Ti-20Al-30V	β_2	25	Ti-40Al	γ, α_2
8	Ti-25Al-13V	β_2	26	Ti-40Al-5V	γ, α_2
9	Ti-25Al-4V	α_2, β_2	27	Ti-40Al-10V	γ, α_2
10	Ti-27Al-10V	α_2, β_2	28	Ti-40Al-15V	γ, α_2
11	Ti-27Al-5V	α_2, β_2	29	Ti-40Al-30V	γ, α_2, β
12	Ti-28Al-4V	α_2, β_2	30	Ti-41Al-40V	γ, δ, β
13	Ti-25Al-25V	β_2, α_2	31	Ti-42Al-46V	$\delta, \xi_1, \beta, \gamma$
14	Ti-26Al-16V	β_2, α_2	32	Ti-45Al-35V	$\gamma, \delta, \xi_1, \beta$
15	Ti-27Al-30V	β_2, α_2	33	Ti-48Al-32V	$\gamma, \delta, \xi_1, \beta$
16	Ti-27Al-20V	$\beta_2, \alpha_2, \gamma$	34	Ti-45Al-51V	γ, β, ξ_2
17	Ti-28Al-24V	$\beta_2, \gamma, \alpha_2$	35	Ti-57Al-27V	ξ_1, δ
18	Ti-30Al-15V	$\alpha_2, \beta_2, \gamma$	-	-	-

Table 2: The solidification paths of the alloys.

Reaction #	Solidification Paths	Alloy #
1	$L \rightarrow \beta \rightarrow \beta_2$	1-8
2	$L \rightarrow \beta \rightarrow \beta+\alpha \rightarrow \beta_2+\alpha_2$	9-12
3	$L \rightarrow \beta \rightarrow \beta_2 \rightarrow \beta_2+\alpha_2$	13-15
4	$L \rightarrow \beta \rightarrow \beta_2+\alpha+\gamma \rightarrow \beta_2+\alpha_2+\gamma$	16, 17
5	$L \rightarrow \beta \rightarrow \beta+\alpha+\gamma \rightarrow \beta_2+\alpha_2+\gamma$	18, 19
6	$L \rightarrow \beta \rightarrow \beta+\gamma$	20
7	$L \rightarrow \beta \rightarrow \alpha \rightarrow \alpha_2+\gamma$	21-23
8	$L \rightarrow \beta_p+L \rightarrow \beta_p+[\alpha]+L \rightarrow \beta_p+[\gamma+\alpha_2]+\gamma$	29
9	$L \rightarrow \beta_p+L \rightarrow \beta_p+[\delta]+\gamma \rightarrow \beta_p+[\delta+\gamma]+\gamma$	30
10	$L \rightarrow \beta_p+L \rightarrow \beta_p+[\delta]+L \rightarrow \beta_p+[\delta+\gamma]+\xi_1+\delta$	31
11	$L \rightarrow \beta_p+L \rightarrow \beta_p+[\delta]+L \rightarrow \beta_p+[\delta+\gamma]+\gamma+L \rightarrow \beta_p+[\delta+\gamma]+\gamma+\xi_1+\delta$	32,33
12	$L \rightarrow \beta_p+L \rightarrow \beta_p+[\delta]+L \rightarrow \beta_p+[\delta]+\xi_2$	34
13	$L \rightarrow \xi_1+L \rightarrow \xi_1+\delta$	35
14	$L \rightarrow [\alpha]+L \rightarrow [\gamma+\alpha_2]+\gamma$	25-28
15	$L \rightarrow [\alpha]+L \rightarrow [\alpha]+\beta \rightarrow [\gamma+\alpha_2]+\beta$	24

β_p: primary β. [] square brackets indicates the phases observed in the dendrites, the secondary phases within dendrites having precipitated in this phase through a solid state reaction.

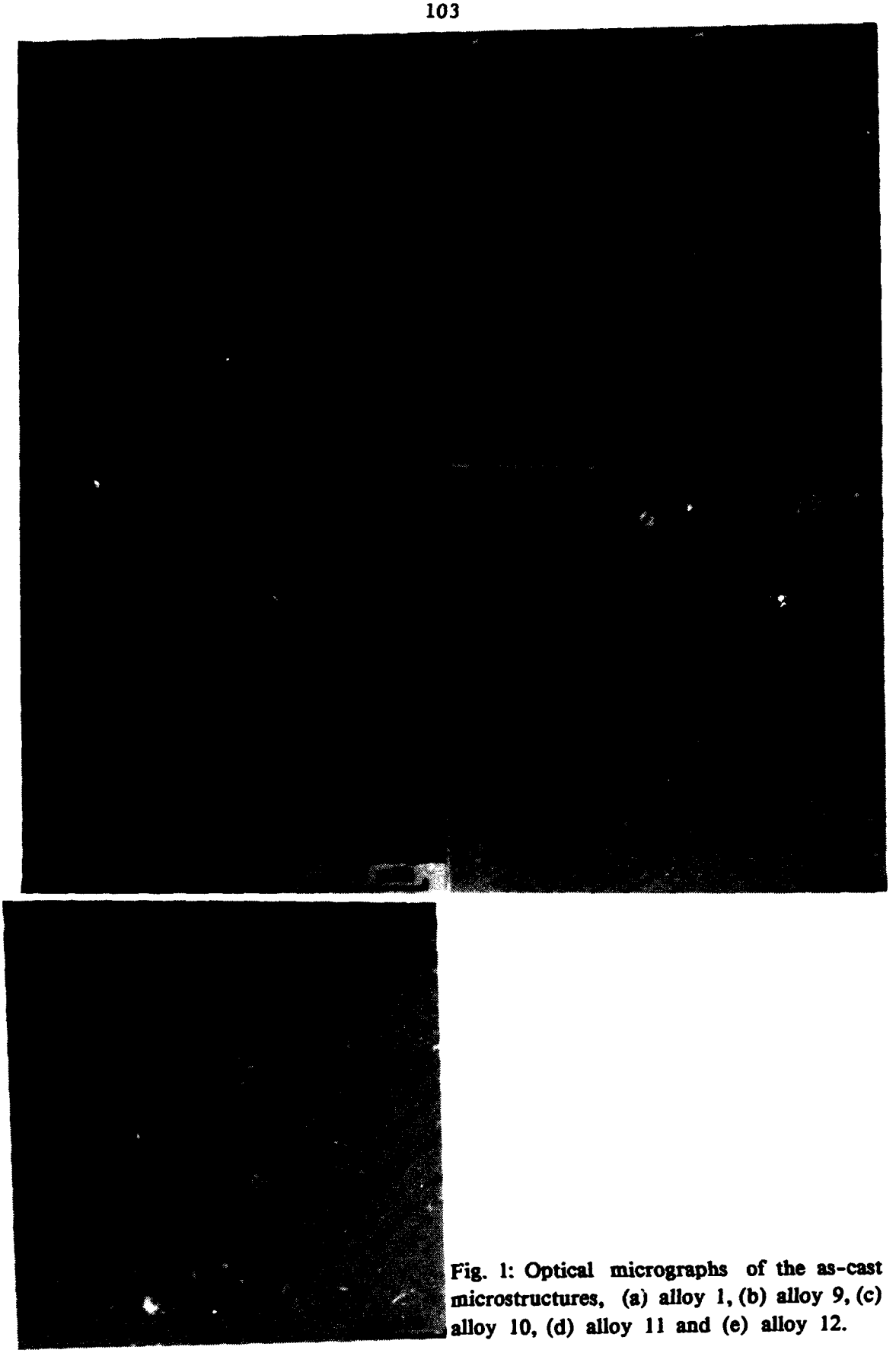

Fig. 1: Optical micrographs of the as-cast microstructures, (a) alloy 1, (b) alloy 9, (c) alloy 10, (d) alloy 11 and (e) alloy 12.

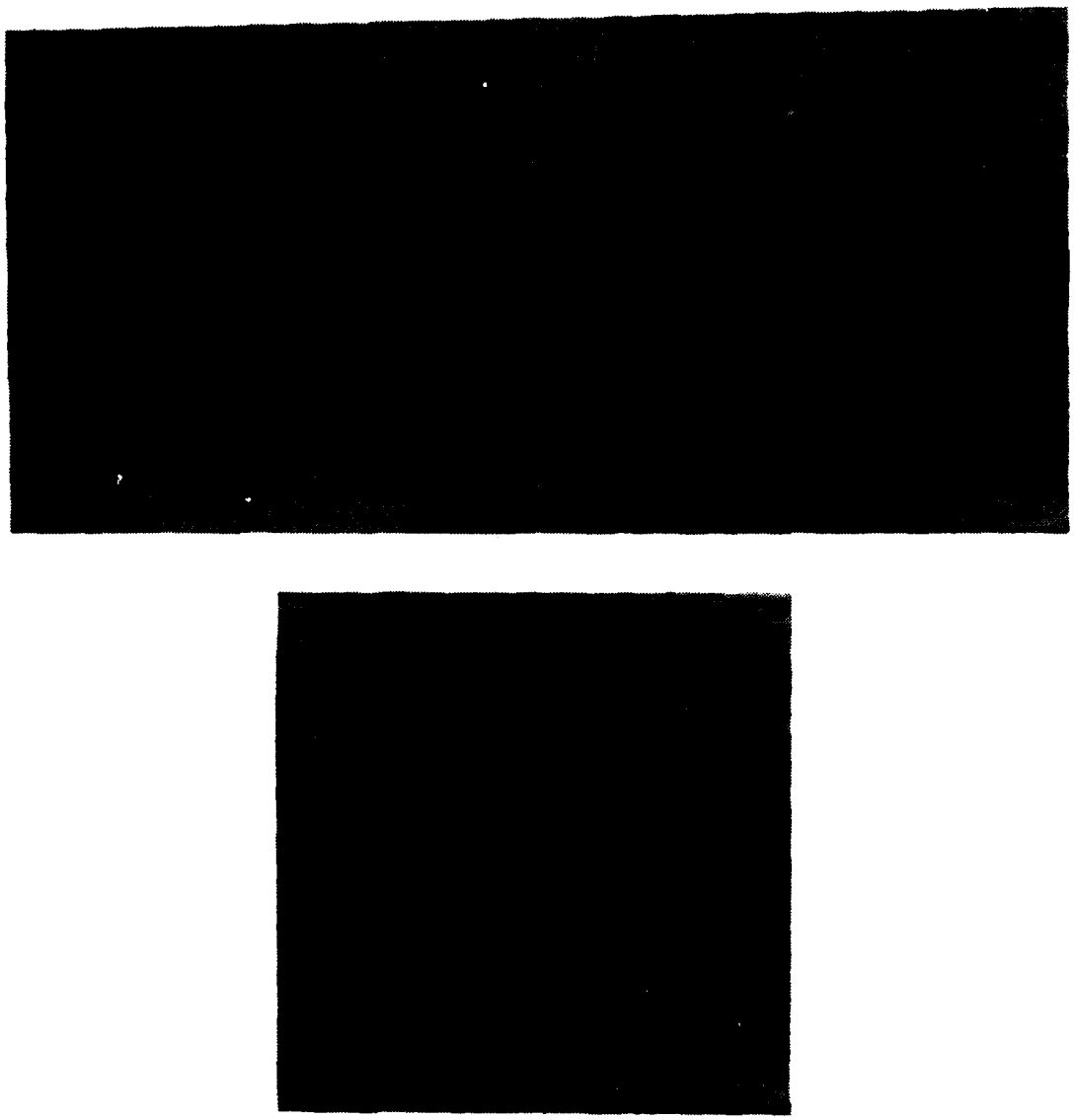

Fig. 2: Optical micrographs of the as-cast microstructures, (a) alloy 15, (b) alloy 16 and (c) alloy 19.

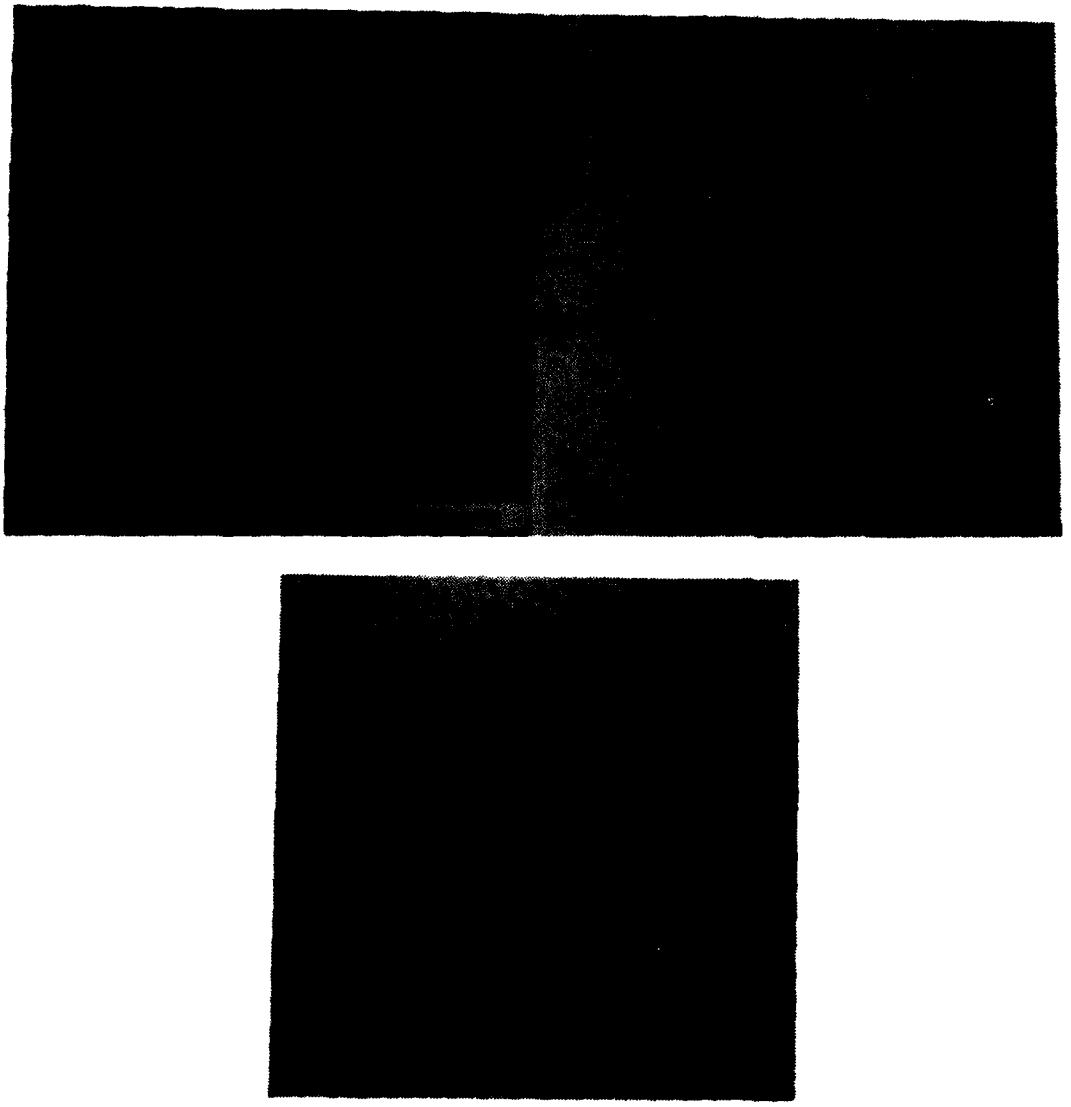

Fig. 3: Optical micrographs of the as-cast microstructures, (a) alloy 20, (b) alloy 21 and (c) alloy 22.

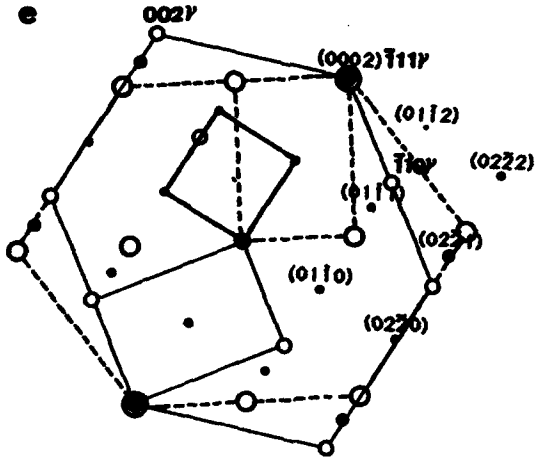

Fig. 4: (a) SEM-BEI of alloy 24. (b) BF micrograph of alloy 24 showing α_2 and γ lamellae present in the dendrites shown in (a). (c) SADP taken from α_2 and γ lamellae present in alloy 24. Zone axis $[2\bar{1}\bar{1}0]\alpha_2$ and <110> γ. See key in (e). (d) BF micrograph of alloy 24 showing α_2, β and γ phases. SADP of zone $[\bar{1}11]\beta$ taken from β area is shown in the inset. (e) Key for SADP shown in (c).

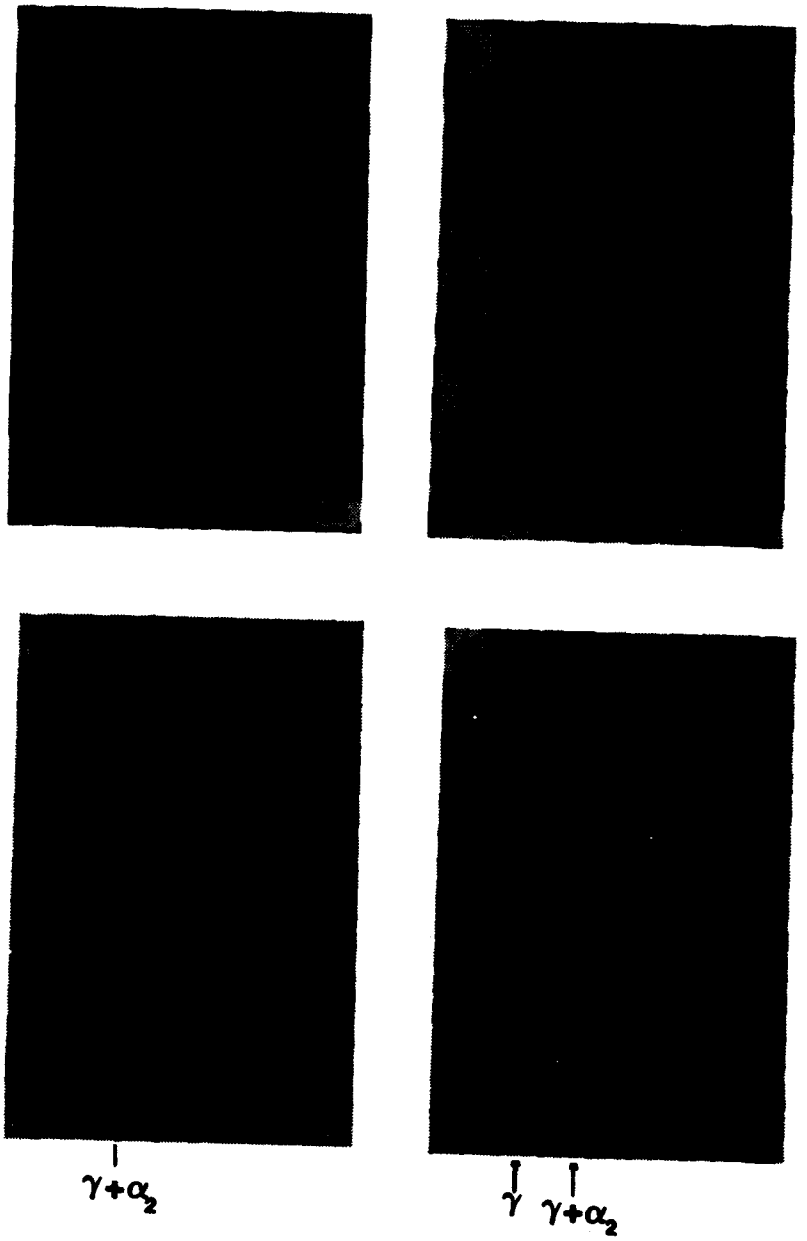

Fig. 5: Optical micrographs of alloy showing hexagonal dendrites, (a) alloy 25, (b) alloy 26, (c) alloy 27 and (d) alloy 28.

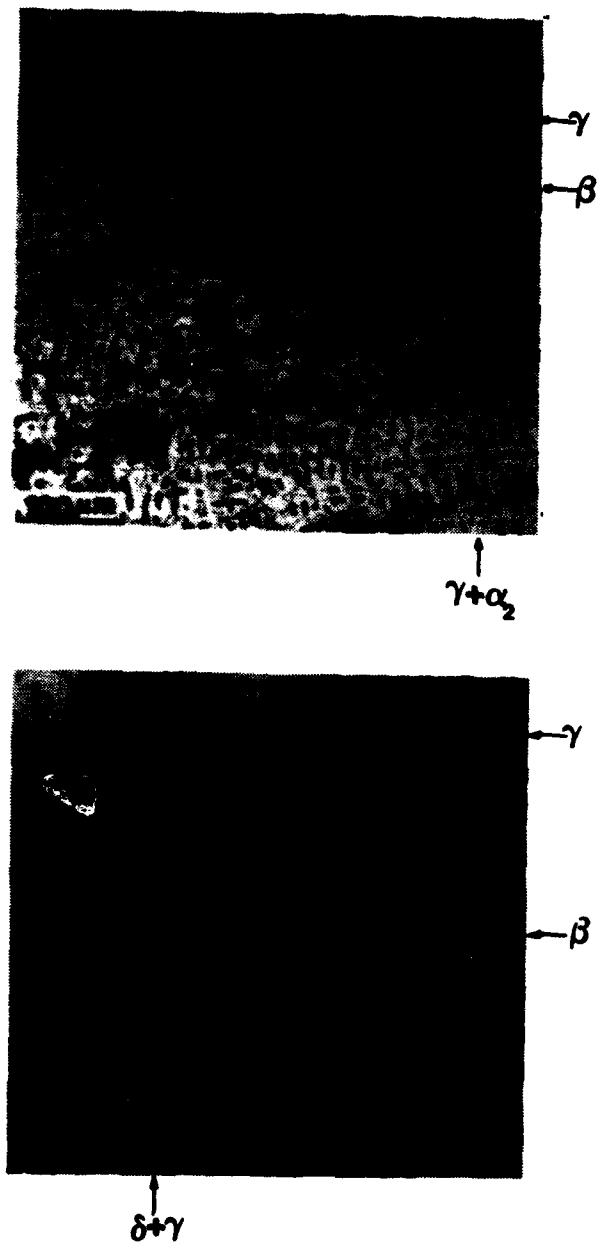

Fig. 6: (a) Optical micrograph of alloy 29 showing orthogonal dendrites. (b) SEM-BEI of alloy 30 showing similar dendrites.

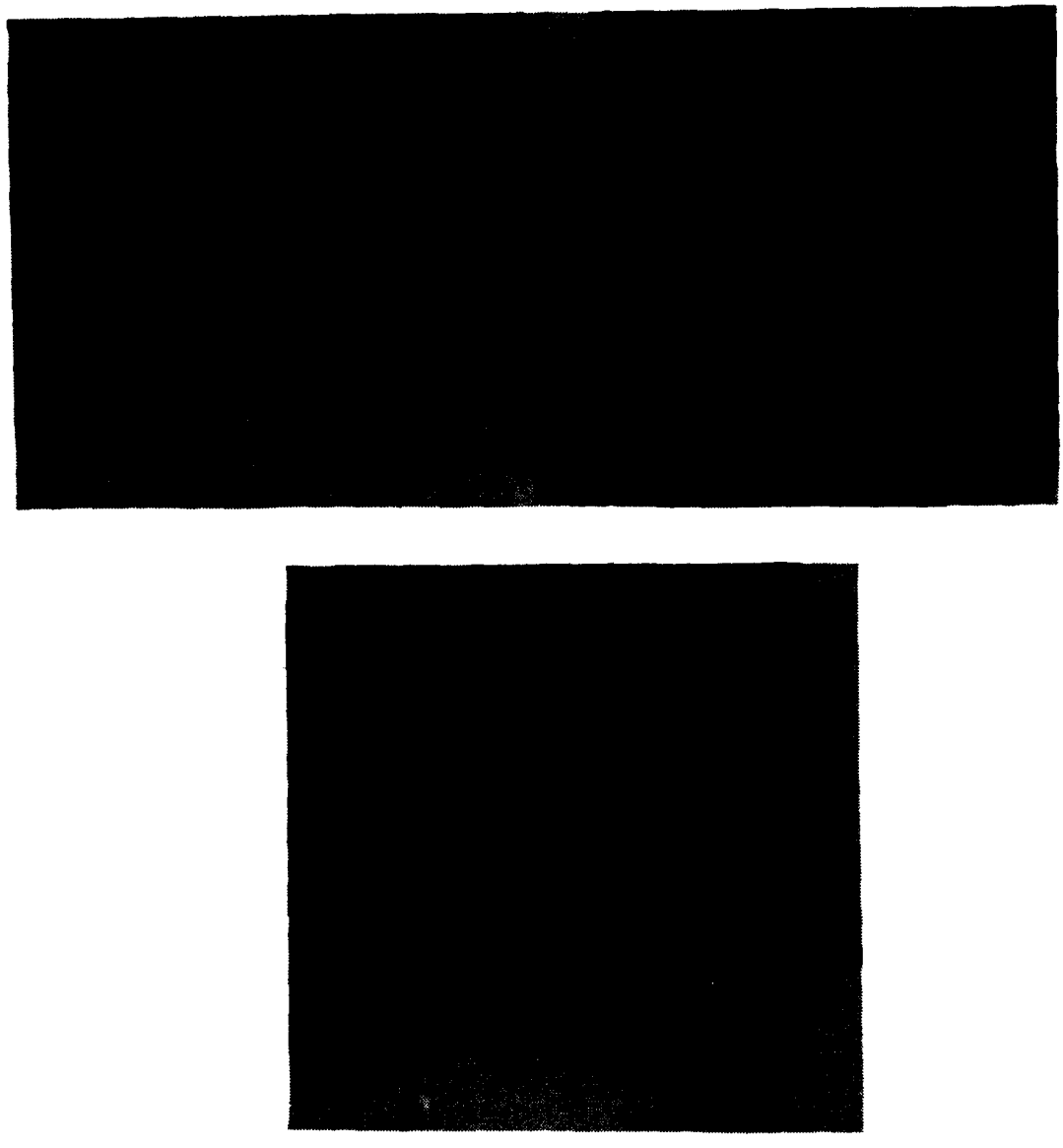

Fig. 7: SEM-BEI of the as-cast microstructures, (a) alloy 31, (b) alloy 32 and (c) alloy 33.

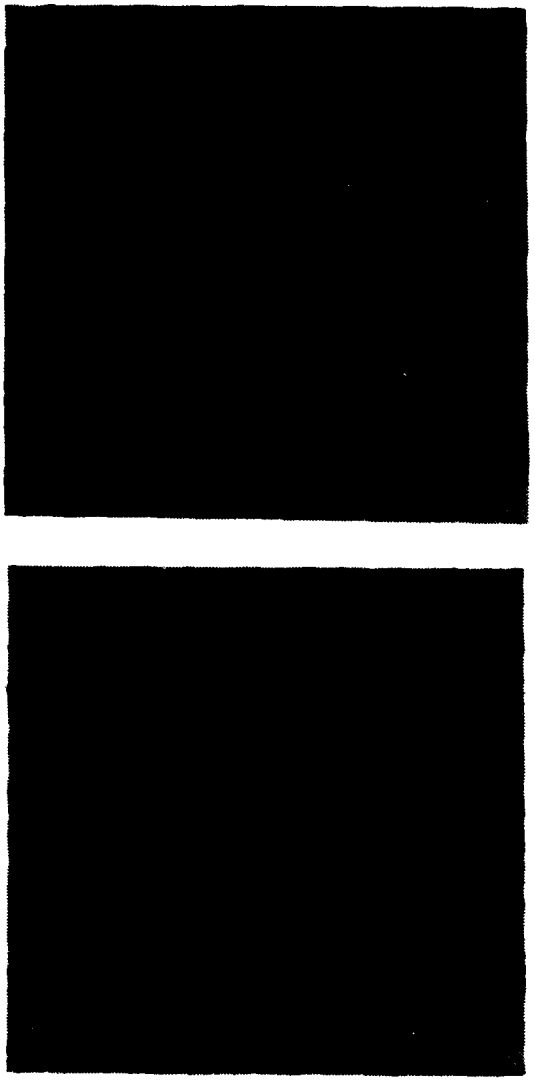

Fig. 8: (a) SEM-BEI of the as-cast microstructure of alloy 34. (b) Optical micrograph of the as-cast microstructure of alloy 35.

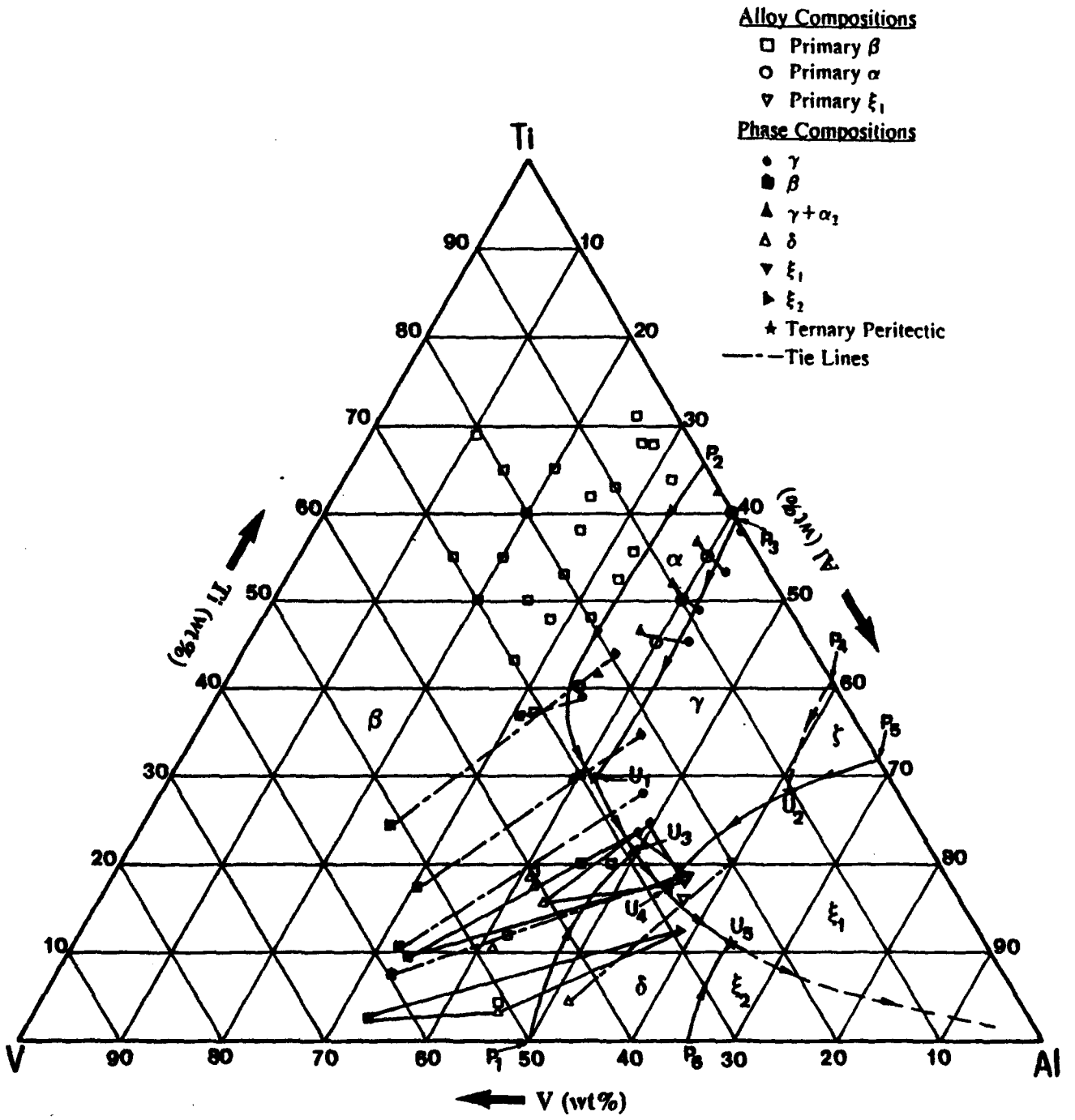

Fig. 9: Tentative liquidus projection of Ti-Al-V system.

BLANK

BLANK

PHASE STABILITY DURING CONTINUOUS HEATING/COOLING OF Ti_3Al-(Nb,V,Mo) TITANIUM ALUMINIDE ALLOYS

M. Long and H. J. Rack
Materials Science and Engineering Program,
Department of Mechanical Engineering,
Clemson University,
Clemson, SC 29634-0921, USA.

To be published in
Materials Science and Technology
1994

Abstract

The elevated temperature phase transitions during continuous heating and cooling of two Ti_3Al-(Nb,V,Mo) titanium aluminides, Ti-25Al-11Nb and Ti-26Al-10Nb-3V-1Mo (at.%), were explored by optical microscopy, calorimetric differential thermal analysis and in-situ high temperature x-ray diffraction.

Both alloys initially consisted of α_2+β+O with continuous heating resulting in the sequential reaction orthorhombic O $\rightarrow$ α_2, dissolution/disordering of α_2, and disordering of B2. Differences in the initial microstructures of the alloys, i.e., blocky and plate-like primary α_2 (α_2^P) colonies in a transformed β {Widmanstätten secondary α_2^S + $(\beta/B2)_t$} matrix in Ti-25Al-11Nb, and Widmanstätten α_2^S + $(\beta/B2)_t$ in Ti-26Al-10Nb-3V-1Mo, was found to affect α_2 dissolution. Dissolution, eventually followed by disordering, of the two morphologically distinct ordered α_2 microconstituents in Ti-25Al-11Nb occurred over two distinct temperature regions, while a single dissolution reaction of Widmanstätten α_2 in Ti-26Al-10Nb-3V-1Mo was observed.

Similar reversible transformations were observed on cooling from the β phase field, the quantities of primary and secondary α_2 being rate dependent, decreasing cooling rate increasing the volume fraction of primary α_2 while decreasing the volume fraction of secondary Widmanstätten α_2.

Introduction

Binary Ti_3Al-base aluminide alloys are excellent candidates for high temperature applications in the 500°-700°C range. Unfortunately, they suffer from poor ductility and fracture toughness at low to intermediate temperatures. These properties may however be enhanced thru alloy modification, notably the addition of β-stabilizing elements (Nb, V, Mo).[1-8] Decomposition of Ti_3Al-(Nb,V,Mo) alloys upon cooling from the single phase β region may involve diffusion controlled processes, diffusional ordering transformations and/or diffusionless reactions, depending upon β-stabilizer content, interstitial content (O, N, H, C) and cooling rate.[9,10] Indeed, B2 (ordered bcc), α/α′ (hcp), α_2 (ordered hcp, DO_{19} structure), O/O′ (orthorhombic phase), "ω-type", and tetragonal phases have all been reported.[8-22]

These observations illustrate that achievement of optimal mechanical performance in Ti_3Al-(Nb,V,Mo) alloys will critically depend upon prior thermomechanical history. In particular appropriate control of deformation processing will require a detailed knowledge of the alloys' microstructural stability, particularly at elevated temperatures where processing is normally undertaken. The present study was undertaken towards this end by examining the elevated temperature phase stability of two semi-commercial Ti_3Al-(Nb,V,Mo) alloys, Ti-25Al-11Nb and Ti-26Al-10Nb-3V-1Mo (at.%), during continuous heating/cooling.

Experimental Details

The two Ti_3Al-(Nb,V,Mo) alloys investigated, Ti-25Al-11Nb and Ti-26Al-10Nb-3V-1Mo (at.%), Table 1, were supplied by TIMET and were received as 152.4 mm thick slabs having undergone initial forging from 3400 kg triple vacuum melted production ingots. During this prior processing, the materials had been heated to 1533K, held at this temperature for 8 hours, forged, and then air cooled.

Metallographic examination of sections prepared from the forged ingots showed that the microstructure of as-received Ti-25Al-11Nb consisted of primary α_2 (α_2^P) colonies in a transformed β/B2 {Widmanstätten α_2^S + $(\beta/B2)_t$} matrix, with no apparent grain boundary α_2 (α_2^{GB}), Figure 1. In comparison, the microstructure of Ti-26Al-10Nb-3V-1Mo consisted of Widmanstätten α_2^S + $(\beta/B2)_t$, with grain boundary α_2^{GB}, Figure 1.

Characterization of these materials' high temperature stability utilized calorimetric differential thermal analysis (CDTA) and high temperature in-situ x-ray diffraction (HTXRD).[23,24] The CDTA system was configured to ensure that the heating/cooling experiments were unaffected by test environment, modification of the CDTA apparatus including installation of an inert gas purifier/oxygen analyzer and introduction of in-situ high purity titanium gettering charges to minimize oxygen pick-up.

The purity of the CDTA system was verified by repeated thermal cycling of a pure titanium sample, the lack of significant change in the β transus temperature (< 5K after 3 cycles to 1723K) being taken as evidence of the system's ability to maintain atmosphere purity control. CDTA instrumental baseline calibration was performed utilizing high purity sapphire, with final temperature calibration of the apparatus being achieved from the solid state standard temperature transformations of pure manganese (β→γ:1361K, γ→δ:1409K, δ→L:1514K) and pure titanium (α→β:1164K).[25] After calibration, temperatures were considered to be accurate within 1 %.

Phase transformation temperatures from 873K to 1573K were determined during both heating and cooling in a high purity argon atmosphere at 5, 10, 20, and 40K/min rates. In order to separately evaluate each transformation, both the heat flow, normalized per unit mass ($mJ.sec^{-1}.mg^{-1}$.), and its first derivative with respect to temperature, $J' = dJ/dT$ ($mJ.sec^{-1}.mg^{-1}.deg^{-1}$), were recorded and analyzed. Transformation temperatures were determined from the CDTA thermograms by establishing those temperatures where J and J′ deviated from the baseline, and in the case of overlapping peaks, where J′ showed a curvature anomaly. The average standard deviation observed for the measured reaction temperatures was ± 5K.

In-situ high temperature x-ray diffraction experiments were also undertaken to complement the CDTA experiments. These utilized a Scintag 2θ-diffractometer equipped with a high temperature furnace/vacuum chamber, again modified in a manner similar to that outlined above for the CDTA apparatus to introduce and maintain a high purity inert argon gas atmosphere at a desired pressure.[23,24]

The high temperature x-ray diffraction samples, 20 mm x 8 mm x 0.25 mm, were prepared by wafering and grinding, with final preparation involving removal of a 20 μm minimum surface layer by chemical thinning in a bath of 10 ml HNO_3 + 5 ml HF + 50 ml H_2O for about 20 seconds, this treatment being designed to eliminate any deformation layer that might have been occasioned by previous preparation.[26] Samples were then repeatedly washed in water and ethanol, and dried in warm air.

The x-ray sample, onto which a type C thermocouple was spot-welded to monitor temperature, was then mounted in the chamber on a tantalum strip heater. Gettering charges were positioned and the furnace sealed, a vacuum of $1x10^{-5}$ mbar inside the chamber being achieved overnight. The chamber was then repeatedly backfilled (≈ 1 atm) with a high purity argon gas and flushed, the initial vacuum being achieved between each step. Finally, an argon pressure of 0.6 atm was maintained prior to heating.

Initially, ambient temperature 2θ-scans from 15° to 85° were acquired utilizing Cu-K_α radiation operating at 40kV and 30mA. Following ambient temperature examination, the sample was heated from 873 to 1623K at a heating rate of 20K/min, diffraction spectra being collected at pre-selected temperatures maintained within an accuracy of ± 5K, the sample being held at temperature approximately 5 minutes prior to scanning at a 10°/min. Typically, four to five samples of each alloy were examined, with rocking curves (θ fixed, Ω varying) being obtained where deemed necessary to verify the presence, or absence, of phases at elevated temperatures. The large grain size of the alloys examined precluded quantitative phase determination. In addition, it should be noted that the x-ray diffraction technique looses its sensitivity when volume fractions of the phases being identified are below approximately 5 %. Following data collection, the x-ray diffraction spectra were analyzed and the peaks indexed utilizing an iterative computer program that was capable of fitting the observed data to given cell structures using a least squares procedure.[27]

Results

Calorimetric Differential Thermal Analysis (CDTA)

The results of the thermal analysis observations during continuous heating and cooling for Ti-25Al-11Nb and Ti-26Al-10Nb-3V-1Mo are shown in Figures 2 thru 5 and summarized in Table II and III, where an estimate of the equilibrium reaction temperatures was obtained by

assuming a linear relationship between reaction temperatures and heating/cooling rates and by extrapolating to an ideal 0 K/min rate. Independent of heating rate, Ti-25Al-11Nb exhibited a low temperature transformation below 1123K starting at T_O^s and ending at T_O^f. This transformation was followed by a complex sequence of transformations, T_S^h thru T_B^h, where both J and J′ deviated from the baseline. Above T_S^h, ensuing reactions defined by anomalies in J′ were observed at T_L^h for both alloys, T_D^h for Ti-25Al-11Nb, Figure 3, and T_A^h for Ti-26Al-10Nb-3V-1Mo, Figure 5. Finally this sequence of transformations was completed at T_B^h.

Cooling thermograms at 40, 20, and 10K/min of Ti-25Al-11Nb, Figure 3, exhibited three distinct transformations between 1348-1173K; at 5K/min, only two reactions were observed. In each instance, the first reaction, which had an onset at T_B^c and completion at T_D^c, was immediately followed by a second reaction which terminated at T_S^c. At cooling rates above 5K/min, a third reaction appeared, interrupting the T_D^c-T_S^c reaction at a temperature T_L^c (T_L^c<T_D^c), with the extent of this peak increasing with increasing cooling rate.

By comparison, cooling thermograms at 40 and 20K/min of Ti-26Al-10Nb-3V-1Mo, Figure 5, exhibited two distinct transformations between 1398-978K; at the lowest rates examined, 10 and 5K/min, an additional reaction was observed. At the former cooling rates, the first reaction had an onset at T_B^c and completion at T_A^c, and was followed by a plateau before a second reaction initiated at T_L^c terminating at T_S^c. At the slower cooling rates, a third reaction initiating at T_D^c appeared. It was characterized by a shoulder on the T_L^c-T_S^c reaction peak, the extent of this additional transformation increasing with decreasing cooling rate.

X-Ray Diffraction

Ambient temperature x-ray scans, Figure 6, confirmed that both alloys were three phase, α_2(ordered hcp) + β(bcc) + orthorhombic phase O, this latter phase having been identified by the appearance of "shoulders" at selected α_2 peaks.[21] The room temperature lattice parameters of the different phases were computed, Table IV.

Typical high temperature x-ray diffraction data for both alloys are shown in Figure 7. HTXRD data show that Ti-25Al-11Nb and Ti-26Al-10Nb-3V-1Mo were three phase (α_2+β+O) to 1123K and 1073K, respectively, the orthorhombic "peaks" vanishing above these temperatures. Between 1173K and 1423K, Ti-25Al-11Nb was two phase (α_2+β) with, moreover, the primary α_2 peak (α_2{0002} / 2θ ≈ 38°) splitting into a doublet, Figure 8. This doublet was not present at 1448K where the alloy was in the α+β phase field, the absence of α_2 being verified with rocking curves at low angles, 2θ ≈ 17.5°, α_2{1010}, and 2θ ≈ 26°, α_2{1120}. Finally, at 1473K and above, the x-ray diffraction scans showed no distinct peaks, although rocking curves indicated that the alloy was single phase, disordered bcc β phase, above this temperature.

Upon cooling, the Ti-25Al-11Nb x-ray scans were found to be qualitatively identical to those on heating, the intensity of the peaks being randomly modified. At 1298 K, the presence of an α+β structure was verified, transforming to α_2+β below 1273 K. Ultimately a three phase α_2+β+O structure appeared below 1123 K, this structure remaining till room temperature.

Orthorhombic dissolution was also observed in Ti-26Al-10Nb-3V-1Mo. The HTXRD results suggested in contrast to the CDTA results that the two phase α_2+β structure in Ti-26Al-10Nb-3V-1Mo was stable to 1548K. Based on previously accepted results,[9-11] Ti-26Al-10Nb-3V-1Mo is expected to be in the single phase β field at temperatures above 1423K. However, the β transus as determined from HTXRD results was estimated to be approximately 1548K. Detailed analysis of these observations, to be published elsewhere, indicates that this anomalous behavior was related to the high sensitivity of Ti-26Al-10Nb-3V-1Mo to oxygen, absorption of

oxygen during the high temperature x-ray exposure resulting in the stabilization of an α_2-case layer on the diffracted surface.

Discussion

The phase transitions of two Ti_3Al-(Nb,V,Mo) alloys, Ti-25Al-11Nb and Ti-26Al-10Nb-3V-1Mo, observed during heating/cooling as determined from CDTA and HTXRD are summarized in Tables 5 and 6, respectively.

Orthorhombic phase

Upon heating, the orthorhombic phase in both alloys transforms to α_2 at temperatures between T_O^s and T_O^f. This agrees with previous studies[28,29] who reported that the O phase is not stable in these alloys at temperatures above 1123K. Although the low volume fraction of O in the initial microstructures made its detection difficult in the CDTA thermograms, HTXRD scans did confirm its presence below 1123K. Indeed, the presence of the orthorhombic phase at high temperature upon cooling precluded this being an artifact due to sample preparation.

α_2 phase

Two different α_2 morphologies were present in the alloys studied, primary α_2 (α_2^P) colonies in a transformed β/B2 {Widmanstätten α_2^S + $(\beta/B2)_t$} matrix in Ti-25Al-11Nb and Widmanstätten α_2^S + $(\beta/B2)_t$, with grain boundary α_2^{GB}, in Ti-26Al-10Nb-3V-1Mo.

The transformation of these morphologically distinct α_2 microconstituents entails initial resolution of α_2^S within the transformed $(\beta/B2)_t$, followed by the dissolution of α_2^P in Ti-25Al-11Nb. Such a process, Tables 5 and 6, eventually followed by the disordering of α_2, was demonstrated by the CDTA thermograms, where complex phase transformations were observed above T_s^h, Figure 2 and 4. The first of these is proposed to represent the dissolution of α_2^S, and is associated with the major peak for each heating rate, the shape of this peak being representative of a diffusion controlled first order transformation.[30] The onset of primary α_2^P dissolution may also be defined from the CDTA thermograms, as the α_2^S dissolution is complemented at T_L^h for Ti-25Al-11Nb (1389K at 20K/min) by another first order reaction, while the α_2^S dissolution is completed at the T_L^h temperature for Ti-26Al-10Nb-3V-1Mo (1374K at 20K/min). Furthermore, the appearance of the α_2/α doublet reflections in the x-ray pattern for Ti-25Al-11Nb suggests that a difference in chemical composition develops between the primary and secondary α_2 phases during dissolution at high temperature. Elemental partitioning between the α_2 and β phases, and consequently between α_2^P and $\{\alpha_2^S+\beta\}$, which become respectively Al-enriched and Nb-enriched, has previously been reported in Ti-24Al-11Nb.[15,16,31]

Support for the proposed dissolution mechanism is given by quantitative measurements of the $\alpha_2\{0002\}$ doublet in Ti-25Al-11Nb. The intensity of each doublet varies with temperature, until a single predominant peak remains at temperatures greater than 1348K. Figure 9 shows that the α_2^S is dominant at temperatures lower than 1173K, whereas above 1273K, the α_2^P dominates as the amount of α_2^S decreases and eventually vanishes at temperatures greater than 1373K. It may be concluded therefore that T_L^h represents the transition temperature where α_2^S becomes virtually extinct.

The x-ray results for Ti-25Al-11Nb indicate further that the α_2 phase has disordered at 1448K, with subsequent transformation to β at 1473K. The development of the $\alpha_2 \rightarrow \alpha \rightarrow \beta$

reaction in this narrow temperature range (1448-1473K) is confirmed by CDTA analysis where the completion of all reactions was determined at 1456K at 20K/min heating rate, the rate selected for HTXRD experiments.

Similar reversible transformations occur on cooling, as depicted by the CDTA cooling thermograms between T_D^c and T_S^c, Figures 3 and 5. The first α_2 precipitation peak (T_D^c-T_L^c), when observed, represents the formation of α_2^P and is followed by a second peak (T_L^c-T_S^c) involving the formation of α_2^S. As demonstrated by HTXRD analysis in Ti-25Al-11Nb on cooling, α_2 precipitation is preceded by formation of disordered α. A similar reaction path was reported by Weykamp et al.[16] who observed that in a Ti-24Al-11Nb alloy ordering of α_2 was preceded by primary, heterogeneous nucleation of α. It has to be recognized that the distinction of a distinct β/B2$\leftrightarrow\alpha$ CDTA peak was not possible, but should be observed as concluded with HTXRD, suggesting that initial formation of α and α_2 ordering on cooling, and by analogy on heating, are represented by a same CDTA peak.

Ultimately, the ratio of α_2^S and α_2^P observed after cooling is expected to be related to cooling rate and alloying content. Figures 3 and 5 support this conclusion, the intensity ratio between the α_2^S peak and the α_2^P peak decreasing with decreasing cooling rate. Therefore, by analogy with the transformations observed on heating, T_L^c represents the transition temperature from α_2^P to the development of α_2^S with increasing cooling rates. Although α_2^P was not present in the initial Ti-26Al-10Nb-3V-1Mo microstructure, and therefore was not observed in the CDTA thermograms, this α_2 morphology may be achieved in this alloy at slow cooling rates, see below, therefore the T_L^h transition would be observed on subsequent heating.

Demonstration of the effect of rate and composition on the phase morphology of Ti-25Al-11Nb and Ti-26Al-10Nb-3V-1Mo was confirmed by observation of the CDTA sample microstructures after cooling, Figure 10 and 11, respectively. As the cooling rate decreased, coarsening of α_2^P was observed, the as-cooled microstructure changing from a fine α_2^S+(β/B2)$_t$ to a scattered formation of α_2^P and ultimately to a coarse α_2^P morphology. This morphological transition was clearly demonstrated at the lowest cooling rate, 5 K/min, where the α_2^S was absent in the microstructure of the Ti-25Al-11Nb CDTA specimen after cooling, Figure 10(d), an observation consistent with the disappearance of the peak associated with α_2^S formation in the CDTA thermogram, Figure 3. On the other hand, formation and coarsening of α_2^P was observed in Ti-26Al-10Nb-3V-1Mo only at rates lower than 10 K/min, the as-cooled microstructure slowly changing from a Widmanstätten {α_2^S+(β/B2)$_t$} to a mixed Widmanstätten{α_2^S+(β/B2)$_t$}+α_2^P morphology. For instance, microstructures at the highest cooling rates, i.e., 40 and 20 K/min, did not display any α_2^P, Figure 11(a) and (b), an observation consistent with the absence of a peak associated with α_2^P formation in the CDTA thermogram Figure 6. Comparison of the as-cooled microstructures again confirms the slower kinetics in Ti-26Al-10Nb-3V-1Mo.

<u>β phase</u>

The β transus temperatures of both alloys as defined by CDTA, were 1432K and 1407K for Ti-25Al-11Nb and Ti-26Al-10Nb-3V-1Mo, respectively, on heating. These results are in good agreement with previous studies on Ti_3Al-Nb alloys where the β transus temperature was reported as 1408K for Ti-24Al-11Nb [31] and 1403K for Ti-24Al-15Nb.[22]

Cooling thermograms suggest that the high temperature reaction observed immediately below the β transus, i.e., between T_B^c and T_D^c (Ti-25Al-11Nb) or T_A^c (Ti-26Al-10Nb-3V-1Mo), is the $\beta\rightarrow$B2 ordering reaction. This reaction is not, as expected of a second order reaction, rate dependent, Tables 3 and 4. Furthermore the proposed $\beta\rightarrow$B2 transformation temperature

observed on cooling is higher in Ti-26Al-10Nb-3V-1Mo (1400K) than in Ti-25Al-11Nb (1354K). Other studies of Ti-24Al-11Nb and Ti-25Al-20Nb [16] have also shown that higher Nb content resulted in higher $\beta \rightarrow$B2 ordering temperatures and enhanced formation of B2. This increase in the ordering temperature for Ti-26Al-10Nb-3V-1Mo vis-a-vis Ti-25Al-11Nb tends also to separate $\beta \rightarrow$B2 from β/B2$\rightarrow\alpha/\alpha_2$ reaction [22] in Ti-26Al-10Nb-3V-1Mo, Figure 5, while both reaction are merged in Ti-25Al-11Nb, Figure 3.

An analogous transformation, identified by T_D^h (Ti-25Al-11Nb) or T_A^h (Ti-26Al-10Nb-3V-1Mo), is observed in the CDTA thermograms on heating in the high temperature range immediately below the β transus. Again, it is suggested that this reaction is associated with $\beta \rightarrow$B2 ordering reaction, which on heating involves disordering of the B2 phase. This conclusion is supported by other studies under isothermal conditions [12,16-18] where the β phase undergoes a $\beta \rightarrow$B2$\rightarrow\beta$ transformation between 1223K and 1448K, disordered β existing below 1223K, ordered B2 between 1223K and the β transus, and disordered β above the β transus.

Conclusions

High temperature phase stability has been examined in Ti-25Al-11Nb and Ti-26Al-10Nb-3V-1Mo. In Ti-25Al-11Nb, transformations on heating involve the sequential transformation of orthorhombic O, dissolution/disordering of the morphologically distinct α_2 phases, α_2^P and α_2^S, present in the as-received alloy, and disordering of the B2 phase. In the case of Ti-26Al-10Nb-3V-1Mo, transformations are limited to the sequential transformation of orthorhombic O and dissolution of Widmanstätten α_2 and α_2^{GB}, followed by disordering of B2. Similar reversible reactions occur on cooling from the high temperature single phase β, the relative amount of the morphologically different α_2 phases exhibiting a cooling rate dependency, the amount of primary α_2 increasing with decreasing cooling rates. Finally solution partitioning during α_2 precipitation or dissolution influenced the disordering/ordering state of the β/B2 phase.

Acknowledgements

This research was initiated under funding by the United States Air Force Office of Scientific Research as part of the Carnegie-Mellon University Research Initiative Program on High Temperature Metal Matrix Composites, contract F49620-87-C-0017, Dr. A. Rosenstein contract monitor, and continued under sponsorship by the Defense Advanced Research Projects Agency under contract N00014-89-J-3166 supervised by Mr. W. Baker and monitored by Dr. G. Yoder of the Office of Naval Research. The alloys utilized were kindly provided by Mr. Ed Mild of TIMET, Inc. Initial assistance of Dr. C. Hubbard and Mr. W. Porter, Oak Ridge National Laboratories, Oak Ridge, Tennessee, for high temperature x-ray diffraction and thermal calorimetry is also acknowledged. Finally the authors also wish to thank Dr. P. K. Chaudhury for valuable discussions during this investigation.

References

1. R. L. Fleischer, D. M. Dimiduk, and H. A. Lipsitt: 'Technical Information Series', Report 88CRD326, GE Research & Development Center, Materials Research Laboratory, December 1988.
2. H. A. Lipsitt: in Materials Research Society Symp. Proc. 'High-Temperature Ordered Intermetallic Alloys', Vol. 39, (ed. C. C. Koch *et al.*), 351-364; 1985, Pittsburgh, Materials Research Society.
3. J. M. Larsen, K. A. Williams, S. J. Balsone, and M. A. Stucke: 'High Temperature Aluminides and Intermetallics', (ed. S. H. Whang et al.), 521-556; 1990, Warrendale, The Minerals, Metals & Materials Society.
4. Y.-W. Kim: *Journal Of Materials*, 1989, **41** (7), 24-30.
5. R. G. Rowe: 'High Temperature Aluminides and Intermetallics', (ed. S. H. Whang *et al.*), 375-401; 1990, Warrendale, The Minerals, Metals & Materials Society.
6. S. M. Sastry and H. A. Lipsitt: *Metallurgical Transactions A*, **8A**, 1977, 1543-1552.
7. D. Koss, D. Banerjee, D. A. Lukasak, and A. K. Gogia: 'High Temperature Aluminides and Intermetallics', (ed. S. H. Whang *et al.*), 175-196; 1990, Warrendale, The Minerals, Metals & Materials Society.
8. P. L. Martin, H. A. Lipsitt, N. T. Nuhfer, and J. C. Williams: in Proc. Int. Conf. 'Titanium '80 Science and Technology', Japan, 1980, (ed. H. Kimura and O Izumi), The Metallurgical Society of AIME, Warrendale, PA, Vol. 2, 1245-1254.
9. C. H. Ward: *International Materials Review*, **38** (2), 1993, 79-101.
10. R. Strychor, J. C. Williams, and W. A. Soffa: *Metallurgical Transactions A*, **19A**, 1988, 225-234.
11. J. H. Perepezko, Y. A. Chang, L. E. Seitzman, J. C. Lin, N. R. Bonda, T. J. Jewett and J. C. Mishurda: 'High Temperature Aluminides and Intermetallics', (ed. S. H. Whang *et al.*), 19-47; 1990, Warrendale, The Minerals, Metals & Materials Society.
12. M. J. Kaufman, T. F. Broderick, C. H. Ward, J. K. Kim, R. G. Rowe and F. H. Froes: in Proc. Int. Conf. 'Sixth World Conference on Titanium', Cannes, France, 1988, Société Française de Métallurgie, (ed. P. Lacombe, R. Tricot, G. Béranger), les éditions de physique, 985-990.
13. L. A. Bendersky and W. J. Boettinger: 'High-Temperature Ordered Intermetallic Alloys III', (ed. C. T. Liu *et al.*), Vol. 133, 45-50; 1989, Pittsburgh, PA, Materials Research Society.
14. J. A. Peters and C. Bassi: *Scripta Metallurgica et Materiala*, **24**, 1990, 915-920.
15. M. J. Cieslak, T. J. Headley, and W. A. Baeslack III: *Metallurgical Transactions A*, **21A**, 1990, 1273-1286.
16. H. T. Weykamp, D. R. Baker, D. M. Paxton, and M. J. Kaufman: *Scripta Metallurgica et Materiala*, **24**, 1990, 445-450.
17. H. T. Kestner-Weykamp, C. H. Ward, T. F. Broderick and M. J. Kaufman: *Scripta Metallurgica*, **23**, 1989, 1697-1702.
18. D. Banerjee, T. K. Nandy, A. K. Gogia and K. Muraleedharan: in Proc. Int. Conf. 'Sixth World Conference on Titanium', Cannes, France, 1988, Société Française de Métallurgie, (ed. P. Lacombe, R. Tricot, G. Béranger), les éditions de physique, 1091-1096.
19. D. Banerjee, A. K. Gogia, T. K. Nandy and V. A. Joshi: *Acta Metallurgica*, **36** (4), 1988, 871-882.

20. L. M. Hsiung and H. N. G. Wadley: *Scripta Metallurgica et Materiala*, **26**, 1992, 35-40.
21. B. J. Marquardt, A. I. Kahveci, and V. M. Sample: 'GE Aircraft Engines, Interim Report No. 3, Contract F33615-89-C-5615', Engineering Materials Technology Laboratories, Cincinnati, OH, 1991.
22. K. Muraleedharan, A. K. Gogia, T. K. Nandy, D. Banerjee and S. Lele: *Metallurgical Transactions A*, **23A**, 1992, 401-415.
23. M. Long: 'Master of Science Thesis', Department of Mechanical Engineering, Clemson University, South Carolina, December 1992.
24. P. K. Chaudhury, M. Long, and H. J. Rack: *Materials Science and Engineering*, **A152**, 192, 37-40.
25. R. Hultgren, P. D. Desai, D. T. Hawkins, M. Gleiser, K. K. Kelley and D. D. Wagman: 'Values corrected to the 1968 International Practical Temperature Scale (IPTS-68)', American Society for Metals, 1973.
26. H. Hu and R. S. Cline: *Transactions of the Metallurgical Society of AIME*, **242**, 1968, 1013-1020.
27. "Least Squares Unit Cell Refinement" Program, after Appleman and Evans (1973), implementation by R. G. Garvey, North Dakota State University, Fargo, ND, June 1984.
28. K. Muraleedharan, S. V. Nagender Naidu and D. Banerjee, *Scripta Metallurgica et Materiala*, **24**, 1990, 27-32.
29. L. M. Hsiung, W. Cai, and H. N. G. Wadley: *Acta Metallurgica et Materiala*, **40** (11), 1992, 3035-3049.
30. R. C. MacKenzie: 'Differential Thermal Analysis', Academic Press, London and New York, Vol. 2, 1972.
31. K. Muraleedharan and D. Banerjee: *Metallurgical Transactions A*, **20A**, 1989, 1139-1142.

Table 1. Chemical composition of the Ti_3Al-Nb alloys.

	Ti-25Al-11Nb		Ti-26Al-10Nb-3V-1Mo	
	Atomic %	Weight %	Atomic %	Weight %
Ti	bal.	bal.	bal.	bal.
Al	24.95	14.25	25.79	14.60
Nb	10.83	21.30	10.26	20.00
V	-	-	3.09	3.30
Mo	-	-	1.04	2.10
O	0.26	0.09	0.23	0.08
C	0.26	0.09	0.11	0.027
N	0.04	0.012	-	-
Fe	0.042	0.05	0.07	0.08

Table 2. Ambient temperature lattice parameters.

Lattice Parameters (nm)[a]	Ti-25Al-11Nb			Ti-26Al-10Nb-3V-1Mo		
	β/B2	α_2 [b]	O	β/B2	α_2 [b]	O
a	0.328	0.580	0.604	0.322	0.584	0.606
c	-	0.466	0.464	-	0.465	0.465
b	-	-	0.971	-	-	0.979

[a] Error = ± 0.001 nm
[b] c/a ratio = 0.80

Table 3. Transformation temperatures as a function of heating/cooling rates, Ti-25Al-11Nb.

Heating/Cooling Rate (K/min)	Transformation Temperatures (K)					
	O phase		Heating(T_x^h) Cooling(T_x^c)			
	T_O	T_O	T_S	T_L	T_D	T_B
40	943 ND[a]	1109 ND	1210 1107	1401 1231	ND 1304	1485 1349
20	928 ND	1091 ND	1211 1172	1389 1238	1425 1320	1456 1353
10	913 ND	1083 ND	1208 1198	1378 1242	1407 1334	1443 1351
5	909 ND	1086 ND	1206 1225	1371 ND	1401 1338	1441 1355
0 [b]	905 ND	1079 ND	1207 1236	1369 1246	1394 1343	1432 1354

Table 4. Transformation temperatures as a function of heating/cooling rates, Ti-26Al-10Nb-3V-1Mo.

Heating/Cooling Rate (K/min)	Transformation Temperatures (K) Heating(T_x^h) Cooling(T_x^c)				
	T_S	T_L	T_D	T_A	T_B
40	1157 1007	1392 1178	ND[a] ND	ND 1342	1445 1397
20	1198 1058	1374 1190	ND ND	1394 1370	1426 1400
10	1201 1089	1369 1190	ND 1215	1388 1380	1417 1400
5	1214 1107	1356 1187	ND 1222	1382 1379	1412 1399
0 [b]	1222 1118	1355 1192	ND 1229	1379 1380	1407 1400

[a] not-detected; [b] extrapolated

Table 5. Phase transformations for Ti-25Al-11Nb.

Temperature Range (K)		Phases
Heating	Cooling	
< 1079	< 1236	$\{(\beta/B2)_t+\alpha_2^S\} + \alpha_2^P + O$
1079 - 1207	< 1236	$\{(\beta/B2)_t+\alpha_2^S\} + \alpha_2^P$
1207 - 1369	1246 - 1236	$\{(\beta/B2)_t+\alpha_2^S\} + \alpha_2^P$
1369 - 1394	1343 - 1246	$(\beta/B2)_t + (\alpha_2 \rightarrow \alpha)^P$
1394 - 1432	1354 - 1343	$B2 \rightarrow \beta$
> 1432	> 1354	β

Table 6. Phase transformations for Ti-26Al-10Nb-3V-1Mo.

Temperature Range (K)		Phases
Heating	Cooling	
≈< 1023	≈< 1118	Widmanstätten$\{(\beta/B2)_t+\alpha_2^S\} + O\ (+\alpha_2^{P(+)})$
≈ 1023 - 1222	1192 - 1118	Widmanstätten$\{(\beta/B2)_t+\alpha_2^S\}\ (+\alpha_2^{P(+)})$
1222 - 1355	1229 - 1192	Widmanstätten$\{(\beta/B2)_t+(\alpha \rightarrow \alpha_2)^S\}\ (+\alpha_2^{P(+)})$
1355 - 1379	1380 - 1229	B2
1379 - 1407	1400 - 1380	$B2 \rightarrow \beta$
> 1407	> 1400	β

(+) Not present on heating nor at 40 and 20 K/min cooling rates

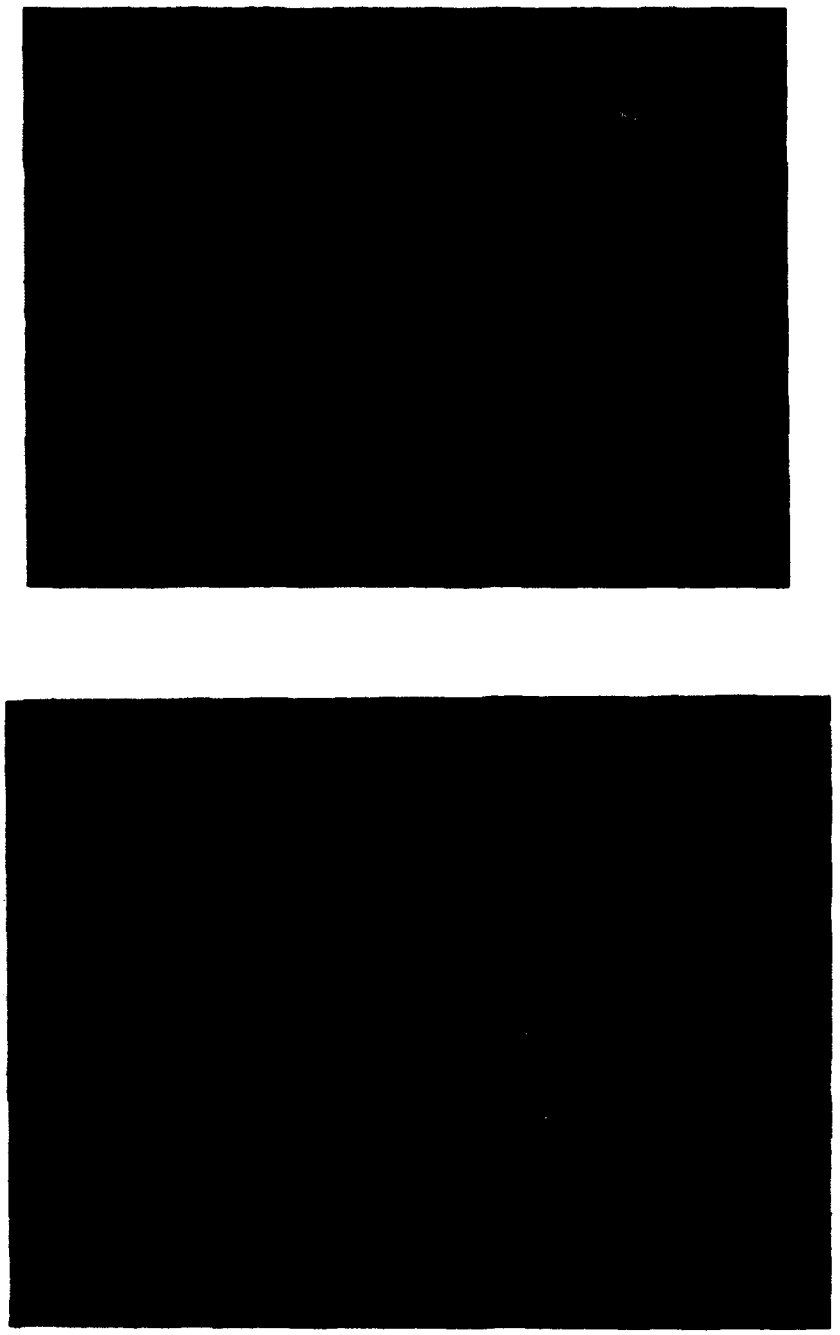

Figure 1. Microstructures of the as-forged materials; (a) Ti-25Al-11Nb exhibiting primary α_2^P [P] and secondary Widmanstätten α_2^S+$(\beta/B2)_t$ [S], (b) Ti-26Al-10Nb-3V-1Mo exhibiting Widmanstätten α_2^S+$(\beta/B2)_t$ [S] and grain boundary α_2^{GB} [GB]

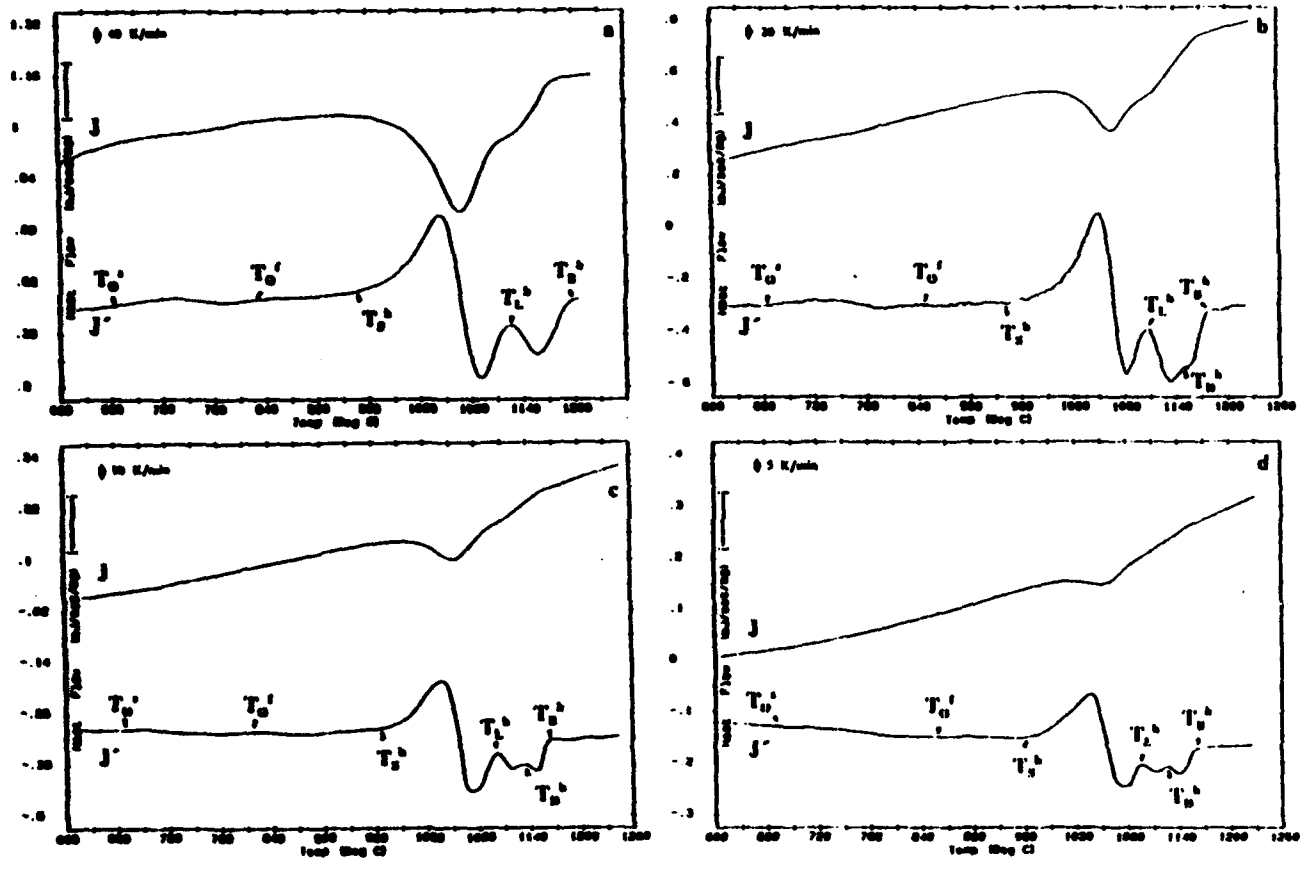

Figure 2. CDTA thermograms for Ti-25Al-11Nb on heating at (a) 40, (b) 20, (c) 10, and (d) 5K/min. Heat flow J ($mJ.sec^{-1}.mg^{-1}$) and its first derivative J' ($mJ.sec^{-1}.mg^{-1}.deg^{-1}$).

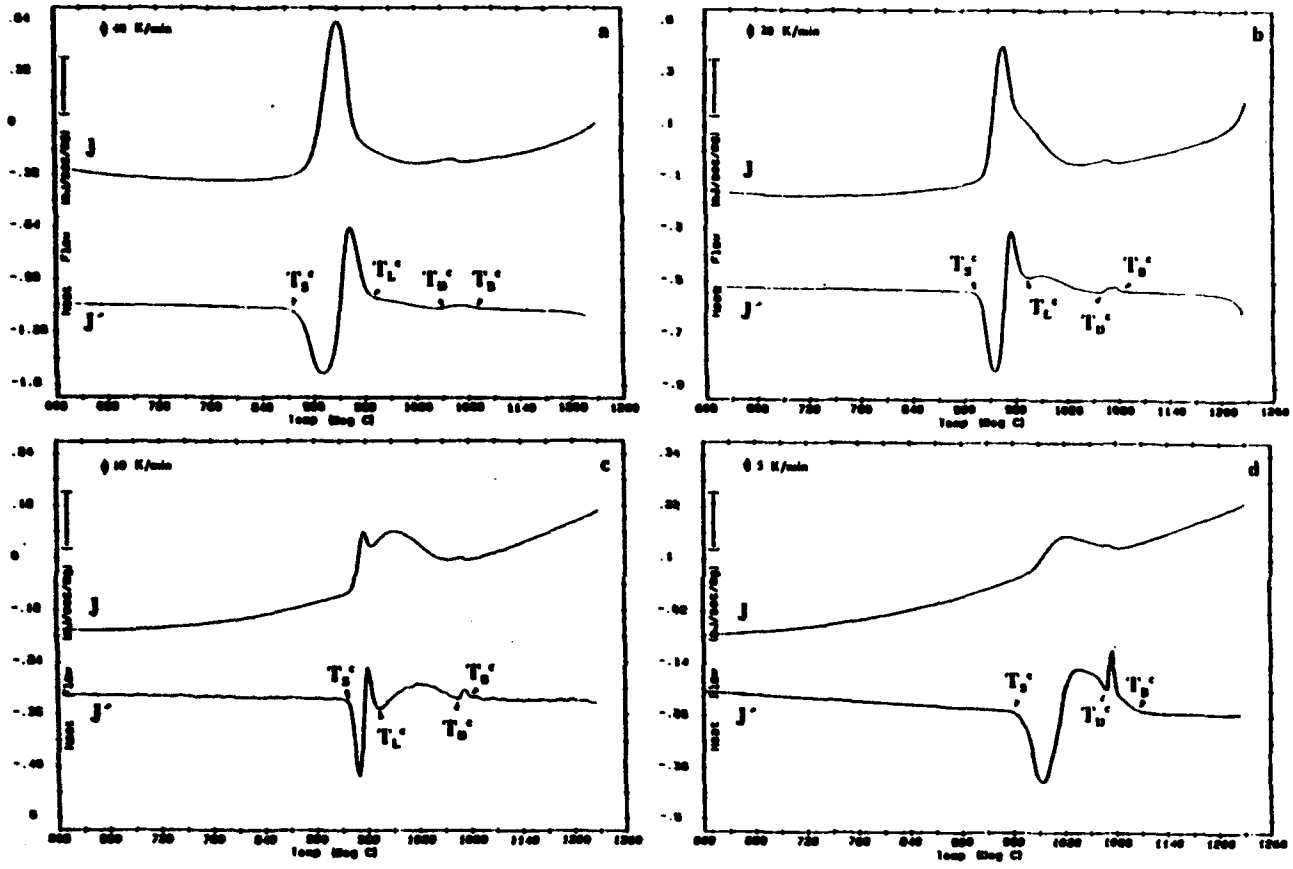

Figure 3. CDTA thermograms for Ti-25Al-11Nb on cooling at (a) 40, (b) 20, (c) 10, and (d) 5K/min. Heat flow J ($mJ.sec^{-1}.mg^{-1}$) and its first derivative J' ($mJ.sec^{-1}.mg^{-1}.deg^{-1}$).

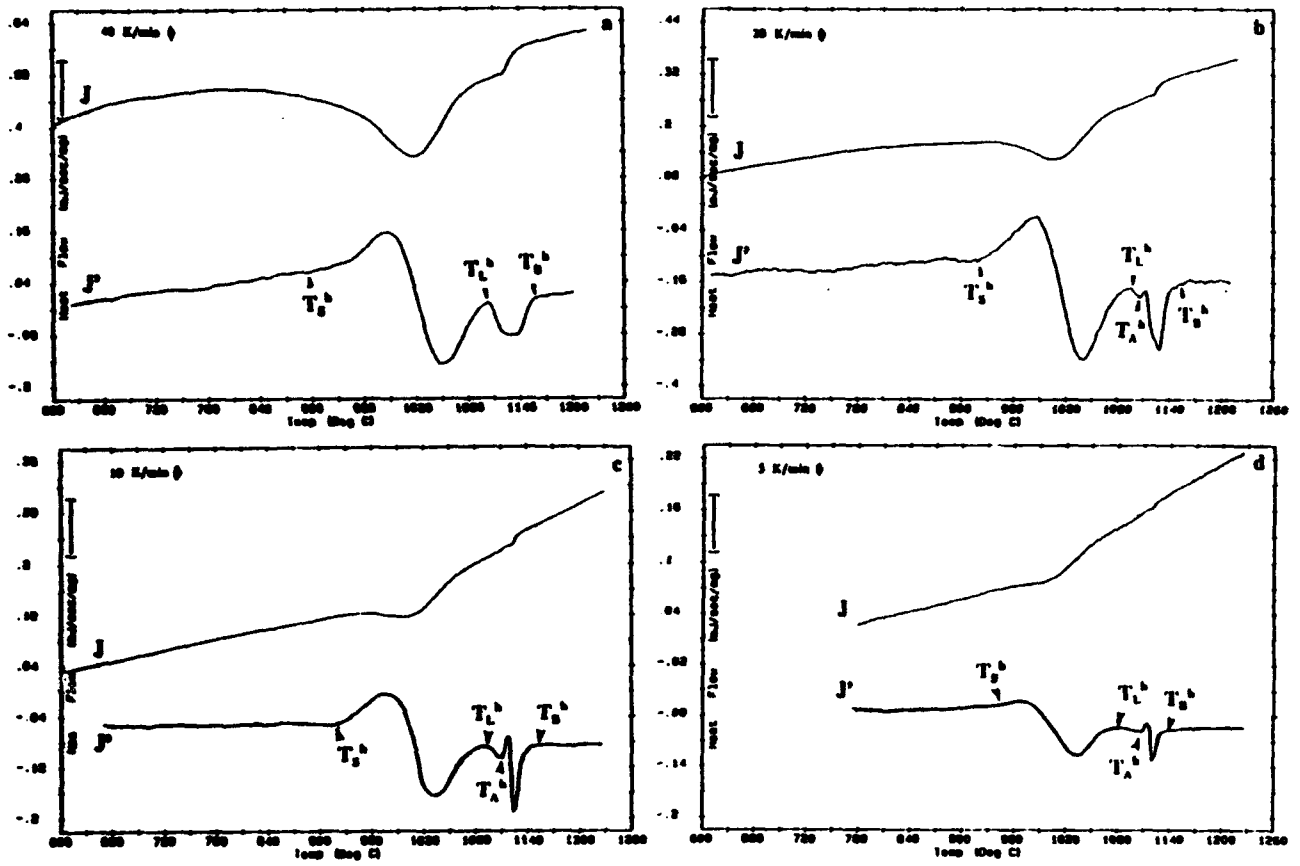

Figure 4. CDTA thermograms for Ti-26Al-10Nb-3V-1Mo on heating at (a) 40, (b) 20, (c) 10, and (d) 5K/min. Heat flow J ($mJ.sec^{-1}.mg^{-1}$) and its first derivative J'($mJ.sec^{-1}.mg^{-1}.deg^{-1}$).

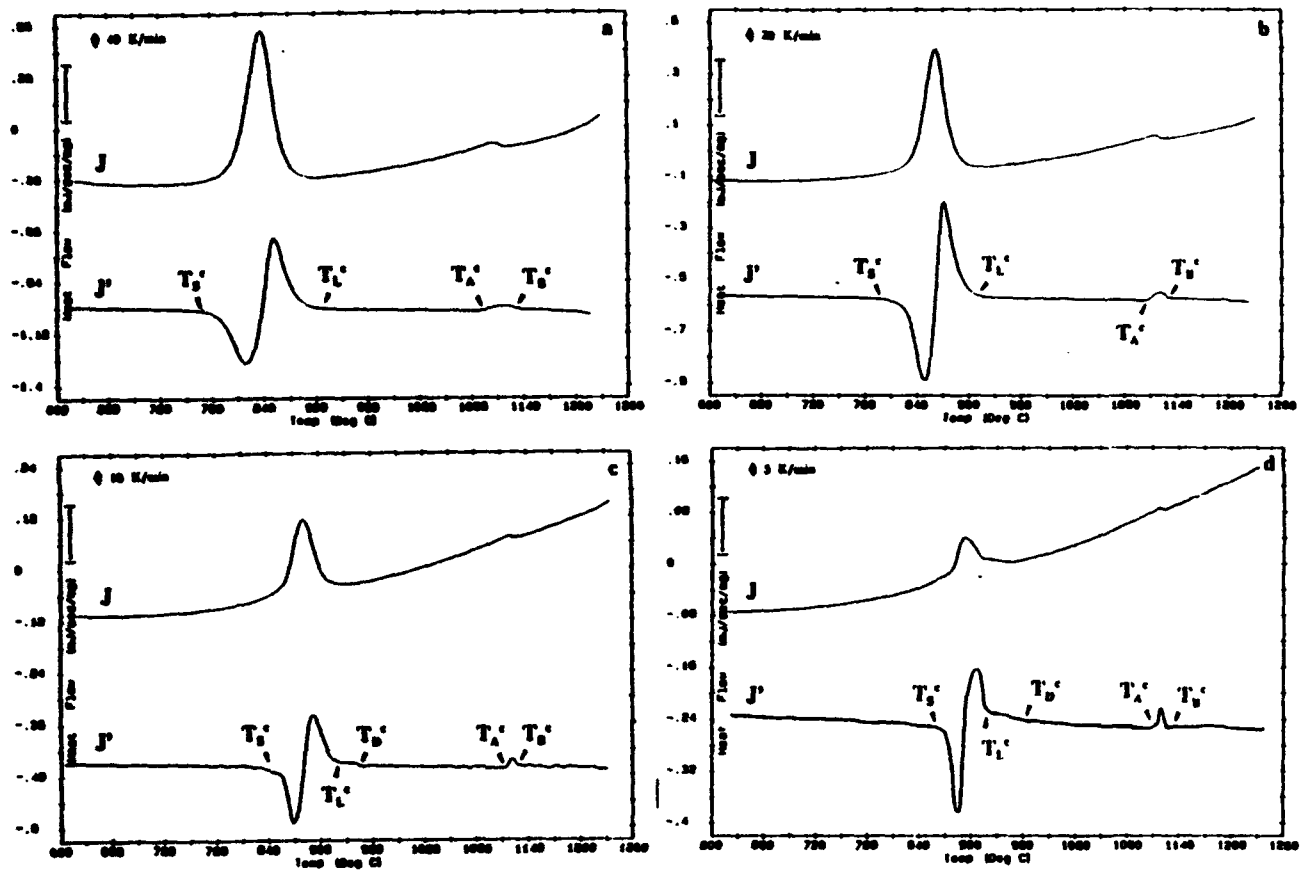

Figure 5. CDTA thermograms for Ti-26Al-10Nb-3V-1Mo on cooling at (a) 40, (b) 20, (c) 10, and (d) 5K/min. Heat flow J ($mJ.sec^{-1}.mg^{-1}$) and its first derivative J'($mJ.sec^{-1}.mg^{-1}.deg^{-1}$).

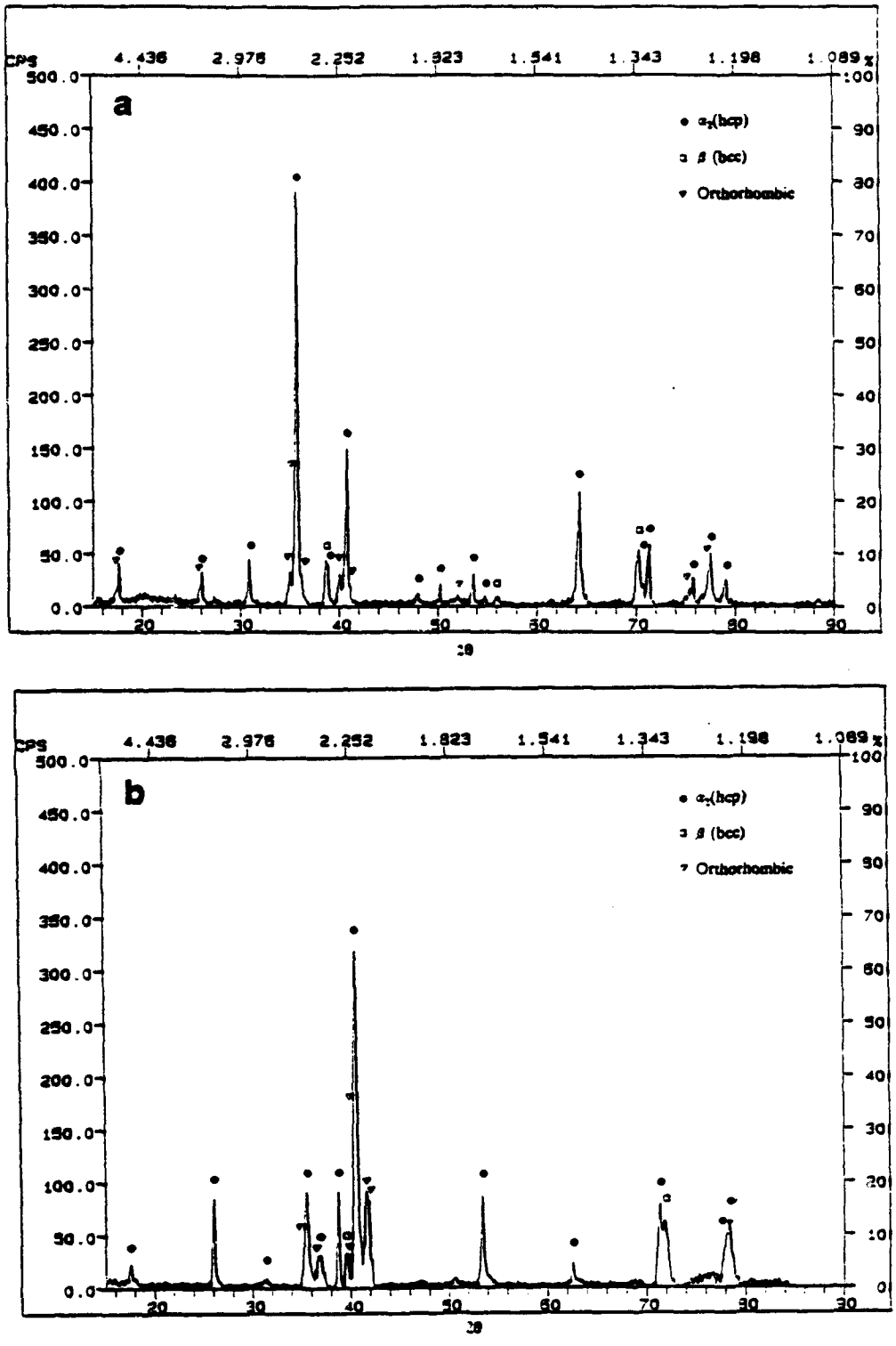

Figure 6. Ambient temperature x-ray diffraction results; (a) Ti-25Al-11Nb, (b) Ti-26Al-10Nb-3V-1Mo.

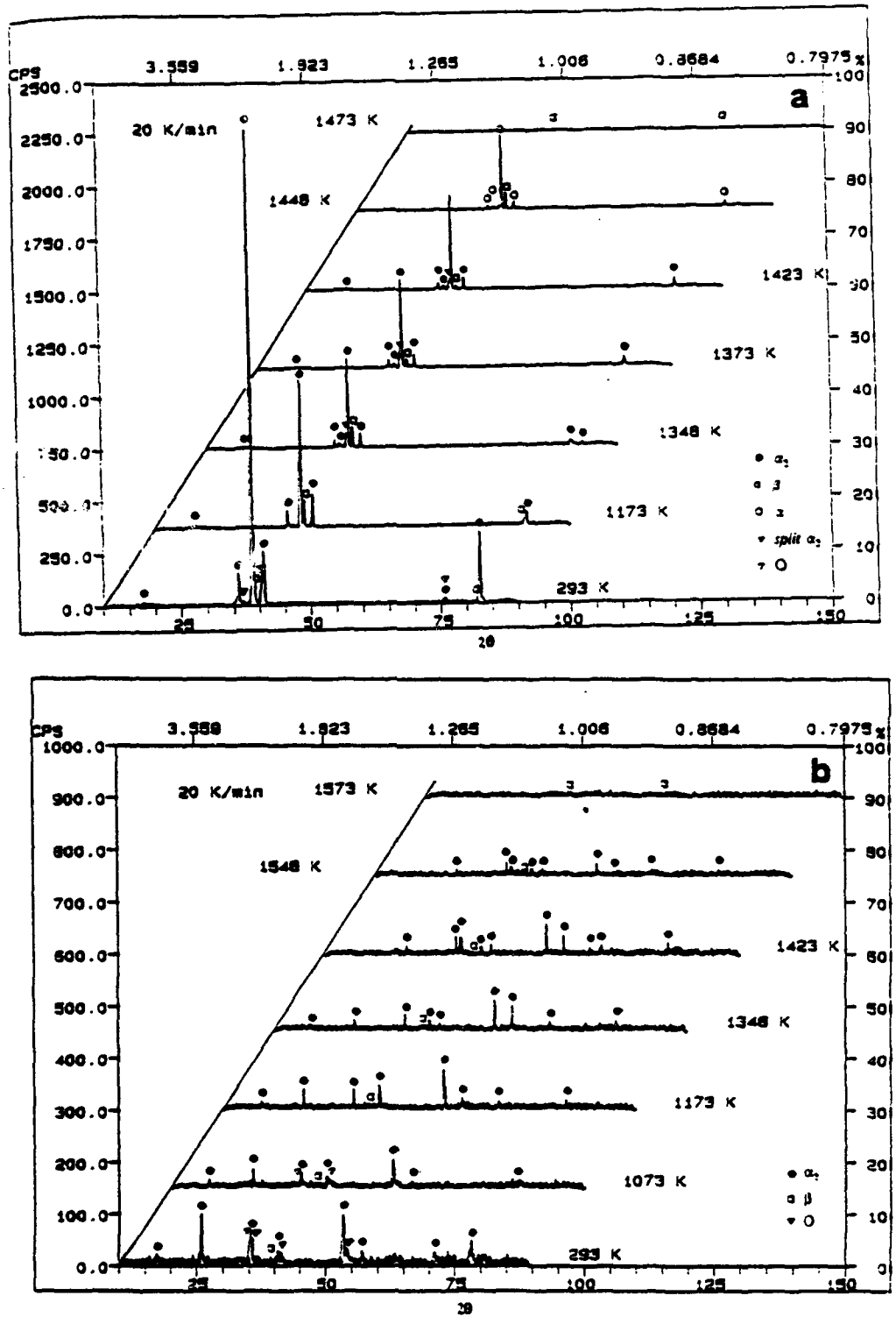

Figure 7. Typical in-situ high temperature x-ray data for (a) Ti-25Al-11Nb and (b) Ti-26Al-10Nb-3V-1Mo.

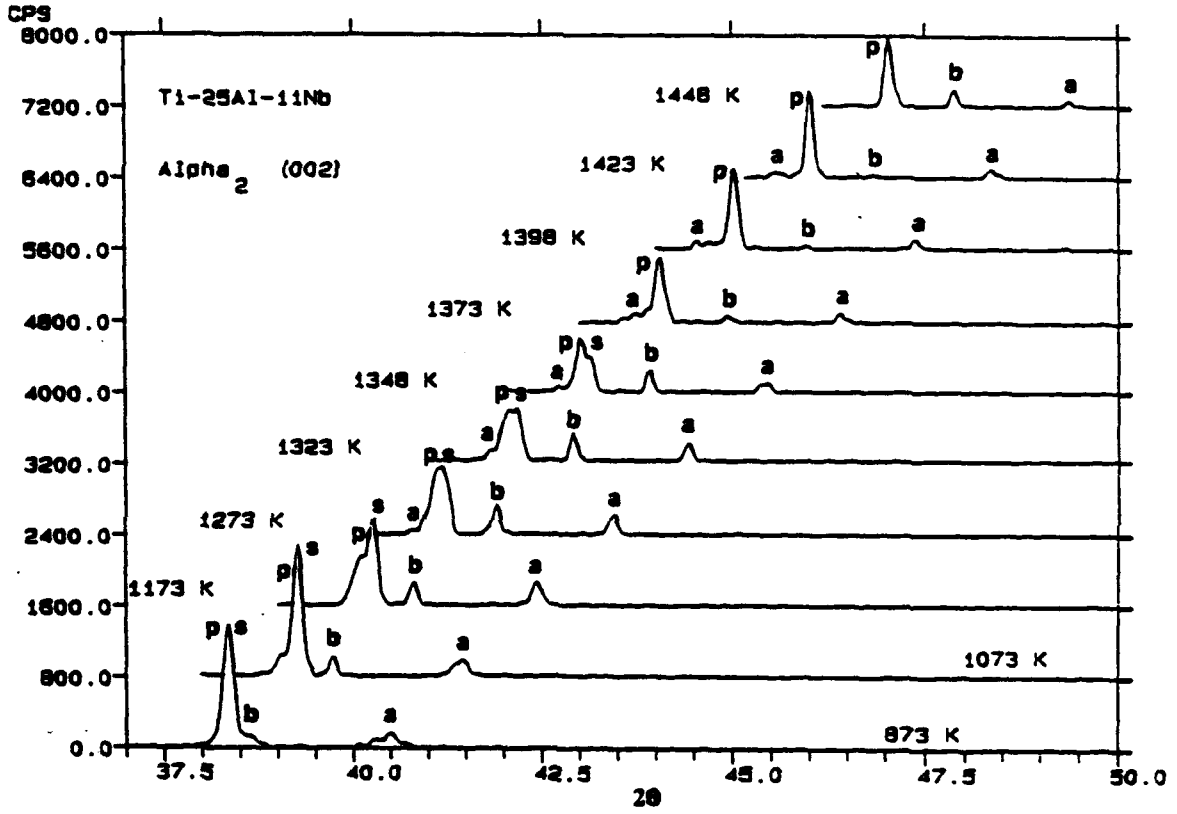

Figure 8. Evolution of the $\alpha_2\{002\}$ peak with increasing temperature in Ti-25Al-11Nb. s, p, a, and b represent primary and secondarespectively.

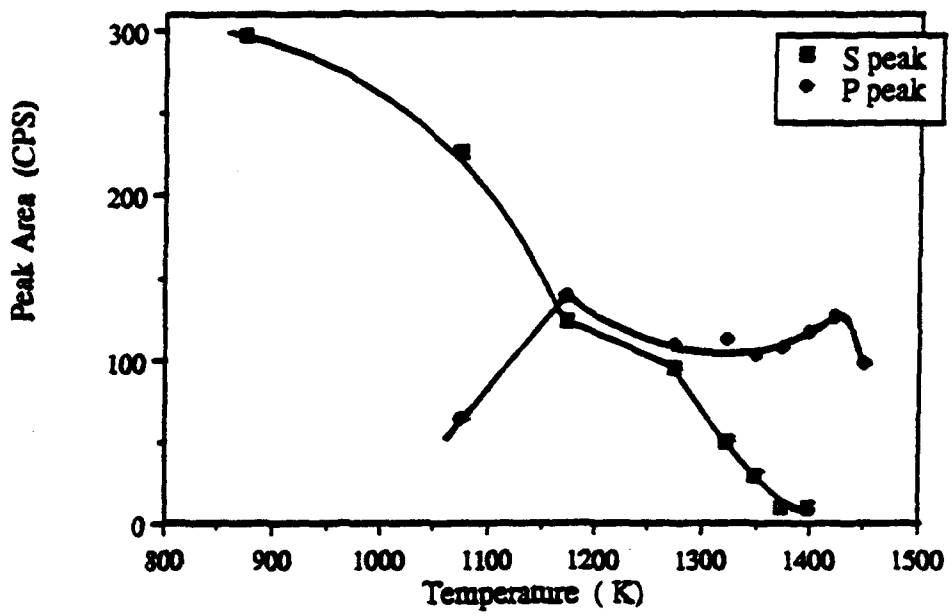

Figure 9. The relative intensity of $\alpha_2^P\{0002\}$ and $\alpha_2^S\{0002\}$ peaks in Ti-25Al-11Nb as a function of temperature, associated with primary α_2^P and secondary α_2^S, respectively.

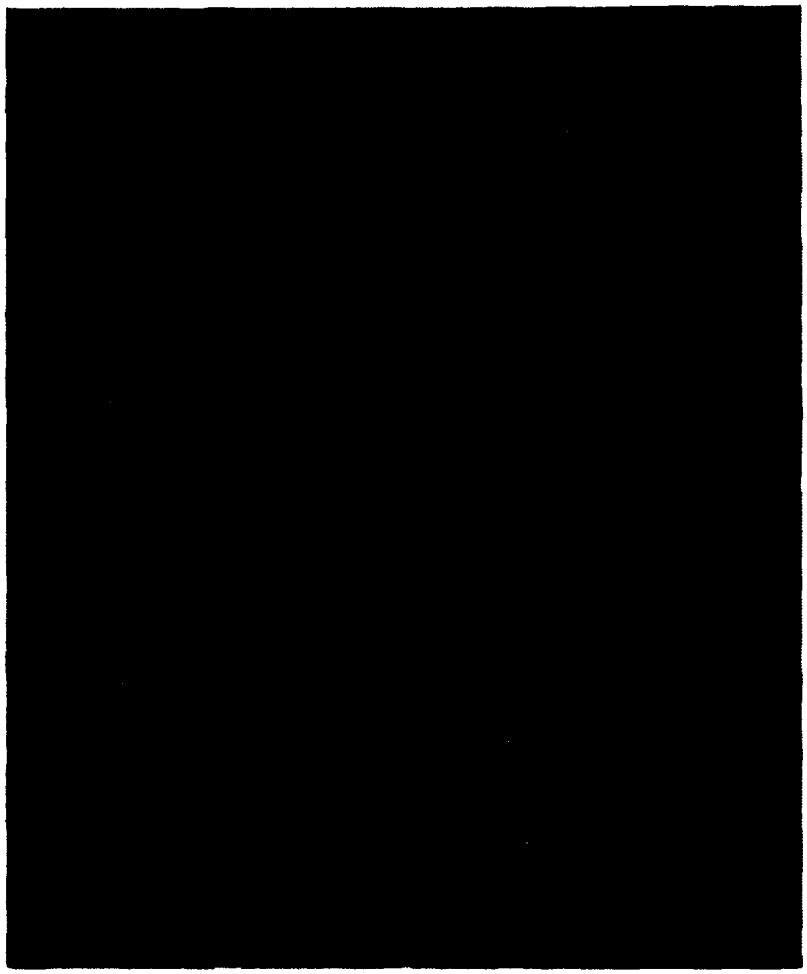

Figure 10. Optical micrographs of the Ti-25Al-11Nb CDTA samples after cooling at rates of (a) 40, (b) 20, (c) 10, (d) 5 K/min.

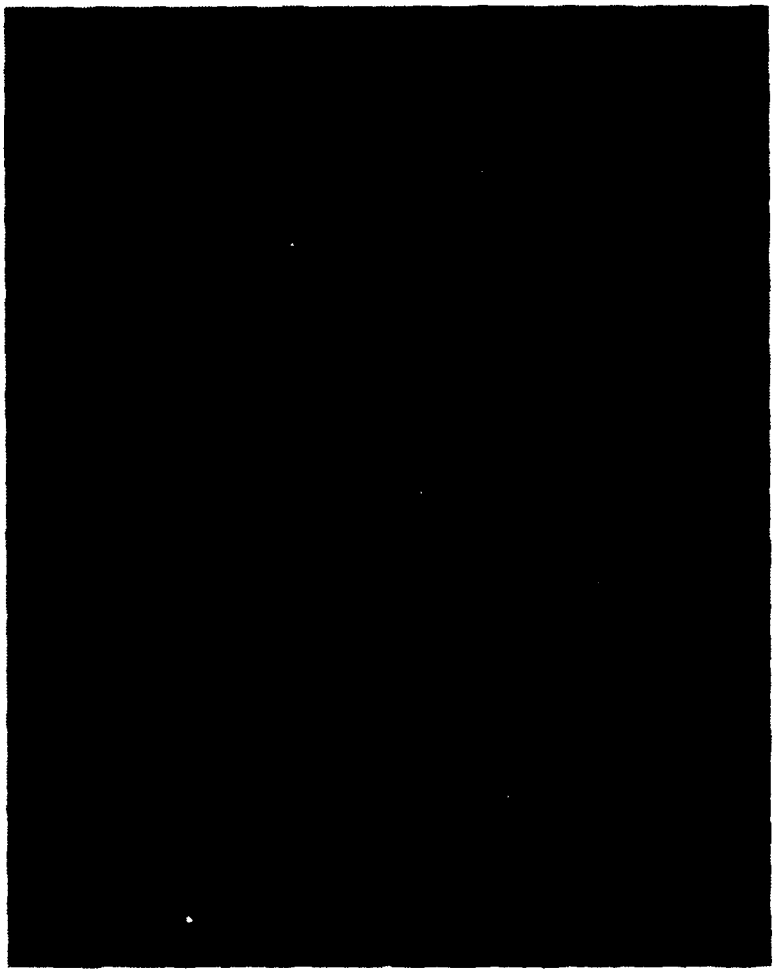

Figure 11. Optical micrographs of the Ti-26Al-10Nb-3V-1Mo CDTA samples after cooling at rates of (a) 40, (b) 20, (c) 10, (d) 5K/min.

ENVIRONMENTAL EFFECTS ON HIGH TEMPERATURE PHASE STABILITY IN Ti-26Al-10Nb-3V-1Mo

M. Long and H. J. Rack
Materials Science and Engineering Program,
Department of Mechanical Engineering,
Clemson University,
Clemson, SC 29634-0921, USA

Submitted to
Scripta Metallurgica et Materiala
December 1993

Introduction

Ordered α_2 titanium aluminides intermetallics have recently received increasing attention for high temperature aerospace applications. Although their relatively low ambient temperature ductility and fracture toughness initially limited their applicability, detailed studies have shown that these properties can be enhanced through the introduction of β isomorphous alloying elements, *e.g.*, Nb, V, or Mo (1,2), these benefits being associated with the formation and incorporation of a controlled quantity of ductile β (or B2, ordered β) within the titanium aluminide microstructure. Other studies have shown that the choice of the β isomorphous addition may however drastically alter and indeed decrease the oxidation resistance of α_2 aluminides vis-a-vis $\alpha+\beta$ titanium alloys (3-5). For example, Schaeffer (5) has shown that the isothermal oxidation rate of Ti-25Al-10Nb-3V-1Mo is not only higher than that of Ti-24.5Al-12.5Nb-1Mo, it actually exceeds that observed in Ti-6Al-2Sn-4Zr-2Mo, an $\alpha+\beta$ titanium alloy often considered for elevated temperature applications.

Much less attention has been placed on the impact elevated temperature exposure may have on $\alpha_2+\beta$ phase stability. These effects may be particularly important when considering *in-situ* measurements, *e.g.*, x-ray and CDTA, to establish phase boundaries and equilibrium phase compositions (6,7). This study examines the potential for environmentally associated phase stabilization in $\alpha_2+\beta$ titanium aluminides.

Experimental Procedure

Ti-26Al-10Nb-3V-1Mo, containing (at.%) Al(25.79), Nb(10.26), V(3.09), Mo(1.04), O(0.23), C(0.11), Fe(0.07), an alloy known for its high sensitivity to oxygen, was selected for this study. Metallographic examination showed that its initial microstructure consisted of Widmanstätten α_2 + β/B2, with α_2^{GB} at prior β grain boundaries, Figure 1.

Characterization of high temperature phase equilibria utilized calorimetric differential thermal analysis (CDTA) and *in-situ* high temperature x-ray diffraction (HTXRD). CDTA samples, weighing approximately 120 mg, were initially chemically cleaned in a solution of 10ml HNO_3 + 5ml HF + 50ml H_2O for about 20 seconds, then washed in ethanol, water and again ethanol, and dried in warm air. Transformation temperatures between 873 and 1573K were determined at rates between 5 and 40K/min during both heating and cooling in a high purity argon atmosphere, the standard deviation observed for the measured reaction temperatures being $\pm$ 5K (6). An estimate of the equilibrium reaction temperatures was obtained by assuming a linear relationship between reaction temperatures and heating/cooling rates and extrapolating to an ideal 0 K/min rate.

In-situ high temperature x-ray diffraction experiments were undertaken to complement the CDTA experiments. These utilized a Scintag diffractometer equipped with a high temperature furnace/vacuum chamber, the high temperature x-ray diffraction samples, having dimensions of 20mm x 8mm x 0.25mm, being prepared by wafering, using a high speed diamond blade cutter and grinding with final chemical thinning eliminating any prior deformed surface layer (6).

Following ambient temperature analysis utilizing Cu-K_α radiation under 40kV and 30mA, the x-ray sample was heated at 20K/min, diffraction spectra being collected at pre-selected temperatures, the latter maintained at $\pm$ 5K, with the sample being at temperature approximately 5 minutes prior to scanning at 10°/min. Rocking curves (θ fixed, Ω varying) were obtained where deemed necessary to verify the presence, or absence, of phases at elevated temperatures and the state of ordering/disordering of these phases.

Results

Typical thermal analysis results during continuous heating and cooling at high, 20K/min, and low, 5K/min, rates are shown in Figures 2. A complex sequence of transformations was observed between T_S^h and T_B^h, where both J (heat flow) and J' (first derivative of the heat flow) curves deviated from the baseline. Above T_S^h, reactions defined by anomalies in J′ were observed at T_L^h and T_A^h, this sequence of transformations being completed at T_B^h. Cooling thermograms at rates of 20K/min and above exhibited two distinct reactions between 1398-978K, the first reaction having an onset at T_B^c and completion at T_A^c, and being followed by a plateau before a second reaction initiated at T_L^c and terminating at T_S^c. At rates below 20K/min, a third reaction initiating at T_D^c appeared, which was characterized by a shoulder on the T_L^c-T_S^c reaction peak. The β transus temperatures on heating, T_B^h, and cooling, T_B^c, were determined to be 1407 and 1400K, respectively.

Ambient temperature x-ray scans showed an α_2(ordered hcp) + β(disordered bcc) structure for Ti-26Al-10Nb-3V-1Mo, with a small quantity of the orthorhombic phase O. Characteristic high temperature x-ray diffraction scans, Figure 3, showed that Ti-26Al-10Nb-3V-1Mo was three phase (α_2+β+O) up to 1073K, the orthorhombic peaks vanishing above this

temperature. These results also suggested that the two phase $\alpha_2+\beta$ structure was stable between 1073 and 1548 K, with erratic fluctuations of the α_2 and β phase lattice parameters being observed at temperatures above 1223K. Finally, the β transus was estimated by HTXRD to lie between 1548 and 1573K, Table 1.

Upon cooling, x-ray scans were found to be qualitatively identical to those on heating, the intensity of the peaks being randomly modified.

TABLE 1
Phase structures determined by HTXRD at 20 K/min heating rate.

Temperature (K)	Phases
298 - 1073	α_2 + β/B2 + O
1173 - 1548	α_2 + β/B2
1573	β/B2

Discussion

Qualitatively, the transformation sequence of Ti-26Al-10Nb-3V-1Mo on continuous heating consisted of orthorhombic O→α_2, α_2 dissolution, followed by α_2→α disordering, and disordering of B2→β. Similar reversible transformations were observed on cooling from the β phase field (6).

Quantitative determination of the related reaction temperatures, in particular that associated with the final dissolution of α_2/α within a β titanium matrix, indicated a wide discrepancy between the two experimental methods employed in this study. HTXRD indicated that α_2/α was stable to temperatures above 1500K while CDTA suggested that the β transus was 1407K.

In order to give further insight into the effect of elevated temperature exposure on the samples, cross-sections of Ti-26Al-10Nb-3V-1Mo samples after *in-situ* high temperature x-ray diffraction were prepared. Observation of these showed that the difference in β transus temperatures was due to the formation of an α_2-case layer, approximately 125 μm thick, on the surface of Ti-26Al-10Nb-3V-1Mo, Figure 4. Further confirmation of this effect was obtained by consideration of the α_2 x-ray extinction thickness (8). If $G_x=1-\exp(-2\mu x/\sin\theta)$ is the fraction of the diffracted intensity which is contributed by a surface layer of depth x, where μ is the linear absorption coefficient of the specimen and θ the diffracted angle, and if it is assumed that 95 % of the diffracted intensity comes from this surface layer, then an effective depth of penetration, $x_{0.95}$, can then be calculated. Substitution of appropriate values for the absorption coefficient of Ti-26Al-10Nb-3V-1Mo, $\mu \simeq 169$ cm^2, results in $x_{0.95}$ values varying between 15 and 90 μm, depending upon the diffraction angle θ, well within the measured α_2 layer thickness in Ti-26Al-10Nb-3V-1Mo. It has to be recognized that the CDTA technique, related to bulk measurement as compared to surface measurement in HTXRD, is not impacted by α_2-case surface formation.

The formation of the α_2-case layer in Ti-26Al-10Nb-3V-1Mo cannot be simply associated with oxygen diffusion. For example, available oxygen diffusivity data for Ti-25Al-11Nb (9) implies that this alloy, in consort with Ti-26Al-10Nb-3V-1Mo, should also exhibit a surface oxidation layer under the temperature/time conditions experienced during HTXRD. Indeed, a first order estimate of the depth of oxidation suggests that an oxidation layer thickness of $\simeq$ 40μm should be observed under the conditions utilized in this study. However, as illustrated in Figure 4, Ti-25Al-11Nb does not exhibit any surface layer. This suggests that, in agreement with Schaeffer (5), the rate limiting step in α_2-case formation appears to be related to enhanced oxygen surface absorption due to the presence of V in Ti-26Al-10Nb-3V-1Mo.

Summary

This study has demonstrated that environmental effects can have an important effect on phase stability of $\alpha_2+\beta$ alloys, and in general reactive alloy systems, at elevated temperature. For instance, O_2 stabilization of the α_2 phase in Ti-26Al-10Nb-3V-1Mo during *in-situ* high temperature x-ray diffraction resulted in an anomaleous estimation of the β transus temperature. Therefore, it is essential that complementary experimental techniques, such as CDTA and HTXRD, be employed in phase stability determination and that any discrepancies between the techniques be carefully considered and documented.

Acknowledgements

Funding for this investigation was provided by the Defense Advanced Research Projects Agency under contract N00014-89-J-3166 supervised by Mr. W. Baker and monitored by Dr. G. Yoder of the Office of Naval Research.

References

1. D. Koss, D. Banerjee, D. A. Lukasak, and A. K. Gogia, High Temperature Aluminides and Intermetallics, The Minerals, Metals & Materials Society, Warrendale, PA, 175 (1990).
2. C. H. Ward. International Materials Reviews, Vol. 38, 79 (1993).
3. A. Szaruga, M. Saqib, R. Omlor, and H. A. Lipsitt, Scripta Metallurgica et Materiala, Vol. 26, 787 (1992).
4. C. H. Ward, J. C. Williams, and A. W. Thompson, Scripta Metallurgica et Materiala, Vol. 28, 1017 (1990).
5. J. C. Shaeffer, Scripta Metallurgica et Materiala, Vol. 28, 791 (1993).
6. M. Long and H. J. Rack, Materials Science and Technology, Vol. A170, 215 (1993).
7. C. McCullough, J. J. Valencia, C. G. Levi, and R. Merhabian, Acta Metallurgica, Vol. 37, 1321 (1989).
8. B. D. Cullity, Elements of X-Ray Diffraction, Addison-Wesley Publishing Company, Reading, MA (1978).
9. K. E. Wiedemann and S. N. Sankaran, Oxidation of High-Temperature Intermetallics, The Minerals, Metals & Materials Society, Warrendale, PA, 195 (1989).

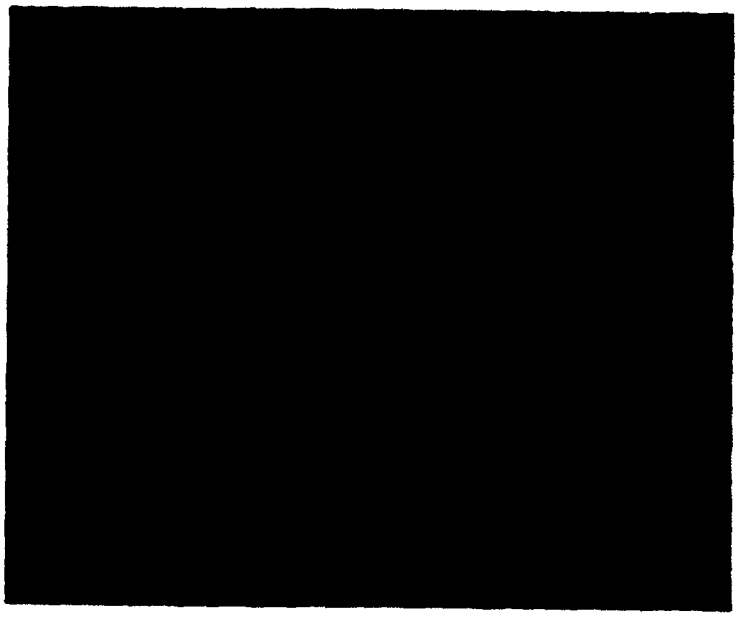

FIG. 1. Microstructure of Ti-26Al-10Nb-3V-1Mo exhibiting Widmanstätten $\alpha_2+\beta_t$ [S] and grain boundary α_2^{GB} [GB].

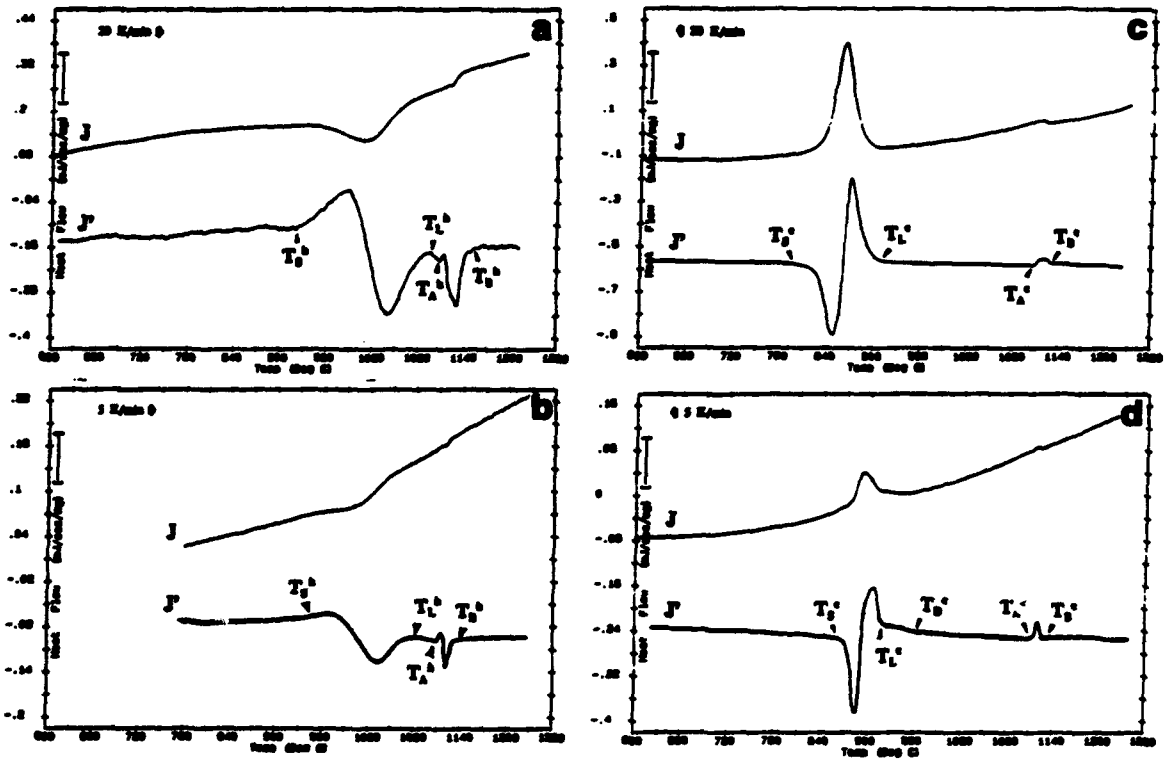

FIG 2. CDTA thermograms for Ti-26Al-10Nb-3V-1Mo on heating at (a) 20 and (b) 5K/min and on cooling at (c) 20 and (d) 5K/min.

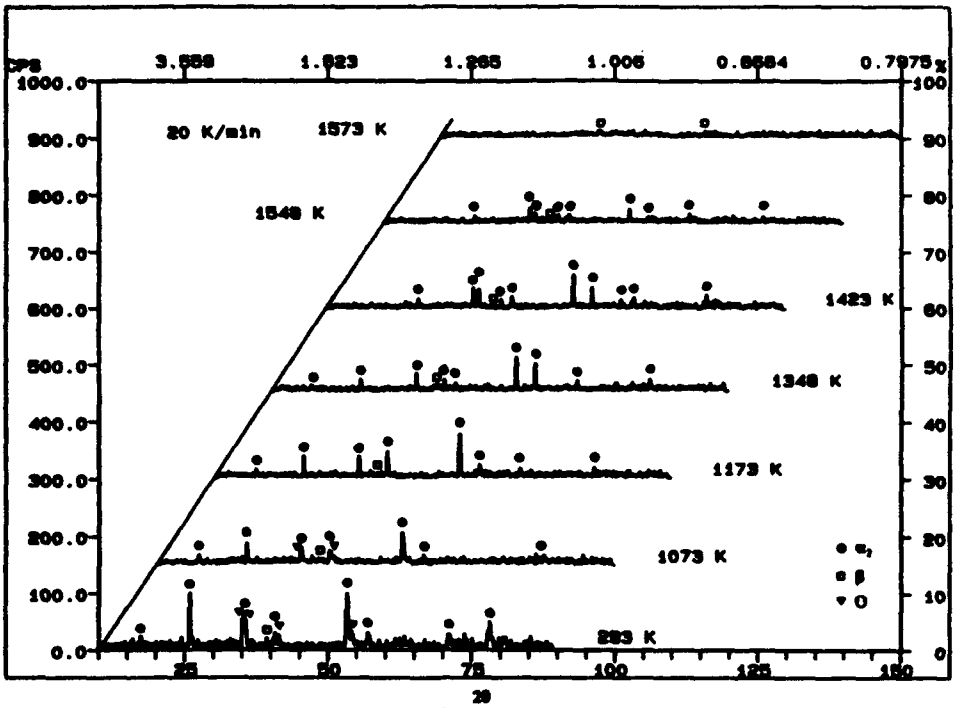

FIG. 3. Typical *in-situ* high temperature x-ray data at 20K/min heating rate for Ti-26Al-10Nb-3V-1Mo.

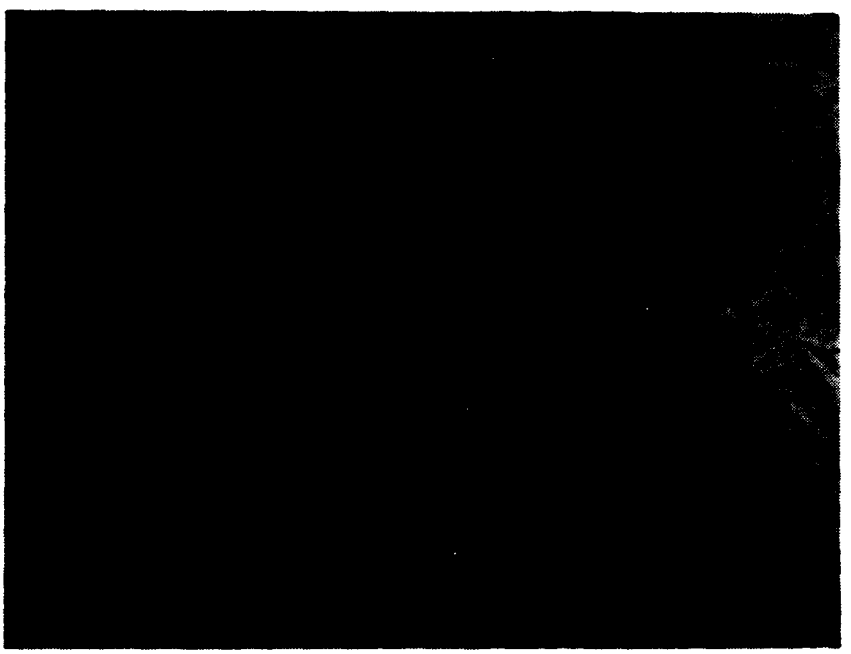

FIG. 4. Optical micrographs of (a) Ti-26Al-10Nb-3V-1Mo and (b) Ti-25Al-11Nb cross-sections after HTXRD.

Age Hardening Response of β_2 Ti-Al-V[1]

T. Ahmed, F. H. Hayes* and H. J. Rack
Materials Science and Engineering Program
Department of Mechanical Engineering
Clemson University, Clemson, SC 29634-0921, USA.
*Manchester Materials Science Center
University of Manchester and UMIST
Manchester, M1 7HS, UK.

Abstract:

The age hardening response of a β_2 Ti-Al-V alloy Ti-39.5Al-21.0V (at%) has been studied. Following arc melting, homogenization and solution treatment the alloy was aged at temperatures of 973 and 873 K for times between 3 and 96 hrs. Aging at 873 K resulted in a gradual increase in hardness while aging at 973 K resulted in a hardness peak after 3 hrs, a second hardness peak being observed when aged this alloy for longer times. X-ray and transmission electron microscopy have shown that the first increase in hardness was due to γ precipitation, longer time precipitation of α_2 resulting in further hardness increase. For each aging condition, the size of former γ plates was observed to vary over a wide range with γ plates being observed to grow randomly. Finally, the observation of plateau and a minima in the aging curves at 873 K and 973 K appears to be due to an increase in γ platelet length with increasing aging times this increase resulting in the loss of coherency at the γ/β interfaces.

Introduction:

Various precipitation phenomena have been reported during aging of commercially significant metastable β titanium alloys. For example these alloys may form athermal or "diffuse" ω upon quenching from their solution treatment temperature. Further thermal exposure at low temperatures <673 K can result in precipitation of either solute lean isothermal ω or β' with precipitation of α occurring at longer times [1]. Direct α precipitation in the β

1-Paper to be presented at 3rd International Conference on High-Temperature Intermetallics, to be held in San Diego, Ca, 16-19 May 1994. The paper will also be published in Materials Science and Engineering.

matrix has also been observed, the mode of precipitation depending upon selection of alloy constituents and the alloy composition [1,2]. In all cases the elevated temperature strength of these alloys is limited by rapid α phase coarsening.

Recently, it has been shown that increased strength and high temperature stability may be possible in metastable β alloys through precipitation of lath-like ordered α_2 [3,4]. In this study of Ti-11Al-23Nb (at%), peak hardness values of 470 VHN (Vicker's Hardness Number using 500 g load), 430 VHN and 360 VHN were observed after aging at 848, 898 and 948 K for 12, 6 and 3 hrs respectively. Notably decreased rates of α_2 coarsening, when compared to disordered α was observed with α_2 precipitates having a Burger's relationship, the broad faces of the α_2 laths being observed to have coherent or semi-coherent interfaces [4].

Prior investigation of phase equilibria in Ti-Al-V alloys within the temperature range of 873-1473 K [5] suggests an alternate approach for increasing the high temperature strength of metastable β titanium alloys , that is through precipitation of γ, the latter exhibiting a face-centered tetragonal, ordered $L1_0$ crystal structure. Within selected regions it was observed that the phase boundary between β_2 and $\beta_2+\gamma$ phase fields moves towards the V rich side with decrease in temperature, for example alloy compositions in the single phase β or β_2 phase field between temperatures of 1273-1473 K are two phase $\gamma+\beta/\beta_2$ at lower temperatures. This study has considered the age hardening response of these alloys recognizing the similarities between the crystal structures of γ ($L1_0$) and β_2 (B2) phases. Both γ and β_2 phases are ordered and should show better strength retention and thermal stability at high temperatures than the existing age hardened alloys. An alloy of composition Ti-39.5Al-21.0V (at%) was selected for this investigation.

Experimental:

The alloying constituents for the selected alloy, high purity Ti (O<240 wppm, N<26 wppm, C<9.9 wppm), V (99.8%) and Al (99.999%) were melted under a partial pressure of high purity argon utilizing a water cooled copper hearth, non-consumable tungsten electrode arc furnace, the melting being repeated six times to ensure homogeneity. Following this procedure the alloy was cleaned with alcohol, wrapped in Ta foil and encapsulated under a partial pressure of high purity argon in a quartz tube together with a small quantity of Ti sponge, the latter being intended to act as a getter for residual oxygen. The encapsulated alloy

was then homogenized/solution treated in a sealed furnace under an argon atmosphere at 1473 K for 24 hrs and water quenched. Interstitial analysis of as-cast and solution treated alloys indicated an oxygen content of 390 and 440 wppm, respectively.

Initially, calorimetric differential thermal analysis (CDTA) of the as-cast and solution treated samples was conducted at heating and cooling rates of 30, 20, 10 and 5 K/min to establish aging temperatures, observed transformation temperatures being determined by extrapolation to 0 K/min [6]. Based on these observations other samples were re-encapsulated following solution treatment and aged at 873 and 973 K for 3, 6, 12, 24, 48 and 96 hrs, the capsule being removed from the furnace following aging and air cooled to room temperature.

The as-cast, solution treated and aged alloys were also prepared for optical microscopy by mechanically polishing and etching with Kroll's Reagent. Additionally, diamond pyramid microhardness measurements were utilized to monitor hardness changes during aging. The hardness samples were mechanically polished prior to testing, the reported results being an average of ten (10) microhardness readings, an average error of ±5 VHN being observed in the determined hardness values.

Phase identification involved room temperature x-ray diffraction and transmission electron microscopy (TEM). The former was utilized Cu Kα radiation at 40 kV and 30 mA at a scan rate of 5° 2θ/min from 20° 2θ to 70° 2θ with rocking curve methods being employed to confirm the presence or absence of superlattice reflections. Following data collection, the x-ray spectra were analyzed and the peak indexed utilizing a least square method iterative computer program [7].

Samples for TEM were prepared by waffering 0.4 mm slices, grinding to 0.15 mm, cutting 3 mm discs from these slices and electropolishing in a solution of 10% H_2SO_4 and 90% methanol under the voltage and temperature conditions of 15 to 20 volts and -35°C. The observations were made utilizing a Hitachi 600 AB TEM operated at 100kV.

Results:

(i) Solution Treated Microstructure:

Optical microscopy of the as-cast alloy showed large equiaxed β grains with the presence of low volume fraction of fine grain boundary α_2 plates, Figure 1. Following solution treatment the alloy contained only a single phase β microstructure. TEM indicated, Figure 2, that this β was ordered, the presence of antiphase boundaries (APBs) implying that the alloy

composition was in the disordered region at the solution treatment temperature and ordered during quenching. Selected area diffraction patterns (SADPs) taken from this alloy indicate streaking and diffuse maxima. A SADP of ZA=[011]β_2, Figure 2(b), shows the presence of strong superlattice reflections, streaking along <112> directions and diffuse maxima at 1/2<112> positions. Higher magnification revealed mottling of the β_2 phase, Figure 2(c), this type of mottled structure along with diffuse maxima being consistent with prior TEM studies of β quenched Ti-Al-Nb [8,9], Ti-Al-Mo [10] and Ti-Al-V [5] alloys containing β_2 phase. The striations in the mottled structure along <110> directions observed by Strychor *et al.* [8,9] and Ahmed and Flower [5] were also seen in the present study. This strain contrast observed in Ti-Al-V and other alloy systems is actually due to the mottled structure, the origin of which has been discussed in detail by Strychor *et al.* [8,9]. Finally, diffuse "ω type" reflections were observed. However, the intensity of these reflections was weak and were not detectable under all expected zone axes. This suggests that the development of the "ω type" phase is not as dramatic in β quenched Ti-Al-V when compared with Ti-Al-Nb [8,9]. This observation is in accordance with athermal ω results obtained in binary Ti-V and Ti-Nb systems, a lower ω_s temperature for the binary Ti-V alloys being observed [1,11].

(ii) Thermal Analysis:

The temperatures of phase transformations were determined by thermal analysis of the alloy under as-cast and solution treated conditions. CDTA plots of both samples show an initial exothermic peak at lower temperatures, Figures 3(a) and 4(a). This exothermic peak, characteristic of precipitation, was followed by a series of endothermic peaks depicting dissolution of these precipitated phases. Further, analysis of the as-cast condition suggests that two overlapping endothermic transformation peaks were present on heating and three overlapping peaks on cooling, Figure 3(a) and (b). In contrast, the solution treated condition showed four overlapping endothermic transformation peaks on heating and three overlapping transformation peaks on cooling, Figures 4(a) and (b). The transformation temperatures for these reactions are summarized in Table 1. The results indicate that the onset and completion temperatures of transformation T1 on heating were not dependent upon the initial condition, whereas transformation T2 in as-cast condition split into two transformations (T2 and T3) following solution treatment. Finally, the transformation T4 is only present in the solution

treated condition. This difference in transformation behavior on heating may be related to the increased homogeneity of the solution treated condition when compared to the as-cast condition. Indeed on cooling, the transformations were not dependent upon initial condition, all three transformations have similar transformation onset and complete temperatures. This implies that the alloy in as-cast conditions was homogenized at temperature > 1439 K resulting in a similar number of transformations as compared to solution treated condition.

(iii) Hardness Response:

The age hardening response of Ti-39.5Al-21.0V is shown in Figure 5. Aging at 873 K resulted in an initial increase in hardness with increase in aging time, which is followed by a plateau in the hardness curve after at about 48 hrs and a maximum hardness value after aging for 96 hrs. In contrast, age hardening at 973 K shows an initial hardness maxima after aging for 3 hrs. Increasing the aging time results in a sharp decrease in hardness, a minima being observed after aging for 24 hrs, with finally, a second maxima being observed after aging for longer times.

(iv) Aged Microstructures:

Selected aged microstructures were characterized by room temperature x-ray diffraction and TEM. Room temperature x-ray analysis after aging at 873 K confirmed the alloy was two phase (β_2+γ) after aging times for 3, 6, 12, 24 and 48 hrs, Figure 6(a), while it was three phase (β_2+γ+α_2) for 96 hrs, Figure 6(b). Similar results were observed after aging at 973 K, Figure 7. These results suggest that this alloy lies within a β_2+γ+α_2 three phase region at the aging temperatures, the absence of α_2 in alloys aged for shorter times being due either to its small size or low volume fraction.

Figures 8(a) and (b) shows the microstructures of samples aged at 873 K for 24 and 96 hrs respectively. It was observed that the γ precipitates have a plate morphology, the size of these plates varying over a wide range in each aging condition. The γ plates also appeared to grow in a random manner with some plates being internally twined. Moreover, little coarsening of γ was observed between sample aged for 24 hrs and 96 hrs. Finally, the α_2 phase present in the latter sample was observed to again have plate morphology with length smaller than the γ plates.

The microstructures of sample aged at 973 K are shown in Figure 9. Again both γ and α_2 precipitates are observed to have plate morphologies with size varying over a wide range. In samples aged at 973 K for 3, 6 and 24 hrs, a lamellar microstructure was also observed in selected plates, Figure 9(b). This lamellar microstructure is consisted of fine γ and α_2 lamellae having a orientation relationship: $(0001)\alpha_2//\{111\}\gamma$, $[1\bar{1}20]\alpha_2//<110>\gamma$. The γ lamellae were observed to present as twins with twin plane being of $\{111\}\gamma$ type. The volume fraction of the plates containing this lamellar microstructure appeared to decrease with increase in aging time from 3 hrs to 24 hrs, while the thickness of remaining lamellar plates increased with increase in aging time. In addition, the volume fraction of the long γ plates was also observed to increase with increase in aging time with considerable number of these plates growing in one direction. A few γ plates in samples aged at both temperatures are also observed to follow Nishiyama-Wasserman type relationship with the β_2 matrix: $\{110\}\beta_2$ // $\{111\}\gamma$, $[001]\beta_2$ // [110], Figure 9(d) and (e).

Discussion:

(i) Phase Equilibria:

Thermal analysis of Ti-39.5Al-21.0V suggests that this alloy undergoes a series of transformation on heating/cooling. Identification of transformation sequence is aided by the reference to recent calculations of vertical sections of Ti-Al-V system, Figure 10, the reactions observed being

T1 T2 T3 T4

$\beta_2+\gamma+\alpha_2$----$>\beta_2+\gamma+\alpha$----$>\beta_2+\gamma$----$>\beta_2$----$>\beta$

where transformation T1 (first endothermic peak) involves disordering of α_2 to α, T2 corresponding to dissolution of α, T3 to dissolution of γ and the transformation T4 is due to the disordering of β_2 to β. On heating the as-cast condition results only two peaks, the first peak corresponds to T1 whereas the second peak involves overlapping T2 and T3 transformations. On cooling from single phase β region, the reverse transformation path is observed.

(ii) Hardness and Microstructure:

Comparison of hardness values obtained in the present study with those from an aged Ti-11Al-23Nb alloy based on a $\beta+\alpha_2$ microstructure [3,4] indicate that while higher absolute

hardness levels can be achieved in aged Ti-Al-V alloys based on a predominantly $\beta_2+\gamma$ microstructure, the former exhibit a more pronounced age hardening response. The difference in absolute hardness between the two alloys is presumably due to the increased hardness of the Ti-Al-V alloy in the solution treated condition, this increase being due to increased solid solution hardening and the ordering of the β matrix. In contrast the larger aging response of Ti-11Al-23Nb indicates that the α_2 phase has a more pronounced hardening effect when compared to the γ phase. This is in accordance with the observations made in Ti-Al-V alloys, that the γ phase acts as a softer phase as compared to the α_2 phase [12].

The aged microstructures in Ti-39.5Al-21.0V were observed to consist of γ and α_2 plates of size varying over a wide range. This diversity made it extremely difficult to establish a quantitative correlation between hardness and aged microstructures. Neverthless a qualitative description of the age hardening behavior of Ti-39.5Al-21.0V may however be given in Figure 11. This figure shows the separate effects of γ and α_2 precipitation on the hardness of a metastable β_2 alloy. Aging at 873 K resulted in an initial increase in hardness with precipitation of γ plates. Subsequent growth of the γ plates resulted in a plateau in hardness with continued aging time expected to lead to a gradual reduction in hardness. This reduction is not observed since precipitation of α_2 also takes place during aging, the hardening effect after longer times *i.e.* 96 hrs being related to more effective α_2 hardening. Similarly, aging at 973 K results in an initial rapid increase in hardness due to fine $\gamma+\alpha_2$ lamellae and γ plates. Increasing aging time at 973 K results in a decrease in hardness, again associated with increase in γ platelet length accompanied at this temperature by a decrease in $\gamma+\alpha_2$ lamellar volume fraction. Longer times again result in an increased precipitation of α_2 and a second increase in hardness. Ultimately, aging for 96 hrs results in a decrease in hardness presumably due to increase in α_2 size.

Additionally it was observed that on continued aging an increasing proportion of γ platelets obeyed Nishiyama-Wasserman orientation relationship with respect to the β matrix. Russell *et al.* [13] have shown that in the alloy systems having this relationship, the matching between {111}fcc and {110}bcc planes is very poor, good matching being restricted to small areas that only contain ≈8% of the interfacial atoms. Therefore, it is impossible to have maintain a coherent or semi-coherent interface between two large interfaces parallel to $\{111\}\gamma$ and $\{110\}\beta_2$ planes. This suggests that a loss of γ coherency may be expected with increasing aging time, this change in interfacial structure contributing to the decrease in hardness with

increase in volume fraction of long γ plates.

Conclusions:

The age hardening response of a β_2 Ti-Al-V alloy, Ti-39.5Al-21.0V (at%), has been studied. The aged alloy showed a plateau after aging at 873 K for 24 hrs whereas aging treatment at 973 K resulted in a peak hardness after 3 hrs. These were ascribed to γ precipitation. A second hardness peak was observed in the aging curves of this alloy after longer times at 973 K, this due to additional precipitation of α_2 as confirmed by x-ray diffraction and transmission electron microscopy. For each aging condition, the size of γ plates was observed to vary over a wide range, the γ plates being observed to grow randomly. Finally, the observation of plateau and a minima in the aging curves at 873 K and 973 K appears to be due to an increase in γ platelet length with increasing aging times this increase resulting in the loss of coherency at the γ/β_2 interfaces.

Acknowledgements:

The project was sponsored by Defence Advanced Research Project Agency (DARPA) under contract N00014-89-J-3166 supervised by Mr. W. Baker and monitored by Dr. G. Yoder of the Office of Naval Research. Authors also thank Ms. E. Benjamin for her help in preparation of optical and TEM samples.

References:

1 J. C. Williams, "Titanium Sci. and Tech.", Ed: R. I. Jaffee and H. M. Burte, Plenum Press, New York, 1973, p1433.

2 J. C. Williams, "Titanium and Titanium Alloys, Scientific and Technological Aspects", Ed: J. C. Williams and A. F. Belov, Plenum Press, New York, 1982, p1477.

3 L. S. Quattrochi, D. A. Koss and G. Scarr, Scripta Metall. Mater., 26 (1992) 267.

4 D. M. Goto, L. S. Quattrochi and D. A. Koss,"Beta Titanium Alloys in 1990's", Ed: D. Eylon, R. R. Boyer and D. A. Koss, TMS, Warrendale, PA, 1993, p321.

5 T. Ahmed and H. M. Flower, to be published in Mater. Sci. and Tech., March 1994.

6 Y. T. Zhu and J. H. Devletian, Metall. Trans., 22A (1991) 1993.

7 "Least Square Unit Cell Refinement" Program after Appleman and Evans (1973), implementation by R. G. Garvey, North Dakota State University, Fargo, ND, June, 1984.

8 R. Strychor and J. C. Williams, Proc. Intl. Conf. on Solid-Solid Phase Transformations, Ed: H. I. Aaronson, D. E. Laughlin, R. F. Sekerka and C. Wyman, TMS-AIME, Warrendale, PA, 1982, p249.

9 R. Strychor, J. C. Williams and W. A. Soffa, Metall. Trans.,19A (1988) 225.

10 S. Djanarthany, C. Servent and R. Penelle, J. Mater. Res., 6 (1991) 969.

11 B. S. Hickman, J. Mater. Sci., 4 (1969) 554.

12 T. Ahmed, PhD. Thesis, University of London (Imperial College), 1992.

13 K. C. Russell, M. G. Hall, K. R. Kinsman and H. I. Aaronson, Met. Trans., 5 (1974) 1503.

Table 1: Transformation temperatures in K determined by CDTA of as-cast and solution treated samples of alloy Ti-39.5Al-21.0V.

Heating				Cooling		
T1 O C	T2 O C	T3 O C	T4 O C	T1 O C	T2 O C	T3 O C
As-cast						
1252 1342	1342 1439			1346 1276	1276 1206	1206 1097
Solution Treated						
1254 1344	1344 1375	1375 1430	1430 1438	1366 1273	1273 1204	1204 1099

O:transformation onset, C:transformation complete

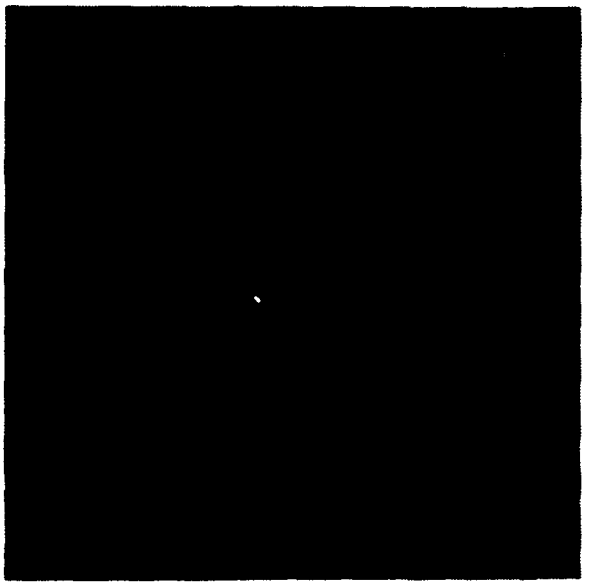

Figure 1: Optical micrograph showing as-cast microstructure of alloy Ti-39.5Al-21.0V.

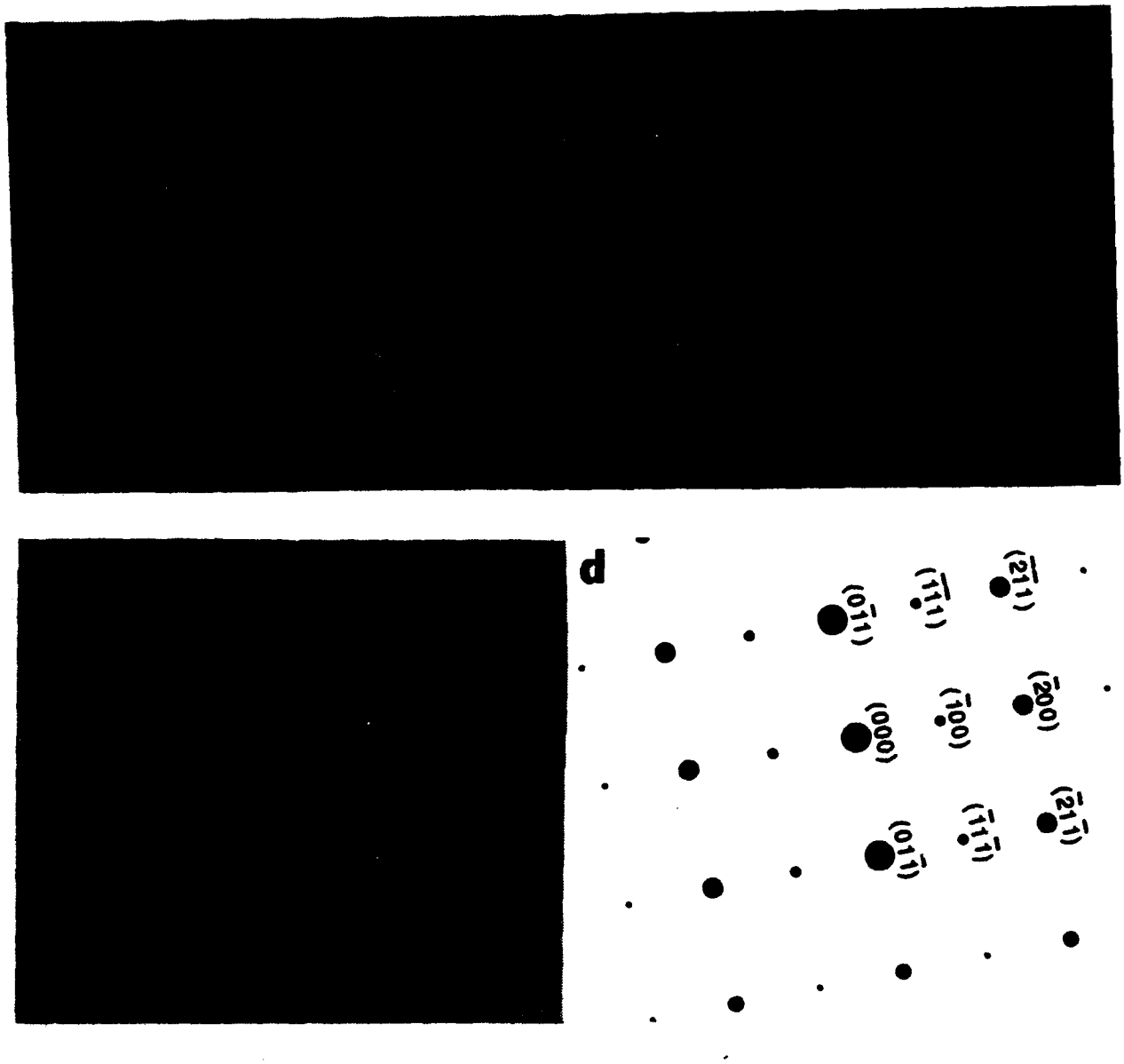

Figure 2: Solution treated microstructure (a) BF-TEM micrograph showing networks of APBs in β_2. (b) SADP taken from the solution treated sample, zone axis [011]β_2, (c) Higher magnification showing mottling, (d) Key to the SADP shown in (b).

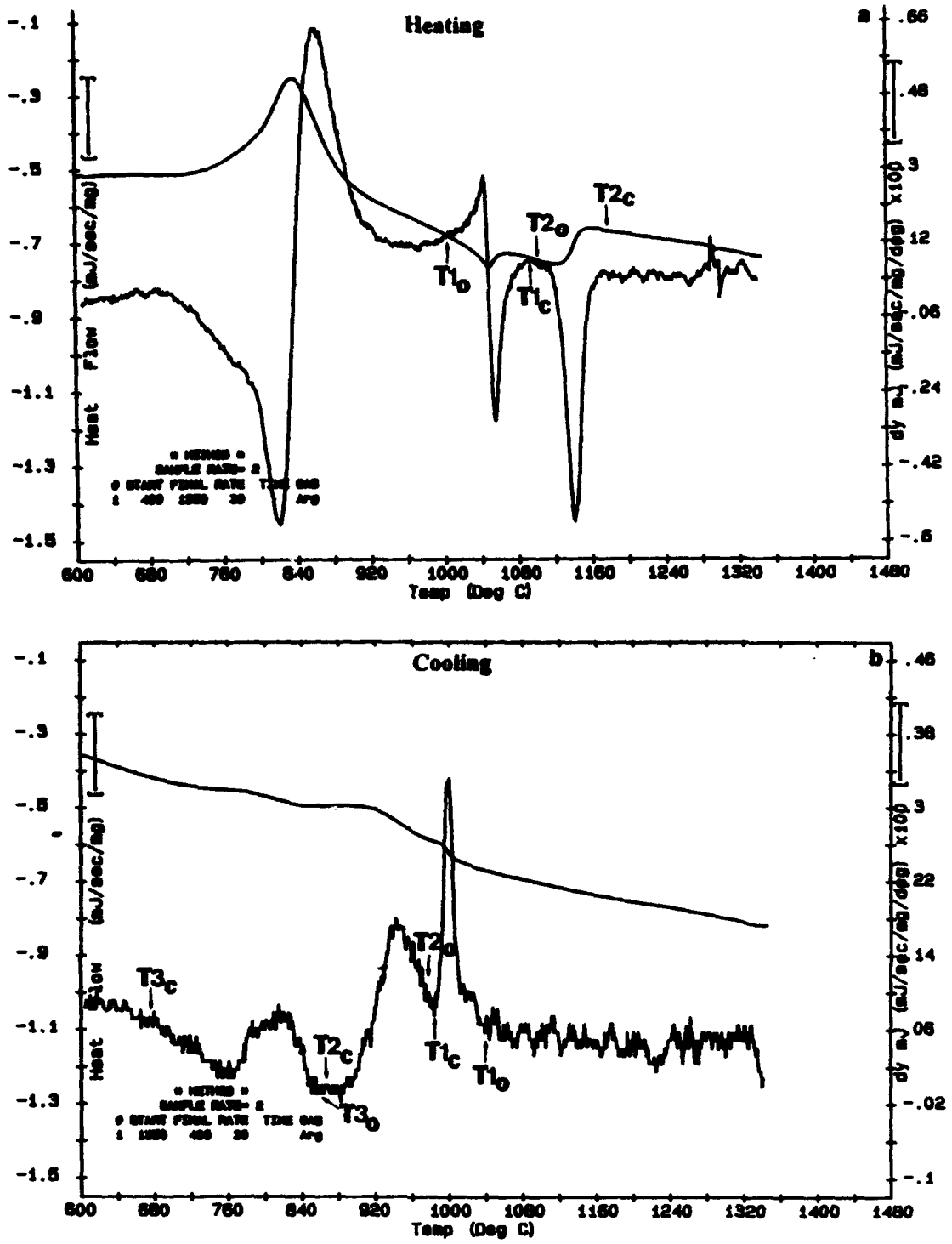

Figure 3: CDTA curves for as-cast sample of Ti-39.5Al-21.0V alloy at the rate of 30 K/min, (a) heating, (b) cooling.

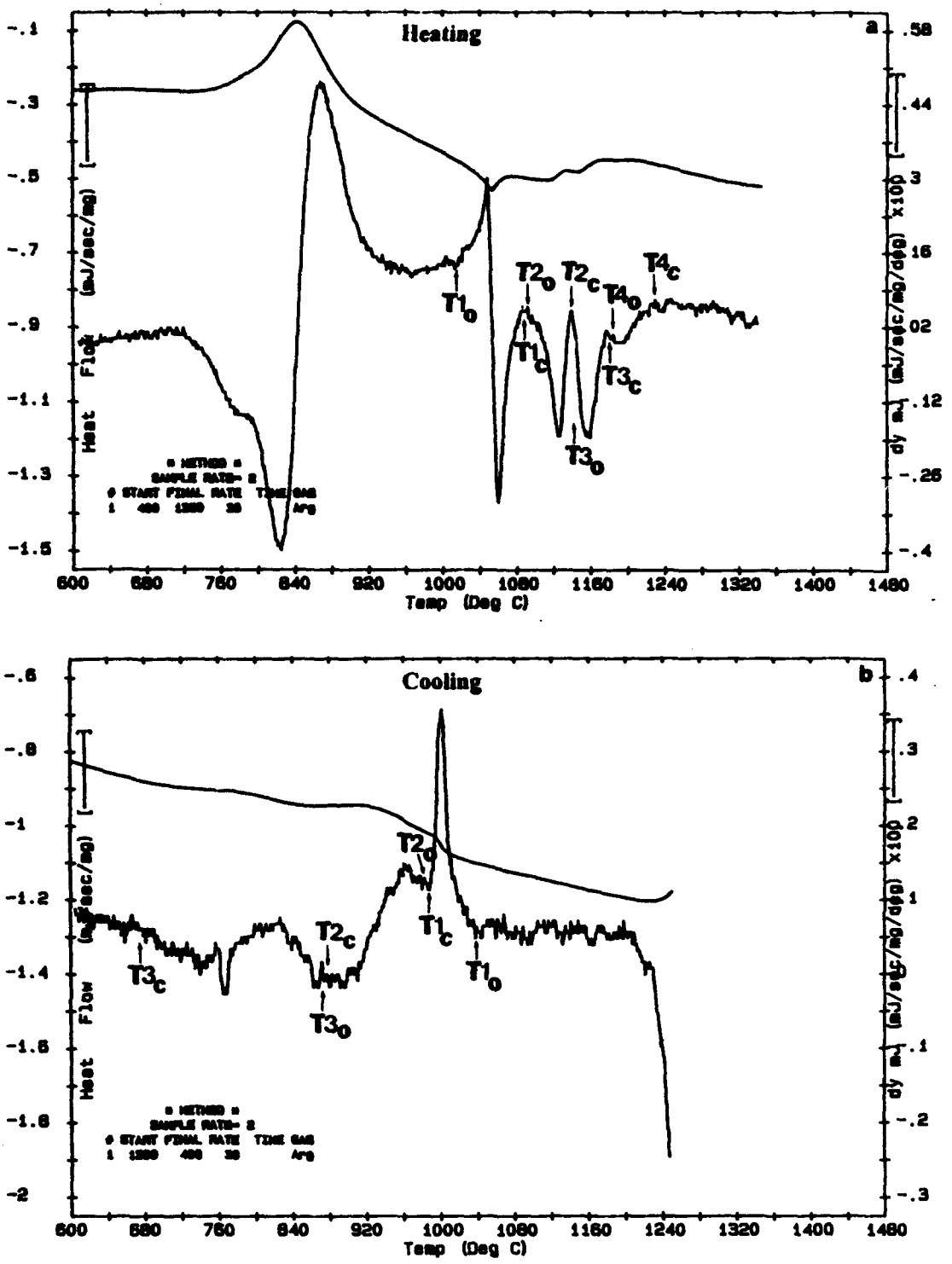

Figure 4: CDTA curves for solution treated sample of Ti-39.5Al-21.0V alloy at the rate of 30 K/min, (a) heating, (b) cooling.

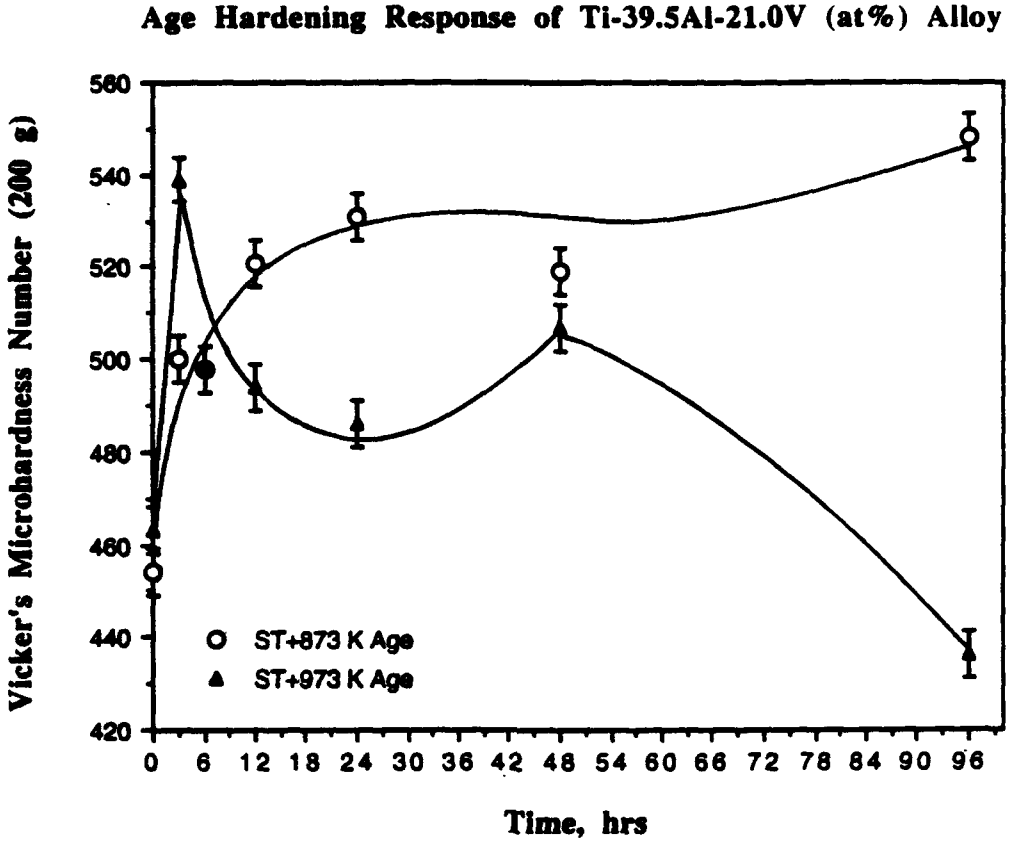

Figure 5: Age hardening response of Ti-39.5Al-21.0V in solution treated condition (1473 K-24hrs-water quench).

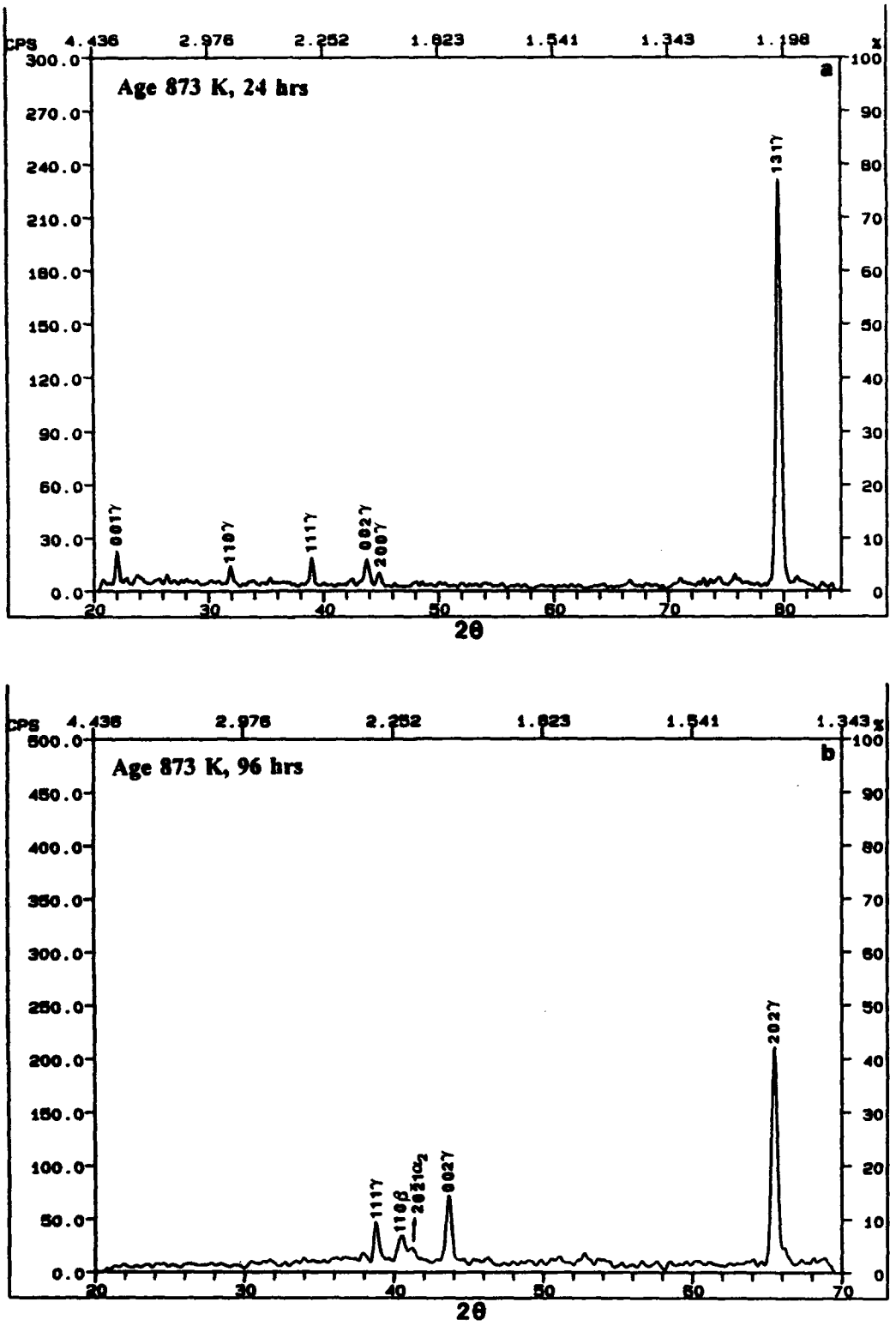

Figure 6: Room temperature x-ray diffraction pattern of sample aged at 873 K (a) for 24 hrs and (b) for 96 hrs.

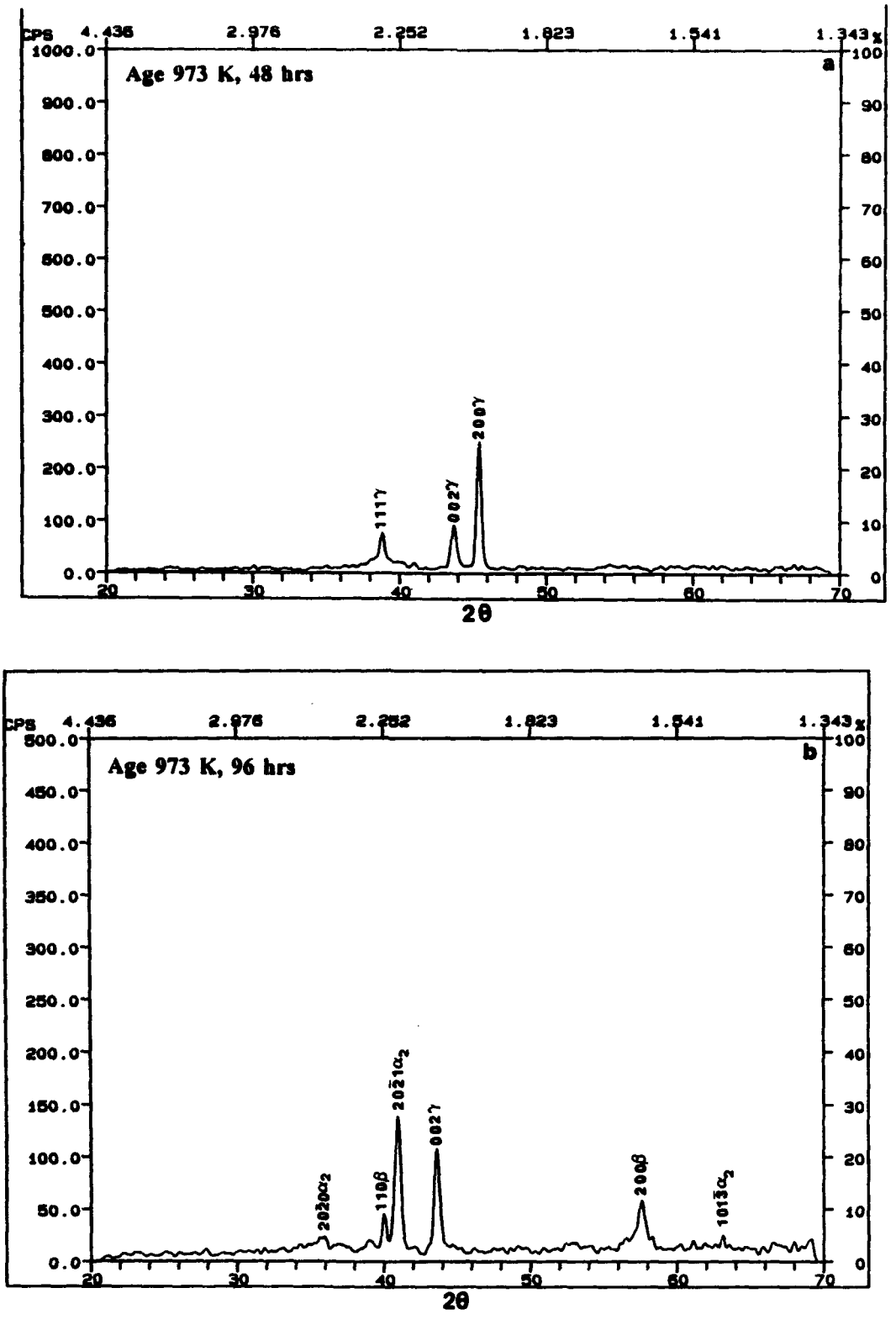

Figure 7: Room temperature x-ray diffraction pattern of sample aged at 973 K (a) for 48 hrs and (b) for 96 hrs.

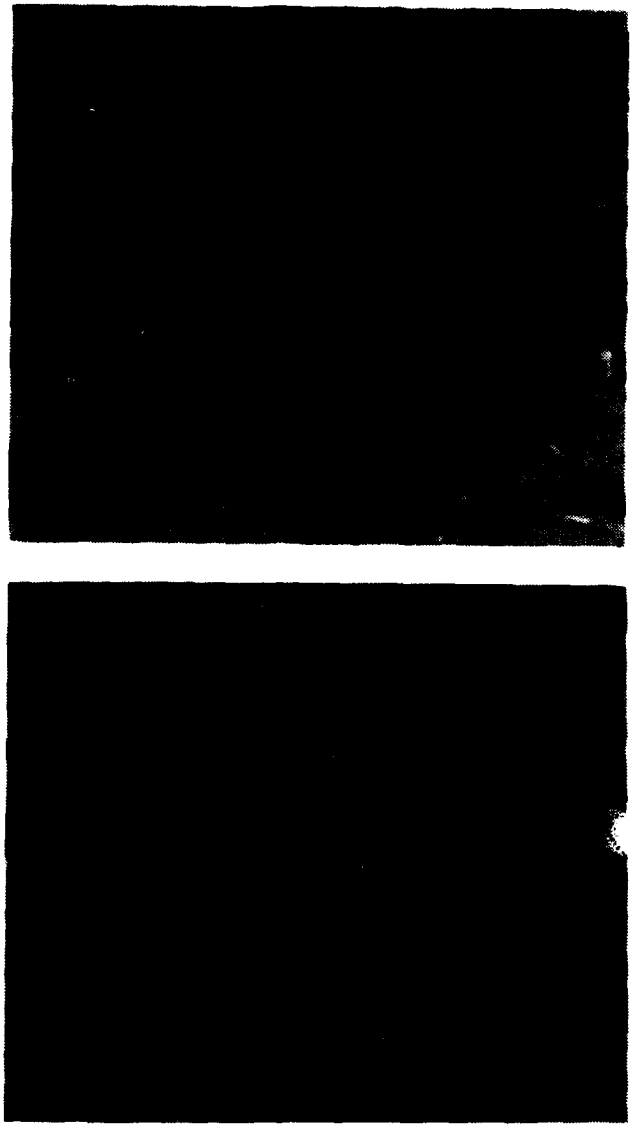

Figure 8: BF-TEM micrographs showing microstructures of samples aged at 873 K (a) for 24 hrs, (b) for 96 hrs. The internally twinned γ plates are also indicated on the figure.

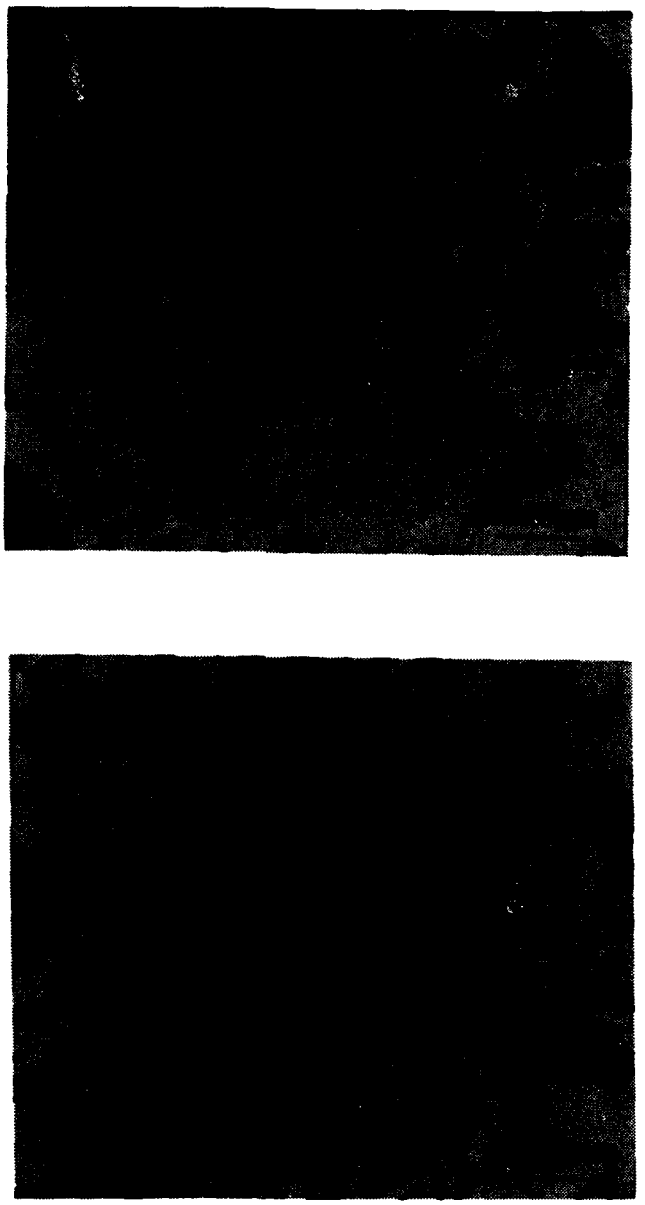

Figure 9: BF-TEM micrographs showing microstructures of samples aged at 973 K (a) for 3 hrs, (b) for 6 hrs, the arrow indicates $\gamma+\alpha_2$ lamellae and (c) for 96 hrs, (d) SADP of zone axis $[001]\beta_2$ with superimposed two variants of $[110]\gamma$ zones, (e) Key for SADP shown in (d).

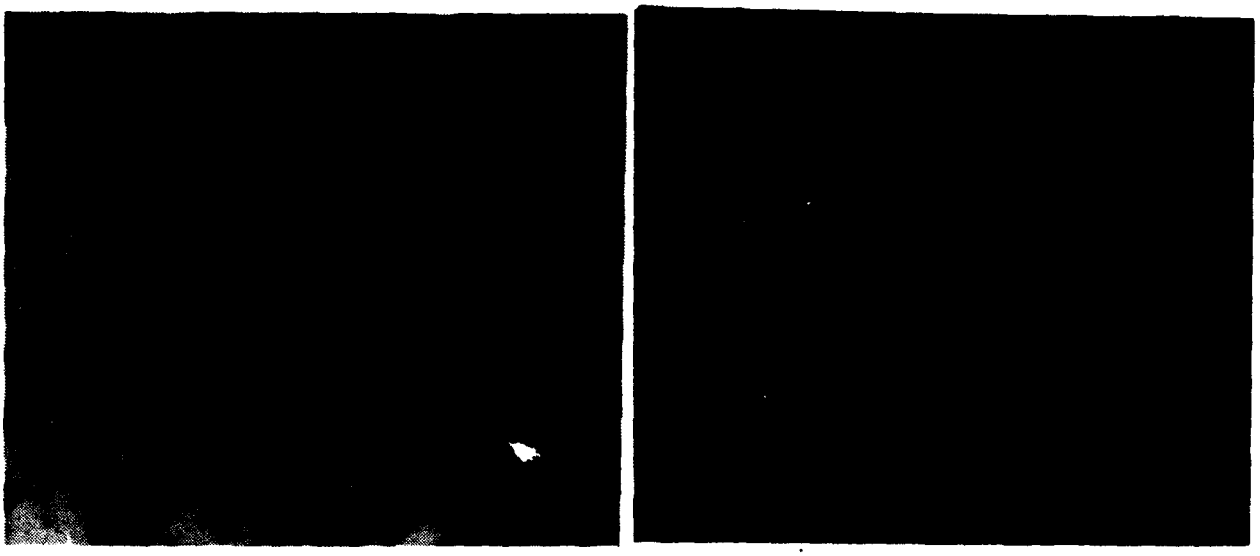

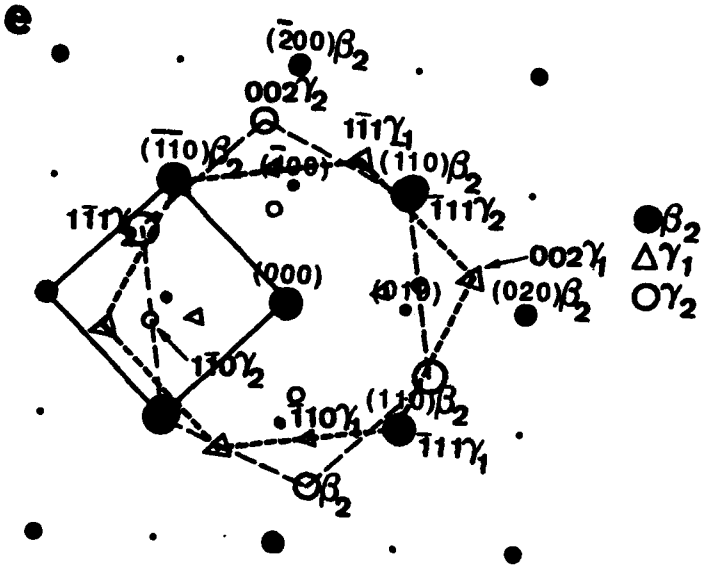

Figure 9 continued

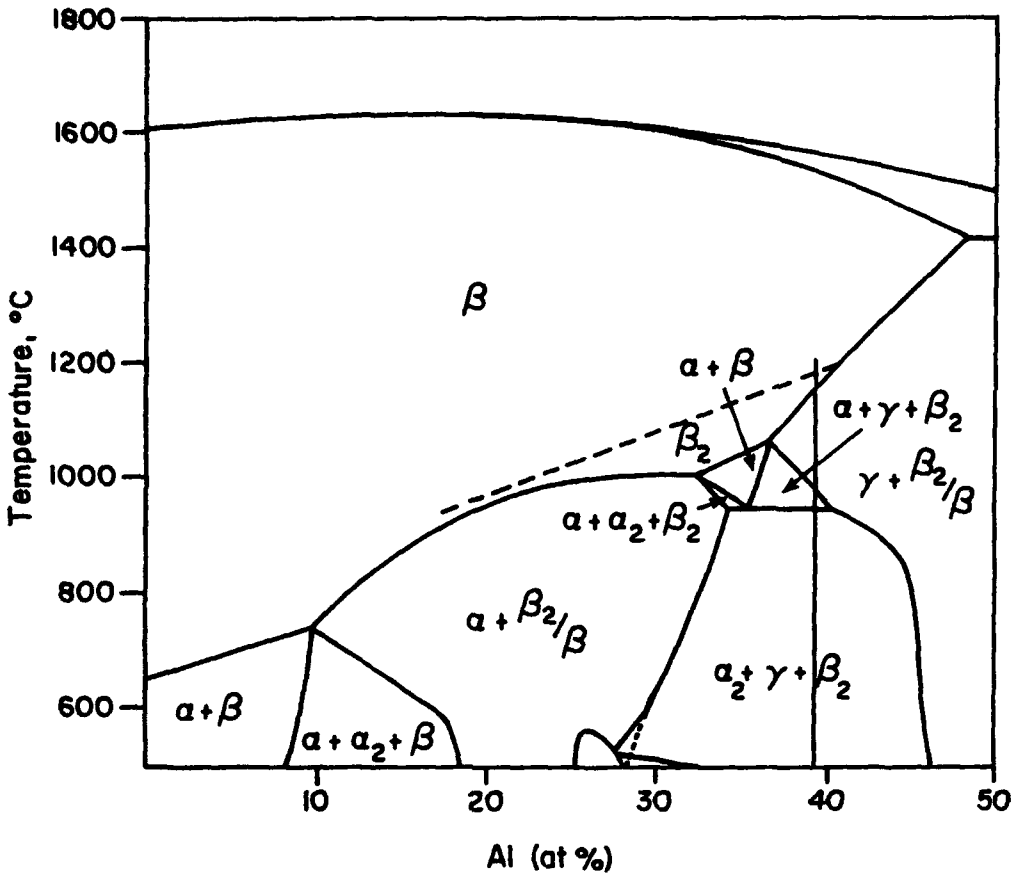

Figure 10: Calculated partial vertical section of Ti-Al-V system at 21 at% V.

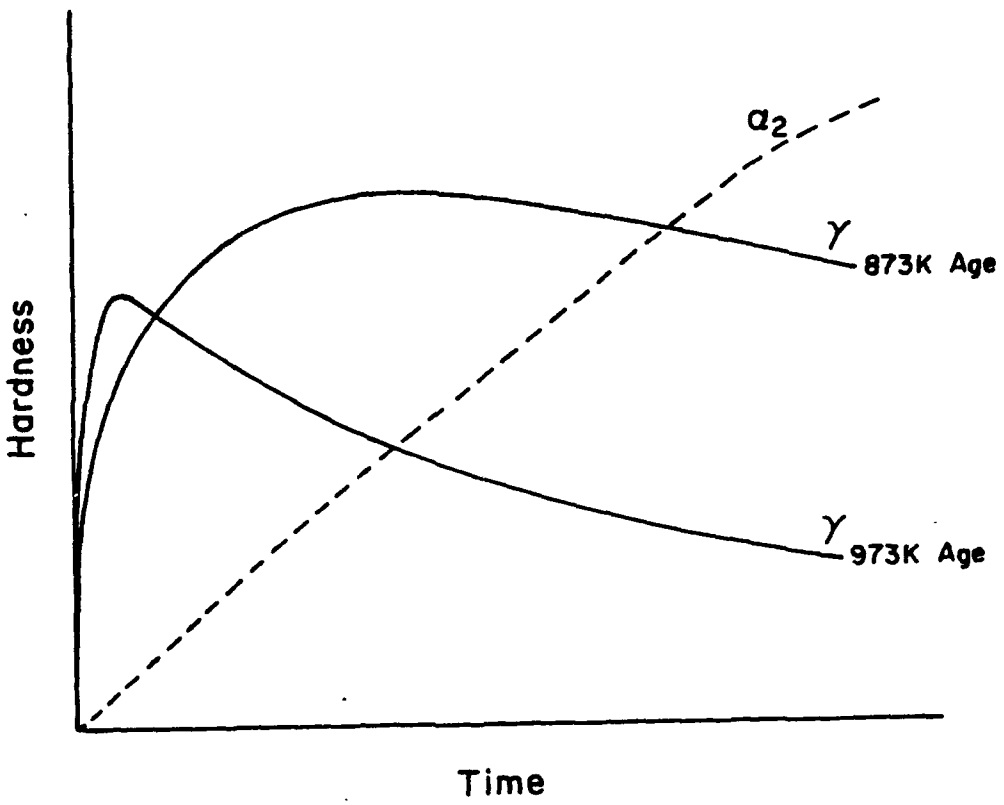

Figure 11: Schematic diagram showing qualitative description of the age hardening behavior of Ti-39.5Al-21.0V alloy. The effect of α_2 precipitation is shown separately.

PART 2

HIGH TEMPERATURE DEFORMATION PROCESSING

BLANK

Titanium '92, Science and Technolgy
F. H. Froes and I. Caplan, eds.,
The Minerals, Metals and Materials Soc., 1993

HIGH TEMPERATURE FLOW LOCALIZATION IN COARSE GRAIN β-PROCESSED TI-6Al-4V

A. Wang and H.J. Rack[1]
Materials Science and Engineering Program
Department of Mechanical Engineering, Clemson University,
Clemson, South Carolina 29634-0921

ABSTRACT

The elevated temperature deformation behavior of β-processed Ti-6Al-4V has been examined under compression conditions in the temperature range 800 to 965°C between strain rates of 10^{-4} and 10^{0} s^{-1}. Macroscopic flow localization in the form of unstable bulging was generally observed throughout the temperature and strain rate regimes investigated. It has been found that the severity of this flow localization can be quantified in terms of the flow localization parameter, α. Metallographic observations revealed that the observed macroscopic flow localization was initiated by microscopic localization associated with the breakup and spheroidization of α platelets situated either at the prior β grain boundaries or within Widmanstätten colonies.

[1] Senior Research Engineer, Howmedica Division, Pfizer Hospital Products Group, Inc., Rutherford, NJ and Professor of Mechanical Engineering and Metallurgy, Clemson University, Clemson, SC.

INTRODUCTION[167]

Various investigators[1-5] have reported that the incidence of flow localization, compressive plastic instability and unstable bulging in $\alpha+\beta$ titanium alloys is critically dependent upon alloy microstructure. Typically, transformed Widmanstätten $\alpha+\beta$ microstructures have been found, under prescribed conditions of strain rate and temperature, to promote flow localization. These microstructurally dependent flow localization phenomena appear to be related to deformation assisted breakup and spheroidization of the Widmanstätten structure in transformed β microstructures[6,7]. However a detailed interrelationship between macroscopic instability, i.e., flow localization, and this microscopic instabilty is still lacking. The present investigation has therefore examined the effects of temperature, strain rate and strain, on plastic flow and microstructural stability in a β-processed Ti-6Al-4V alloy. The objective was to reveal the microstructural origins of flow localization and to correlate the degree of flow localization with microstructural stability.

MATERIAL AND EXPERIMENTAL PROCEDURES

Coarse grained β processed Ti-6Al-4V (5.86 Al, 4.01 V, 0.28 Fe, 0.02 C, 0.04 N, 0.112 O) was investigated.[2] The initial microstructure consisted of a Widmanstätten colony structure and grain boundary α, Figure 1, the average prior β grain size and the mean Widmanstätten interlamellar spacing being 1.1 mm and 1.8 μm, respectively.

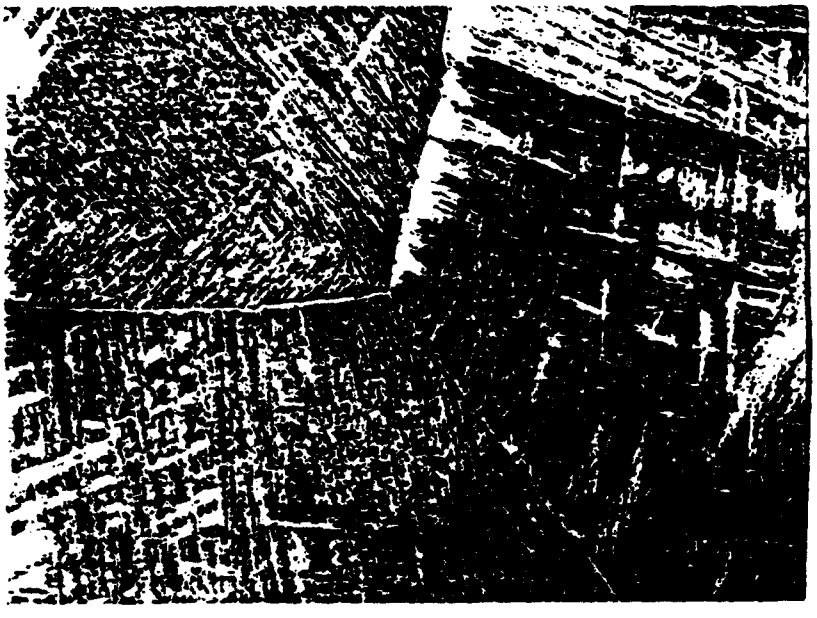

Figure 1. Microstructure of Ti-6Al-4V alloy.

Elevated temperature characterization of this alloy utilized both ring and cylindrical compression samples. The former were 25.4 mm OD, 12.7 mm ID and 8.458 mm height (6:3:2) and were intended for simultaneous determination of friction factors and flow stress behavior. Compression samples were 20.3 mm in diameter and 30.5 mm in height and served to further define the stress-strain behavior, frictional correction of the compressive stress-strain curves being accomplished utilizing procedures described previously[8].

Hot compression of the ring and cylindrical specimens was conducted within the temperature range 800 to 965°C, i.e., below the β transus, in a ultra-high purity argon atmosphere (O_2 content less than 10^{-7} ppm) at three different constant strain rates (10^{-4}, 10^{-2}, 10^{0} s^{-1}). The specimens were heated to temperature in 20 to 30 minutes and soaked at temperature for 5 minutes prior to testing, with boron nitride serving as the lubricant between the specimen and platens. All specimens were furnace cooled at approximately 20 °C/min to room temperature after deformation.

Optical microscopy was utilized to examine the specimens both prior to and after deformation, both the prior β grain size and the Widmanstätten lamellae spacing and aspect ratio being measured randomly.

---

[2] The β transus of this alloy, as determined by calorimetric differential thermal analysis, was 973°C.

RESULTS

Stress-Strain Curves

Representative true stress-true strain curves are shown in Figure 2. In each instance the true stress increases to a maximum and then decreases, the flow stress tending at higher strains towards a saturation value. The extent of this flow softening (Pct. Flow Softening = $\sigma_{max} - \sigma_{ss} / \sigma_{max}$) was a function of both strain rate and temperature, Table 1. For example, at 800°C the extent of softening increased with decreasing strain rate, while at 965°C it increased with increasing strain rate. Similarly, at a strain rate of 10^{-4} s^{-1} the extent of flow softening decreased with increasing temperature, while at 10^{0} s^{-1} the extent of softening increased with increasing temperature. Finally, at the highest temperature examined, i.e., 965°C, periodical oscillations in the true stress-true strain curves were observed, the amplitude of these oscillations tending to be a maximum at intermediate strain rates.

The effect of temperature on the maximum flow stress and the flow stress at a true strain of 0.30 are shown in Figure 3. Both measurements of the flow stress were sensitive to temperature at lower temperatures, this sensitivity decreasing as the β transus was approached. If a power law relationship between flow stress and strain rate, i.e., $\sigma = k\dot{\varepsilon}^{m}$, is assumed, the rate sensitivity parameter m can be obtained from a log-log plot of flow stress vs. strain rate. This determination, Table 2, suggests that the strain rate sensitivity of Widmanstätten Ti-6Al-4V is generally lower than that observed in equiaxed microstructures[9]. Moreover the strain rate sensitivity was a function of both temperature and strain rate, generally decreasing with increasing strain rate at each temperature investigated. Finally, the strain rate sensitivity appeared to have its maximum value at an intermediate temperature, 900°C.

Macroscopic Observations

Macroscopic observations indicated that the dimensional changes of the ring samples after compression were generally non-uniform. Both external and internal barreling was observed, the degree of barreling varying with temperature and strain rate. A measure of the specimen non-uniformity was obtained by normalizing the areal difference between the maximum and minimum areas following deformation, i.e.,

$$\lambda = \frac{A_{max} - A_{min}}{A_o} \qquad (1)$$

where λ is the degree of non-uniformity introduced during deformation of the ring samples, and A_{max}, A_{min} and A_o represent the maximum, minimum and original cross-sectional areas, respectively. Application of this procedure, Table 3, shows that, at 800° and 900°C the degree of non-uniformity decreased with increasing strain rate, while at 965°C the degree of non-uniformity was a maximum at intermediate strain rates.

Table 1. Percent Flow Softening

Temp.(°C)	Strain Rate(s^{-1})		
	10^{-4}	10^{-2}	10^{0}
800	40	42	20
900	27	37	26
965	7	23	32

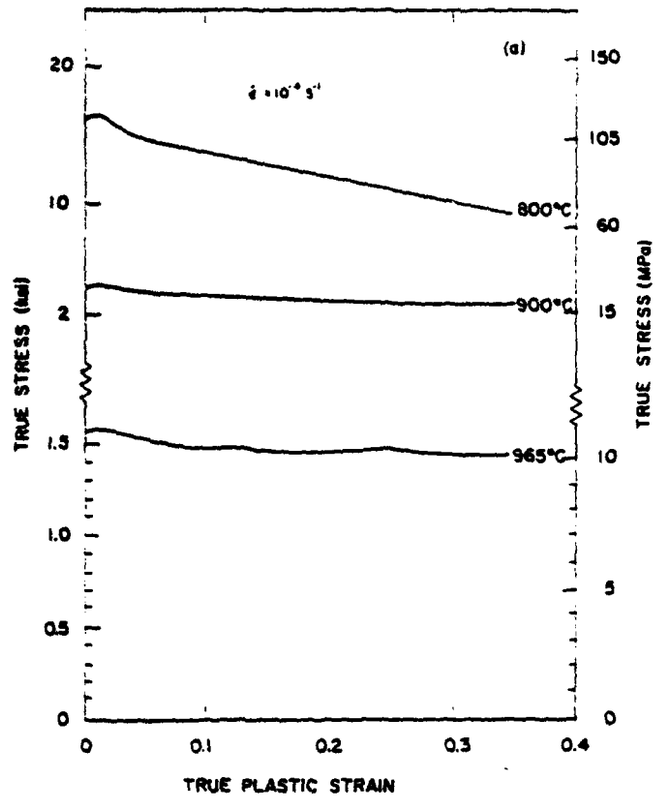

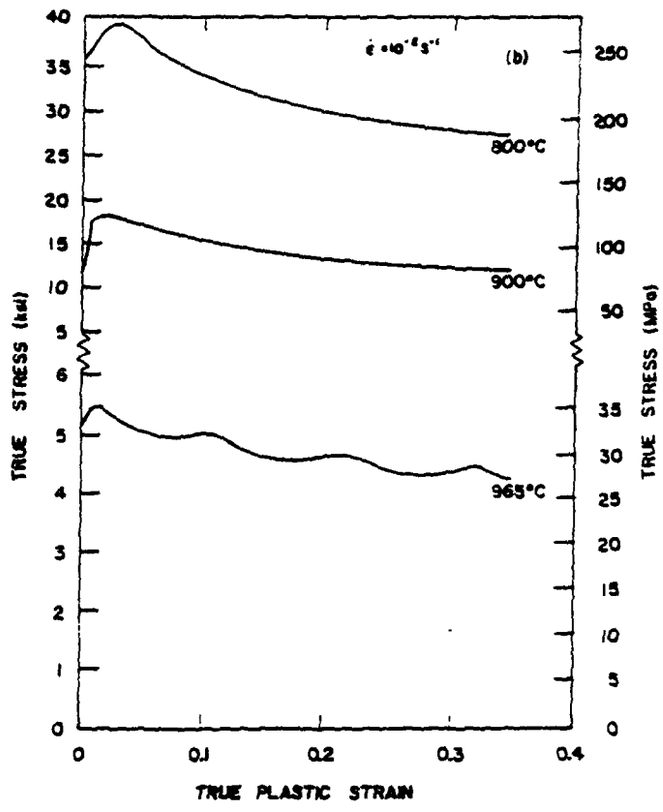

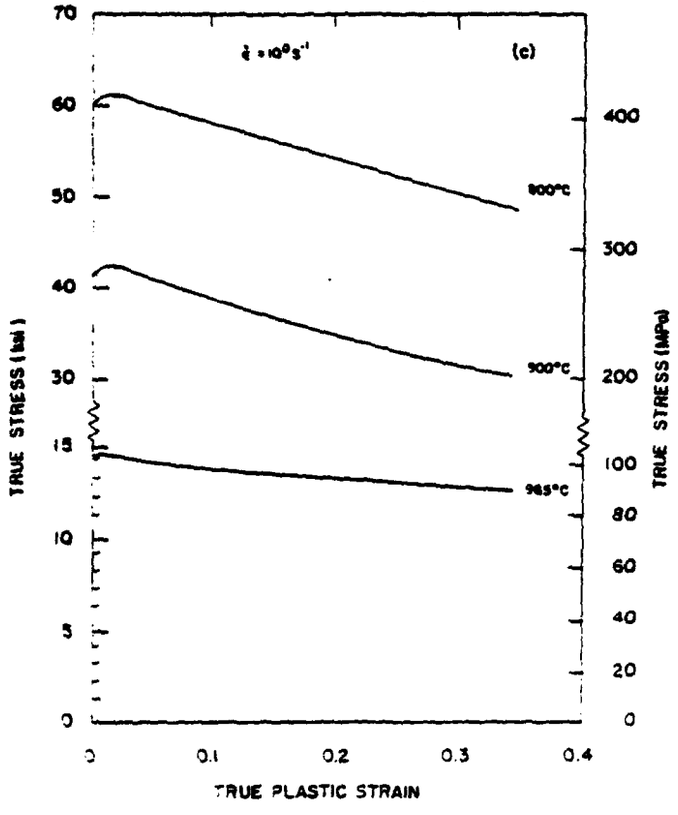

Figure 2. True stress-true strain curves at a strain rate of (a) 10^{-4} s^{-1}, (b) 10^{-2} s^{-1} and (c) 10^{0} s^{-1}

Table 2. Strain-Rate Sensitivity m

Temp. (°C)	Strain Rate(s^{-1})	m (σ_{max})	m (ϵ=0.3)
800	10^{-4}	0.22	0.25
	10^{-2}	0.15	0.25
	10^{0}	0.1	0.11
900	10^{-4}	0.28	0.35
	10^{-2}	0.27	0.26
	10^{0}	0.04	0.11
965	10^{-4}	0.26	0.22
	10^{-2}	0.3	0.26
	10^{0}	0.05	0.2

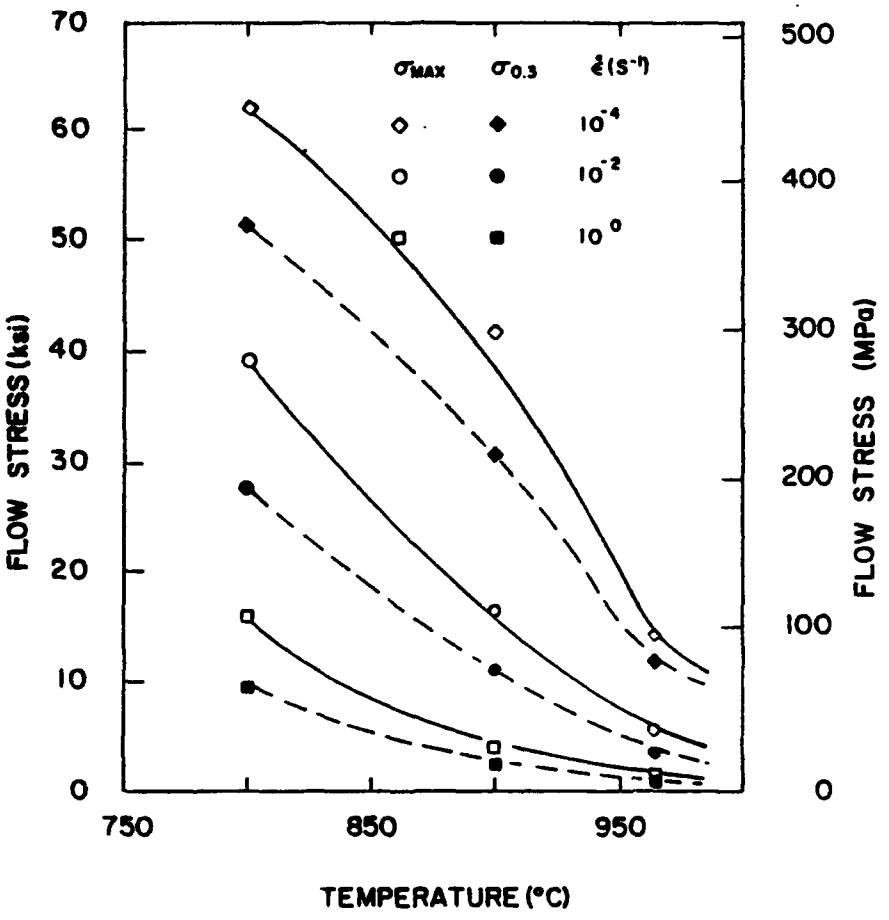

Figure 3. Flow stress as a function of temperature and strain rate.

Microstructural Observations

Quantitative comparison of the β grain size prior to deformation with that following straining indicated that variations in strain rate had little effect on the grain size, while increasing the deformation temperature from 800°C to 965°C at a constant strain resulted in an approximate 25 pct. reduction in the β grain size.

Microstructural observations within regions where bulging and non-uniform deformation occurred revealed various degrees of grain boundary and lamellar α spheroidization, Figure 4. At 800°C and low strain rates(10^{-4} and 10^{-2} s^{-1}) breakup and spheroidization occurred preferentially within the grain boundary α region, particularly at grain boundary triple points, Figure 4a. Increasing the deformation temperature to 900°C promoted spheroidization of both grain boundary and matrix lamellar α, Figure 4b. The latter occurred initially through unstable kinking of the α lamellae within those colonies which were favorably oriented in the direction of the maximum shear stress, i.e., at approximately 45° to the compression axis. When the deformation temperature was increased to 965°C, spheroidization occurred within all colonies, although its extent varied substantially from grain to grain and from colony to colony, Figure 4c.

Finally, quantitative measurements demonstrated that decreasing strain rate and increasing deformation temperature resulted in an increase in the lamellar spacing and a decrease in the lamellar aspect ratio, Figure 5.

DISCUSSION

Macroscopic Aspects of Flow Localization

Jonas et al.[10] and Dadras and Thomas[11] have suggested that the onset of compressive plastic instability will occur when:

$$\alpha = -\frac{\delta \ln \dot{\epsilon}}{\delta \epsilon} = \frac{\gamma' - 1}{m} > 0 \tag{2}$$

$$\gamma' > 1 \tag{3}$$

where α is the rate of strain rate localization subsequent to the onset of instability, ϵ the true plastic strain, $\dot{\epsilon}$ the strain rate, m the strain-rate sensitivity and γ' is related to the strain-strain-rate parameter, γ,

$$\gamma' = \gamma + \left(\frac{\eta \phi}{\rho c}\right) = \left(\frac{\partial \ln \sigma}{\partial \epsilon}\right)_{\dot{\epsilon},T} + \left(\frac{\eta \phi}{\rho c}\right) \tag{4}$$

where η is the efficiency of deformation heating, ρ, the density, c, the specific heat and $\phi = \partial\sigma/\partial T$.

Numerical evaluation of γ', for example, at 900°C/10^{-2} s^{-1}, indicated that γ' reached a maximum at an early stage of plastic deformation and decreased with increasing strain. Accordingly, under these conditions, deformation is predicted to be non-uniform at low strains, becoming increasingly uniform with increasing strain. This prediction was examined and verified by straining a series of ring compression samples, the degree of specimen non-uniformity, λ, exhibiting the predicted strain dependence, Figure 6. Finally, excellent agreement was achieved between the prediction of flow localization, i.e., $\alpha > 0$, and observed non-uniformity, Table 3.

Microscopic Aspects of Flow Localization

A prominent characteristic of the hot-deformation behavior of the Ti-6Al-4V alloy under the compression conditions examined was extensive flow localization at relatively slow strain rates. This phenomenon may ascribed to either adiabatic heating or to microstructural effects. Flow localization associated with adiabatic heating is expected, at a given deformation temperature, to occur more readily at higher strain rates. In contrast, the results indicate that flow localization was generally more severe at lower strain rates, Table 3.

Furthermore metallographic observations revealed that the onset of flow localization was always associated with breakup and subsequent spheroidization of the α phase either at grain boundaries or within those Widmanstätten colonies having a preferred orientation for shear deformation. Enhanced spheroidization of lamellar α during deformation in Ti-6Al-4V is expected to involve: (i) breakup of the α platelets by deformation, and (ii) coalescence of the broken lamellae by thermal diffusion. Experimental verification of this may be provided by comparing samples having undergone identical thermal histories, with and without simultaneous deformation.

Figure 4. Optical micrographs of sample after $\epsilon = 0.3$ at (a) 800°C/10^{-4} s^{-1}, (b) 900°C/10^{-2} s^{-1}, and (c) 965°C/$10^{-4}s^{-1}$.

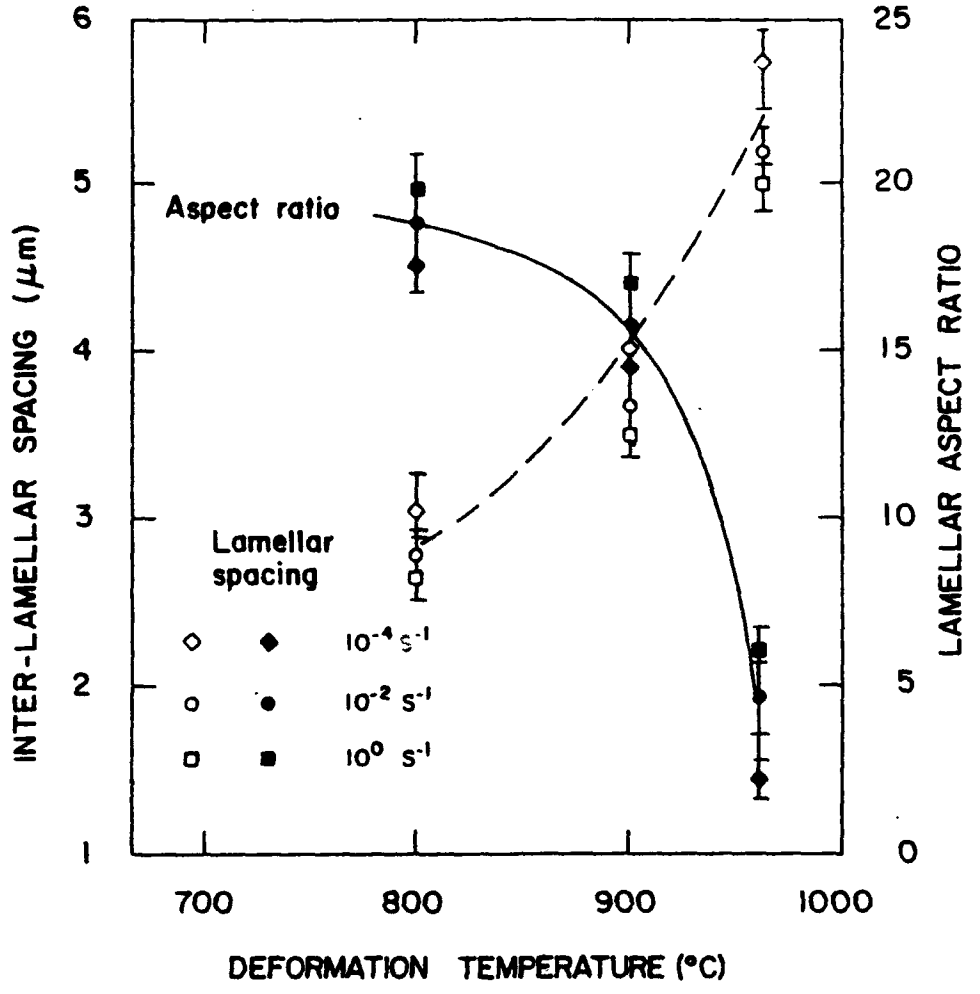

Figure 5. Effect of temperature and strain rate on the α lamellar spacing and aspect ratio.

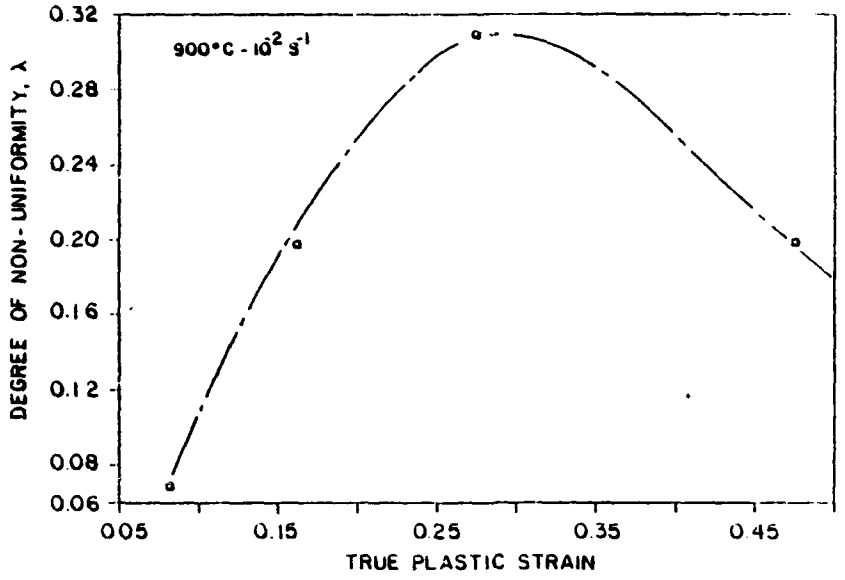

Figure 6. The degree of non-uniformity as a function of strain at 900 °C/10^{-2} s^{-1}.

In contrast to the microstructures of deformed specimens which showed some degree of breakup and spheroidization of both grain boundary and lamellar α at all temperatures, the thermally treated specimens exhibited only a limited degree of spheroidization below 965°C, Figure 7. Therefore thermal activation by itself was not sufficient to cause spheroidization of the α phase at lower temperatures. However, at higher temperatures, e.g., 965°C, partial spheroidization of α lamellae can occur prior to deformation, provided that the holding time is sufficiently long, e.g., 60 minutes. For the latter case, since the actual microstructure of the specimens had already been partially spheroidized prior to deformation, flow localization is expected to be, and indeed was, significantly reduced when compared with specimens deformed at lower temperatures and/or rates, see Table 3.

Table 3. Flow Uniformity and Localization

Temp./Rate	λ	m	γ'	α	Localization
800°C-10^{-4}	0.34	0.22	5.0	18.2	yes
800°C-10^{-2}	0.22	0.15	2.65	11	yes
800°C-10^{0}	0.05	0.1	0.98	-0.2	no
900°C-10^{-4}	0.33	0.28	4.50	12.5	yes
900°C-10^{-2}	0.31	0.27	4.40	15.5	yes
900°C-10^{0}	0.16	0.04	2.25	31.25	yes
965°C-10^{-4}	0.23	0.26	4.25	12.5	yes
965°C-10^{-2}	0.30	0.3	5.81	16.0	yes
965°C-10^{0}	0.20	0.05	1.10	2.0	yes

Observations that breakup and spheroidization of the α phase initiated within the grain boundary α region suggests that either this region was weaker than its surroundings, and/or that at least one of the grains was oriented with its slip plane favorably oriented parallel to the maximum shear stress direction, i.e., 45° to the compression axis. A previous study[12] on the tensile ductility loss of β processed Ti-6Al-4V have indicated that flow localization during hot tensile deformation also occurred more readily at the prior β grain boundary region, these authors suggesting that this was due to the presence of a weaker β zone along the grain boundary α. Thus, the existence of this weaker zone along the grain boundary α phase was postulated to result in flow localization within this region, when for example, the slip plane within the weaker β region coincides with that of the grain boundary α, shear bands forming within the grain boundary α. Indeed, the latter has been identified by Weiss, et al., [6,7] to be precusors for the breakup of the α platelets during high temperature, high strain deformation.

CONCLUSIONS

The hot deformation characteristics of β-processed Ti-6Al-4V has been examined under compression conditions in the temperature range 800 to 965°C between strain rates of 10^{0} to 10^{-4} s^{-1} utilizing both ring and conventional cylindrical samples.

Flow localization in the form of unstable bulging was observed under most conditions. The severity of macroscopic flow localization may be quantified in terms of the flow localization parameter α.

Metallographic observations revealed that macroscopic flow localization was initiated by microscopic breakup and spheroidization of α platelets situated either at the prior β grain boundaries or within Widmanstätten colonies.

ACKNOWLEDGEMENTS

The authors would like to acknowledge receipt of the experimental material from RMI, Inc., Niles, Ohio. This effort was funded by DARPA thru ONR Contract No.0014-89-J-3166 supervised by Mr. W. Barker and monitored by Dr. G. Yoder. The assistance of M. Long in completing this investigation is gratefully acknowledged.

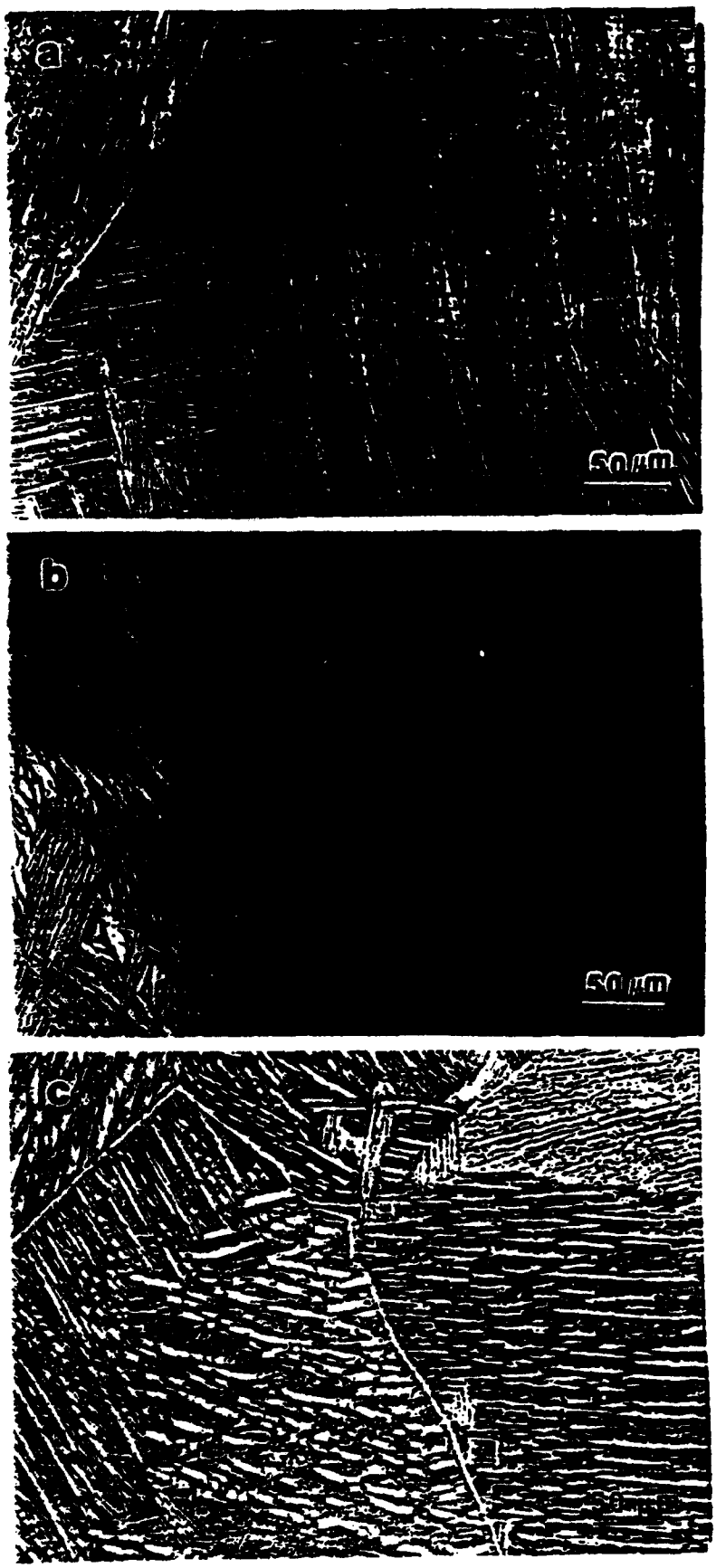

Figure 7. Optical micrographs of samples exposed for 1 hr at (a) 800°C, (b) 900°C and (c) 965°C.

REFERENCES

1. S.L. Semiatin, G.D. Lahoti and T. Altan, Process Modeling: Fundamentals and Applications to Metals, T. Altan, H. Burte, H. Gegel and A. Male, eds., ASM, Metals Park, OH, 1980, p. 387.
2. S.L. Semiatin and G.D. Lahoti,"Deformation and Unstable Flow in Hot Forging of Ti-6Al-2Sn-4Zr-2Mo-0.1Si", Metall. Trans., 12A (1981) 1705-1717.
3. P. Dadras and J. Thomas, Jr.,"Characterization and Modeling for Forging Deformation of Ti-6Al-2Sn-4Zr-2Mo-0.1Si", Metall. Trans., 12A (1981) 1867-1876.
4. S. L. Semiatin, J. F. Thomas, Jr., amnd P.Dadras, "Processing-Microstructure Relationships for Ti-6Al-2Sn-4Zr-2Mo-0.1Si", Metall. Trans., 14A (1983) 1867-2374.
5. S. L. Semiatin and J. J. Jonas, Formability and Workability of Metals, ASM, Metals Park, Ohio, 1984, p. 55.
6. I. Weiss, F.H. Froes, D. Eylon and G.E. Welsch, "Modification of Alpha Morpholgy in Ti-6Al-4V by Thermomechanical Processing", Metall. Trans., 17A (1986) 1935-1947.
7. G. Welsch, I. Weiss, D. Eylon and F.H. Froes, "Shear Deformation and Breakup of Lamellar Morpholgy in Ti-6Al-2Sn-4Zr-2Mo Alloy", Sixth World Conf. on Titanium, Part III, P. Lacombe, R. Tricot, G. Berangen, eds., Societe Francais de Metallurgie, Les Ulis Cedex, France, June 6-9, 1988, p. 1289.
8. J. R. Douglas and T. Altan, "Flow Stress Determination for Metals at Forging Rates and Temperatures", Trans. ASME, 97B (1974) 66-76.
9. V. Seetharaman, L.Boothe and C. M. Lombard, "Compressice Defromation Behavior of a Ti-6Al-4V Alloy at High Temperatures and Strain Rates", Microstructure/Property Relationships in Titanium Aluminides and Alloys, Y-W. Kim and R. R. Boyer, eds., The Minerals, Metals and Materials Society, Warrendale, PA, 1991, p.605.
10. J.J. Jonas, R.A. Holt and G.E. Coleman, "Plastic Instability in Tension and Compression", Acta Met., 24 (1976) 911-918.
11. P. Dadras and J.F. Thomas, Jr., "Compressive Plastic Instability and Flow Localization in Ti-6242", Res Mechanica Letters, 1 (1981) 97-103.
12. H. Fujii and H.G. Suzuki, "A Model for Ductility Loss at Intermediate Temperatures in an Alpha+Beta Titanium Alloy", Scripta Metall., 24 (1990) 1843-1846.

THERMO-MECHANICAL STABILITY OF FORGED Ti-25Al-11Nb (at.%)

M. Long and H. J. Rack
Materials Science and Engineering Program
Department of Mechanical Engineering
Clemson University
Clemson, SC 29634-0921, USA.

Published in
Materials Science and Engineering
A170 (1993) 215-226

Abstract

Dynamic material modeling (DMM) has been applied to the analysis of the mechanical behavior of a {Widmanstätten + primary α_2 + β} Ti-25Al-11Nb alloy to establish the flow stress-strain rate-temperature-strain criteria for stable flow.

Unstable and stable flow regimes predicted by DMM were correlated to microstructural observations. Unstable flow zones were related to transformation of orthorhombic O $\rightarrow$ α_2, kinking of the α_2 lamellae, shear band formation and coarsening of the dynamically recrystallized grain structure; stable flow regimes were shown to be associated with dissolution of the Widmanstätten α_2, coarsening of primary α_2, and dynamic spheroidization of the lamellar α_2 microconstituents.

Introduction

Increased attention has recently focused on substitution of low-density titanium aluminides for nickel-base superalloys at high temperatures. While various aluminide systems have been examined, Ti_3Al-Nb ($\alpha_2+\beta$)-base alloys, which exhibit intermediate properties between conventional $\alpha/\alpha+\beta$ Ti-alloys and γ-TiAl intermetallics[1], appear to offer the highest potential for near-term application. Moreover, several studies have shown that an excellent balance between low temperature ductility/fracture toughness and high temperature performance can be achieved in these materials through control of grain size, α_2/β volume fraction, α_2 phase morphology and β phase distribution[2].

Attainment of these properties will require careful selection of manufacturing process control parameters. For example, understanding and developing a control strategy which considers the relationship between initial microstructure, processing conditions and final microstructure will be necessary. Previous attempts at process control have been based on either a knowledge of atomic processes that define selected deformation mechanisms[3], or mechanistic models for defect nucleation[4]. Unfortunately their applicability is limited to simple engineering materials, e.g., stable single phase alloys. Recently a newer method has been formulated that removes these constraints[5-7]. This method, Dynamic Material Modeling (DMM), combines a continuum mechanics based stability analysis with the principles of irreversible thermodynamics to define "stable" regions of strain, strain rate and temperature.

Dynamic material modeling assumes that the instantaneous power P absorbed by the workpiece during plastic flow is dissipated by partitioning into a dissipator content G, which is the work dissipated by plastic work, and is related to continuum effects, and a dissipator co-content J, which is the work related to the metallurgical mechanisms which occur dynamically to dissipate power, and is therefore related to microstructural changes. The power P can then be written as:

$$P = \bar{\sigma}.\dot{\bar{\varepsilon}} = \int_0^{\bar{\sigma}} \dot{\bar{\varepsilon}}.d\bar{\sigma} + \int_0^{\dot{\bar{\varepsilon}}} \bar{\sigma}.d\dot{\bar{\varepsilon}} = J+G \qquad (1)$$

where σ is the effective stress and $\dot{\varepsilon}$ is the effective strain rate.

Specific DMM parameters are defined as efficiency, η, and the entropy factor, s. The efficiency represents the power dissipating ability of the workpiece normalized with respect to the total power input to the system:

$$\eta = \frac{J}{J_{Max}} = \frac{2m}{m+1} \qquad (2)$$

where m is the strain rate sensitivity:

$$m = \left[\frac{\delta(\log\bar{\sigma})}{\delta(\log\dot{\bar{\varepsilon}})}\right]_{\bar{\varepsilon},T} \qquad (3)$$

The entropy factor in turn is related to the ratio of the rate of entropy produced by the system with respect to the rate of entropy applied to the system:

$$s = -\left(\frac{1}{T}\right)\left[\frac{\delta(\ln \bar{\sigma})}{\delta\left(\frac{1}{T}\right)}\right]_{\dot{\bar{\varepsilon}},\bar{\varepsilon}} \tag{4}$$

Based on continuum mechanics and extremum irreversible thermodynamics principles, four stability criteria can be derived and utilized to establish "stable" zones within strain rate-temperature processing maps. The four stability criteria are:

$$0 < m < 1 \tag{5}$$

$$\left[\frac{\delta \eta}{\delta(\log \dot{\bar{\varepsilon}})}\right]_{T,\bar{\varepsilon}} < 0 \tag{6}$$

$$s > 1 \tag{7}$$

$$\left[\frac{\delta s}{\delta(\log \dot{\bar{\varepsilon}})}\right]_{T,\bar{\varepsilon}} < 0 \tag{8}$$

This approach has been validated for deformation of several simple and advanced materials[7-13], wherein dynamic recrystallization and, to a lesser extent, dynamic recovery have been shown to be predominant energy dissipative mechanisms in "stable" regions. "Unstable" regions have similarly been associated with cavitation, wedge cracking, kinking, and particle cracking.

Studies of titanium-base alloys[8,14-18] also indicate that morphological rearrangements, principally those associated with dynamic spheroidization of Widmanstätten or lamellar microstructures during deformation processing, are important high temperature dissipative machanisms. These studies have shown that dynamic spheroidization is a highly efficient process, $\eta \approx$ 30-40% [8,16]; indeed optimized processing of Widmanstätten and lamellar α-β microstructures is best undertaken within the strain rate-temperature region associated with this dissipative mechanism.

This study was undertaken to examine to what extent the contribution and benefits associated with morphological rearrangements in high temperature "stable" deformation might be realized in a forged Ti_3Al+Nb (α_2+β) intermetallic alloy [Ti-25Al-11Nb (at.%)], the latter possessing an initial lamellar microstructure.

Experimental details

Material characterization

The Ti_3Al-Nb alloy investigated, Ti-25Al-11Nb (at.%), was supplied by TIMET and was received as a 152.4 mm thick slab having previously been forged from a 3400 kg triple vacuum melted production ingot. Prior thermal history consisted of heating to 1533 K (1260°C), holding at this temperature for 8 hours, forging, and then air cooling to ambient temperature. Table 1 lists the chemical composition of the alloy.

The as-received microstructure exhibited primary α_2 (α_2^P) colonies in a transformed secondary Widmanstätten α_2^S + β_t matrix, Figure 1. Ambient temperature x-ray diffraction revealed an α_2 + β (ordered DO_{19} + disordered bcc) structure, with a small quantity of an orthorhombic phase O, the latter characterized by the presence of "shoulders" at the identified α_2 peaks.

Elevated temperature compression testing

Cylindrical samples (L_0=30.48mm, D_0=20.32mm, L/D ratio=1.5) were machined parallel to the forging axis. Ring samples with a typical OD/ID/H (outside diameter, inside diameter, and height, respectively) ratio of 6/4/2, were also deformed to evaluate frictional correction factors[20]. Boron nitride was used as the lubricant with HfC dispersion strengthened Mo (T < 1373 K) or SiC (T > 1373 K) compression platens.

Uniaxial hot-compression was performed in high purity argon environment (<1ppb O_2). Prior to testing, a vacuum of 1 mPa was achieved and the chamber was then backfilled to a pressure of 13.8 kPa with high purity gettered argon gas. A titanium gettering charge was also placed next to the sample for additional oxidation protection. In all tests, specimens were heated at a constant heating rate of 20 K/min, soaked at deformation temperature for 10 minutes prior to testing, tests being conducted at temperatures of 1073 K, 1173 K, 1273 K, 1348 K, 1398 K, 1423 K, and 1473 K, the deformation temperature being monitored within ± 1 K by two type C thermocouples spotwelded to the sample. Compression testing to a true strain of ≈ 0.65 (50 % deformation) at five different constant true strain rates (10^{-4}, 10^{-3}, 10^{-2}, 10^{-1}, and 1 s^{-1}) was performed in stroke control, the constant strain rate being achieved by utilizing an exponential decay signal input. Deformation times at temperature were approximately 117 min., 11 min., 70 sec., 7 sec., and 0.7 sec, respectively.

In order to retain the in-situ microstructure after deformation for subsequent microstructure observations, the samples were gas-jet cooled (≈ 200 K/min down to 873 K, the cooling decreasing to ≈ 10 K/min from 873 K to ambient temperature) immediately following straining. Non-deformed samples were also prepared in the same system by heating at 20 K/min, soaking for ≈ 2 hours (soak time similar to the longest deformation processing time, that is at a strain rate of $10^{-4}s^{-1}$), and cooled using the same quenching procedure.

Data acquisition involved recording load and stroke vs. time. Corrections of the flow stress-strain data for friction and deformation-heating effects were performed. Friction corrections were derived from the conventional ring testing procedure[20,21], in which the average pressure/true plastic strain data were converted to true stress/true plastic strain using:

$$\sigma = p\left[1 + \frac{f}{3\sqrt{3}}\frac{D_0}{L_0}\exp\left(\frac{3\bar{\varepsilon}}{2}\right)\right] \qquad (9)$$

where σ = average axial true flow stress corrected for friction, $\bar{\varepsilon}$ = true plastic strain, p = average pressure, f = interfacial friction factor, and D_0/L_0 = initial diameter / initial height of the cylindrical samples.

Corrections for deformation heating effects were achieved using a procedure previously described[22], where the temperature rise due to deformation, ΔT, could be calculated as:

$$\Delta T = \frac{1}{1+m}\frac{\beta}{c\rho}\int_0^{\bar{\varepsilon}} \sigma d\bar{\varepsilon} \qquad (10)$$

where m is the strain rate sensitivity. The other coefficients are[23]: c = 0.63 J.(gm.°C)$^{-1}$ = specific heat; ρ = 4.30 gm.(cm^3)$^{-1}$ = density; β = fraction of heat not dissipated into the dies during testing, generally a function of strain rate, values having been chosen from 0.7 (1 s^{-1}) to 0.3 (10^{-4}s^{-1}).

The integral equation (10) was calculated by using the trapezoid formula. For each flow curve, plots of flow stress *vs.* temperature $T^{\Delta T}$ ($T^{\Delta T} = T(\varepsilon=0) + \Delta T(\varepsilon_i)$) were constructed at various regularly incremented strain levels (ε_i = 0.05, 0.2, 0.35, 0.5, 0.65) for a given strain rate, true flow stress values corresponding to true deformation temperatures being then calculated by linear extrapolation of these plots.

Microstructural observations

Metallographic studies were performed by optical and electron microscopy on the as-deformed ($\bar{\varepsilon}$ = 0.65) samples. The latter were sectioned at their medium section parallel to the compression axis, surfaces of observation then being polished and finally etched with Kroll's reagent for optical metallography studies. Microstructural observations were conducted in the center zone of the sections, disregarding all surface features.

Results

Representative corrected true stress - true plastic strain curves for Ti-25Al-11Nb are shown in Figure 2 [1]. At low temperatures and high strain rates the flow curves exhibit continuous strain hardening, Figure 2a. By comparing Figure 2a and 2b, it can be noted that as the test temperature increases and/or the strain rate decreases, a gradual transition in the plastic flow behavior is observed. Initial strain hardening at low strains is followed by flow softening, until at high strains steady state flow is established. Ultimately increasing temperature and/or decreasing strain rate resulted in elimination of the initial strain hardening regime, flow softening

[1] At the lowest temperature examined, 1073K, the uncorrected flow curves exhibited strain hardening at low strains, followed by a maxima and flow softening, with a steady state stress beiHx achieved Hx high strains. Following correction for adiabatic heating this flow softening was eliminated at the highest strain rate, e.g., 1 s^{-1}, the isothermal flow stress curves exhibiting strain hardening.

commencing upon yielding, Figure 2b [2].

As the β transus (1432 K)[19] is approached, that is, at temperatures where an $\alpha_2 \rightarrow \alpha$ transformation occurs[19] and the volume fraction of β phase is high (> 80 %)[24], the flow curves exhibit an initial flow stress drop followed by steady-state behavior. This flow stress drop is not observed at temperatures below 1398 K, nor at 10^{-4} and 10^{-3} s^{-1} above this temperature. The amplitude of the yield drop decreases with increasing temperature and decreasing strain rate. The importance of the β phase in controlling the initial deformation behavior at these temperatures is confirmed by the observation of the same initial yield behavior at 1473 K, i.e., above the β transus, where the material is single phase β. The appearance of this flow stress peak in the deformation behavior of near β / β phase alloys has been previously reported in Ti-6Al-2Sn-4Zr-2Mo-0.1Si [15], Ti-Mn and Ti-V[25] and Ti-15V-3Al-3Cr-3Sn[26] alloys where it has been related to an initial rapid increase in mobile dislocation density at small strains.

Figure 3 summarizes the dependence of the flow stress of Ti-25Al-11Nb upon temperature and strain rate. The flow stress generally decreases with increasing temperature, the flow stress-temperature dependence being a distinct function of strain rate and strain, with the rate of change of flow stress with temperature increasing with increasing strain rate and strain. Finally, comparison of the flow stress - temperature dependence of Ti-25Al-11Nb with more conventional α+β alloys[15-17] demonstrates that the former exhibits a stronger flow stress dependence upon temperature, i.e., $(d\sigma/dT)\{\alpha_2+\beta\} \approx 1.3(d\sigma/dT)\{\alpha+\beta\}$.

Discussion

The results of Ti-25Al-11Nb high temperature compression experiments have confirmed that the flow stress-strain-temperature-strain rate behavior of this alloy is complex and cannot be simply described based on single phase, thermally stable materials. Indeed, it has previously been established that the initial Widmanstätten + primary α_2 microstructure examined in this study is thermally unstable[19]. Isochronal exposure to elevated temperatures first results in transformation of the orthorhombic O phase to α_2, with sequential coarsening and dissolution of the morphologically distinct α_2 phases, Table 2. Furthermore, the relative proportion of Widmanstätten and primary α_2 exhibits a clear dependency upon temperature, the volume fraction of Widmanstätten α_2 decreasing with decreasing temperature. Indeed, at temperature above 1394 K only primary disordered α is observed [3] [19].

This knowledge of the thermal stability can be coupled with dynamic materials modeling (DMM) to select optimal deformation conditions, temperature and strain rate, for high temperature processing of Ti-25Al-11Nb. In this approach, the strain rate sensitivity, m, is considered to be a function of both temperature and strain rate, Figure 4. Such a dependence of

---

[2] The low temperature flow curves exhibit an inverse strain rate behavior corresponding to negative m values at low strain, $\varepsilon < 0.1$, and at the two extreme strain rates, 1 and $10^{-4}s^{-1}$.

[3] The existence of disordered α immediately below the β transus was established by high temperature x-ray diffraction, the absence of characteristic ordered α_2 diffraction peaks being confirmed through the use of rocking curves which showed no trace of ordered peaks at temperatures just below the β transus.

m upon temperature and strain rate in Ti-24Al-11Nb has been confirmed by Dutta and Banerjee[24]. They reported that this alloy may be superplastic (m ≈ 0.6) at low strain rate ($3.3x10^{-4}s^{-1}$) and intermediate temperatures (1233 - 1293 K), the maximum elongation (520 %) being observed at 1253 K. In comparison, the highest m values observed in this study lay within two distinct temperature regions, between 1348-1398 K where the microstructure was $\alpha_2/\alpha + \beta$, and between 1423-1473 K where the deformation behavior was controlled by the β phase. Furthermore, within the lower temperature region, high m values were noted at both low strain rates, $10^{-4}s^{-1}$, and at high rate, $1s^{-1}$.

Figure 5 summarizes the effect of strain rate and temperature on the deformation efficiency, η, at three different strains, i.e., 0.05, 0.35, and 0.65. At low and intermediate strains, the efficiency increases with increasing temperature within the $\alpha_2/\alpha + \beta$ phase field. Maximum values are obtained at ≈ 1373 K, approximately 70 K below the β transus, where the microstructure contains 75 vol.% β and 25 vol.% α_2/α[24]. A secondary maximum is also observed under these strain conditions at intermediate rates above the β transus.

Increasing the deformation strain to 0.65 results in the introduction of an additional efficiency maximum at 1273 K / $10^{-4}s^{-1}$ within the $\alpha_2/\alpha + \beta$ phase region and the elimination of the maximum previously observed at temperatures above the β transus. This low temperature, low strain rate maximum is observed under similar conditions reported by Dutta and Banerjee[24].

Unstable regions combining both mechanistic stability criteria, $0 < m < 1$ and $\delta\eta/\delta\log\dot{\varepsilon} < 0$, are also shown as grey-shaded areas in Figure 5. Unstable deformation based on these criteria is observed at high strain rate, e.g, 1 s^{-1}, at temperatures below the β transus, and at low strain rates both near/above the beta transus and at low temperatures, e.g., 1073 K. In addition, at the highest strain examined, an instability region is observed at
1373 K / $10^{-4}s^{-1}$.

At the lowest temperature examined, 1073 K, previous studies[19,27] have shown that the orthorhombic phase is unstable, transforming to α_2. Presumably the negative strain rate sensitivity observed at both high and low rates [4] is associated with this transformation[9]. This instability is accompanied by concurrent observations of flow localization, Figure 6. At high strain rates in the $\alpha_2+\beta$ phase field, flow localization was also associated with kinking and/or cracking of the brittle α_2^P lamellae, Figure 7a, and shear band formation, Figure 7b.

Microstructural studies indicated that coarsening of the dynamically recrystallized grain structure was a primary cause for flow instability within the low strain rate / high temperature regime. A comparison with the initial grain size, d ≈ 0.7 mm, ℓ/d ≈ 1.5, [5] indicates that deformation at 1 s^{-1} within the temperature range, 1423-1473 K, results in a decrease in d, ≈ 0.28 mm, and an increase in ℓ/d, ≈ 2.0. Decreasing the strain rate to $10^{-2}s^{-1}$ results in dynamic recrystallization of the single phase β grain structure which becomes equiaxed, d ≈ 0.25 mm. Finally, with a further decrease in strain rate to $10^{-4}s^{-1}$, the grain structure remains equiaxed, the

---

[4] At high rates, adiabatic heating assists the $O \rightarrow \alpha_2$ transformation. For example, large temperature corrections (ΔT_{Max} increase = 76 K) to the flow stresses were required at strain rates $\geq 10^{-1}s^{-1}$ and at temperatures ≤ 1173 K.

[5] Since the initial grain size of the as-forged alloy was not equiaxed, characterization involved measurement of both minor, d, and major, ℓ, dimensions, the former lying parallel, the latter perpendicular to the compressive axis.

grain size however increasing to d ≈ 0.76mm.

Further DMM deliberation of flow involves consideration of the entropy factor, s, Figure 8. Maximum values of s are observed at low strain rates, $10^{-4}s^{-1}$ and intermediate temperatures, 1273-1373 K. While this location is independent of strain, the absolute value of s decreases with increasing strain. Unstable regions combining both thermodynamic stability criteria, $s > 1$ and $\delta s/\delta \log \dot{\varepsilon} < 0$, are also shown in Figure 8. Unstable deformation based on these criteria is observed at (i) low temperature and medium to high strain rates, (ii) low strain rates and high temperatures, and (iii) for low strains at high temperatures. The former conditions, (i) and (ii), are similar to those previously considered by the mechanistic criteria and have been related respectively to the $O \rightarrow \alpha_2$ transformation and coarsening of the dynamically recrystallized grain structure. In contrast, the instability region observed at low strains, high rates and high temperatures appears to be related to the appearance of the initial yield drop phenomenon, Figure 2(c) and (d).

Values of activation energy for Ti-25Al-11Nb were calculated to assist in defining operative microstructural mechanisms in high temperature deformation. A general power law equation was assumed to characterize the deformation process:

$$\bar{\dot{\varepsilon}} = A\bar{\sigma}^{n}\exp\left(\frac{-Q_a}{RT}\right) \tag{25}$$

where A is a microstructure-dependent constant, n the stress dependence of the strain rate, R is the gas constant, and Q_a is the apparent activation energy. In order to eliminate microstructural changes induced by deformation, computations of Q_a were performed at low strain, $\bar{\varepsilon} = 0.05$, activation energy considerations being generally based on isostructural conditions.

Q_a values for Ti-25Al-11Nb, Figure 9, could be divided in three regions, i.e., (i) a low temperature, $T < 1173$ K, region with a low Q_a (< 400 kJ/mol), (ii) an intermediate/high temperature region, $1173 \text{ K} < T < 1398$ K, with high Q_a values ranging from 700 to 1100 kJ/mol, Q_a being maximum at ≈ 1298 K and at strain rates $< 10^{-1}s^{-1}$, and (iii) a high temperature region near/above the β transus associated with low activation energy values (≈ 400 kJ/mol), the latter increasing slightly with increasing rate. The low activation energy in region (i) is in good agreement with values between 200 and 370 kJ/mol reported in the case of creep and superplastic deformation of Ti-24Al-11Nb [28,29]. The Q_a values computed in regions (ii) and (iii) are similar to previous values obtained by Semiatin et al. [18] in cast Ti-24Al-11Nb where Q values of 815-1080 and 278 kJ/mol were found in testing conditions laying within zones (ii) and (iii), respectively. Furthermore, the high values of activation energy observed at intermediate/high temperatures, region (ii), have been suggested to be related to the deformation characteristics of the ordered α_2 phase, in contrast to disordered α+β titanium alloys [30].

As illustrated by Figure 10, which combines both mechanistic and thermodynamic criteria to establish the optimal strain rate and temperature regime for "stable" flow, this high Q regime is located within the stable processing window predicted by DMM, i.e., within temperatures ranging from 1223 to 1398 K at strain rates below 10^{-1} s^{-1}. Comparison of microstructural observations for undeformed and deformed specimens, Figure 11 and 12 respectively, indicate that this stable flow region in {Widmanstätten + primary}α_2 / β Ti-25Al-11Nb is associated with dissolution of the Widmanstätten secondary α_2, coarsening of the primary α_2, and dynamic spheroidization of the lamellar α_2 microconstituents.

Conclusions

Analysis of the mechanical behavior of Widmanstätten + primary α_2 + β Ti-25Al-11Nb has confirmed that dynamic material modeling (DMM) can be utilized to establish the flow stress-strain rate-temperature-strain criteria for stable flow.

The corrected true stress-true plastic strain behavior of this alloy at low temperatures and high strain rates was characterized by continuous strain hardening. As the test temperature increased and/or the strain rate decreased, the extent of this strain hardening regime decreased. Ultimately initial yielding was immediately followed by flow softening with steady state flow conditions being observed at higher strains.

Unstable regions predicted by DMM were related to transformation of orthorhombic O $\rightarrow \alpha_2$, kinking of the α_2 lamellae, shear band formation and coarsening of the dynamically recrystallized grain structure.

Stable flow regimes as predicted by DMM were shown to be associated with dissolution of the Widmanstätten α_2, coarsening of primary α_2, and dynamic spheroidization of the lamellar α_2 microconstituents.

Acknowledgements

This research was sponsored by the Defense Advanced Research Projects Agency under contract N00014-89-J-3166 supervised by Mr. W. Barker and monitored by Dr. G. Yoder of the Office of Naval Research. The Ti-25Al-11Nb alloy utilized was provided by Mr. Ed Mild of TIMET, Inc. Finally, the authors thank Dr. J. C. Malas, Dr. P. K. Chaudhury and Mr. S. Guillard for helpful discussions.

References

1. R. G. Rowe, in S. H. Wang, C. T. Liu, D. P. Pope and J. O. Stiegler (eds.), *High Temperature Aluminides and Intermetallics*, The Minerals, Metals, and Materials Society, Warrendale, PA, 1989, p. 375.
2. D. A. Koss, D. Banerjee, D. A. Lukasak and A. K. Gogia, in S. H. Wang, C. T. Liu, D. P. Pope and J. O. Stiegler (eds.), *High Temperature Aluminides and Intermetallics*, The Minerals, Metals, and Materials Society, Warrendale, PA, 1989, p. 175.
3. H. J. Frost and M. F. Ashby, *Deformation-Mechanism Maps, The Plasticity and Creep of Metals and Ceramics*, Pergamon Press, New York, 1982.
4. R. Raj, *Metall. Trans. A, 12A* (1981) 1089.
5. J. C. Malas, *Master Thesis*, Wright State University, Ohio, December 1985.
6. Y. V. R. K. Prasad, H. L. Gegel, J. T. Morgan and J. C. Malas, in F. H. Froes and D. Eylon (eds.), *Titanium Net Shape Technologies*, The Metallurgical Society of AIME, PA, 1984, p. 279.
7. Y. V. R. K. Prasad, *Indian J. Technology, 28* (1990) 435.
8. H. L. Gegel, *Computer Simulation in Materials Science*, ASM International, Materials Park, Ohio, 1986, p. 291.
9. J. C. Malas, *Ph. D. Thesis*, Ohio University, November 1991.
10. J. C. Malas and V. Seetharam, *J. Mater., 44[6]* (1992) 8.

11. J. K. Chakravartty, Y. V. R. K. Prasad and M. K. Asundi, *Metall. Trans. A, 22A* (1991) 829.
12. S. Guillard, *Master Thesis*, Clemson University, August 1991.
13. B. V. Radhakrishna Bhat, Y. R. Mahajan, H. Md. Roshan and Y. V. R. K. Prasad, *Metall. Trans. A, 23A* (1991) 2223.
14. I. Weiss, F. H. Froes, D. Eylon and C. C. Chen, in F. H. Froes and D. Eylon (eds.), *Titanium Net Shape Technologies*, The Metallurgical Society of AIME, PA, 1984, p. 79.
15. P. Dadras and J. F. Thomas, Jr., *Metall. Trans. A, 12A* (1981) 1867.
16. V. Seetharaman, L. Boothe and C. M. Lombard, in Y-W. Kim and R. Boyer (eds.), *Microstructure/Property Relationships in Titanium Aluminides and Alloys*, The Minerals, Metals & Materials Society, Warrendale, PA, 1991, p. 605.
17. H. J. Rack and A. Wang, in *Proc. 7th World Conf. on Titanium, San Diego, USA, August 1992*, The Minerals, Metals & Materials Society, Warrendale, PA, in press.
18. S. L. Semiatin, K. A. Lark, D. R. Baker, V. Seetharam and B. Marquardt, *Metall. Trans. A, 23A* (1992) 295.
19. M. Long, P. K. Chaudhury and H. J. Rack, in *Proc. 7th World Conf. on Titanium, San Diego, USA, August 1992*, The Minerals, Metals & Materials Society, Warrendale, PA, in press.
20. A. T. Male and M. G. Cockcroft, *J. Inst. Met., 93* (1964) 38.
21. V. DePierre and A. T. Male, *Technical Report AFML-TR-69-28, Part I*, Air Force Materials Laboratory, Wright-Patterson Air Force Base, OH, 1969.
22. T. Altan and S-I Oh, *Metal Forming-Fundamentals and Applications*, American Society for Metals, Metal Park, OH, 1983.
23. S. L. Semiatin, Materials Directorate, Wright Laboratory, Wright-Patterson Air Force Base, OH 45433, Private Communication, 1992.
24. A. Dutta and D. Banerjee, *Scripta Met. et Mater., 24* (1990) 1319.
25. M. N. Vijayshankar and S. Ankem, in *Mater. Sci. Eng., A129* (1990) 229.
26. R. Srinivasan, *Scripta Met. et Mater., 27* (1992) 925.
27. L. M. Hsiung, W. Cai and H. N. G. Wadley, *Acta Met. et Mater., 40* (1992) 3035.
28. M. G. Mendiratta and H. A. Lipsitt, *J. of Mater. Sci., 15* (1980) 2985.
29. M. A. Morris, *Mater. Sci. Eng., A148* (1991) 33.
30. Y. Combres, K. Takahashi, A.-M. Chaze and Ch. Levaillant, *Mém. Ét. Sci. Rev. Mét., 89* (1992) 225.

Table 1. Chemical composition of Ti-25Al-11Nb.

	Ti	Al	Nb	O	C	N	Fe
at.%	bal.	24.95	10.83	0.26	0.26	0.04	0.042
wt.%	bal.	14.25	21.30	0.09	0.09	0.012	0.05

Table 2. Phase transformations of Ti-25Al-11Nb [19].

Temperature (K)	Phases
< 1079	$\{\beta_t+\alpha_2^S\}+\alpha_2^P+O$
1079 - 1394	$\{\beta+\alpha_2^S\}+\alpha_2^P$ Dissolution/Disordering Morphological rearrangement
1394 - 1432	$\beta+\alpha$
> 1432	β

Figure 1. Optical micrograph of Ti-25Al-11Nb microstructure in the as-forged condition, exhibiting primary α_2^P colonies in a transformed β matrix (Widmanstätten secondary $\alpha_2^S+\beta_t$).

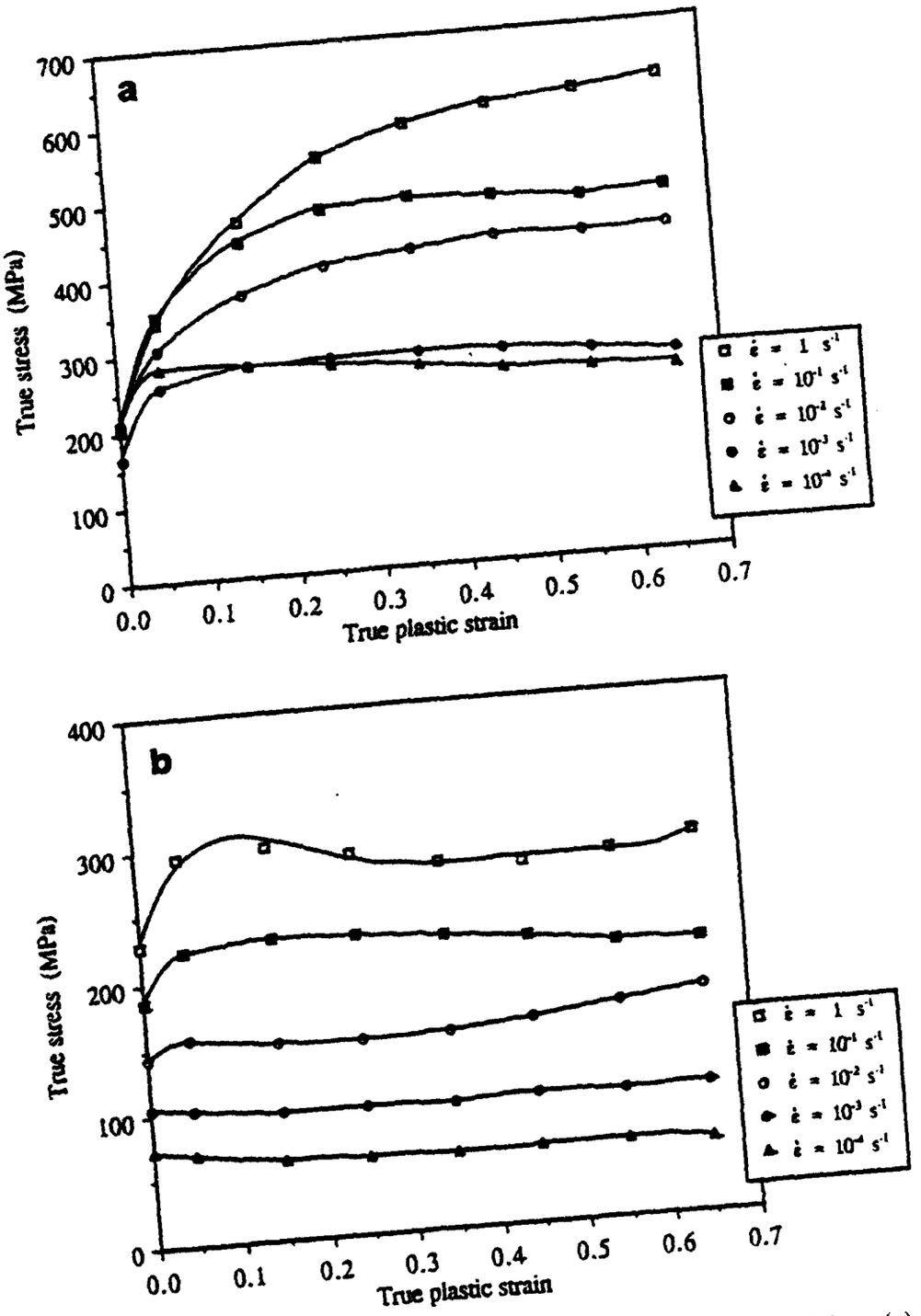

Figure 2. Typical true corrected stress - true plastic strain curves of Ti-25Al-11Nb at (a) 1073 K, (b) 1273 K, (c) 1398 K, (d) 1473 K.

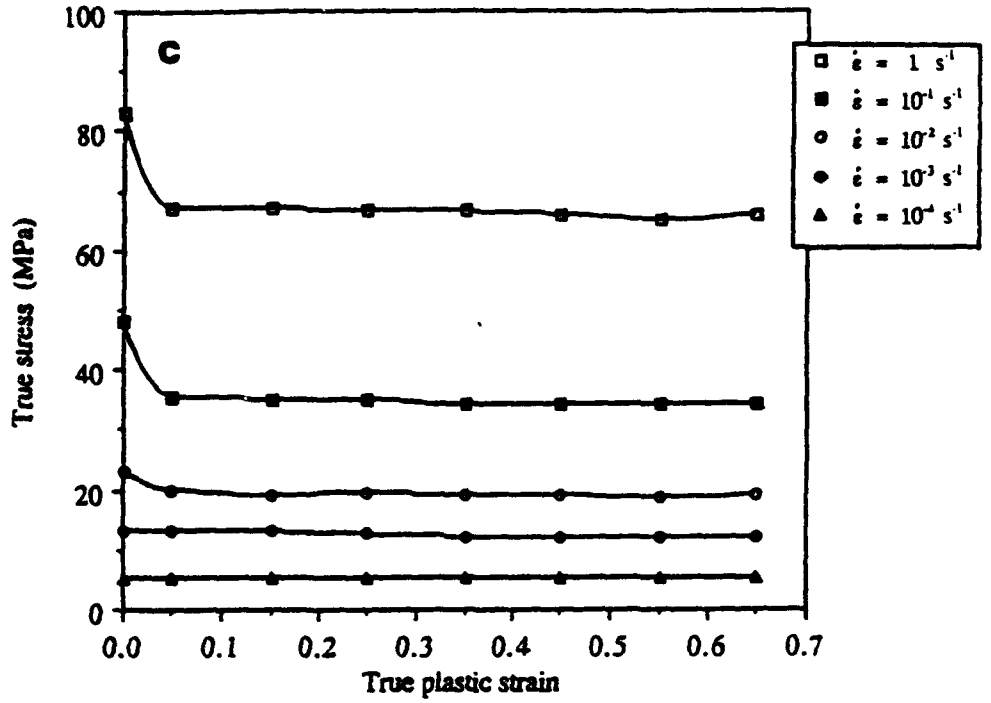

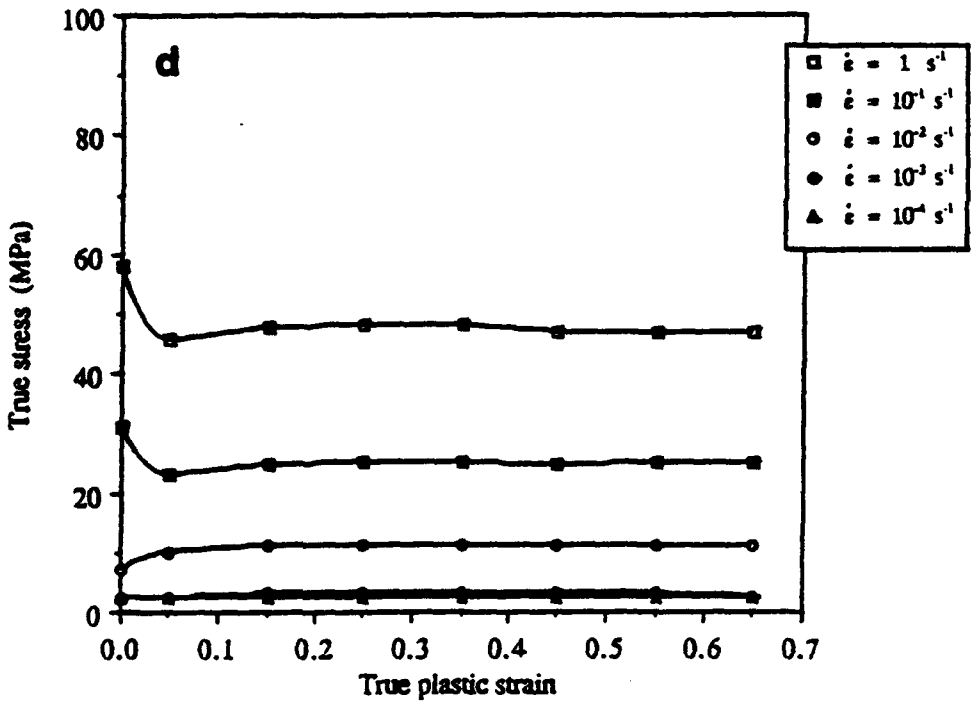

Figure 2. Continued

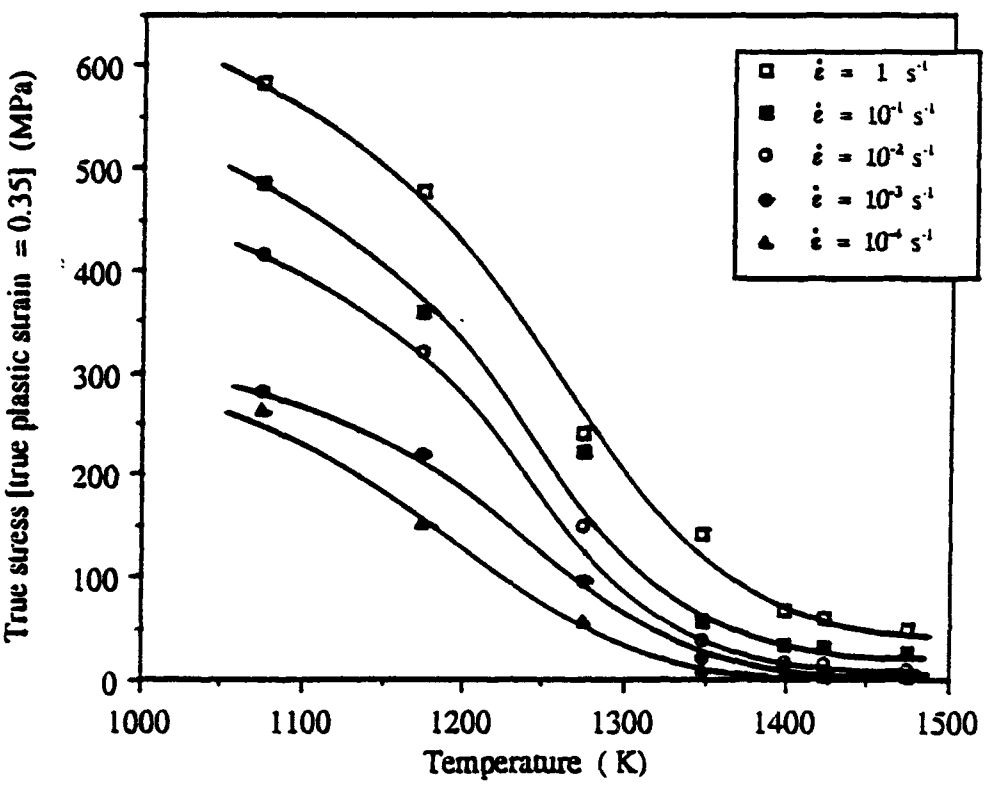

Figure 3. Dependence of temperature and strain rate on flow stress at 0.35 true plastic strain in Ti-25Al-11Nb.

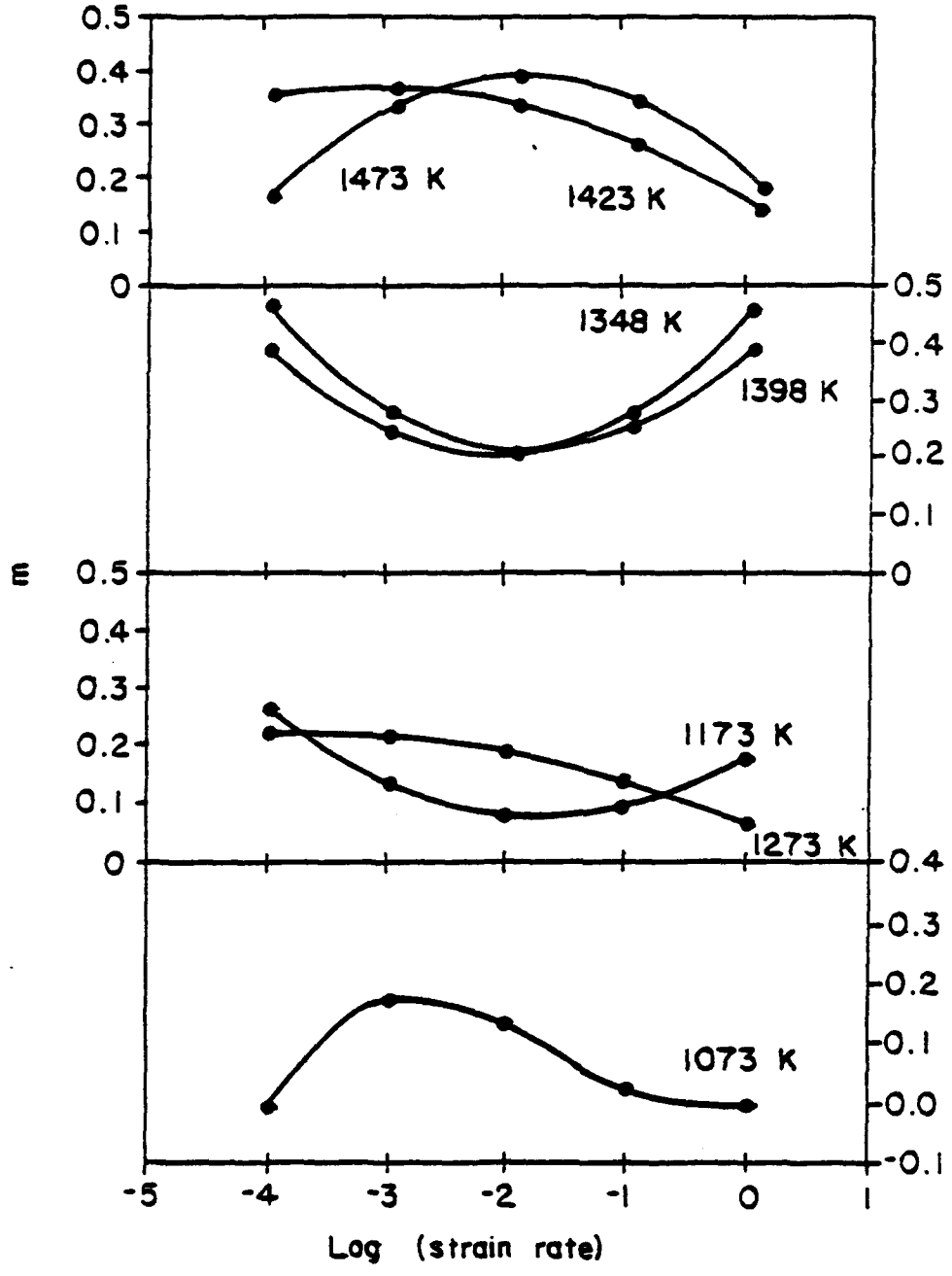

Figure 4. Dependence of temperature and strain rate on strain rate sensitivity m at $\bar{\varepsilon} = 0.35$ in Ti-25Al-11Nb.

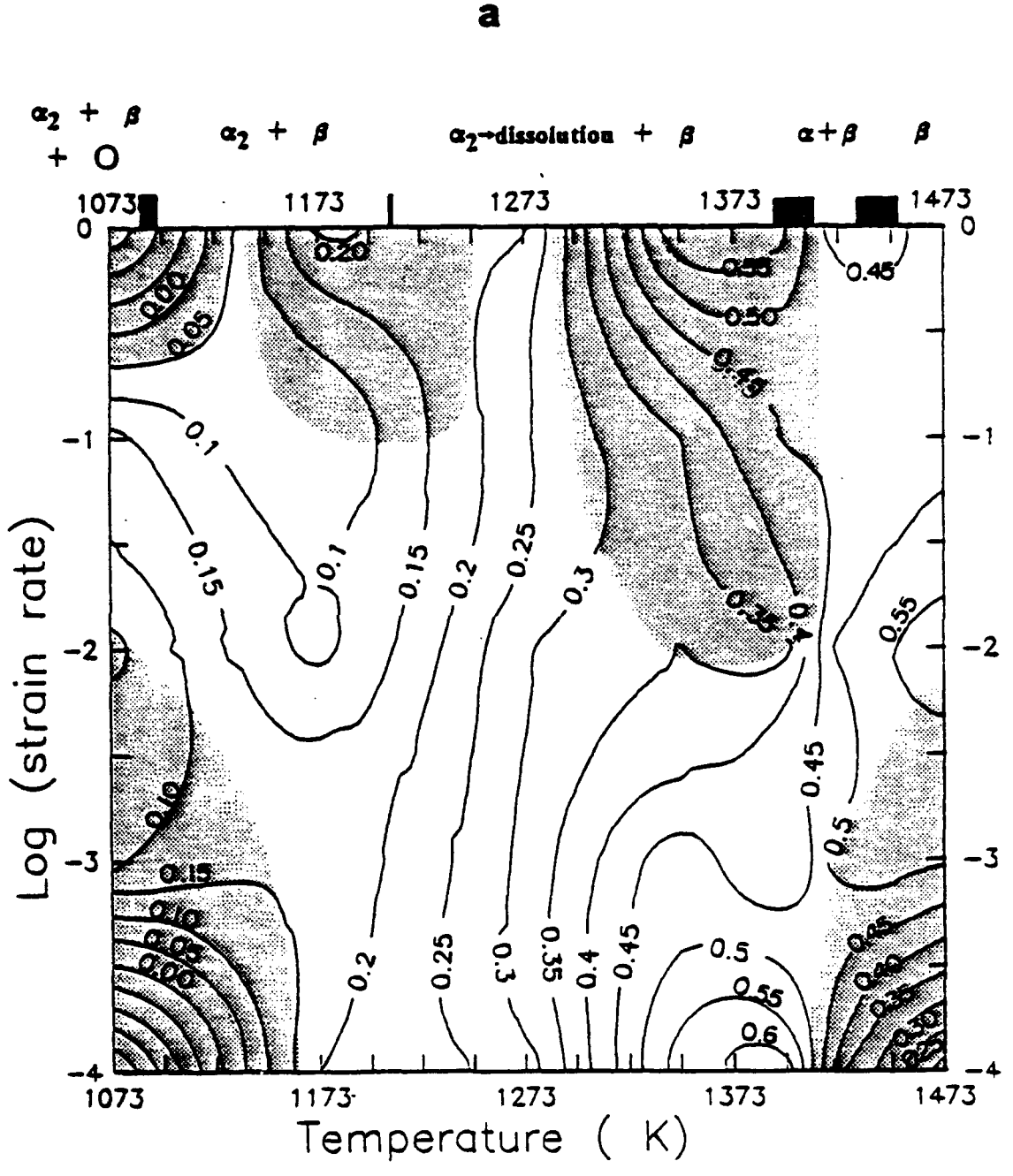

Figure 5. Efficiency, η, as a function of temperature and strain rate at strains of (a) 0.05, (b) 0.35, (c) 0.65. The shaded areas are unstable zones as defined by mechanistic stability criteria.

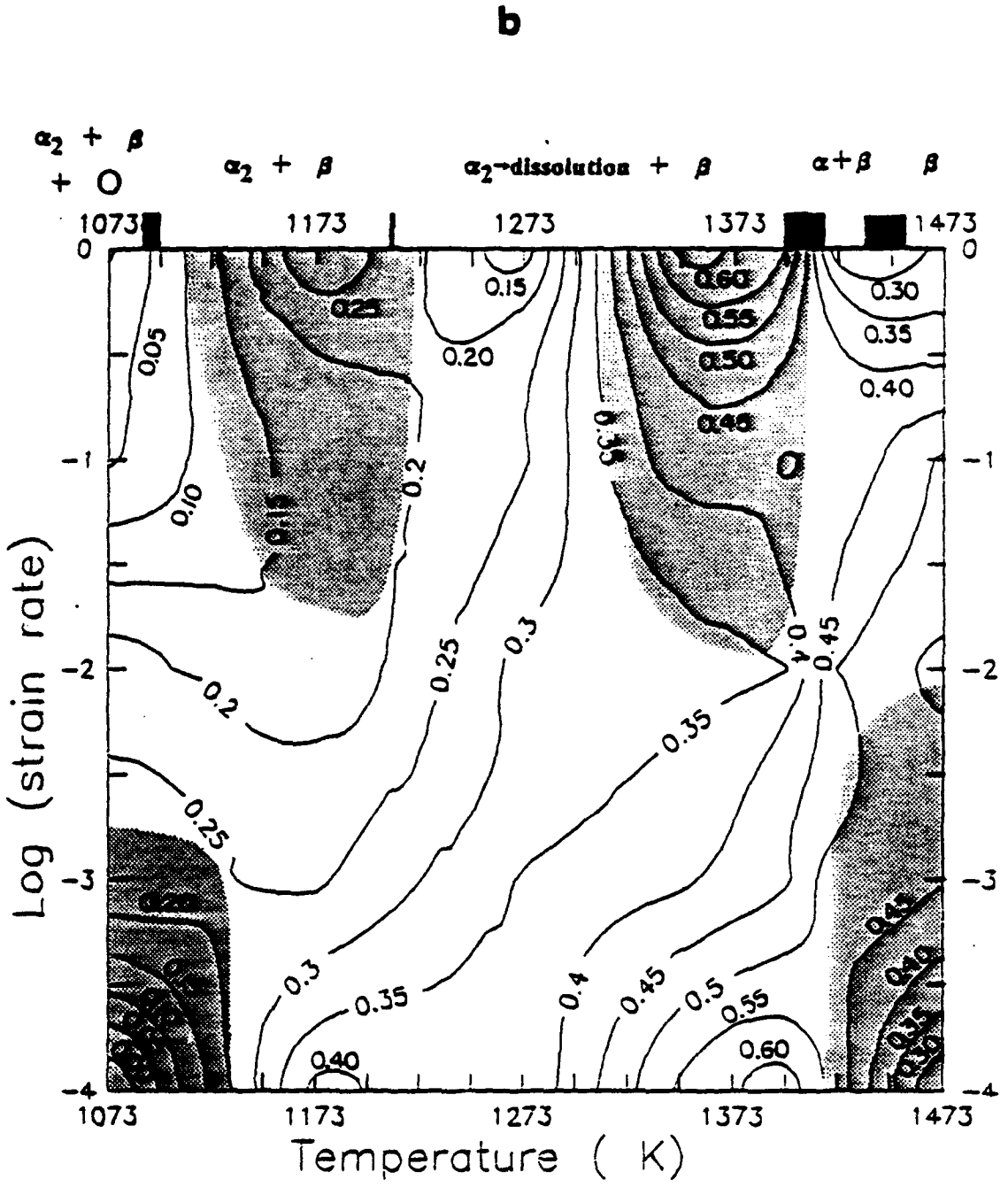

Figure 5. Continued.

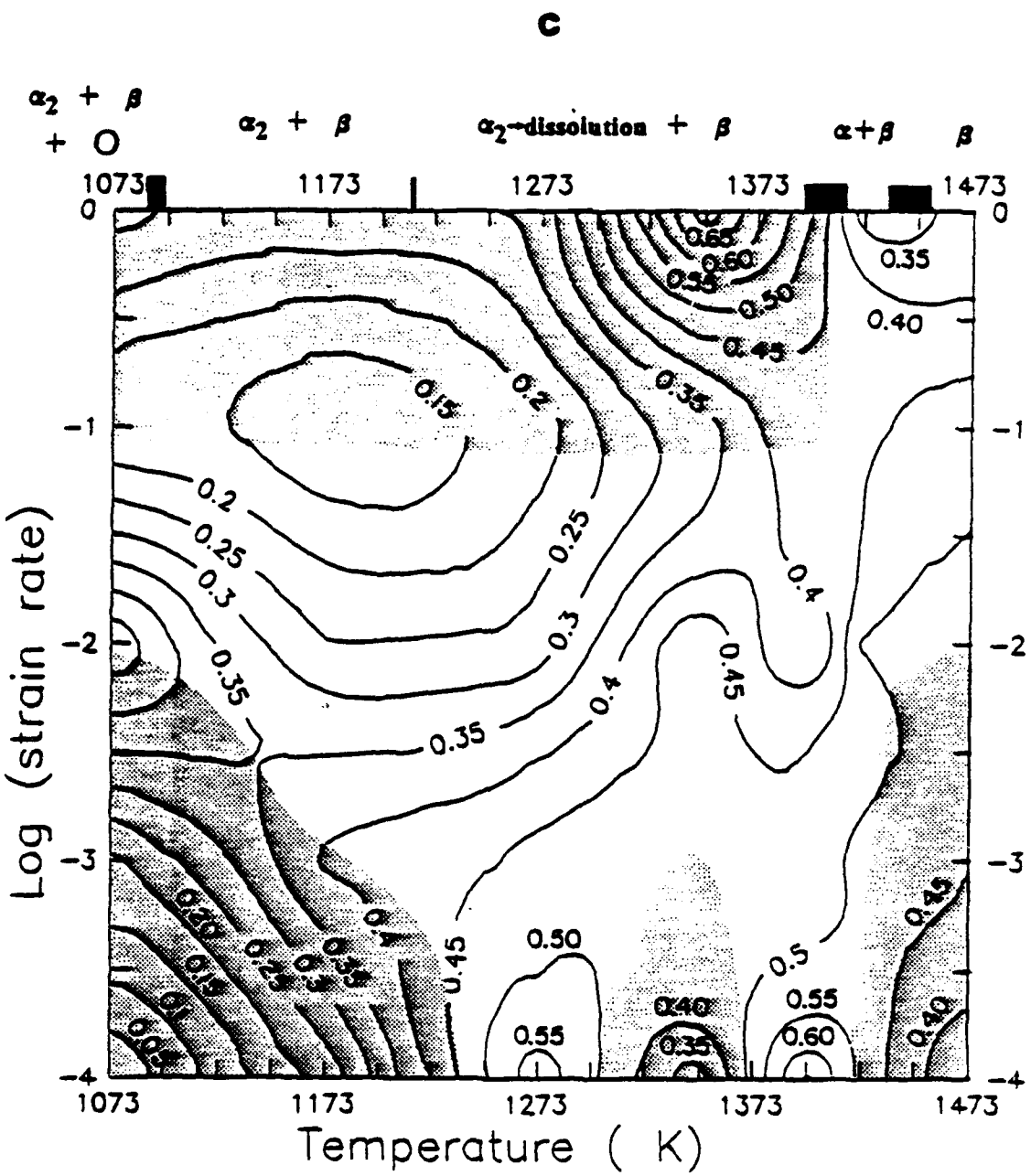

Figure 5. Continued.

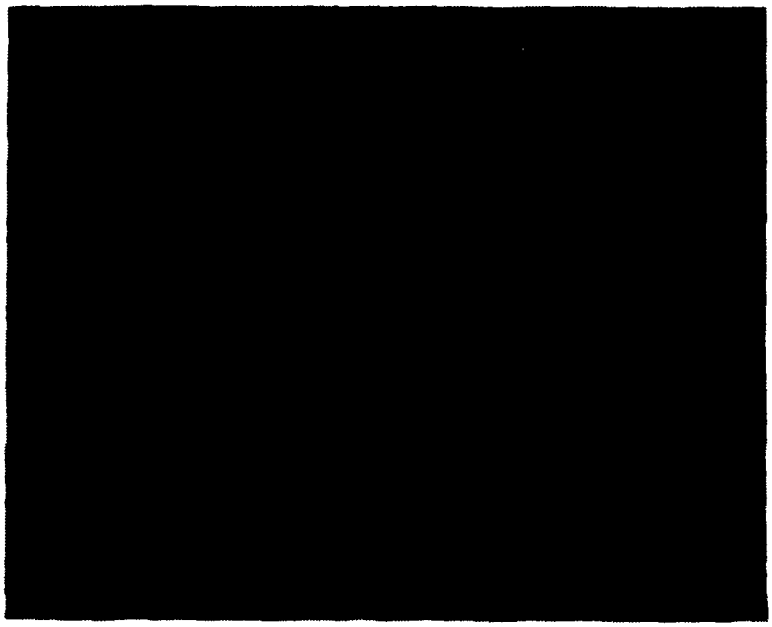

Figure 6. Optical microstructure of the as-deformed ($\bar{\varepsilon} = 0.65$) Ti-25Al-11Nb sample at constant true strain rate of $10^{-4}s^{-1}$ and deformation temperature of 1173 K.

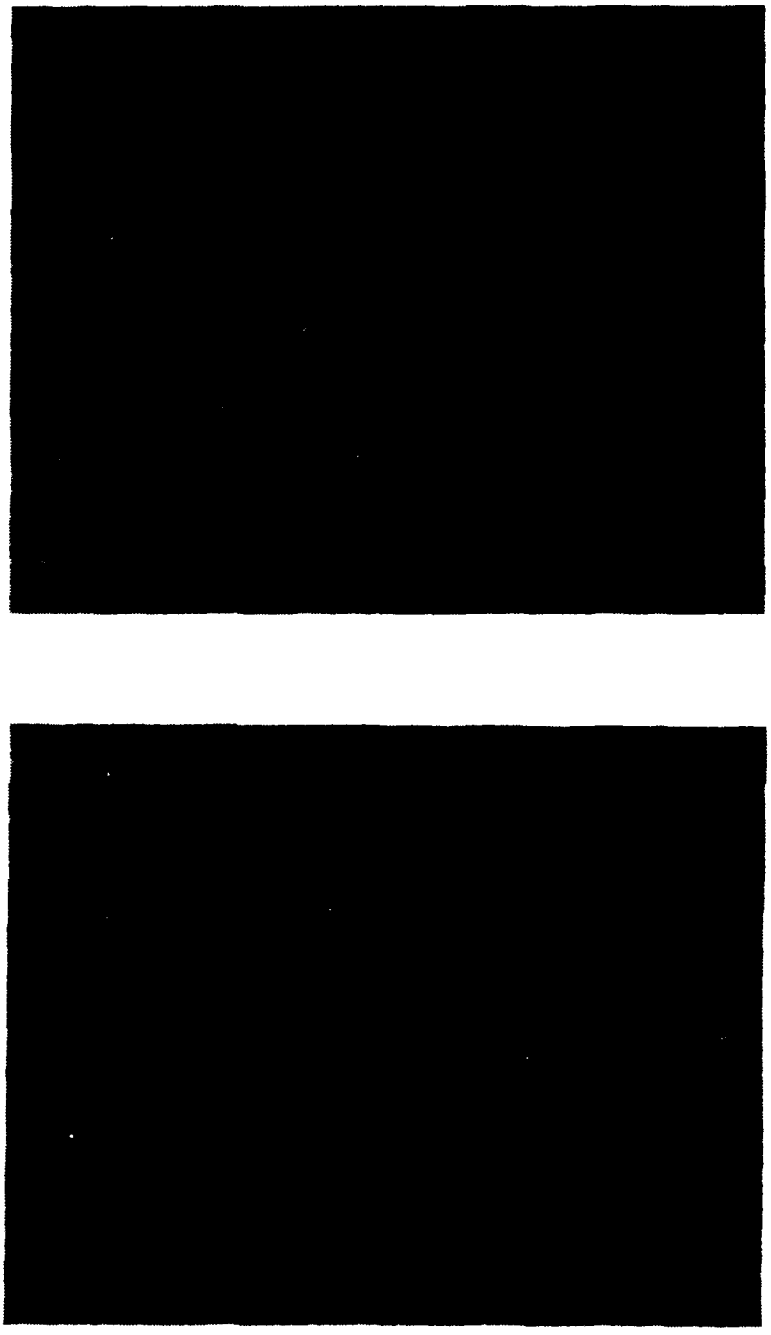

Figure 7. Optical microstructures of the as-deformed ($\bar{\varepsilon}$ = 0.65) Ti-25Al-11Nb samples at constant true strain rate of 1 s^{-1} and deformation temperature of (a) 1173 K and (b) 1273 K.

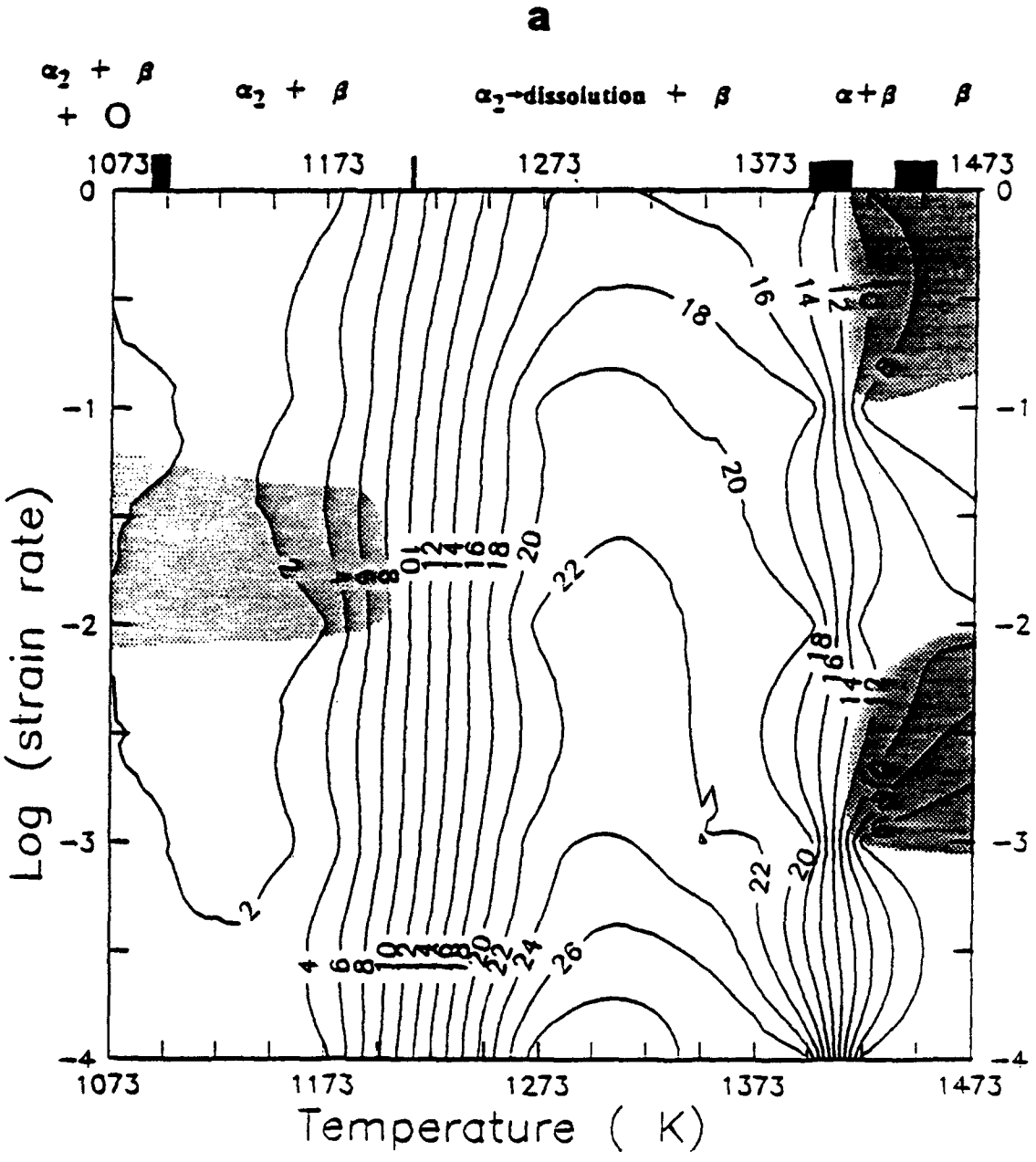

Figure 8. Entropy parameter, s, as a function of temperature and strain rate at strains of (a) 0.05, (b) 0.35, (c) 0.65. The shaded areas are unstable zones as defined by thermodynamic stability criteria.

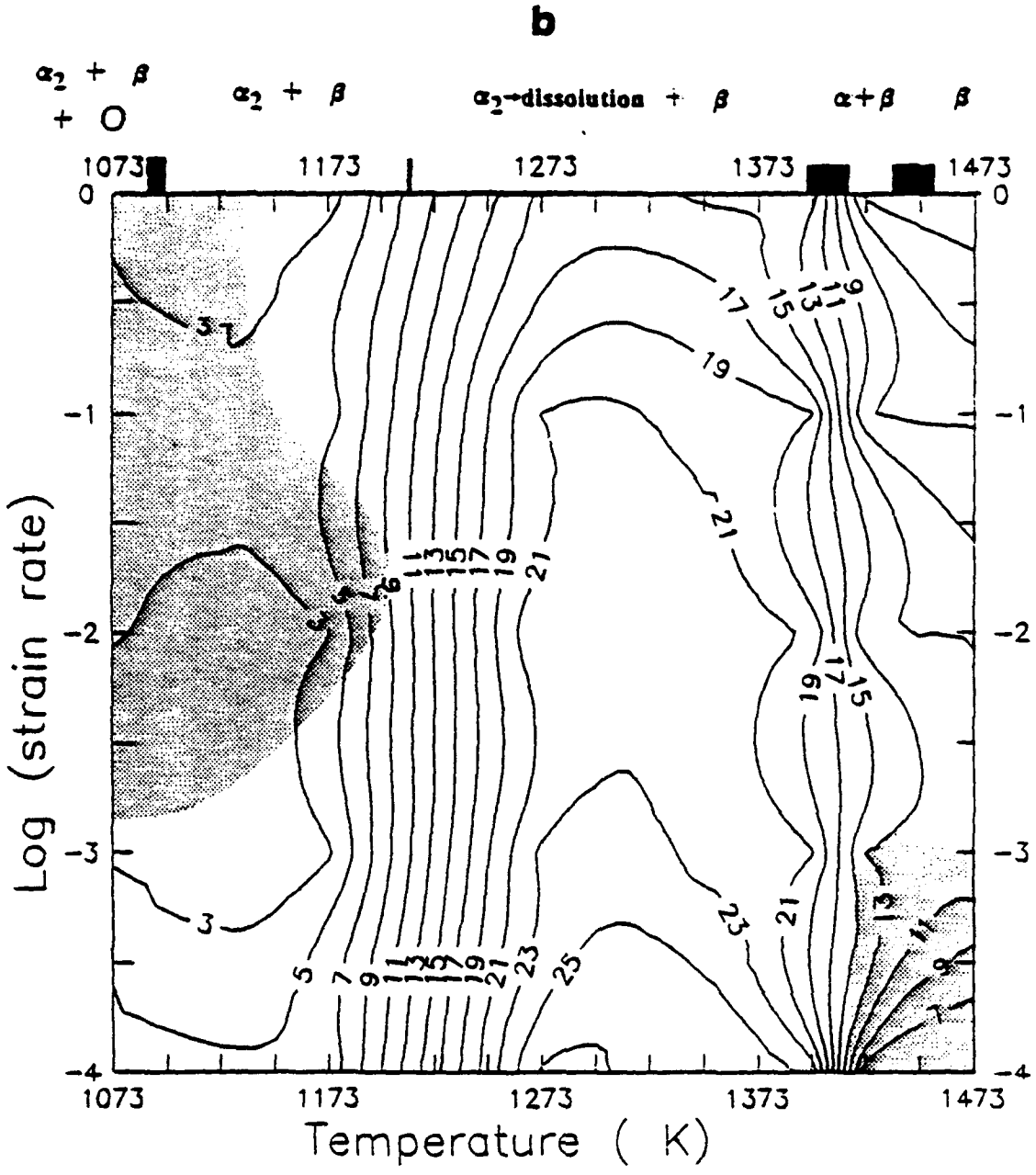

Figure 8. Continued.

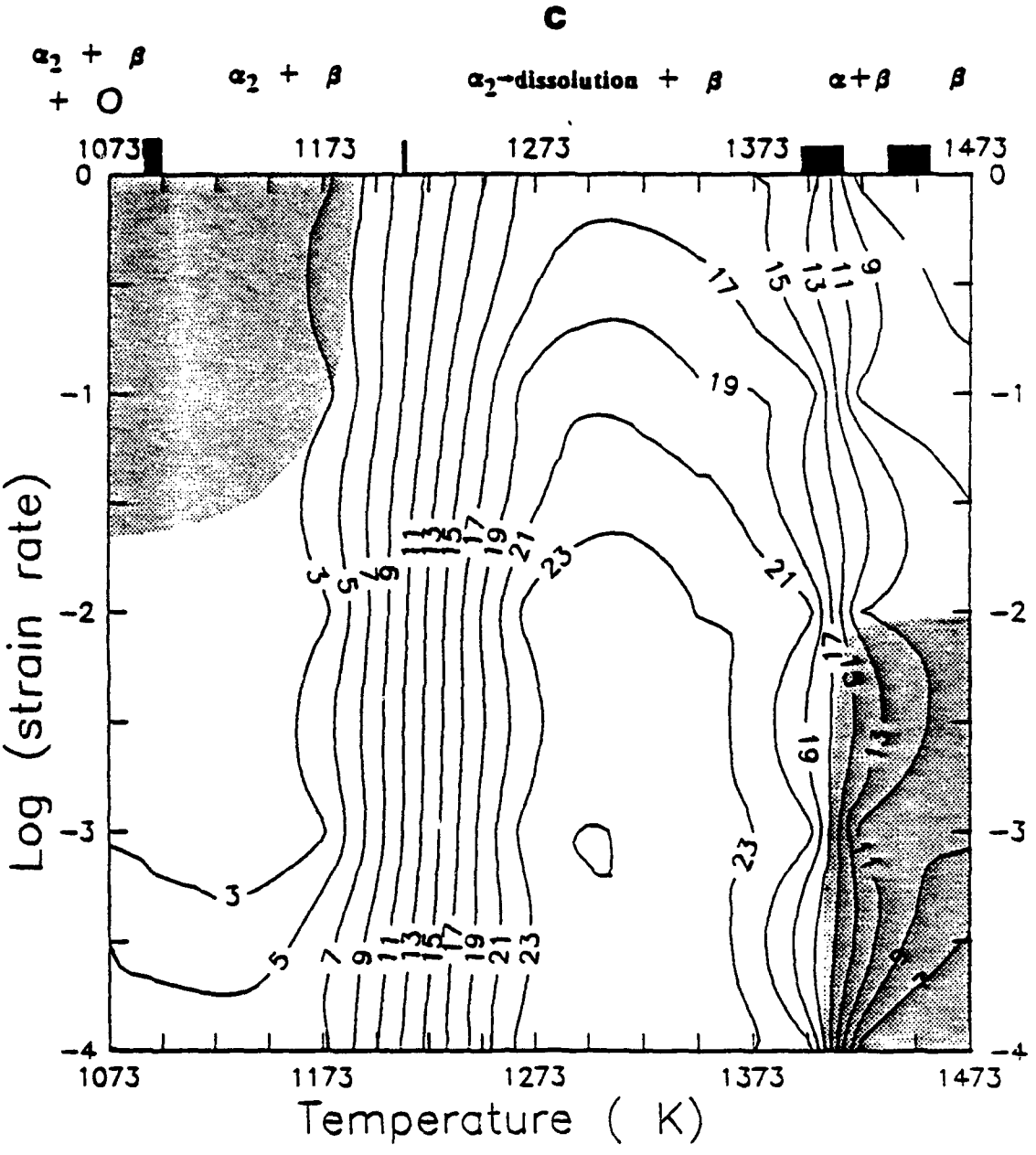

Figure 8. Continued.

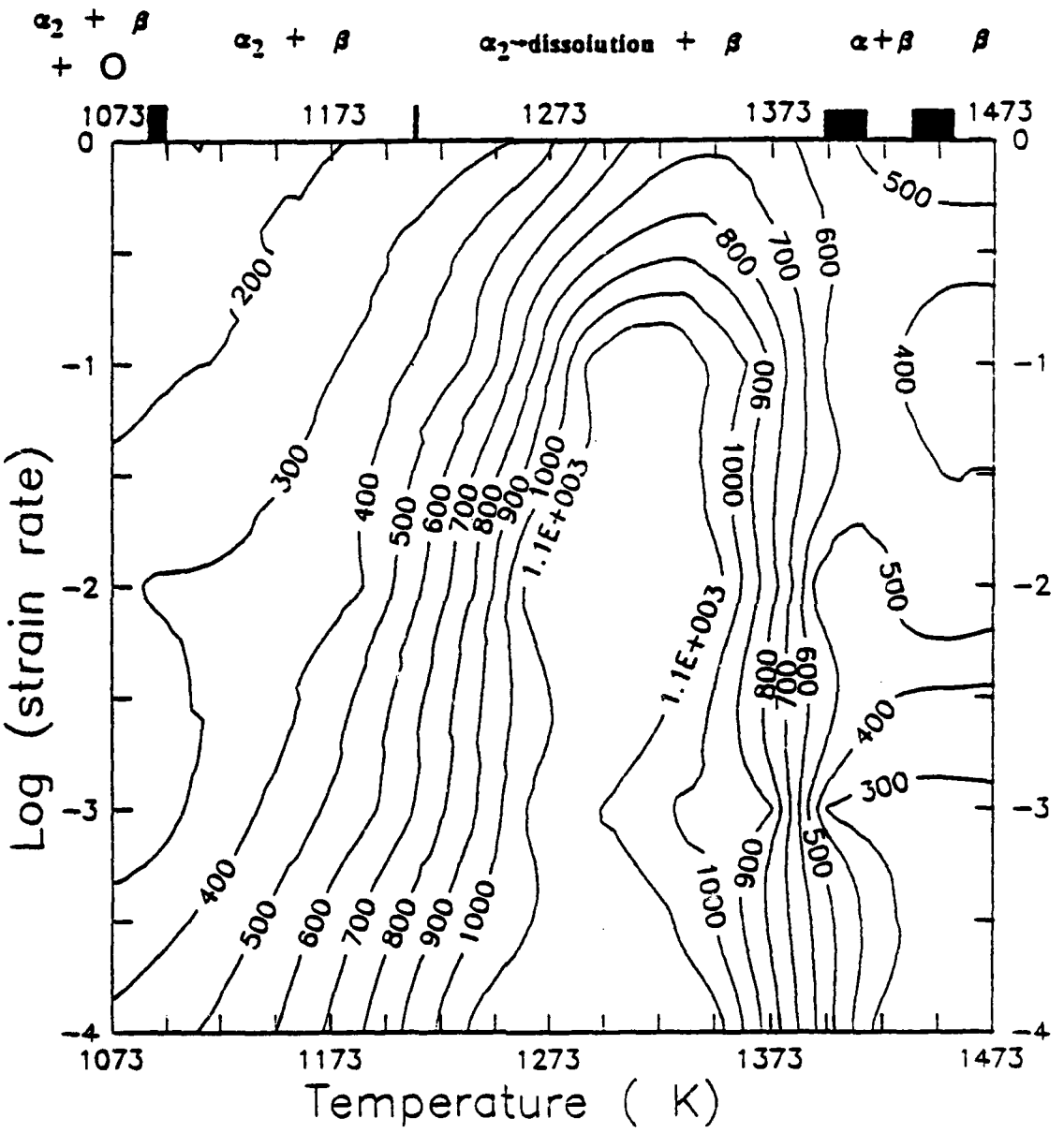

Figure 9. Contour maps illustrating activation energy (kJ/mol) in Ti-25Al-11Nb as a function of temperature and strain rate.

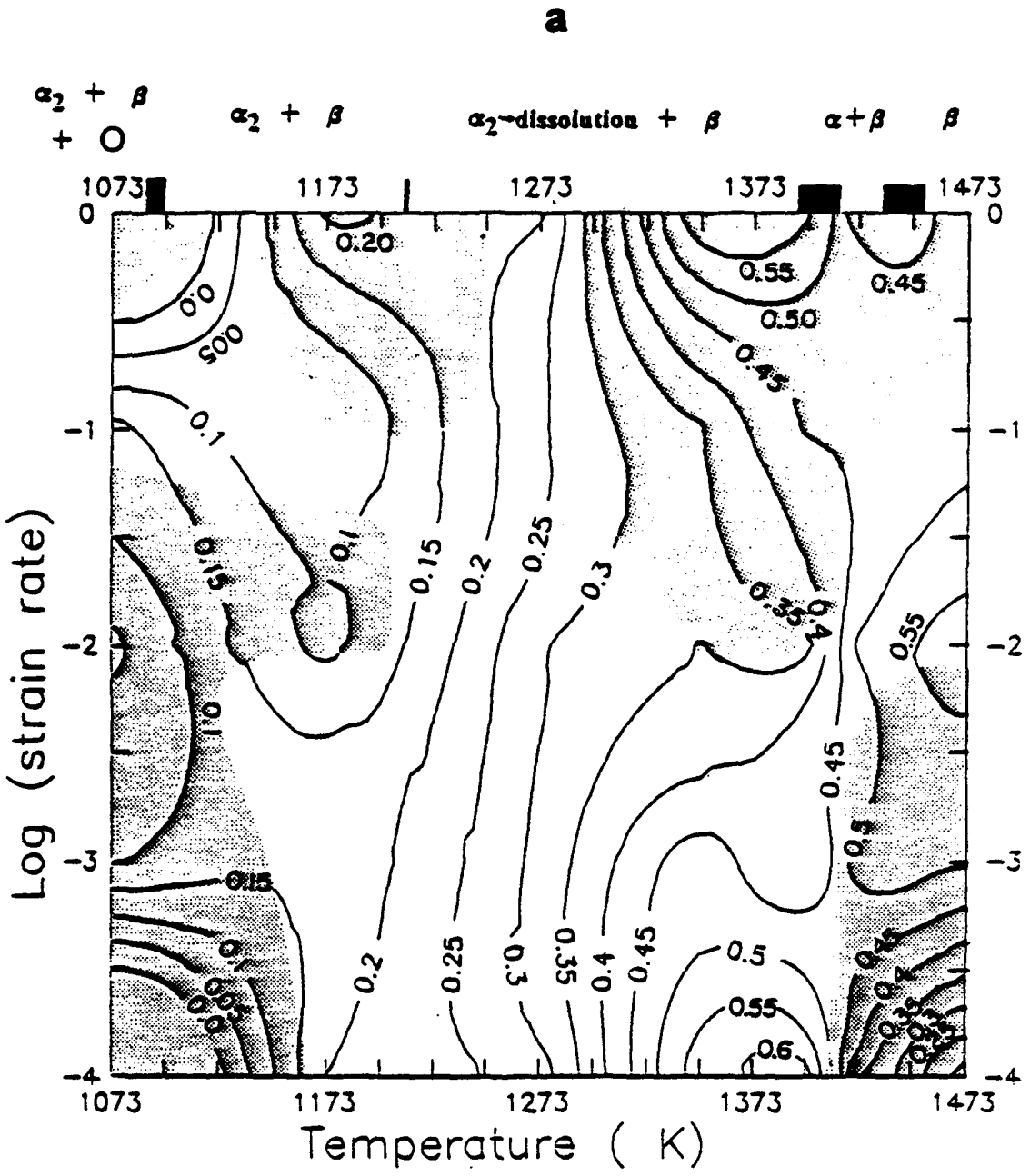

Figure 10. Ti-25Al-11Nb DMM stability maps as a function of temperature and strain rate at strains of (a) 0.05, (b) 0.35, (c) 0.65. The shaded areas are unstable zones as defined by all four stability criteria.

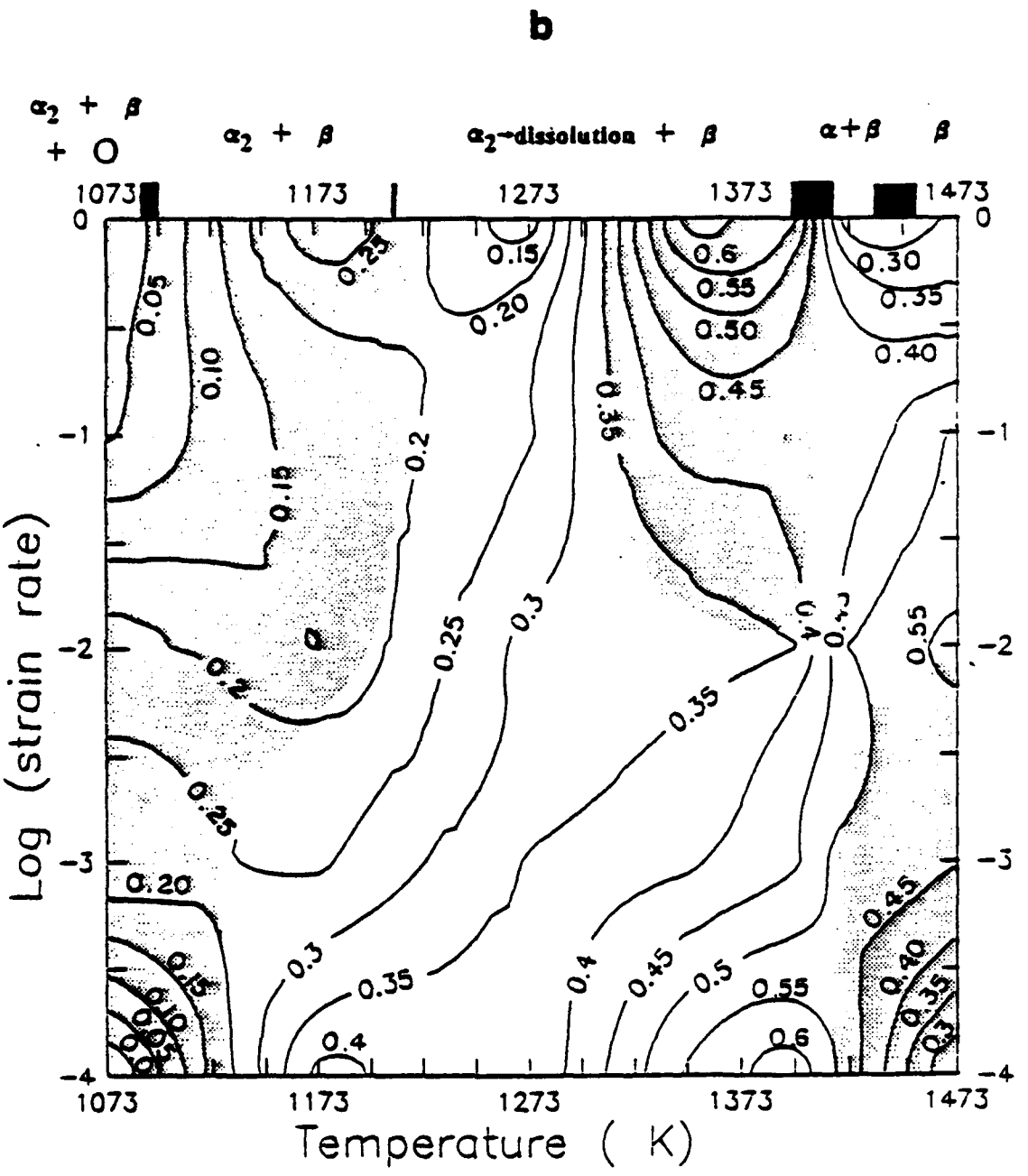

Figure 10. Continued.

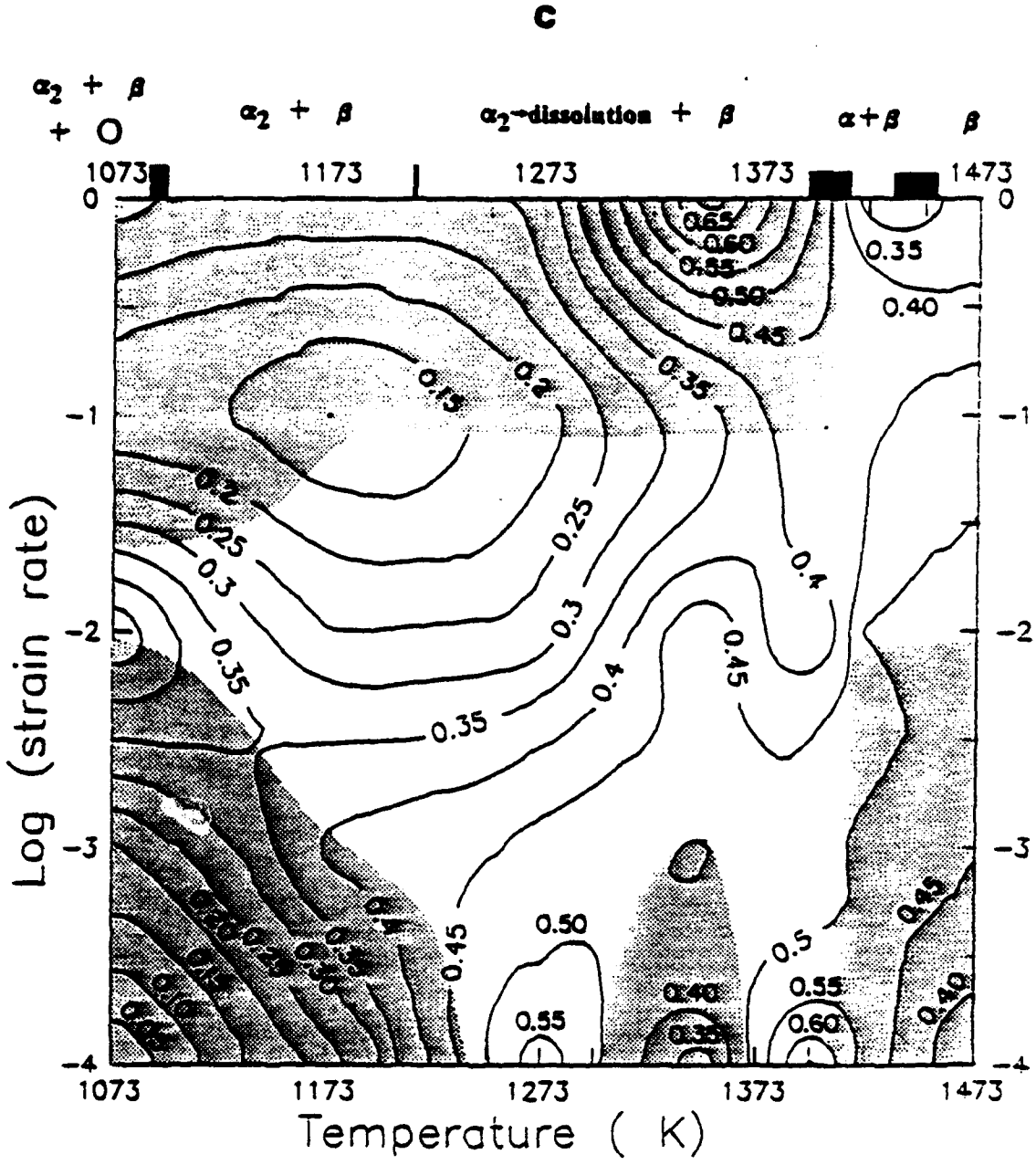

Figure 10. Continued.

Figure 11. Optical microstructure of a non-deformed Ti-25Al-11Nb sample held at 1273 K for ≈ 2 hours.

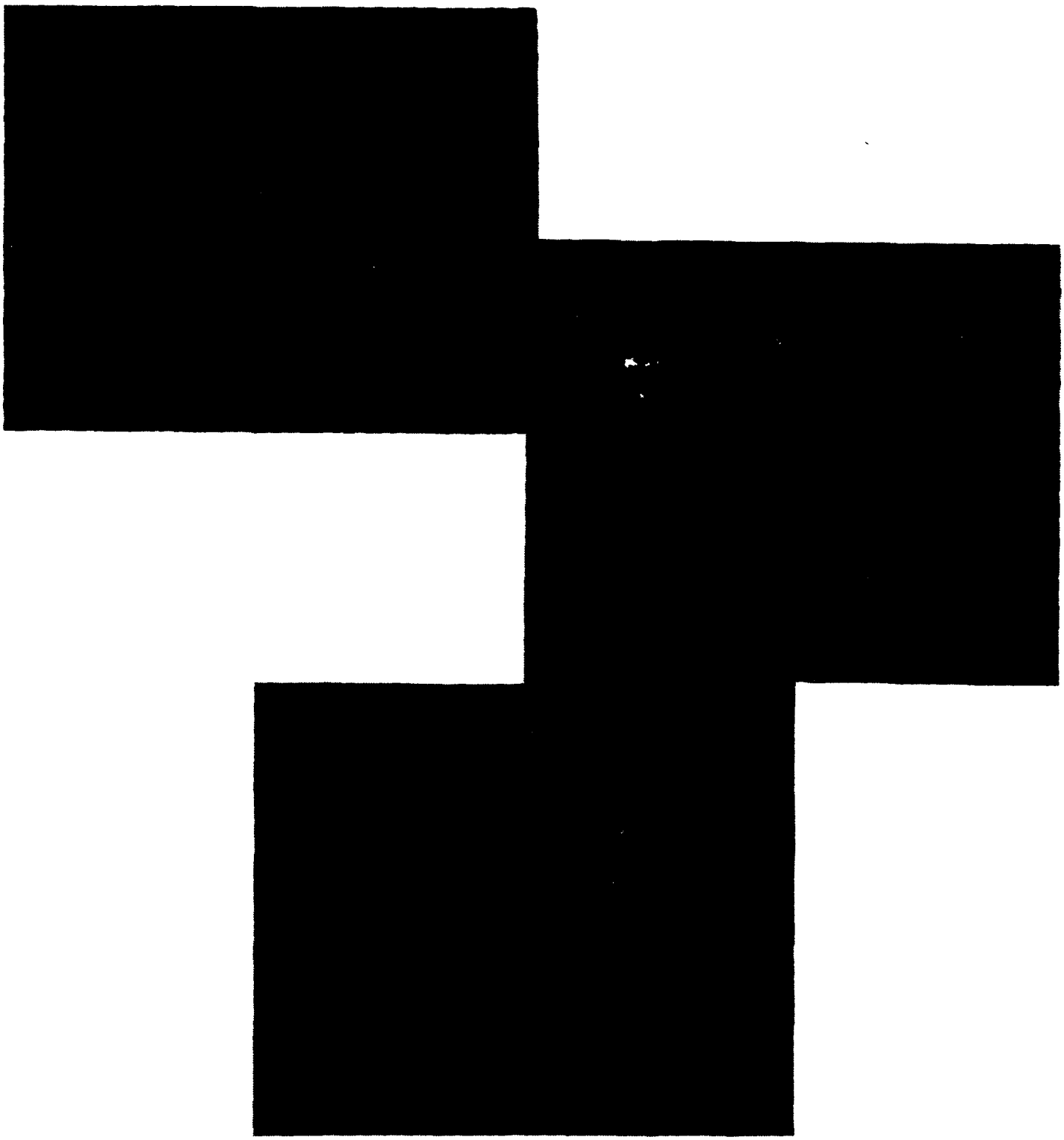

Figure 12. Optical microstructures of the as-deformed ($\bar{\varepsilon} = 0.65$) Ti-25Al-11Nb samples at 1273 K at constant true strain rate of (a) 1 s^{-1}, (b) $10^{-2}s^{-1}$, (c) $10^{-4}s^{-1}$.

THERMO-MECHANICAL STABILITY OF FORGED Ti-26Al-10Nb-3V-1Mo (at.%)

M. Long and H. J. Rack
Materials Science and Engineering Program
Department of Mechanical Engineering
Clemson University
Clemson, SC 29634-0921, USA

To be published in
Proceedings of 3rd International Conference on High-Temperature Intermetallics
Submitted to
Materials Science & Engineering
May 1994

Abstract

Dynamic material modeling (DMM) analysis has been employed to examine the high strain, elevated temperature mechanical behavior of Widmanstätten (α_2 + β) Ti-26Al-10Nb-3V-1Mo. Flow regimes predicted by this analysis were then correlated with microstructural observations. Unstable flow zones were associated with α_2 platelets kinking and shear band formation in the $\alpha_2+\beta$-phase field; with flow localization at grain boundaries and dynamic grain growth in the β-phase field. Stable flow regimes were associated with dynamic spheroidization of the Widmanstätten α_2 platelets in the $\alpha_2+\beta$-phase field, and to dynamic recrystallization in the β-phase field.

Introduction

Numerous studies of the titanium aluminides have been undertaken during recent years aimed at increasing the high temperature capability of titanium-base alloys eventually leading to the substitution of these low-density materials for nickel-base superalloys. While various aluminide systems have been examined, Ti_3Al-base alloys, which exhibit intermediate properties between conventional $\alpha/\alpha+\beta$ Ti-alloys and γ-TiAl intermetallics [1], appear to offer the highest potential for near-term application. The necessity to improve the poor ductility and fracture

toughness of these alloys has required the additions of β-stabilizing elements, such as Nb, V, or Mo. For this purpose, a series of Ti_3Al-(Nb,V,Mo) alloys were developed based on an $\alpha_2+\beta$ microstructure, Ti-25Al-10Nb-3V-1Mo (at.%) "super-α_2" being among the most promising compositions.

Further investigations [2-4] have shown that the room temperature ductility and fracture toughness of ($\alpha_2+\beta$)-titanium aluminides can be additionally enhanced through control of α_2/β volume fraction, α_2 phase morphology, β phase distribution and grain size. Therefore, attainment of optimized properties requires careful selection and control of manufacturing process control parameters. As a consequence, relationships between initial microstructure, processing conditions and final microstructure should be investigated. In this regard, previous attempts at process control have been based on either a knowledge of atomic processes that define selected deformation mechanisms [5], or mechanistic models for defect nucleation [6]. Unfortunately their applicability is limited to simple engineering materials, *e.g.*, stable single phase alloys. A newer method, Dynamic Material Modeling (DMM), has been recently formulated [7-9] that allows the study of advanced materials, *e.g.*, multi-phase alloys. This method defines "stable" plastic flow regions of strain rate and temperature at selected strains.

Dynamic material modeling assumes that the instantaneous power P absorbed by the workpiece during plastic flow is dissipated by partitioning into a dissipator content G, which is the work dissipated by plastic work, and is related to continuum effects, and a dissipator co-content J, which is the work related to the metallurgical mechanisms which occur dynamically to dissipate power, and is therefore related to microstructural changes. The power P can then be written as:

$$P = \bar{\sigma}.\dot{\bar{\varepsilon}} = \int_0^{\bar{\sigma}} \dot{\bar{\varepsilon}}.d\bar{\sigma} + \int_0^{\dot{\bar{\varepsilon}}} \bar{\sigma}.d\dot{\bar{\varepsilon}} = J+G \qquad (1)$$

where σ is the effective stress and ε is the effective strain rate.

Based on continuum mechanics and extremum irreversible thermodynamics principles, four stability criteria can be derived and utilized to establish "stable" zones within strain rate-temperature processing maps. The four stability criteria are:

$$0 < m < 1 \qquad (2)$$

$$\left[\frac{\delta m}{\delta(\log\dot{\bar{\varepsilon}})}\right]_{T,\bar{\varepsilon}} < 0 \qquad (3)$$

$$s > 1 \qquad (4)$$

$$\left[\frac{\delta s}{\delta(\log\dot{\bar{\varepsilon}})}\right]_{T,\bar{\varepsilon}} < 0 \qquad (5)$$

where m, the strain rate sensitivity factor, is defined as

$$m = \left[\frac{\delta(\log\bar{\sigma})}{\delta(\log\dot{\bar{\varepsilon}})}\right]_{\bar{\varepsilon},T} \tag{6}$$

and s, the entropy factor, is related to the ratio of the rate of entropy produced by the system with respect to the rate of entropy applied to the system:

$$s = \left(\frac{1}{T}\right)\cdot\left[\frac{\delta(\ln\bar{\sigma})}{\delta\left(\frac{1}{T}\right)}\right]_{\dot{\bar{\varepsilon}},\bar{\varepsilon}} \tag{7}$$

This approach has been applied and validated for deformation of several simple and advanced materials [9-14] wherein dynamic microstructural rearrangements, *e.g.*, dynamic recrystallization-recovery or spheroidization, have been shown to be predominant energy dissipative mechanisms in "stable" regions. "Unstable" regions have similarly been associated with microstructural features such as cavitation, wedge cracking, kinking, and particle cracking. In particular, studies of titanium-base alloys and titanium aluminides indicate that morphological rearrangements, principally those associated with dynamic recrystallization of α- or α_2-phase microconstituents [14,15-16,19] or spheroidization of lamellar $\gamma+\alpha_2/\alpha$ microstructures [11,12] during deformation processing, are primary high temperature dissipative mechanisms, optimized processing of titanium alloys/aluminides being best undertaken within the strain rate-temperature region associated with these dissipative mechanism.

This study was undertaken to investigate various influences of morphological rearrangements on the high strain, high temperature deformation mechanisms in a forged Ti-26Al-10Nb-3V-1Mo (at.%) alloy, exhibiting an initial Widmanstätten$\{\alpha_2+\beta\}$ + grain boundary α_2 microstructure. Further comparison with Ti-25Al-11Nb [14], which possesses an initial Widmanstätten$\{\alpha_2+\beta\}$ + primary α_2 microstructure, will be also presented to provide a general framework detailing the high temperature, high strain flow characteristics of Ti_3Al-(Nb,V,Mo) $(\alpha_2+\beta)$ intermetallics.

Experimental details

Material characterization

The Ti_3Al-Nb alloy investigated, Ti-26Al-10Nb-3V-1Mo (at.%), was supplied by TIMET and was received as a 152.4 mm thick slab having previously been forged from a 3400 kg triple vacuum melted production ingot. Prior thermal history consisted of heating to 1533K, holding at this temperature for 8 hours, forging, and then air cooling to ambient temperature. Table 1 lists the chemical composition of the alloy.

The as-received alloy exhibited a Widmanstätten α_2 + β/B2 microstructure with grain boundary α_2^{GB}, Figure 1. Ambient temperature x-ray diffraction confirmed this α_2 + β/B2 structure, with in addition a small quantity of the orthorhombic phase O.

Elevated temperature compression testing

Cylindrical samples (L_0=30.48mm, D_0=20.32mm, L/D ratio=1.5), machined parallel to the forging axis, were utilized to examine the high strain, high temperature deformation behavior of Ti-26Al-10Nb-3V-1Mo. In addition, ring samples with an OD/ID/H (outside

diameter, inside diameter, and height, respectively) ratio of 6/3/2 were deformed to evaluate frictional correction factors [20]. In each instance, boron nitride was used as the lubricant with HfC dispersion strengthened Mo (T < 1373K) or SiC (T > 1373K) compression platens.

Uniaxial hot-compression was performed in high purity argon environment (< 1ppb O_2). Prior to testing, a vacuum of 1 mPa was achieved and the chamber was then backfilled to a pressure of 13.8 kPa with high purity gettered argon gas. In all tests, specimens were heated at a constant heating rate of 20 K/min, soaked at deformation temperature for 10 minutes prior to testing, tests being conducted at temperatures between 1073 and 1473K, the deformation temperature being monitored within ± 1K by two type C thermocouples spotwelded to the sample. Compression testing at constant true strain rates between 10^{-4} and 1 s^{-1} was performed in stroke control, the constant strain rate being achieved by utilizing an exponential decay signal input. Deformation times at temperature were approximately 117 min., 11 min., 70 sec., 7 sec., and 0.7 sec, respectively.

In order to retain the in-situ microstructure after deformation for subsequent microstructure observations the samples were argon gas-jet cooled immediately following straining. Undeformed samples were also prepared in the same system by heating at 20K/min, soaking for ≃ 2 hours (soak time similar to the longest deformation processing time), and cooling.

Data acquisition involved recording load and stroke vs. time. Corrections of the flow stress-strain data for friction and deformation-heating effects were performed, details of both procedures being given in a previous publication [21].

Microstructural observations

Metallographic studies were performed by optical microscopy on the as-deformed samples, the latter being sectioned at their medium section parallel to the compression axis. Surfaces of observation were polished and finally etched with Kroll's reagent prior to microstructural observations which were conducted in the center zone of the sections.

Results

At the lowest temperatures examined, 1073-1273K, the uncorrected flow curves exhibited strain hardening at low strains, followed by a maxima and flow softening, ultimately achieving steady state flow.[1] Following correction for adiabatic heating this flow softening was eliminated at the highest strain rates, *i.e.*, 10^{-1} and 1 s^{-1}, the isothermal flow stress curves exhibiting strain hardening at high strains, Figure 2. Finally, with increasing test temperature and/or decreasing strain rate, the initial strain hardening regime was eliminated, flow softening commencing upon yielding.

As the β transus (1407K) [21] was approached the flow curves also exhibited an initial flow stress drop followed by steady-state behavior, the amplitude of the yield drop decreasing with increasing temperature and decreasing strain rate. A more complete description of this phenomenon will be presented elsewhere [22].

---

[1] Samples examined at 1073-1123K/>10^{-2} s^{-1} and 1173K/>10^{-1} s^{-1} failed by catastrophic shear during compression and therefore lower temperature and higher strain rate conditions were not considered for further testing.

Figure 3 summarizes the dependence of the flow stress of Ti-26Al-10Nb-3V-1Mo upon temperature and strain rate. The flow stress decreased with increasing temperature, with the rate of change of flow stress with temperature decreasing with increasing strain. Comparison of the flow stress - temperature dependence of Ti-26Al-10Nb-3V-1Mo with conventional Ti-6-4 and Ti-6242 $\alpha+\beta$ alloys [17-19] and with another $\alpha_2+\beta$ (Ti-25Al-11Nb [14]) alloy demonstrates a stronger flow stress dependence upon temperature, *e.g.* $(d\sigma/dT)\{\alpha_2+\beta\} \simeq 2.2(d\sigma/dT)\{\alpha+\beta\}$ and $\simeq 1.7(d\sigma/dT)\{\alpha_2+\beta(\text{Ti-25-11})\}$ within the β_t-100 and β_t-300 temperature range.

Discussion

As illustrated by Figure 2, the flow stress-strain-temperature-strain rate behavior of Ti-26Al-10Nb-3V-1Mo is complex. Interpretation of this flow behavior requires a detailed knowledge of the microstructural stability. For example a previous study [21] has shown that isochronal exposure of Ti-26Al-10Nb-3V-1Mo, with an initial Widmanstätten $\alpha_2+\beta$/B2 microstructure, first results in transformation of the orthorhombic O phase to α_2, followed by dissolution of the α_2 phase, and subsequent B2 disordering below the β transus (1407K), Table 2. Knowledge of this microstructural stability can be coupled with dynamic material modeling (DMM) to select optimal deformation conditions, temperature and strain rate, for high temperature processing of Ti-26Al-10Nb-3V-1Mo.

In this approach, the strain rate sensitivity, m, is considered to be a critical parameter function of temperature and strain rate, Figure 4. High m values were observed within two temperature/strain rate regions, at 1398K and $10^{-4}s^{-1}$, and at 1423 K and 1 s^{-1}, where the alloy is primarily β and completely β, respectively. These high m values may be associated with grain boundary sliding or more generally with grain boundary associated deformation [11] at these high temperatures where deformation is controlled by the β phase. Indeed, the presence of a yield drop, which is related to initiation of plastic flow at/within the grain boundary region, in this temperature range supports this suggestion [22]. Maximum m values representative of superplasticity ($m > 0.5$) were also observed in the present study at 1273K and $10^{-4}s^{-1}$, Figure 4. This regime coincides with a previous study by Yang *et al.* [23] who reported that Ti-25Al-10Nb-3V-1Mo is superplastic ($m \simeq 0.6$) at low strain rates ($5x10^{-5}$-$1.5x10^{-4}s^{-1}$) and intermediate temperatures (1223-1283K), a maximum elongation of 570 pct. being reported at 1253K and $1.5x10^{-4}s^{-1}$.

Application of the DMM mechanistic stability criteria, $0 < m < 1$ and $\delta m/\delta \log \dot{\bar{\varepsilon}} < 0$, to the high temperature deformation of Ti-26Al-10Nb-3V-1Mo at three different strains (0.05, 0.35, and 0.65) is shown in Figure 5 where unstable flow regions are shown as grey-shaded areas.[2] Unstable deformation at low strain (0.05) based on these criteria is observed at low temperature, $T < 1273K$, and low strain rate, $< 10^{-2}s^{-1}$. As the deformation strain increases, this unstable region ultimately expands to higher temperatures. In addition, unstable flow is observed at high temperatures ($T > 1323K$) at both high ($> 10^{-1}s^{-1}$) and low ($< 10^{-3}s^{-1}$) strain rates, the extent of these unstable zones increasing with increasing strain. Finally, at high strain (0.65) an additional instability appears in the low temperature / high strain rate regime.

---

[2] According to Footnote 1, samples examined at the lowest temperatures and highest strain rates are included within the unstable region at the highest strain (0.65), as illustrated by the addition of dashed lines in the following processing maps.

Additional DMM deliberations involve consideration of the entropy factor, s, as defined by Equation (7). This factor, calculated from the computation of the slope of the Log (σ) vs. 1000/T plots in Figure 6, distinguishes three regions at low, intermediate, and near/above the β transus temperatures. These three regions are associated with the $O+\alpha_2+\beta$, $\alpha_2+\beta$, and β phase fields, respectively.

Figure 7 summarizes the application of the DMM "thermodynamic" stability criteria, $s > 1$ and $\delta s/\delta \log \dot{\bar{\varepsilon}} < 0$, to the high temperature behavior of Ti-26Al-10Nb-3V-1Mo at three different strains (0.05, 0.35, and 0.65). High s values are observed at low strain rates and intermediate temperatures. While this maximum location is independent of strain, the absolute value of s increases with increasing strain. Three distinct regions based on these criteria were observed at low strain (0.05) within the (i) low temperature and low strain rate, (ii) high temperature and low strain rate, and (iii) high temperature and high strain rate regimes. As strain increases (0.35 and 0.65), both the low temperature/low strain rate and high temperature/high strain rate instabilities disappear while the high temperatures/low strain rates region is shifted to higher rates. A new region of instability is observed at low temperature/high rates at high strain (0.65).

In order to assist in defining operative microstructural mechanisms in high temperature deformation, values of activation energy for Ti-26Al-10Nb-3V-1Mo were calculated by assuming the general power law functional relationship:

$$\dot{\bar{\varepsilon}} = A\bar{\sigma}^{n}\exp\left(\frac{-Q_a}{RT}\right) \qquad (9)$$

where A is a microstructure-dependent constant, n the stress dependence of the strain rate, R is the gas constant, and Q_a is the apparent activation energy. Computations of Q_a were performed at low strain, $\bar{\varepsilon} = 0.05$, in order to minimize microstructural changes induced by deformation. The results of these computations could discern three regimes, *i.e.* a warm working (< 1123K), a hot working (> 1123K - β transus), and a β-working (near-above β transus) regime, as previously endorsed by [15] in cast Ti-24Al-11Nb. Values of the activation anergies were < 700 kJ/mol, 700-900 kJ/mol, and < 500 kJ/mol, respectively, for the three aforementioned regimes, comparable with [15]. However the absence of primary α_2 colonies in the Ti-26Al-10Nb-3V-1Mo alloy resulted in lower activation energies in the intermediate hot working temperature range (1173-1423K) as compared to Ti-24Al-11Nb [15], plastic flow in this region apparently being associated with the deformation characteristics of the α_2 phase.

According to the DMM theory [10,11], stable processing windows predicted by DMM criteria should be located within "stable" Q regimes, *i.e.*, where a plateau of Q_a values exists over the temperature/strain rate range considered. The DMM maps shown in Figure 8 combines both mechanistic and thermodynamic criteria at each of the three selected strains with activation energy values of Ti-26Al-10Nb-3V-1Mo, where the optimal strain rate and temperature regimes for "stable" flow are specified at each strain. Indeed Q_a values for Ti-26Al-10Nb-3V-1Mo, Figure 8, do not exhibit large variations throughout the stable temperature/strain rate regime examined. Stable conditions according to DMM criteria exist within temperatures ranging from 1173 to 1378 K at strain rates between 10^{-3} and 10^{-1} s^{-1}, and above the β transus at strain rates between 10^{-2} and 10^{-1}s, both regions exhibiting "stable" Q_a behavior.

Verification of the utility of the DMM approach also requires microstructural information in order to correlate DMM predictions with high strain deformation characteristics. These

microstructural features are summarized in Figure 9 where observed deformation mechanisms are indicated for each stable/unstable region.

During low temperature deformation in the $\alpha_2+\beta$ phase field at high strain rates and low temperatures, extensive macroscopic flow localization accompanied by cracking was observed, Figure 10 [3], with shear band fracture developing at high strains (0.65). Catastrophic shear failure was observed at the lowest temperature and highest strain rate conditions investigated. Microscopic kinking and/or breakage of the fine Widmanstätten α_2 platelets, Figure 11, was also observed with the unstable low temperature / high strain rate regime.

Unstable flow in the high temperature regions, T > 1323 K, was ascribed to non-uniform deformation within the predominantly β microstructure [22]. At high rates, $>10^{-1}s^{-1}$, where strain is localized at β grain boundaries, relaxation may eventually be achieved by dynamic recrystallization or by grain boundary cracking, Figure 12. At lower rates, $< 10^{-3}s^{-1}$, serrated grain boundaries resulting from repeated steps of grain boundary sliding and migration are observed, Figure 13. These microstructural observations reinforce the importance of grain boundary-controlled deformation at these temperatures, where high m values and the presence of yield stress drops [22] were observed at low strains. At low strain rates, long time exposure corresponding to these low rates results in dynamic grain growth, an unstable mechanism in this regime.

Microstructural features of the two stable regions, Figure 9, were also evaluated in order to correlate stable flow with related microstructural evolutions. Microstructural observations of undeformed specimens in the same conditions were also conducted. Above the β-transus, as it is suggested by microstructural observation of recrystallized grains in samples deformed in the β-phase field and also by the presence of oscillations in the stress-strain curves associated with this regime, stable flow is to be related to dynamic recrystallization. Below the β transus, stable flow is associated with microstructural changes of the platelet-like α_2 phase. Comparison of microstructural observations for undeformed and deformed specimens, Figure 14 and 15 respectively, indicate that this stable flow region in Ti-26Al-10Nb-3V-1Mo is associated with dynamic spheroidization of the Widmanstätten α_2 platelets.

Comparison with Ti-24/25Al-11Nb : Generalization to Ti_3Al-(Nb,V,Mo) aluminides

The strain-stress behavior of Ti-26Al-10Nb-3V-1Mo is similar to those previously presented for Ti-25Al-11Nb [14], implying that these variations of flow behavior with temperature and strain rate are characteristic of Ti_3Al-(Nb,V,Mo) alloys. Schematically, this behavior can be described by a progression from continuous strain hardening, to flow softening with strain hardening at high strains, to flow softening followed by steady-state, to flow softening upon yielding, to continuous steady-state flow, and finally, to the observation of a yield point, as temperature increases and/or strain rate decreases, Figure 16.

The present results of activation energy computations are similar to those reported for studies in cast Ti-24Al-11Nb [15] and forged Ti-25Al-11Nb [14], Table 3. Comparable Q_a values were observed in the warm working regime (< 700 kJ/mol) as well as in the β-working regime (< 500 kJ/mol) for the three compositions. However, the absence of primary α_2 colonies in the Ti-26Al-10Nb-3V-1Mo alloy appears to be responsible for the lower activation

[3] The non-symmetric deformation was not associated with a developing temperature gradient [24] across the samples as the temperature difference between top and bottom was only 4K.

energies in the intermediate hot working temperature range (1173-1423K), where plastic flow in this region is apparently defined by the morphology and deformation characteristics of the α_2 phase.

DMM predictions for the Ti_3Al-base aluminides are also comparable. Tables 4 and 5 parallel our previous results for Ti-25Al-11Nb [14] with the present Ti-26Al-10Nb-3V-1Mo instability results for each "mechanistic" and "thermodynamic" criteria. Warm working temperatures in this table are described by those temperatures where the microstructure is a stable α_2 + small volume fraction of β, and hot working temperatures are those where the microstructure is unstable $\alpha_2 + \beta$, *i.e.* where the α_2 phase transforms. It is interesting to note that the singular difference between the two alloys results from their respective grain boundary constitution, grain boundary α_2 precipitates being only present in Ti-26Al-10Nb-3V-1Mo. Indeed, higher alloying additions induces higher solute concentration at grain boundaries, which are responsible for unstable flow at high strain rates in the β-phase temperature range [22]. The influence of grain boundary precipitates is also illustrated at intermediate temperatures where they induce grain boundary cracking due to the characteristics of the α_2 phase lining this boundaries which is not present in Ti-25Al-11Nb. Finally these observations may be generalized to $\alpha_2+\beta$ aluminides, where unstable flow is a result of (i) macro-flow localization and (ii) α_2-kinking at low temperatures and/or high strain rates, (iii) grain boundaries flow localization associated with β-phase deformation (yield point) and (iv) dynamic grain coarsening at high temperatures and slow strain rates. Additionally, the presence of the orthorhombic phase in Ti_3Al-(Nb,V,Mo) may contribute to unstable flow as it is suggested that this instability is related to transformations involving this orthorhombic phase, which occurs during long term deformation/aging [25].

Stable conditions for Ti-26Al-10Nb-3V-1Mo can also be correlated with Ti-25Al-11Nb results where the principal stable deformation mechanism in the latter is dynamic spheroidization of primary α_2 colonies. In Ti-26Al-10Nb-3V-1Mo, dynamic spheroidization is also predominant but involves spheroidization of Widmanstätten α_2 platelets. Stable flow in $\alpha_2+\beta$ Ti_3Al-aluminides may therefore be generalized to be associated with (i) dynamic spheroidization of the α_2 microconstituent(s), being present in the microstructure as primary colonies (Ti-24/25Al-11Nb) or Widmanstätten platelets (Ti-26Al-10Nb-3V-1Mo), and (ii) dynamic recrystallization in the β-phase range.

Conclusions

Analysis of the mechanical behavior of Widmanstätten $\alpha_2+\beta$/B2 Ti-26Al-10Nb-3V-1Mo has confirmed that dynamic material modeling (DMM) can be utilized to establish the flow stress-strain rate-temperature-strain criteria for stable flow.

The corrected true stress-true plastic strain behavior of this alloy at low temperatures and high strain rates was characterized by strain hardening followed by flow softening. As the test temperature increased and/or the strain rate decreased, the extent of this strain hardening regime decreased. Ultimately initial yielding was immediately followed by flow softening with steady state flow conditions being observed at higher strains.

Unstable regions predicted by DMM were microstructurally related to kinking of the α_2 platelets and shear band formation within the $\alpha_2+\beta$-phase deformation zone, while related to flow localization at grain boundaries and dynamic grain growth in the β-phase deformation region. Stable flow regimes as predicted by DMM were shown to be associated with dynamic

spheroidization and coarsening of the platelet-like Widmanstätten α_2 in the $\alpha_2+\beta$-phase deformation field, and to dynamic recrystallization in the β-phase deformation field.

Typical elevated temperature plastic flow behavior of $(\alpha_2+\beta)$ Ti_3Al-base aluminides has been defined where instabilities are generally associated with macro/micro flow localization due to the characteristics of the α_2 microconstituent(s) in the $\alpha_2+\beta$-phase range, grain boundary flow localization and dynamic grain coarsening in the β-phase field; stable regimes are representative of dynamic spheroidization of the α_2 microconstituent(s) in the $\alpha_2+\beta$-phase regime and dynamic recrystallization when the alloy is β.

Acknowledgements

This research was initiated under funding by the United States Air Force Office of Scientific Research as part of the Carnegie-Mellon University Research Initiative Program on High Temperature Metal Matrix Composites, Dr. A. Rosenstein contract monitor, contract F49620-87-C-0017, and continued under sponsorship by the Defense Advanced Research Projects Agency under contract N00014-89-J-3166 supervised by Mr. W. Baker and monitored by Dr. G. Yoder of the Office of Naval Research. The alloys utilized were kindly provided by Mr. Ed Mild of TIMET, Inc. Finally, the authors wish to thank Dr. J. C. Malas and Dr. S. Guillard for beneficial discussions.

References

1. R. G. Rowe, in S. H. Wang, C. T. Liu, D. P. Pope and J. O. Stiegler (eds.), *High Temperature Aluminides and Intermetallics*, The Minerals, Metals, and Materials Society, Warrendale, PA, 1989, p. 375.
2. D. A. Koss, D. Banerjee, D. A. Lukasak and A. K. Gogia, in S. H. Wang, C. T. Liu, D. P. Pope and J. O. Stiegler (eds.), *High Temperature Aluminides and Intermetallics*, The Minerals, Metals, and Materials Society, Warrendale, PA, 1989, p. 175.
3. T. Jia, B. Wang, D. Zou, H. Ma, and Z. Zhong, *Mater. Sci. Eng., A152* (1992) 317.
4. F. C. Dary and A. W. Thompson, *Mat. Res. Soc. Symp. Proc., Vol.288* (1993) 703.
5. H. J. Frost and M. F. Ashby, *Deformation-Mechanism Maps, The Plasticity and Creep of Metals and Ceramics*, Pergamon Press, New York, 1982.
6. R. Raj, *Metall. Trans. A, 12A* (1981) 1089.
7. J. C. Malas, *Master Thesis*, Wright State University, Ohio, December 1985.
8. Y. V. R. K. Prasad, H. L. Gegel, J. T. Morgan and J. C. Malas, in F. H. Froes and D. Eylon (eds.), *Titanium Net Shape Technologies*, The Metallurgical Society of AIME, PA, 1984, p. 279.
9. H. L. Gegel, *Computer Simulation in Materials Science*, ASM International, Materials Park, Ohio, 1986, p. 291.
10. J. C. Malas, *Ph. D. Dissertation*, Ohio University, November 1991.
11. J. C. Malas and V. Seetharam, *J. Mater., 44[6]* (1992) 8.
12. S. Guillard, *Ph.D. Dissertation*, Clemson University, May 1994.
13. S. Menon, *Master Thesis*, Clemson University, May 1994.
14. M. Long and H. J. Rack, *Mater. Sci. Eng., A170* (1993) 215.
15. S. L. Semiatin, K. A. Lark, D. R. Baker, V. Seetharam and B. Marquardt, *Metall. Trans. A, 23A* (1992) 295.

16. I. Weiss, F. H. Froes, D. Eylon and C. C. Chen, in F. H. Froes and D. Eylon (eds.), *Titanium Net Shape Technologies*, The Metallurgical Society of AIME, PA, 1984, p. 79.
17. P. Dadras and J. F. Thomas, Jr., *Metall. Trans. A, 12A* (1981) 1867.
18. V. Seetharaman, L. Boothe and C. M. Lombard, in Y-W. Kim and R. Boyer (eds.), *Microstructure/Property Relationships in Titanium Aluminides and Alloys*, The Minerals, Metals & Materials Society, Warrendale, PA, 1991, p. 605.
19. H. J. Rack and A. Wang, in *Proc. 7th World Conf. on Titanium, San Diego, USA, August 1992*, The Minerals, Metals & Materials Society, Warrendale, PA, in press.
20. A. T. Male and M. G. Cockcroft, *J. Inst. Met., 93* (1964) 38.
21. M. Long and H. J. Rack, to be published in *Mater. Sci. Tech.* (1994).
22. M. Long and H. J. Rack, to be submitted (1994).
23. H. S. Yang, P. Jin, E. Dalder and A. K. Mukherjee, *Scripta Metallurgica et Materiala, 25* (1991) 1223.
24. Oh, Semiatin, and Jonas, *Metall. Trans. A, 23A* (1992) 963.
25. J. A. Peters and C. Bass., *Scripta Met. et Mater., 24* (1990) 915.

Table 1. Chemical composition of Ti-26Al-10Nb-3V-1Mo.

	Ti	Al	Nb	V	Mo	O	C	Fe
at.%	bal.	25.79	10.26	3.09	1.04	0.23	0.11	0.07
wt.%	bal.	14.60	20.00	3.30	2.10	0.08	0.027	0.08

Table 2. Phase transformations of Ti-26Al-10Nb-3V-1Mo [19].

Temperature (K)	Phases
$\simeq <$ 1023	Widmanstätten$\{(\beta/B2)_t+\alpha_2{}^S\}$ + O
$\simeq$ 1023 - 1222	Widmanstätten$\{(\beta/B2)_t+\alpha_2{}^S\}$
1222 - 1355	Widmanstätten$\{(\beta/B2)_t+(\alpha_2\rightarrow\alpha)^S\}$
1355 - 1379	B2
1379 - 1407	B2 $\rightarrow \beta$
> 1407	β

Table 3. Comparison of estimated activation energies of $\alpha_2+\beta$ titanium aluminides.

High-Temperature Deformation Domain	Ti-26Al-10Nb-3V-1Mo (forged)	Ti-25Al-11Nb (forged) [16]	Ti-24Al-11Nb (cast) [15]
Warm Working (<1123K)	< 700	< 700	< 815
Hot Working (below β transus)	700-900	1100	1080
β-Working (near-above β transus)	< 500	< 500	278

Table 4. Comparison of instability deformation mechanisms between Ti-26Al-10Nb-3V-1Mo and Ti-25Al-11Nb, when considering "mechanistic" stability criteria.

High-Temperature Deformation Domain	Ti-26Al-10Nb-3V-1Mo (forged)	Ti-25Al-11Nb (forged) [14]
Warm working Low strain rate	flow localization, kinking of α_2 platelets	flow localization, kinking of α_2 lamellae
Warm working High strain rate	shear band, grain boundary cracking	shear band
Hot working Low strain rate	grain boundary flow localization, dynamic grain coarsening	grain boundary flow localization, dynamic grain coarsening
Hot working high strain rate	grain boundary microcracking	stable (yield drop at low strains)

Table 5. Comparison of instability deformation mechanisms between Ti-26Al-10Nb-3V-1Mo and Ti-25Al-11Nb, when considering "thermodynamic" stability criteria.

High-Temperature Deformation Domain	Ti-26Al-10Nb-3V-1Mo (forged)	Ti-25Al-11Nb (forged) [14]
Warm working Low strain rate	flow localization, unstable morphology of α_2 platelets	flow localization, unstable morphology of α_2 platelets
Hot working Low strain rate	grain boundary sliding, dynamic grain coarsening	grain boundary sliding, dynamic grain coarsening
Hot working high strain rate	grain boundary flow localization	stable (yield drop at low strains)

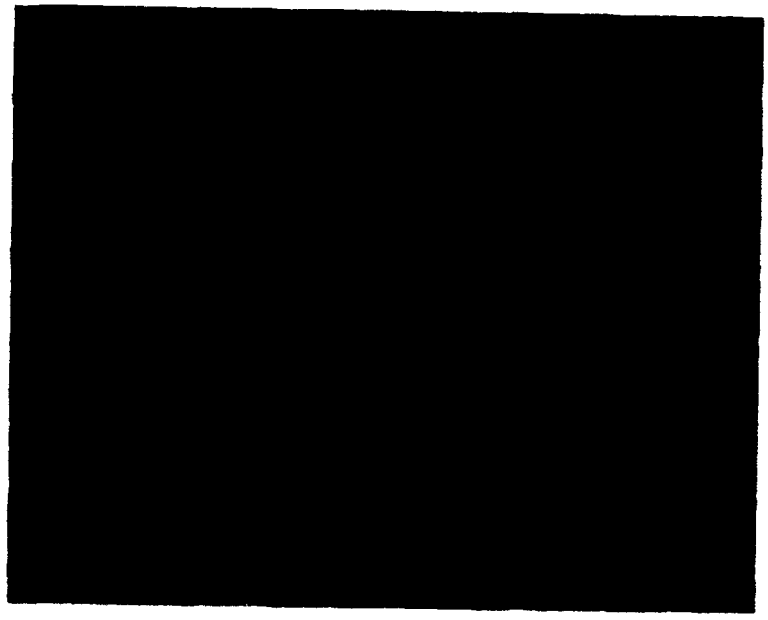

Figure 1. Optical micrograph of Ti-26Al-10Nb-3V-1Mo microstructure in the as-forged condition, exhibiting Widmanstätten $\alpha_2^S+(\beta/B2)_t$ [S] and grain boundary α_2^{GB} [GB].

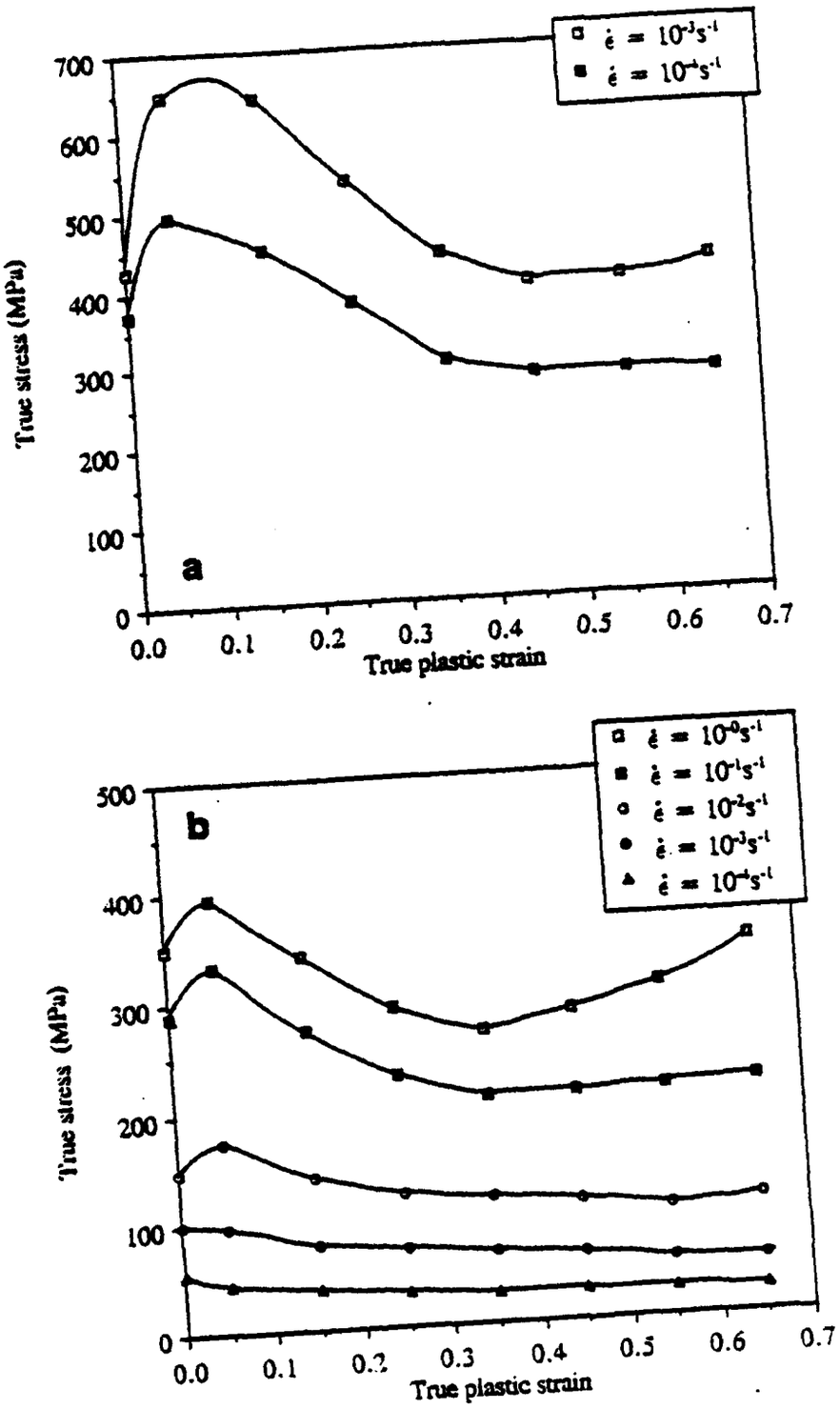

Figure 2. Typical true corrected stress - true plastic strain curves of Ti-26Al-10Nb-3V-1Mo at (a) 1073 K, (b) 1273 K, (c) 1348 K, (d) 1473 K.

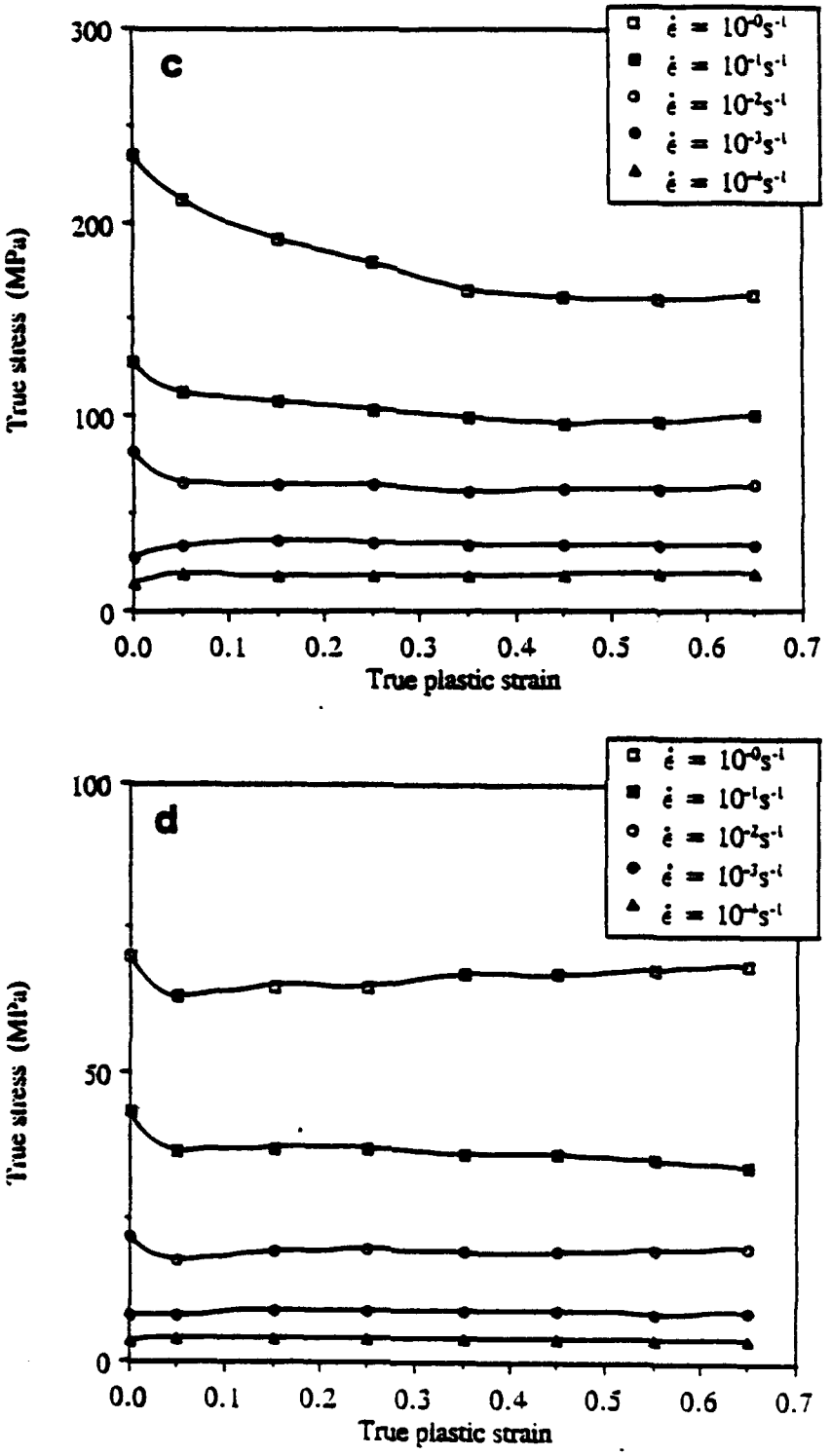

Figure 2. Continued.

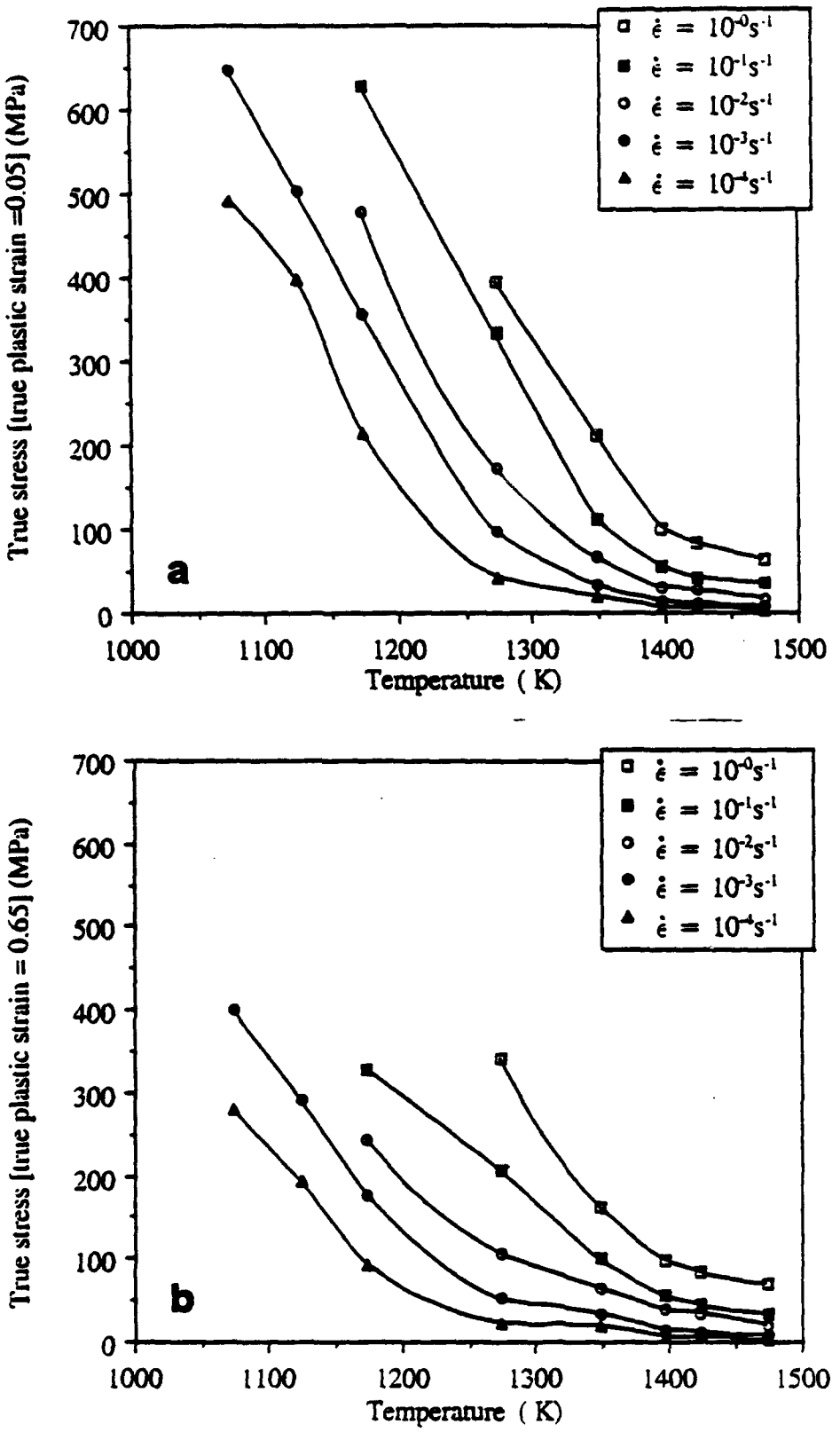

Figure 3. Typical dependence of temperature and strain rate on flow stress at (a) 0.05 and (b) 0.65 true plastic strain in Ti-26Al-10Nb-3V-1Mo.

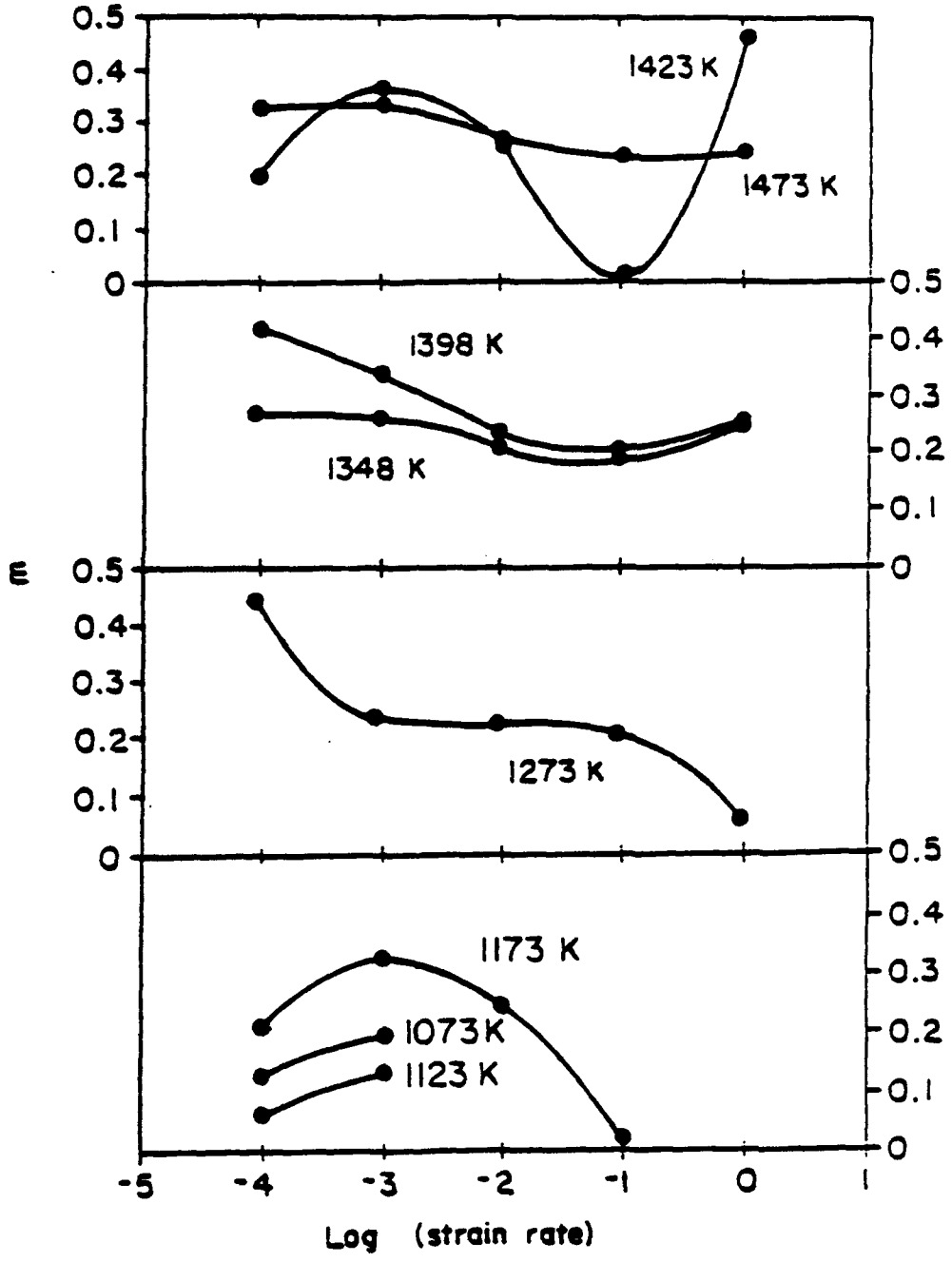

Figure 4. Dependence of temperature and strain rate on strain rate sensitivity m at $\bar{\varepsilon} = 0.35$ in Ti-26Al-10Nb-3V-1Mo.

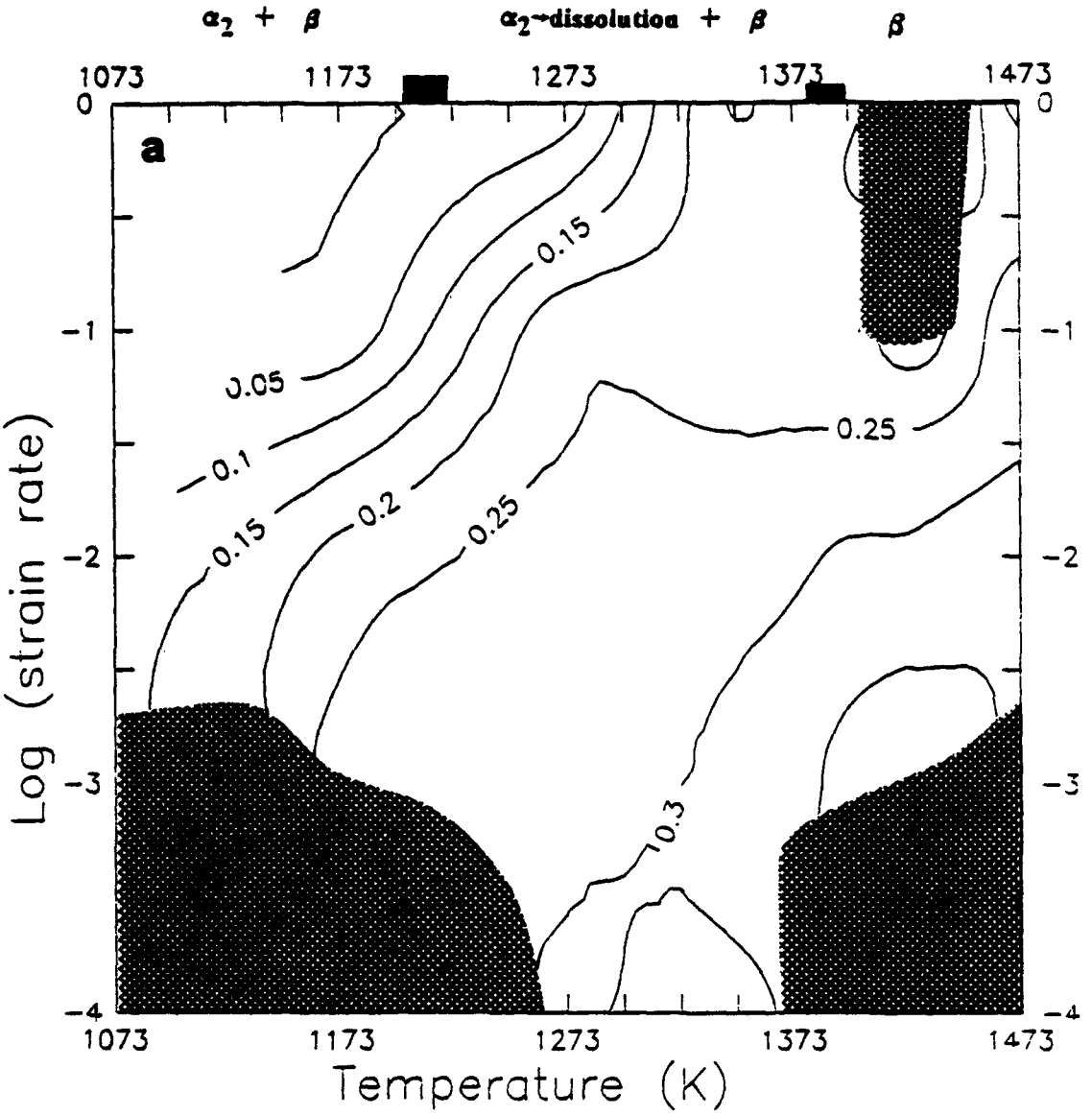

Figure 5. Strain rate sensitivity factor, m, as a function of temperature and strain rate at strains of (a) 0.05, (b) 0.35, (c) 0.65. The shaded areas are unstable zones as defined by mechanistic stability criteria.

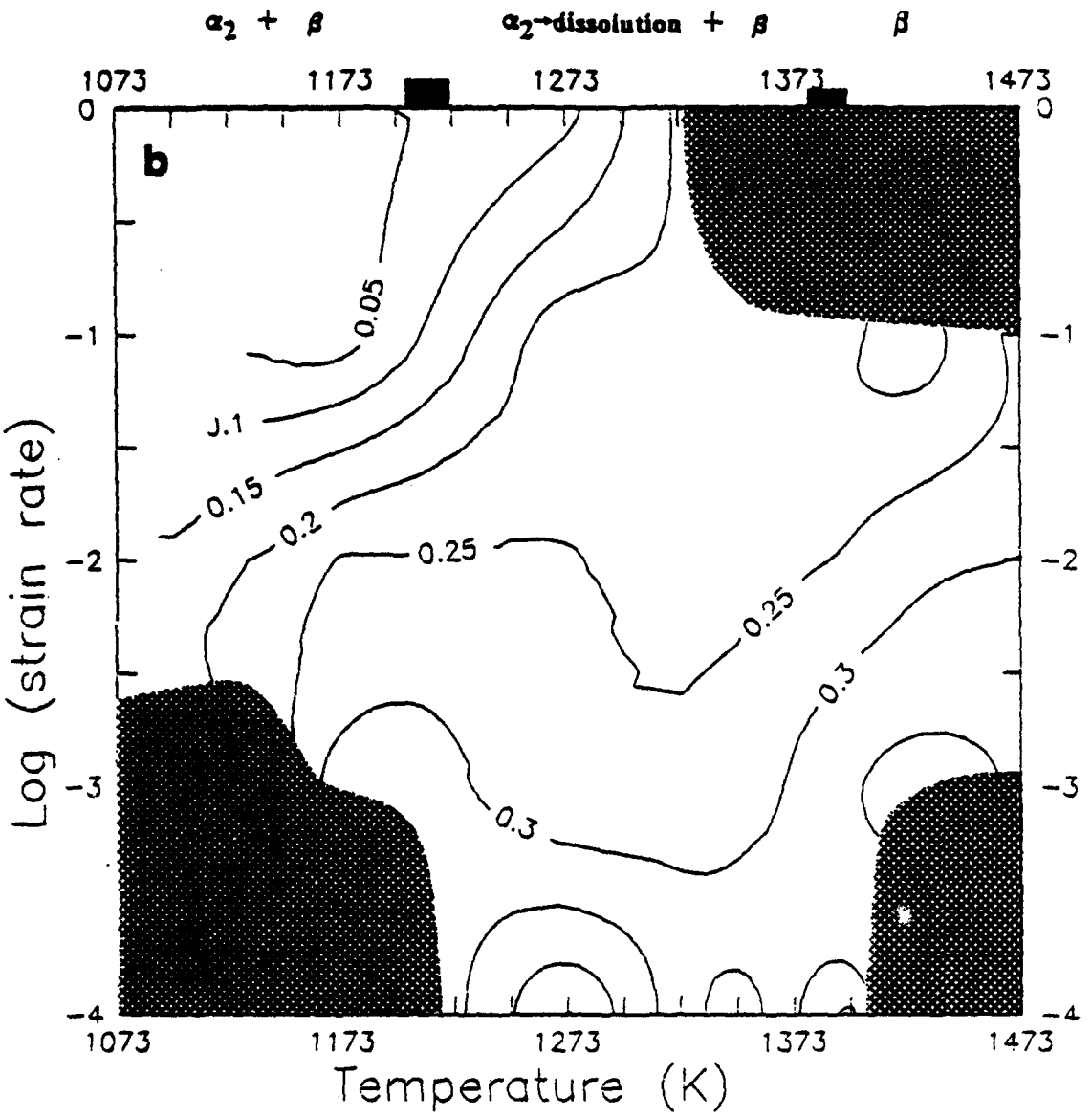

Figure 5. Continued.

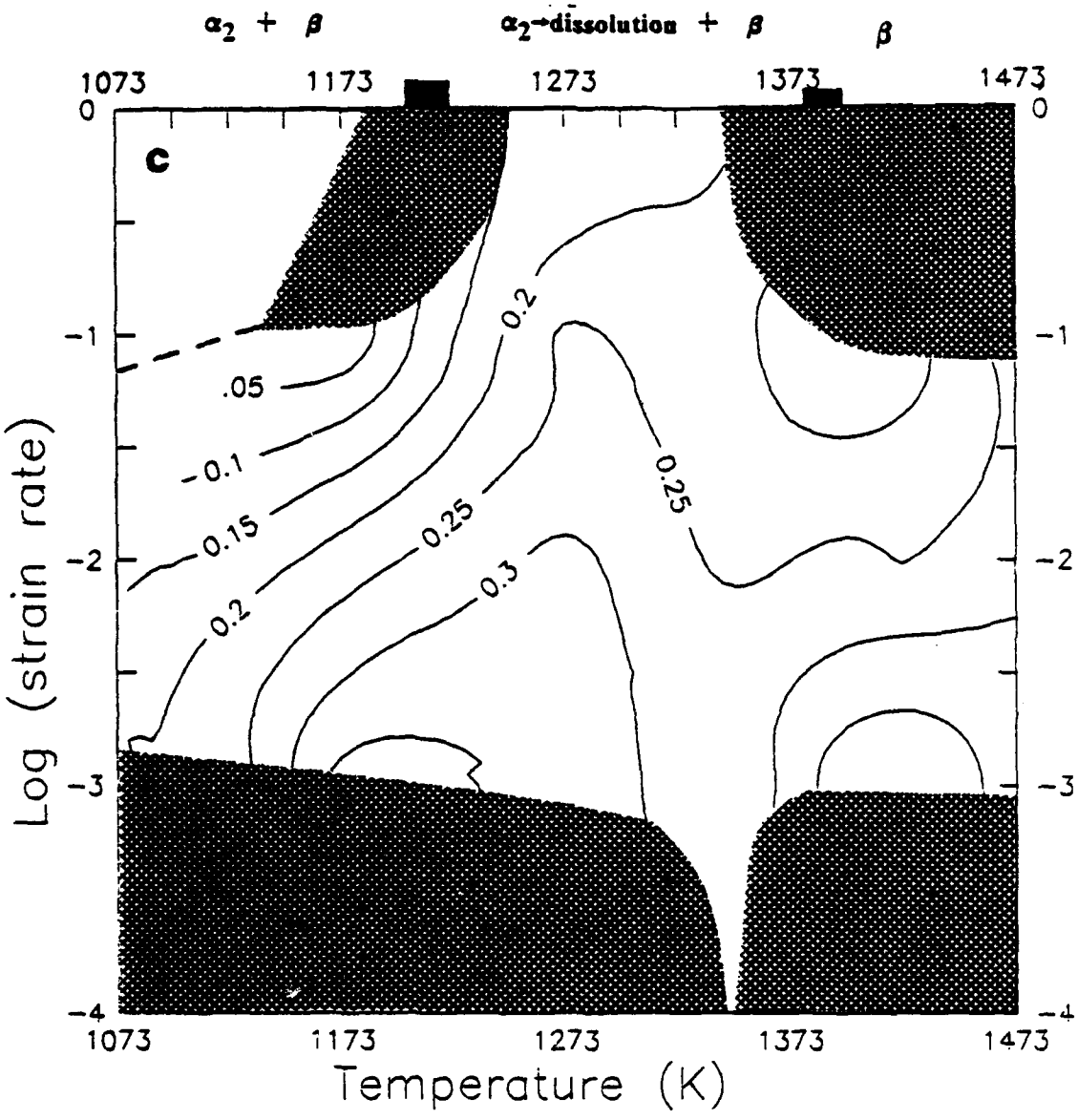

Figure 5. Continued.

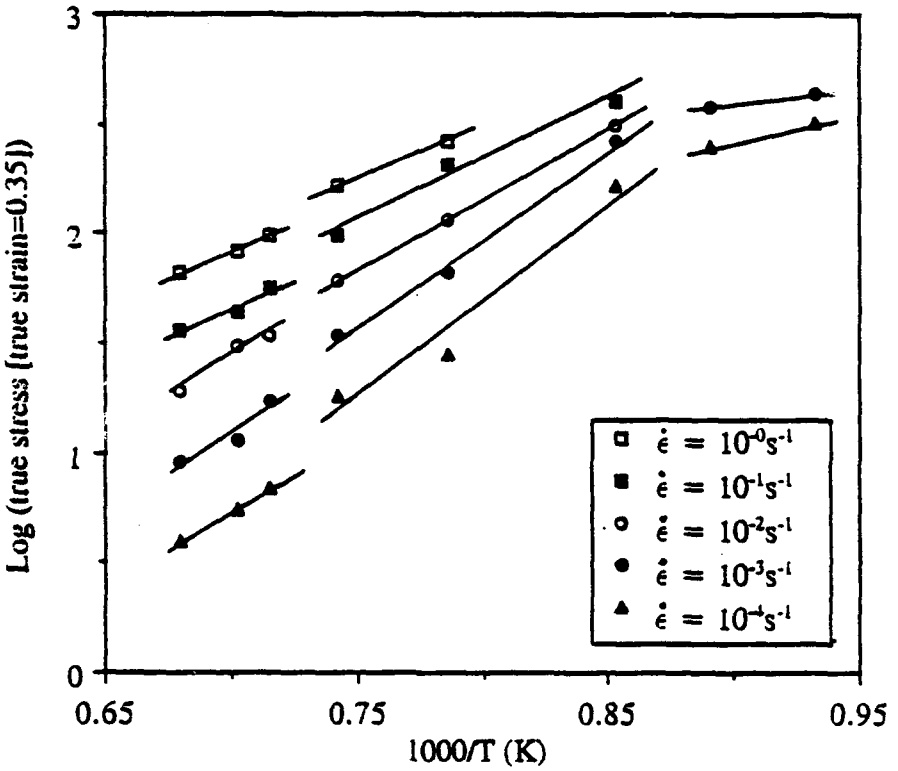

Figure 6. Log (corrected true stress) vs. 1000/T(K) at 0.35 strain. The slope of the different regimes are directly proportional to the entropy factor s.

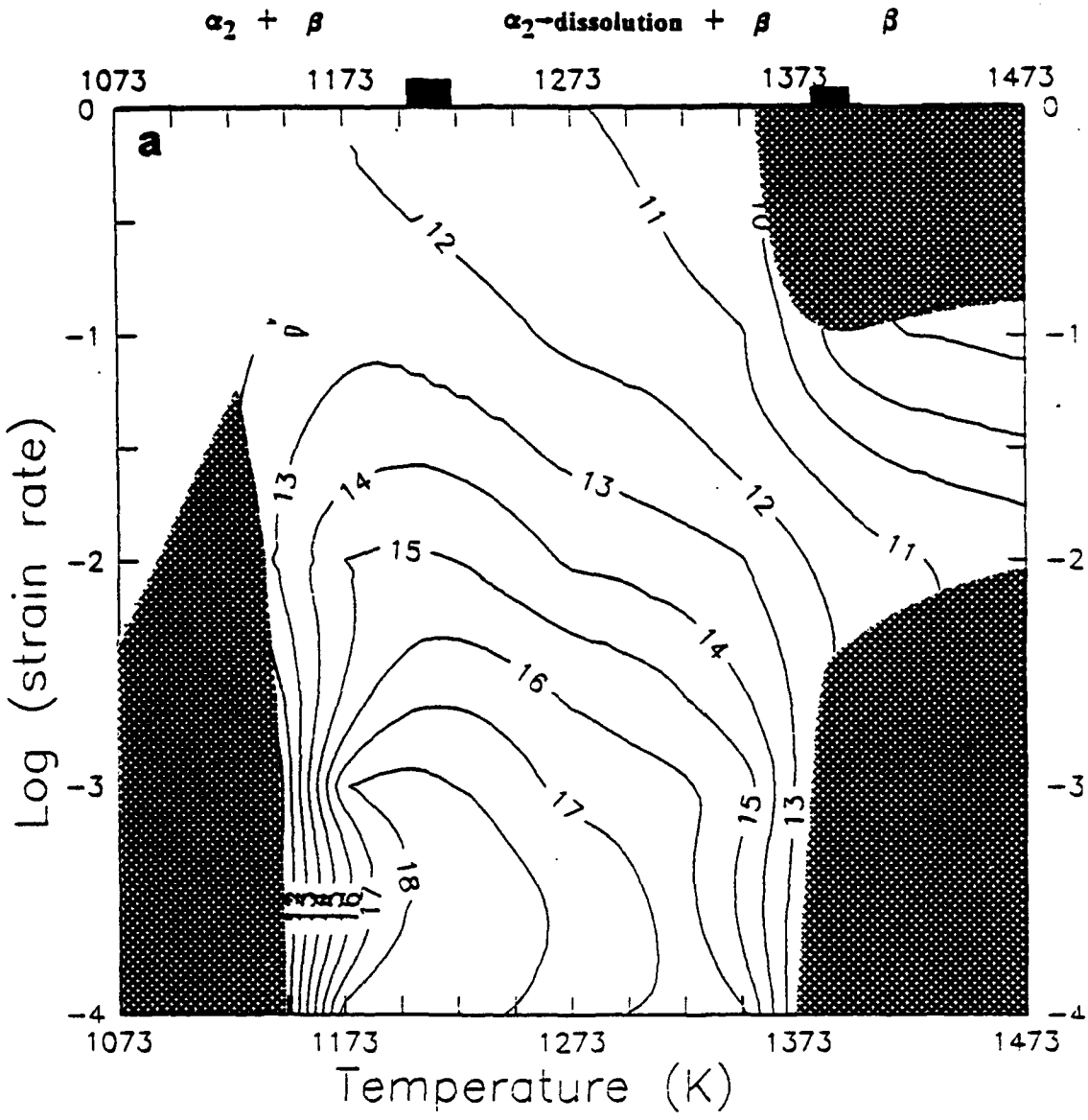

Figure 7. Entropy parameter, s, as a function of temperature and strain rate at strains of (a) 0.05, (b) 0.35, (c) 0.65. The shaded areas are unstable zones as defined by "thermodynamic" stability criteria.

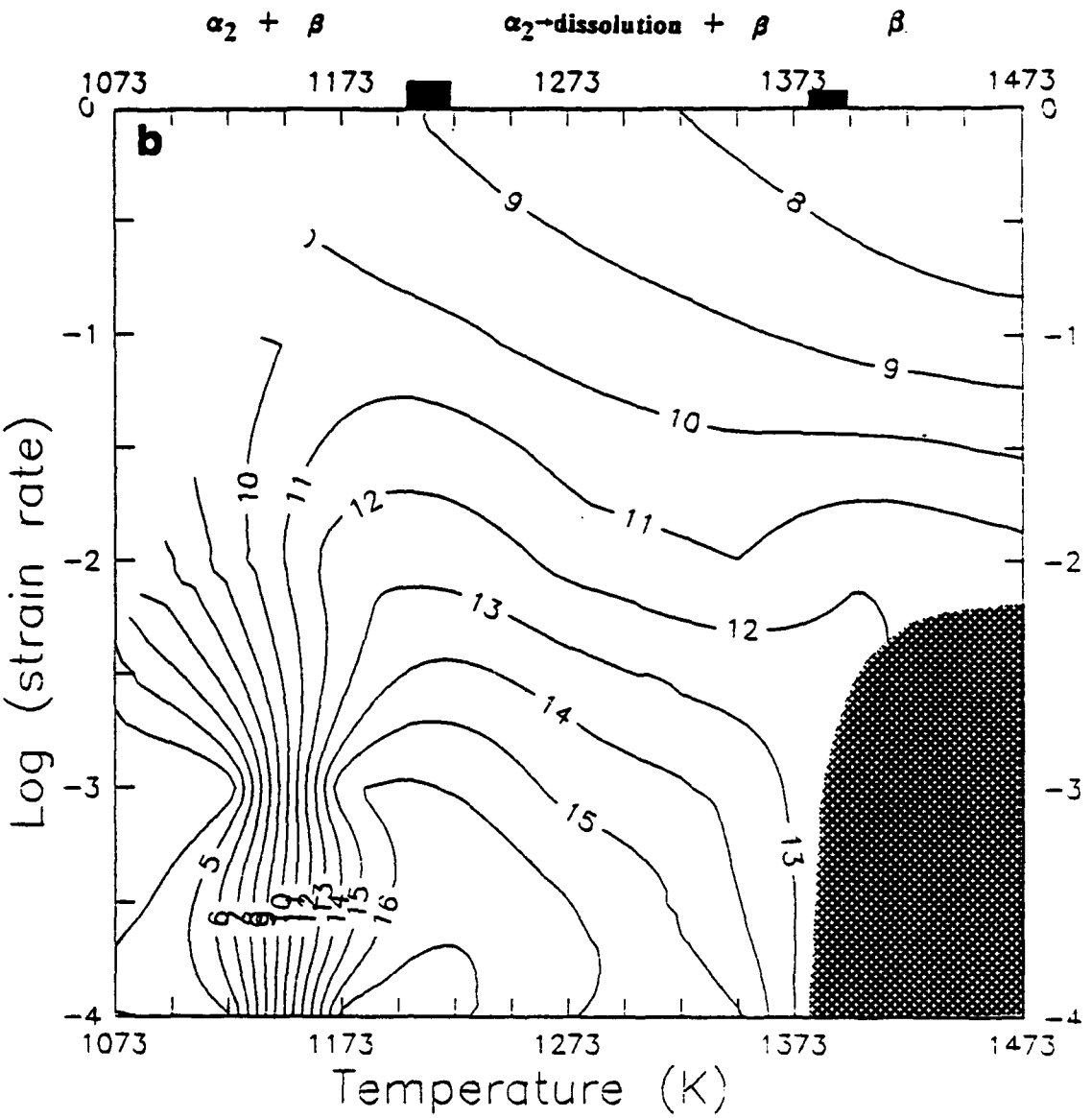

Figure 7. Continued.

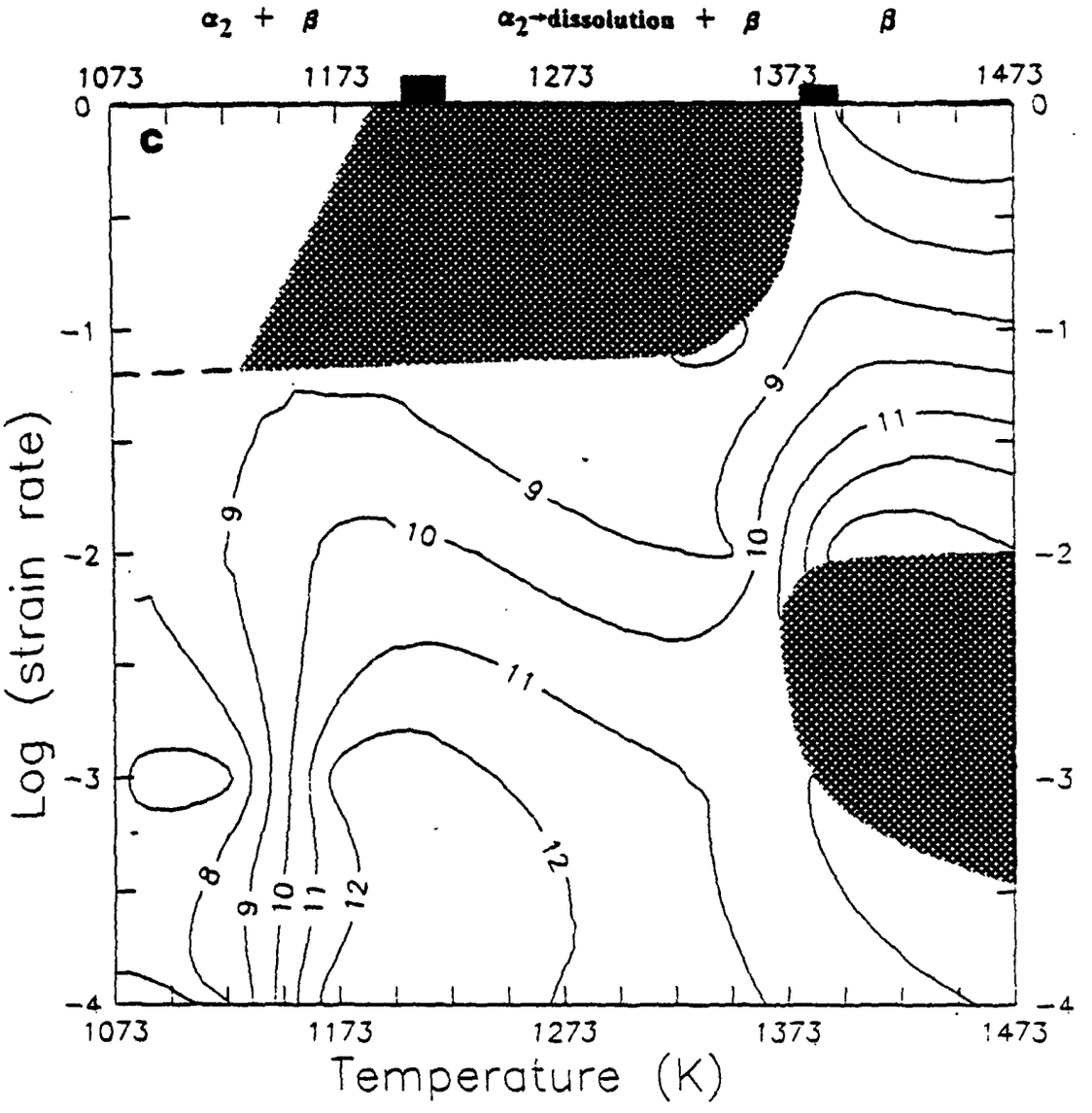

Figure 7. Continued.

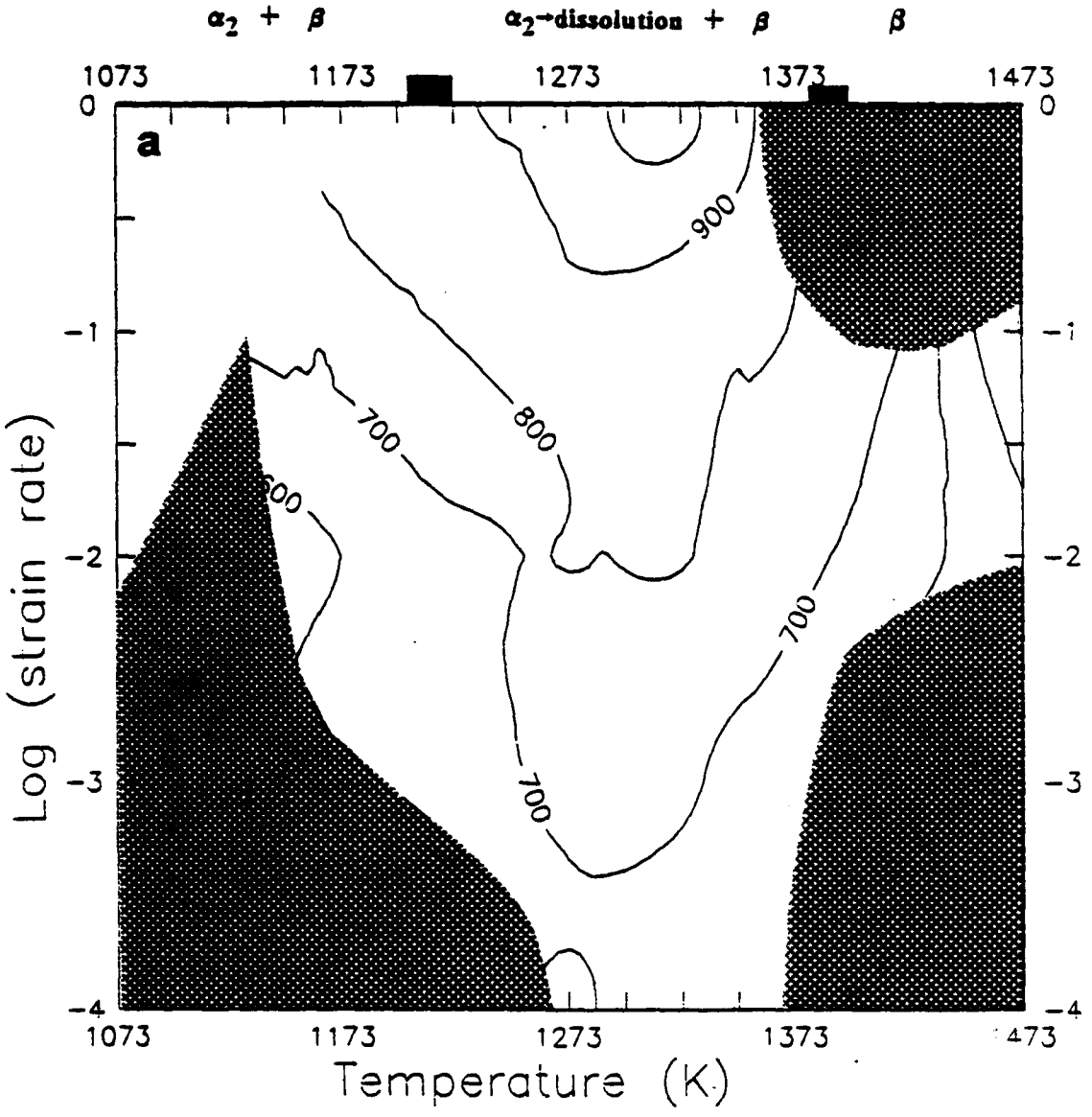

Figure 8. Ti-26Al-10Nb-3V-1Mo DMM stability maps as a function of temperature and strain rate at strains of (a) 0.05, (b) 0.35, (c) 0.65. The shaded areas are unstable zones as defined by all four stability criteria. Q_a values ($kJ.mol^{-1}$) contour lines are plotted as background.

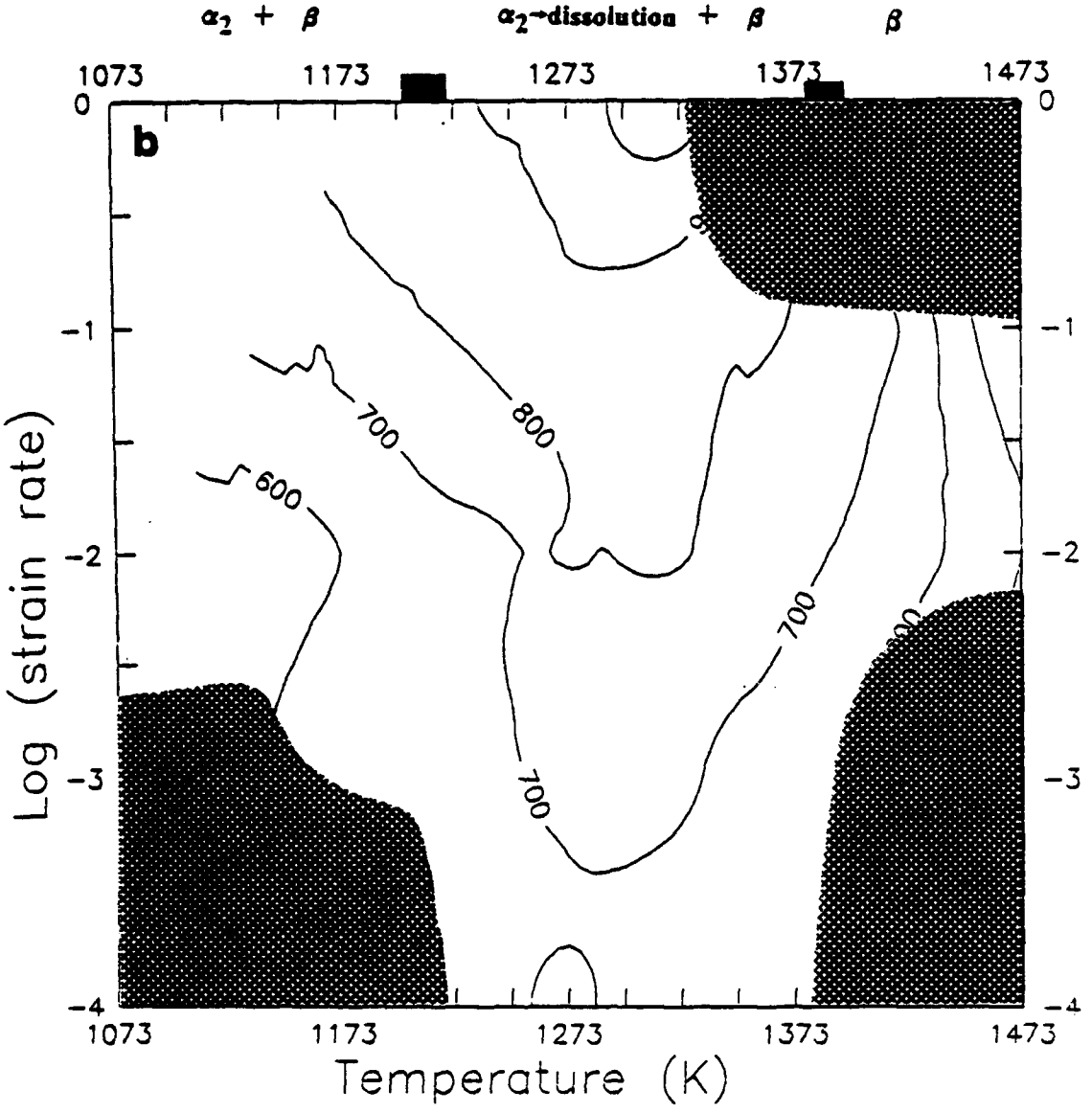

Figure 8. Continued.

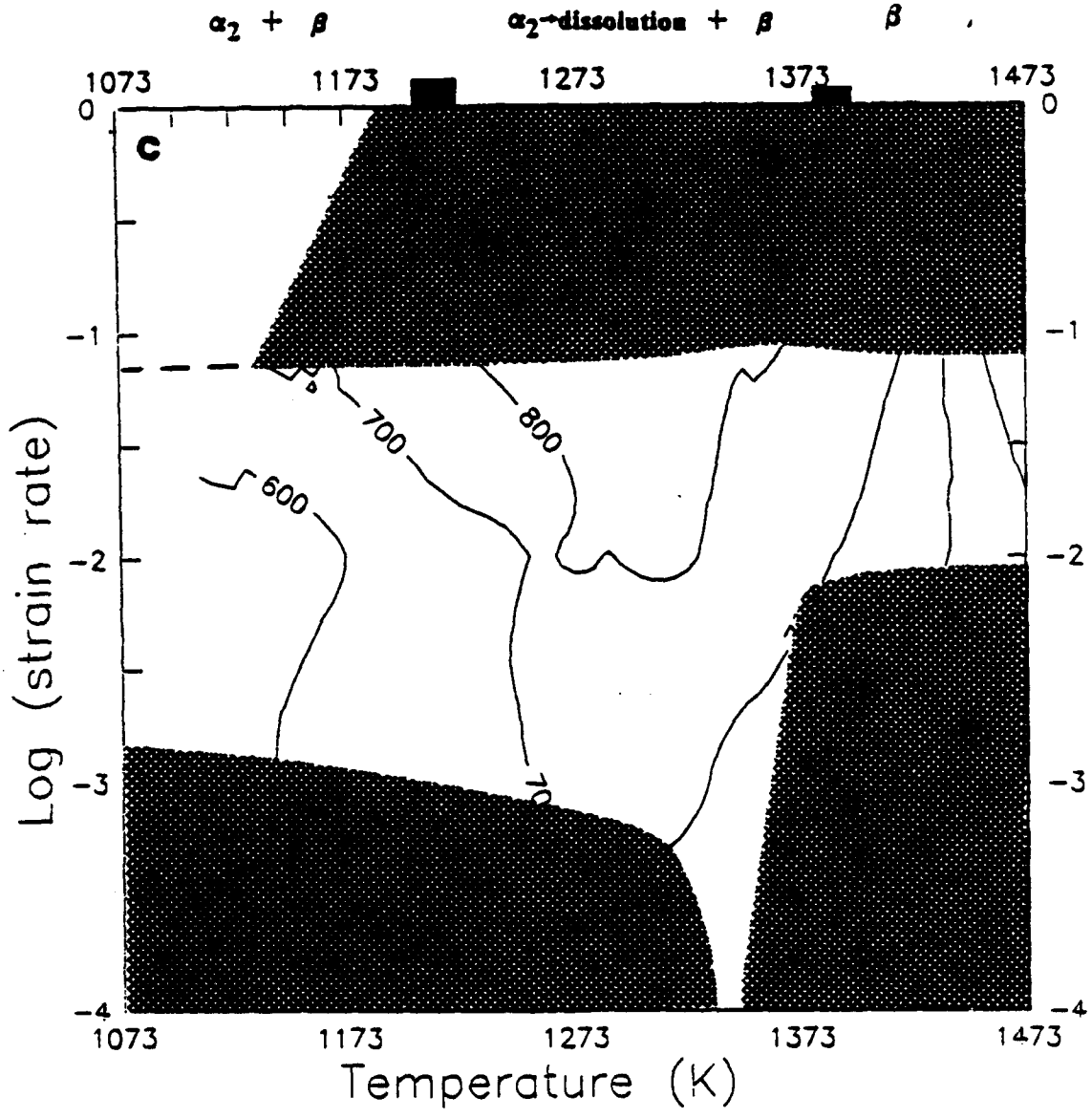

Figure 8. Continued.

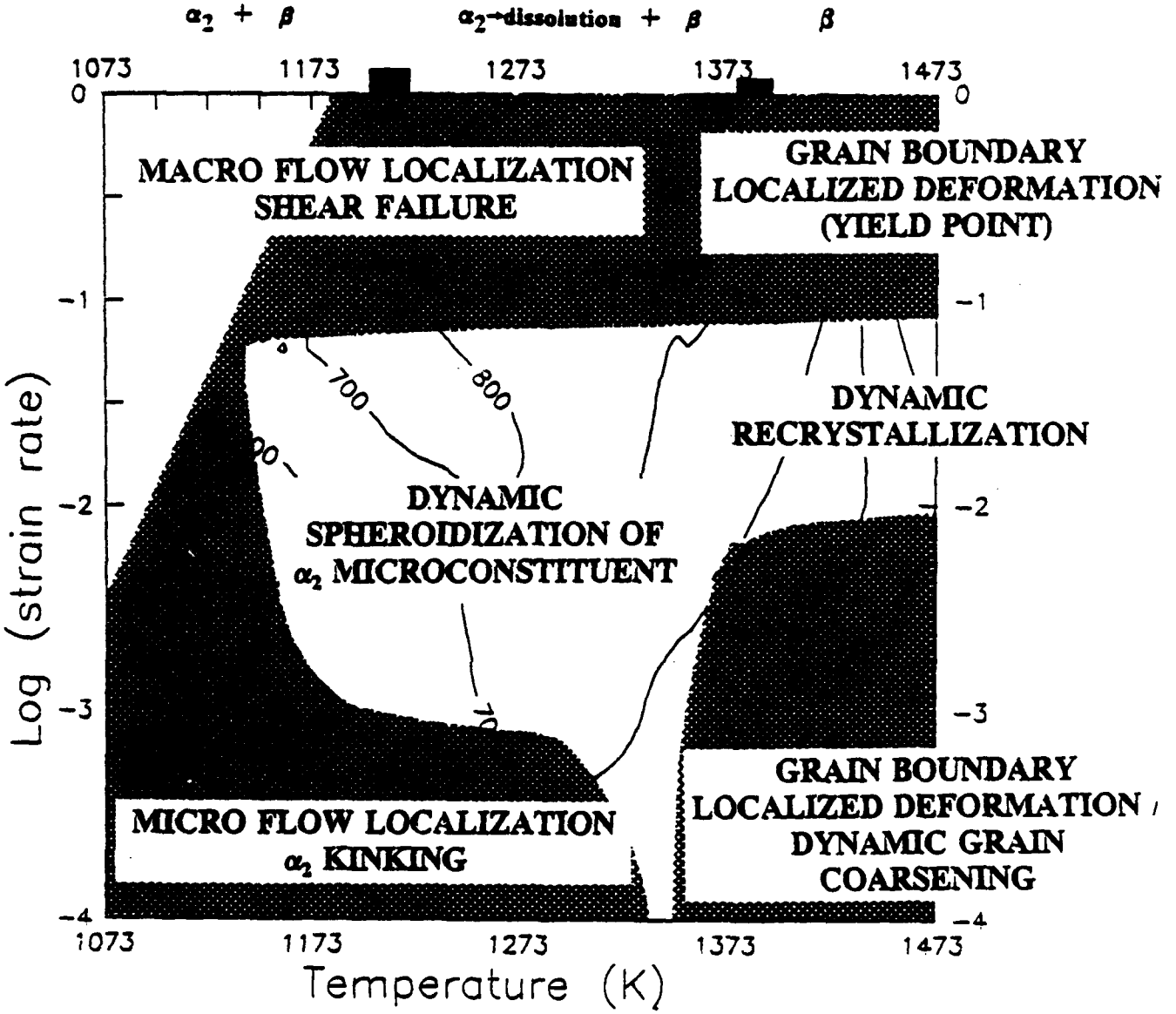

Figure 9. DMM stability maps after merging all four criteria at three different strains with Q_a values (kJ.mol^{-1}) contour lines plotted as background; Ti-26Al-10Nb-3V-1Mo. Deformation mechanisms are indicated for each stable/unstable region.

Figure 10. Optical microstructure of the as-deformed ($\bar{\varepsilon}$ = 0.65) Ti-26Al-10Nb-3V-1Mo sample at constant true strain rate of $10^{-1}s^{-1}$ and test temperature of 1173 K showing shear band formation.

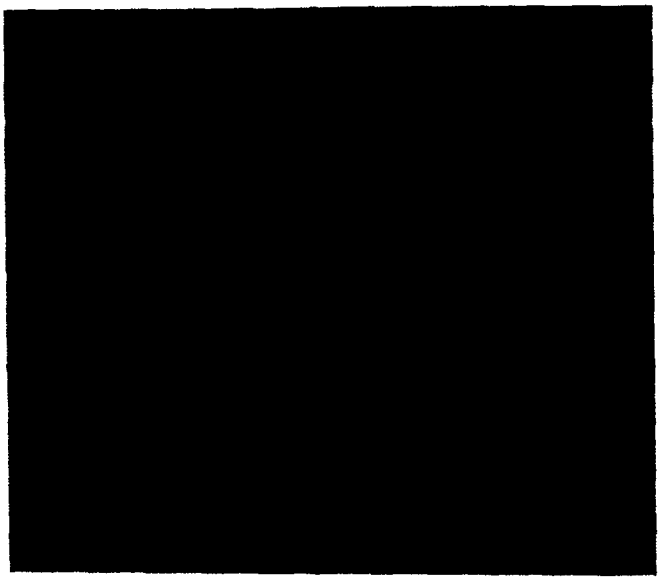

Figure 11. Optical microstructure of the as-deformed ($\bar{\varepsilon}$ = 0.65) Ti-26Al-10Nb-3V-1Mo sample at constant true strain rate of $10^{-3}s^{-1}$ and test temperature of 1173 K showing α_2 kinking/micro-flow localization (arrows).

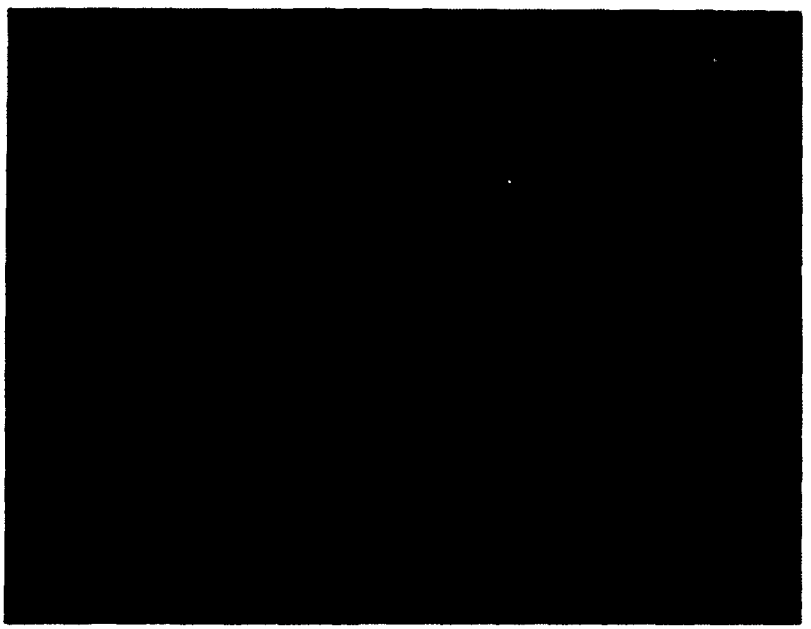

Figure 12. Optical microstructure of the as-deformed ($\bar{\varepsilon}$ = 0.65) Ti-26Al-10Nb-3V-1Mo sample at constant true strain rate of 1 s^{-1} and test temperature of 1473 K. The black arrows indicate recrystallized grains; the white arrows indicate grain boundary cracking.

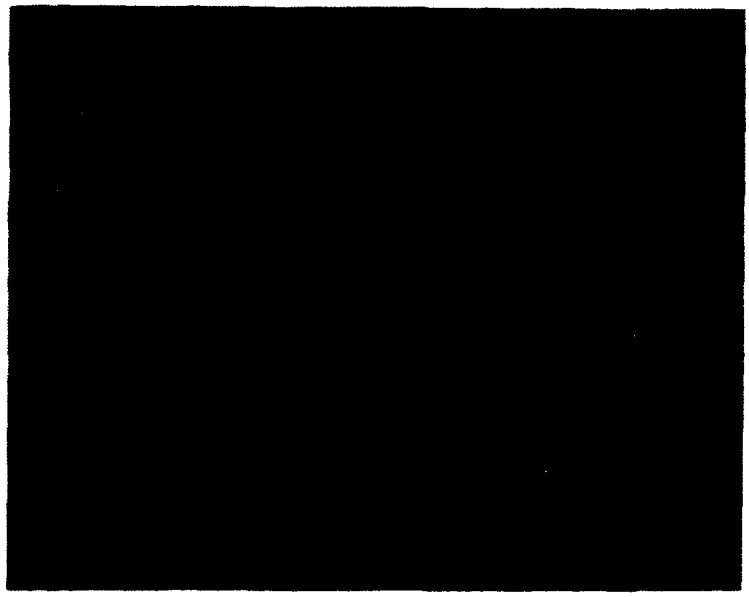

Figure 13. Optical microstructure of the as-deformed ($\bar{\varepsilon}$ = 0.65) Ti-26Al-10Nb-3V-1Mo sample at constant true strain rate of $10^{-4}s^{-1}$ and test temperature of 1348 K.

Figure 14. Optical microstructure of a non-deformed Ti-26Al-10Nb-3V-1Mo sample held at 1348 K for ≈ 2 hours.

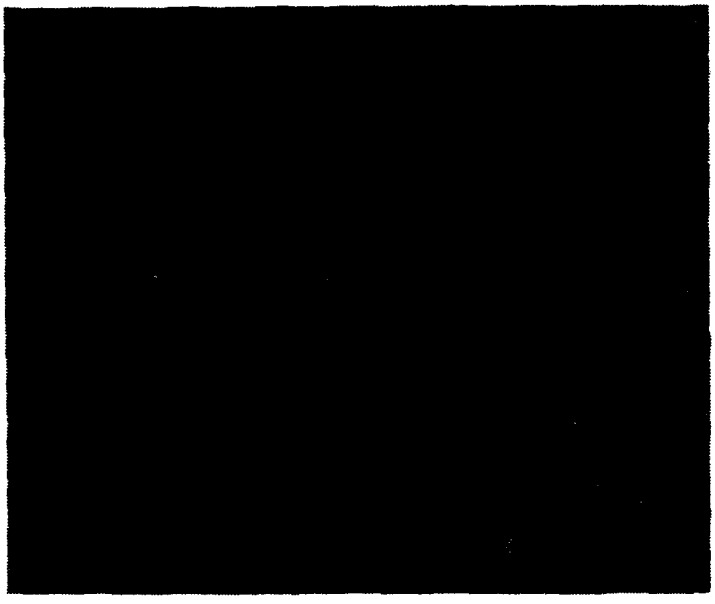

Figure 15. Optical microstructures of the as-deformed ($\bar{\varepsilon}$ = 0.65) Ti-26Al-10Nb-3V-1Mo sample at 1348 K at constant true strain rate of $10^{-2}s^{-1}$.

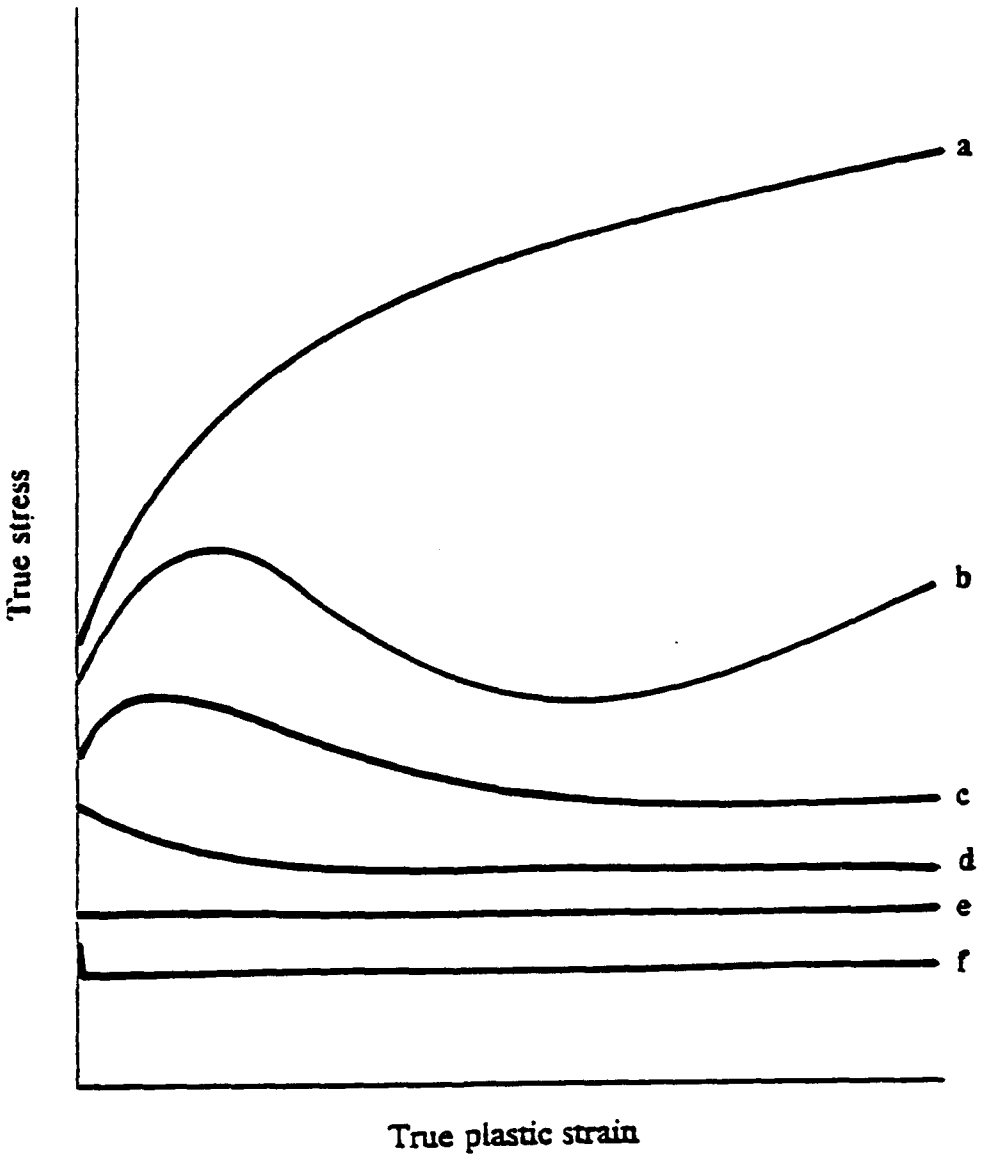

Figure 16. Illustration of the flow behavior of Ti_3Al-(Nb,V,Mo) alloys with increasing temperature and decreasing strain rate; (a) continuous strain hardening, (b) flow softening followed by strain hardening, (c) flow softening followed by steady state, (d) flow softening upon yielding, (e) continuous steady-state flow, and (f) yield point phenomenon.